Optical and X-ray Spectroscopy of Wide Band Gap Semiconductors and Organic Thin Films

THESIS

Submitted to

Aberystwyth University

by

Andrew G. McGlynn *BSc (Hons)*

In candidature for the degree of

Philosophiae Doctor

February 2010

DECLARATION

This work has not previously been accepted in substance for any degree and is not being concurrently submitted in candidature for any degree.

Signed……. (candidate)

Date……..

STATEMENT 1

This thesis is the result of my own investigations, except where otherwise stated.
Where correction services have been used, the extent and nature of the correction is clearly marked in a footnote(s).
Other sources are acknowledged by footnotes giving explicit references. A bibliography is appended.

Signed……. (candidate)

Date……..

STATEMENT 2

I hereby give consent for my thesis, if accepted, to be available for photocopying and for inter-library loan, and for the title and summary to be made available to outside organisations.

Signed……. (candidate)

Date……..

Acknowledgements

During my PhD studies I have had the chance to work with many people, and unfortunately I am unable to thank them all individually for their input. However thanks must go firstly to Prof. Andrew Evans as my supervisor, who gave me the opportunity to join the Aberystwsyth University Materials Research Group and for his continual support and enthusiasm throughout my time studying. I would also like to thank Dr. Nigel Poolton for his assistance with the synchrotron and luminescence based work presented in this thesis. Dave Francis and John Parry in the mechanical workshop have been of invaluable help by building parts for the ESD as has Matthew Gunn for his technical support with the system. Thanks must go to my fellow PhD students, past and present, Dr Alex Vearey-Roberts, Dr. Owain Roberts, Geraint Jones, Gruffudd Williams and Tom Chase for their support and the entertainment they have provided, especially during beamtime sessions. I would like to acknowledge the following funding sources; Scanwel Ltd for supplying a Case Award (and special thanks to Ian Owen at Scanwel); the Engineering and Physical Sciences Research Council (EPSRC); Element Six Ltd, for supplying the c-BN samples and Bangor University for supplying the organic molecules through the CafMAD project.

I would like to say thanks to all my friends and family and a special mention to my Mum and to my girlfriend Nicki.

ABSTRACT

This thesis reports upon synchrotron based luminescence studies of wide band gap semi-conductors and organic thin films.

The optical and structural electronic properties of cubic and hexagonal boron nitride have been studied using X-ray Excited Optical Luminescence (XEOL) and Optically Detected X-ray Absorption Spectroscopy (OD-XAS). UV/visible emission was identified in both h-BN and c-BN with additional exciton related deep UV emission for the former. UV excited luminescence measurements were used to determine the band gap energies of h-BN and c-BN, these were found to be 5.96eV ± 0.04eV and 6.36eV ± 0.03eV respectively. Spatially resolved XEOL and OD-XAS was used to investigate c-BN microcrystals revealing lateral differences in luminescence and local structure. Synchrotron/laser pump probe spectroscopy was applied to investigate defect states in h-BN and c-BN. Subsequent correlation to the XEOL emission was made proving these defects states to be responsible for the lowest energy emission bands in both materials.

Angular resolved NEXAFS, photo-luminescence (PL) and OD-XAS was used to characterise spin coated thin organic films of poly(phenylamine). The material was shown to exhibit preferred orientation within the film, but spatially resolved imaging OD-XAS revealed lateral variation in the molecular orientation. Electrospray deposition was developed for the growth of thin organic semiconducting films in ultra high vacuum. PL and OD-XAS studies were carried out on pure and mixed films of tetra sulfonated copper phthalocyanine (tsCuPc) and poly(ethyleneoxide) (PEO). Only the mixed complexes displayed infrared emission resulting from disstacking of the tsCuPc by the PEO within the film.

Table of Contents

Glossary of Abbreviations

AFM		Atomic force microscope
	C-AFM	Contact AFM
	NC-AFM	Non-contact AFM
	DF-AFM	Dynamic force AFM
ARUPS		Angular resolved ultra violet photo-electron spectroscopy
CCD		Charge coupled device
CLASSIX1		Chemical, luminescence and structure of surface by micro-imaging X-ray
CVD		Chemical vapour deposition
	PECVD	Plasma enhanced CVD
DAP		Donor accepter pair
DFT		Density functional theory
DOS		Density of states
E		Energy
	Eg	Band gap energy
ES		Electrospray
	ESD	ES deposition
	ESI	ES ionisation
	ES-MS	ES mass spectroscopy
FTIR		Fourier transform infra red spectroscopy
FWHM		Full width half maxima
HOMO		Highest occupied molecular orbital
HPHT		High pressure high temperature
HTM		Hole transport material
I		Intensity
	I_0PP	Intensity of pump probe signal
	$I_{0,XEOL}$	Intensity of XEOL signal
IR		Infra red
ITO		Indium tin oxide
LASER		Light amplification by stimulated emission radiation

LED		Light emitting diode
	OLED	Organic LED
	PLED	Polymer LED
LINAC		Linear accelerator
LO		Longitudinal optical phonon
LUMO		Lowest unoccupied molecular orbital
MAPLE		Matrix assisted pulsed laser evaporation
MoLES		Mobile luminescence end station
MPW		Multi pole wiggler
NEA		Negative electron affinity
n-type		Negatively doped semi-conductor
OD		Optically detected
OL		Optical luminescence
	CL	Cathodoluminescence
	EL	Electroluminescence
	PL	Photoluminescence
	XEOL	X-ray excited OL
OSL		Optically stimulated luminescence
PES		Photo-electron spectroscopy
PMT		Photo multiplier tube
PP		Pump probe spectroscopy
p-type		Positively doped semi-conductor
PY		Partial yield
	PEY	Partial electron yield
	PLY	Partial luminescent yield
RF		Radio Frequency
rms		Root mean square
SEM		Scanning electron microscope
SR(S)		Synchrotron radiation (source)
STM		Scanning tunnelling microscope
TY		Total yield
	TEY	Total electron yield
	TLY	Total luminescent yield
TO		Transverse optical phonon

UHV			Ultra high vacuum
UV			Ultra violet
	DUV		Deep UV
	VUV		Vacuum UV
	XUV		X-ray UV
VIS			Visible
XAS			X-ray absorption spectroscopy
	XANES		X-ray absorption near edge spectroscopy
	XAFS		X-ray absorption fine structure
		EXAFS	Extended X-ray absorption fine structure
		NEXAFS	Near edge X-ray absorption fine structure
XPS			X-ray photo-electron spectroscopy

Chapter 1

Introduction

Luminescence is the induced emission of low energy photons from within a material. Whilst this quantised light may be useful in terms of device function its origin is also of physical importance as the energy of emission corresponds to charge recombination at optical transitions; therefore luminescence can yield information regarding electronic structure. In this thesis luminescent techniques were used to investigate two classes of semi-conducting materials; inorganic III-V materials and organic small molecules and polymers.

Wide band gap III-V materials are of significant interest as they have optical activity in the ultra violet (UV) region of the spectrum, thus making them suitable for devices such as UV lasers and sensors. An example is boron nitride (BN) which has a band gap in the deep UV (~6eV). The photo absorption of BN is around its band gap energy but its luminescent emission is shifted to lower energies due to the presence of defect states within its structure. The characterisation of these defects states within BN is therefore of critical importance for its future use within light emissive devices [1, 2].

Carbon based organic molecules, considered as either polymers or small molecules can be deposited in thin films for electronic applications. Polymers are materials made up from long chains of repeating chemical units (monomers), whereas small molecules are self contained monomeric structures. Optoelectronic organic molecules

all exhibit similar conjugated bonding within their structure, resulting in delocalised electron states through which radiative charge recombination can occur [3]. The luminescent emission of organic molecules is therefore an intrinsic property of a material rather than defect related as seen in many wide band gap semi-conductors [4, 5].

Semi-conducting organic molecules are an attractive alternative to inorganic materials due to their favourable properties of mechanical flexibility, light weight, low toxicity and intrinsic luminescence. Organics can form flexible thin films due to weakly bound intermolecular structures unlike inorganic materials which are generally rigid and brittle due to their crystalline structure. Organic materials are also easily manufactured and processed, leading to low production costs when compared to inorganic materials which require expensive production methods such as vacuum growth and chemical etching. In particular the application of organic materials in light emitting diodes (OLED) is of both scientific and commercial interest. Several of the world's largest electronics companies are investing heavily in OLED technologies with some small displays already integrated into consumer goods. A typical OLED is shown in figure 1.1.

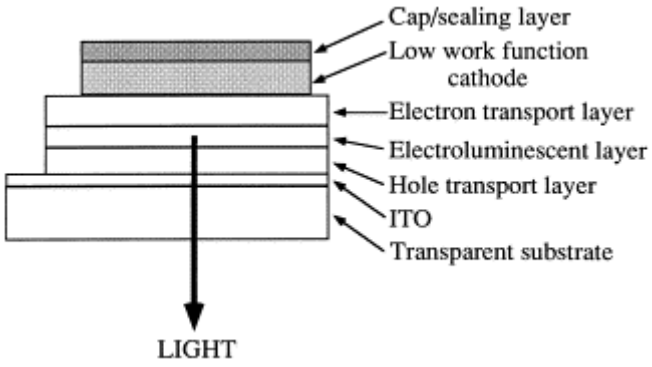

Figure 1.1 –Schematic of a basic OLED structure reproduced from the literature [6].

The electronic behaviour of materials can be investigated using surface science techniques such as X-ray absorption spectroscopy (XAS) and Photo-electron spectroscopy (PES). These techniques probe the surface states (~5nm) of materials using photo-electric interactions and require an ultra high vacuum (UHV) measurement environment in order to preserve surface cleanliness and reduce photo-electron gas molecule collisions. The materials investigated using these techniques are usually prepared *in situ* and as such many organic materials have not been studied using surface science techniques due to difficulties of depositing within UHV and irreversible degradation caused by preparation procedures. Polymers in particular are volatile molecules which cannot survive UHV sublimation and are therefore usually deposited *ex situ*. The surface states of organic thin films are also susceptible to oxidation from exposure to atmosphere [7], therefore the deposition of these materials directly into UHV is of critical importance.

There are many different techniques employed in the deposition of organic thin films including spin coating [8], inkjet printing [9, 10], roll to roll printing and Langmuir-Blodgett dip processing [11]. There are also techniques of plasma deposition [12] and laser vapour deposition [13, 14] which can be used to produce thin films in clean gas atmospheres. However there are two UHV deposition methods which have been developed over the last decade, the first being Matrix Assisted Pulsed Laser Evaporation (MAPLE) and the second Electrospray Deposition (ESD).

MAPLE is a novel polymer deposition technique developed by the Naval Research Laboratories, Washington [15].

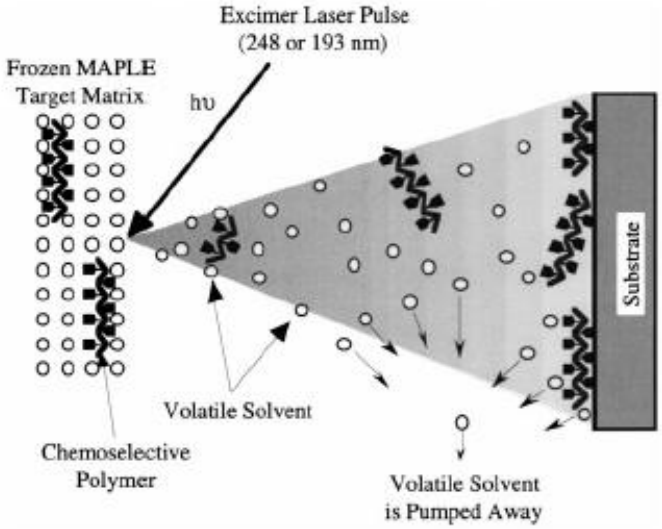

Figure 1.2 – Schematic of the MAPLE process, reproduced from the literature [15].

The MAPLE process is diagrammatically represented in figure 1.2. A frozen target of polymer/solvent solution is irradiated by a pulsed laser causing the solvent to vaporise. The polymer molecules obtain sufficient kinetic energy through collisions with the solvent to be transferred into the vapour phase. This evaporation of the target creates a plume of polymer and solvent molecules from which films of polymer grow on a target substrate in direct line of sight of the target matrix.

ESD is a deposition technique based upon electrospray mass spectroscopy (ES-MS) methodology [16], developed into a deposition technique as depicted in figure 1.3.

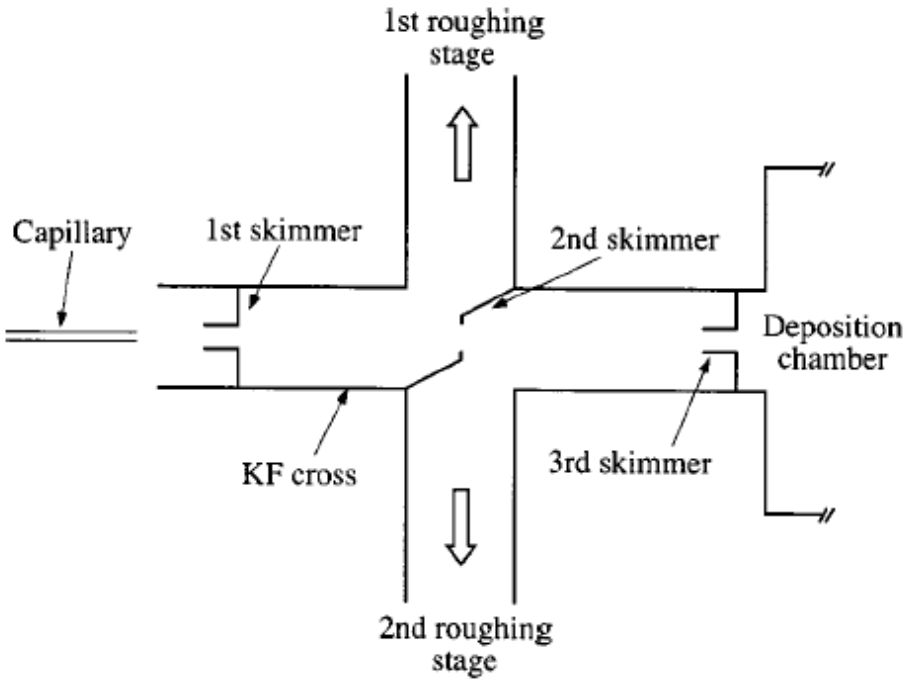

Figure 1.3 –Schematic of UHV electrospray deposition apparatus reproduced from the literature [17].

This technique transfers ionised droplets of solute molecules from air into UHV via a differentially pumped vacuum system, yielding a beam of molecules for deposition onto substrates within UHV [18-21].

ESD was chosen as a suitable deposition technique as it could be easily integrated into the existing systems of the Aberystwyth University Materials Research Group. The ESD system built as part of this work is presented in Chapter 4 with a more detailed explanation of the technique.

As explained the nature of luminescent emission from wide band gap semi-conductors and organic thin films is markedly different, but its presence allows for similar experimental techniques to be applied. This work will demonstrate how luminescence detection methods can be used to probe the electronic structure of wide band gap

semi-conductors and organic thin films. The thesis is presented in the following manner; in Chapter 2 the theory of optically detected XAS and other experimental techniques are introduced. Chapter 3 will present details of the experimental instrumentation used within this study including an introduction to synchrotron radiation and the relevant beamlines of the synchrotron radiation source, Daresbury. Chapter 4 describes the ESD system built as part of this study including background research, design considerations and commissioning tests. In Chapter 5 the boron nitride results are presented following a detailed introduction to the materials. Experimental investigations into the luminescent emission, band gap energies and charge trapping dynamics are included. In Chapter 6 the results of investigations into organic thin films are presented. Experimental investigations of photo-luminescence, molecular orientation and regional growth of thin films of poly(tri-phenylamine) are presented along with photo-luminescent and structural investigations of organic thin films produced with the ESD system. Finally in Chapter 7 conclusions are made regarding the results and possible future investigations are proposed.

1. T.K. Paul, P. Bhattacharya and D.N. Bose. *Characterization of pulsed laser deposited boron nitride thin films on InP,* Applied Physics Letters, 1990. **56**(26): 2648.

2. M.A. Reshchikov. *Strong suppression of the yellow luminescence in C-doped GaN in air ambient,* Applied Physics Letters, 2006. **89**(23): 232106.

3. B. Liu and W. Huang. *Novel deep blue fluorescent fluorene-based copolymer containing hole-transporting arylamine segments,* Thin Solid Films, 2002. **417**: 206-210.

4. D.Y. Kim, H.N. Cho and C.Y. Kim. *Blue light emitting polymers,* Progress in Polymer Science, 2000. **25**(8): 1089.

5. R.E. Martin, F. Geneste and A.B. Holmes. *Synthesis of conjugated polymers for application in light-emitting diodes (PLEDs),* Comptes Rendus de l'Academie des Sciences - Series IV - Physics, 2000. **1**(4): 447.

6. P.E. Burrows, V. Bulovic, G.R. Gu, V.G. Kozlov, S.R. Forrest and M.E. Thompson. *Light emitting devices using vacuum deposited organic thin films,* Thin Solid Films, 1998. **331**(1-2): 101-105.

7. D. Posadas, M.J. Rodriguez Presa and M.I. Florit. *Apparent formal redox potential distribution in electroactive arylamine-derived polymers,* Electrochimica Acta, 2001. **46**: 4075-4081.

8. V. Vohra, G. Calzaferri, S. Destri, M. Pasini, W. Porzio and C. Botta. *Toward White Light Emission through Efficient Two-Step Energy Transfer in Hybrid Nanofibers,* ACS Nano, 2010. **4**(3): 1409-1416.

9. P. Calvert. *Inkjet Printing for Materials and Devices,* Chemistry of Materials, 2001. **13**: 3299.

10. T.R. Hebner, C.C. Wu, D. Marcy, M.H. Lu and J.C. Sturm. *Ink-jet printing of doped polymers for organic light emitting devices,* Applied Physics Letters, 1998. **72**(5): 519-521.

11. D. Braun. *Semiconducting polymer LEDs,* Materials Today, 2002. **5**(6): 32.

12. I. Sugimoto, M. Nakamura, N. Kasai and T. Katoh. *Gas-sorption effects on plasma polymer films characterized by XPS and quartz crystal resonator,* Polymer, 2000. **41**(2): 511-522.

13. S.L. Johnson, H.K. Park and R.F. Haglund Jr. *Properties of conductive polymer films deposited by infrared laser ablation,* Applied Surface Science, 2007. **253**(15): 6430.

14. K. Grytsenko, O. Lytvyn, L.F. Ivanov, P.N. Grakovich, M. Sonntag and S. Schrader. *Polymer films filled with organic molecules by CO2 laser evaporation in vacuum,* Applied Surface Science, 2007. **253**(19): 8028-8031.

15. A. Pique, R.A. McGill, D.B. Chrisey, D. Leonhardt, T.E. Mslna, B.J. Spargo, J.H. Callahan, R.W. Vachet, R. Chung and M.A. Bucaro. *Growth of organic thin films by the matrix assisted pulsed laser evaporation (MAPLE) technique,* Thin Solid Films, 1999. **355-356**: 536.

16. S.D. Hanton, I.Z. Hyder, J.R. Stets, K.G. Owens, W.R. Blair, C.M. Guttman and A.A. Giuseppetti. *Investigations of electrospray sample deposition for polymer MALDI mass spectrometry,* Journal of the American Society for Mass Spectrometry, 2004. **15**(2): 168.

17. N. Dam, M.M. Beerbom, J.C. Braunagel and R. Schlaf. *Photoelectron spectroscopic investigation of in-vacuum-prepared luminescent polymer thin films directly from solution,* Journal of Applied Physics, 2005. **97**(2): 024909.

18. J.C. Swarbrick, J.B. Taylor and J.N. O'Shea. *Electrospray deposition in vacuum,* Applied Surface Science, 2006. **252**(15): 5622-5626.

19. J.N. O'Shea, J.B. Taylor, J.C. Swarbrick, G. Magnano, L.C. Mayor and K. Schulte. *Electrospray deposition of carbon nanotubes in vacuum,* Nanotechnology, 2007. **18**(3): 035707.

20. A. Saywell, G. Magnano, C.J. Satterley, L.M.A. Perdigao, N.R. Champness, P.H. Beton and J.N. O'Shea. *Electrospray deposition of C-60 on a hydrogen-bonded supramolecular network,* Journal of Physical Chemistry C, 2008. **112**(20): 7706-7709.

21. A.J. Cascio, J.E. Lyon, M.M. Beerbom, R. Schlaf, Y. Zhu and S.A. Jenekhe. *Investigation of a polythiophene interface using photoemission spectroscopy in combination with electrospray thin-film deposition,* Applied Physics Letters, 2006. **88**(6): 062104.

Chapter 2

Experimental Theory

In this chapter the theoretical considerations applicable to the experimental results are introduced. The interaction of light with matter is the initial point from which the concept of X-ray absorption spectroscopy (XAS) is introduced. Experimental XAS methods are explored with the concept of luminescence detection explained. Finally pump probe spectroscopy is considered in reference to the charge trapping dynamics of semi-conducting materials.

The inter-atomic distribution of bonding electrons within solids dictate intrinsic electronic, chemical, structural, optical and magnetic properties. Electrons exist in discrete allowed energy states which can be derived from modification of the Schrödinger equation. Probing of the electronic states can be achieved by photo-electric excitation with radiation wavelengths energetically comparable to the band gap (UV/visible), intra-bonding levels (VUV) or core level (X-ray).

2.1 The interaction of light with matter

Quantum mechanical consideration of electron photo-excitation describes the interaction of the incident radiation's electric field component with an electron's momentum vector [1].

An electron system can be said to be in an initial ground state in the absence of external forces. The ground state Hamiltonian $V(r)$, can be solved explicitly and is

considered a time-independent constant. However when photons are introduced the system is subjected to a small time-dependent perturbation, $\mathbf{\Delta}$, whereby electrons can become excited from an initial to a final state wavefunction. Thus the Hamiltonian describing the system can be written as;

$$H = V(r) + \mathbf{\Delta} \tag{2.1}$$

The transition probability per unit time, P_{if}, of exciting an electron from an initial state *i* to a final state *f* can be described by "Fermi's 2nd Golden Rule" [1].

$$P_{if} = \frac{2\pi}{\hbar}\left|\langle f|\mathbf{\Delta}|i\rangle\right|^2 \delta_f(E) \tag{2.2}$$

Where $\langle f|\mathbf{\Delta}|i\rangle$ represents the matrix element of the perturbation Hamiltonian between the two states due to the incident photon and $\delta_f(E)$ represents the energy density of the final state, which can be either normalised to a Dirac delta function of the photo-electron kinetic energy for a continuum state or unit normalisation for a bound state.

In the general case, the perturbation Hamiltonian can be expressed in the terms of the incident photon vector field (**A**), the electron momentum operator (**p**), and the scaler potential (ϕ);

$$\mathbf{\Delta} = \frac{e}{2mc}(\mathbf{A}\cdot\mathbf{p} + \mathbf{p}\cdot\mathbf{A}) - e\phi + \frac{e^2}{2mc^2}(\mathbf{A}\cdot\mathbf{A}) \tag{2.3}$$

The $(\mathbf{A}\cdot\mathbf{A})$ term which describes the photon-photon interaction is extremely small for all experimental work conducted during this study and can be considered negligible. By application of the Coulomb gauge, the scaler potential is a constant with time and is therefore considered within the time independent term $V(r)$.

By consideration of the momentum vector $\mathbf{p} = i\hbar\nabla$ the commutation,

$$\mathbf{A}\cdot\mathbf{p} + \mathbf{p}\cdot\mathbf{A} = 2\mathbf{A}\cdot\mathbf{p} + i\hbar(\nabla\cdot\mathbf{A}) \tag{2.4}$$

can be applied, the final term of which reduces to zero with translational invariance of the vector field over the whole volume. Thus, the perturbation Hamiltonian can be simplified to;

$$\mathbf{\Delta} = \frac{e}{mc}(\mathbf{A}\cdot\mathbf{p}) \tag{2.5}$$

By substitution of equation 2.5 into 2.2 the transition probability becomes;

$$P_{if} = \frac{2\pi e^2}{\hbar m^2 c^2}\left|\langle f\left|(\mathbf{A}\cdot\mathbf{p})\right|i\rangle\right|^2 \delta_f(E) \tag{2.6}$$

The photon vector potential can be written in the form of a planer electromagnetic wave of wave vector **k**, frequency ω and unit vector **e**;

$$\mathbf{A} = \mathbf{e}A_0\cos(\mathbf{k}\cdot\mathbf{x} - \omega t) = \mathbf{e}\frac{A_0}{2}(e^{i(\mathbf{k}\cdot\mathbf{x}-\omega t)} + e^{-i(\mathbf{k}\cdot\mathbf{x}-\omega t)}) \tag{2.7}$$

The $e^{-(k\cdot x-\omega t)}$ term can be disregarded, as this would describe the emission of a photon if the atom had a core hole. At photon energies <<10keV the dipole approximation can be applied, where **A** can be considered constant as atomic separation is significantly larger than the photon wavelength, thus only the first term in the expansion of the exponential need be retained, $e^{i(\mathbf{k}\cdot\mathbf{x})} \approx 1$. Therefore the transition probability can be finally expressed as equation 2.8.

$$P_{if} = \frac{\pi e^2}{2\hbar m^2 c^2} A_0{}^2 \left| \langle f | (\mathbf{e}\cdot\mathbf{p}) | i \rangle \right|^2 \delta_f(E) \qquad (2.8)$$

2.1.1 The X-ray absorption cross section

The X-ray absorption cross section (σ_x) sums electron transition probabilities as a function of incident radiation energy, defined as, the number of electrons excited per unit time divided by the number of incident photons per unit time per unit area [2].

$$\sigma_x = \frac{P_{if}}{F_{ph}} \qquad (2.9)$$

The photon flux F_{ph} is given by the electromagnetic field energy flux divided by the photon energy;

$$F_{ph} = \frac{A_0{}^2 \omega}{8\pi\hbar c} \qquad (2.10)$$

By combining the terms for electron transition probability and photon flux the X-ray absorption cross section can be expressed in its final form;

$$\sigma_x = \frac{4\pi^2 e^2}{m^2 c\omega} \left| \langle f | \mathbf{e} \cdot \mathbf{p} | i \rangle \right|^2 \delta_f(E) \qquad (2.11)$$

2.2 X-ray Absorption Spectroscopy (XAS)

X-ray absorption spectroscopy (XAS) explores the chemistry and structure of materials by measuring X-ray absorption as a function of incident photon energy. The fundamental dynamics of XAS are governed by the X-ray absorption cross section (σ_x), whereby measured X-ray absorption is the sum of σ_x for all possible transitions. Historically XAS techniques have concentrated upon the measurement of induced photo-electron (surface sensitive) or X-ray fluorescent (bulk) emission. However, optically detected XAS (OD-XAS) has shown potential as a complementary technique, able to correlate differences in surface and bulk bonding. OD-XAS measures the induced low energy luminescent intensity as a function of X-ray excitation energy, linking light emission directly to its chemical origin [3-8].

The development of tuneable radiation sources such as synchrotrons (Chapter 3) has led to XAS becoming a widely used and powerful research technique. At X-ray photon energies below 100keV the dominant absorption process is the photo-electric effect, where the complete absorption of a photon results in the emission of a photo-electron. The X-ray photo-electric absorption coefficient decreases proportionally

with increasing photon energy. However, when the photon energy reaches the ionisation of a core electron shell a marked increase in absorption occurs as depicted in figure 2.1 (a).

This sharp jump, referred to as an absorption edge, indicates the opening of an additional absorption channel within the material. Electrons are promoted from the core shell to the lowest unoccupied electron state. The absorption edges of the L and K shells are of the greatest importance as they have significant energy separation to be resolved. For the work contained within this thesis only K-edge absorption was studied. The K shell consists of only the 1s state and can therefore be considered as a delta energy function in terms of density of states (DOS), thus the measurement of X-ray absorption directly maps the density of bound states in the conduction band. The absorption edge ionisation energies of atoms are element specific, therefore XAS techniques can selectively probe atomic sites within a material.

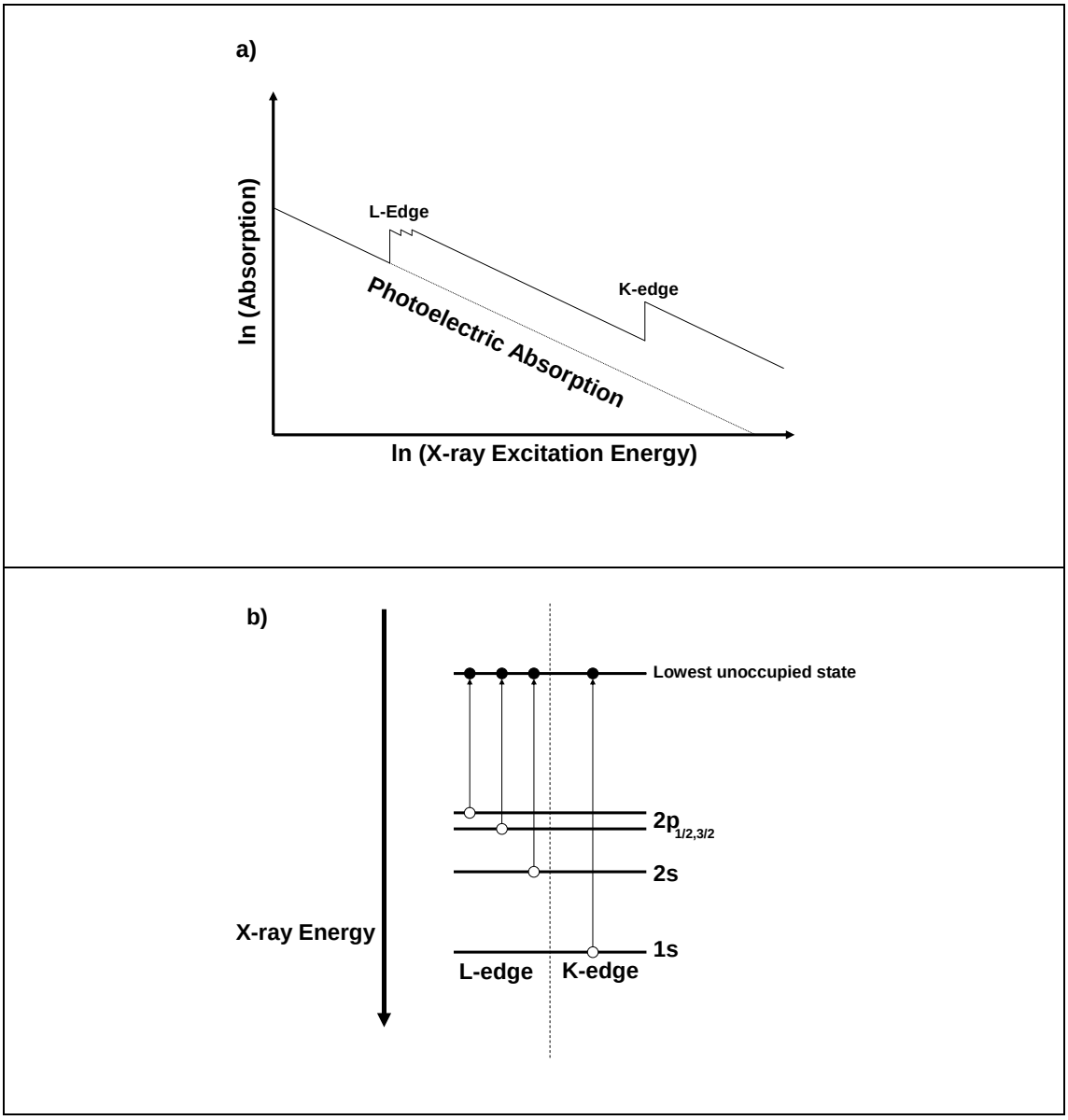

Figure 2.1 – a) Schematic representation of the X-ray absorption coefficient as a function of X-ray excitation energy. Marked increases in absorption occur at the core state ionisation energies of the L and K shell. b) Schematic of electron excitation at the L and K edges with reference to annotation of a).

On closer inspection an absorption edge has structure relating to atomic spacing and chemical state. This leads to specialised XAS spectroscopic techniques as indicated in figure 2.2, each concerned with separate regions of the absorption edge spectra.

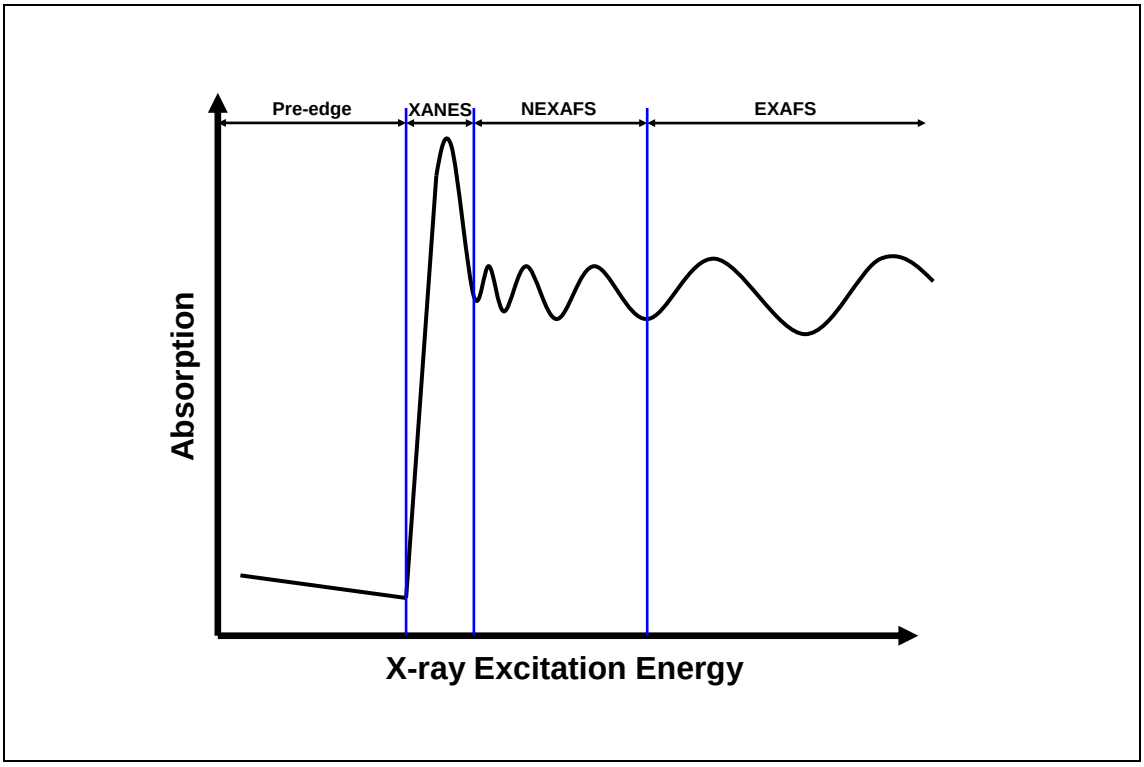

Figure 2.2 – Detailed view of absorption edge features. Regions indicated with respect to XAS spectroscopic techniques as detailed in the text.

2.2.1 XANES

X-ray Absorption Near Edge Structure (XANES) measures absorption across the onset of the edge, the core to lowest unoccupied state transition, as depicted in figure 2.3. XANES establishes the energy at which the edge occurs comparing the pre-edge and edge absorption.

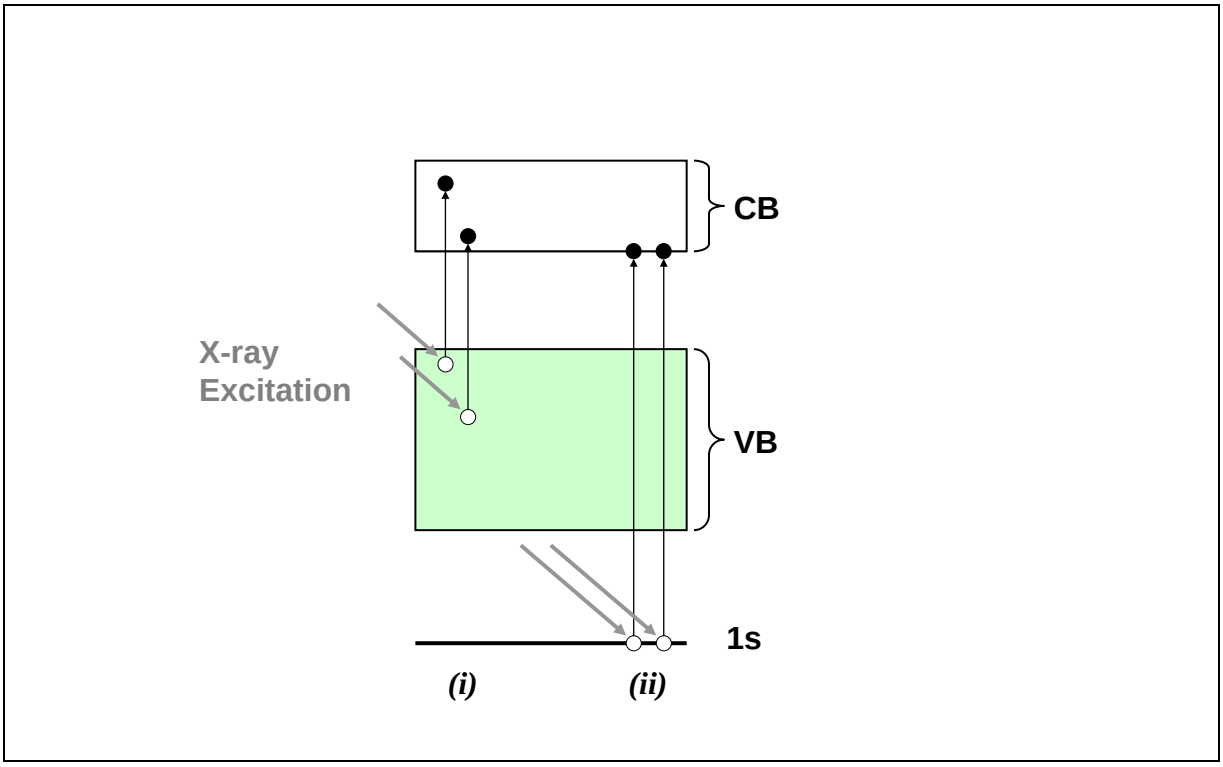

Figure 2.3 – Schematic representation of X-ray absorption (i) pre-edge (ii) at the K-edge.

Pre-edge absorption of X-rays results in the promotion of valence electrons to higher conduction or continuum energy states. This is a non-resonant process with electrons being excited from a high density of states (valence band) to a high density of states (conduction band/ continuum), creating a general non-resonant absorption background.

At the absorption edge energy, ionisation of the core state establishes a core to lowest unoccupied state resonance, increasing absorption significantly from the pre-edge condition.

The energy at which the absorption edge occurs contains important information about the chemical state of the atoms within the material [9]. XANES is particularly sensitive to bonding differences, being able to differentiate between π^* and σ^*

resonances. Thus, XANES can and has been used to in differentiate between phase differences in materials with identical chemical constituents [2, 10].

2.2.2 XAFS

X-ray Absorption Fine Structure (XAFS) analyses ripples in the post edge absorption spectra. These ripples are due to interference between the outgoing photo-electron waves and the back scattered waves from neighbouring atoms. The interference acts to enhance (constructive) or diminish (destructive) the detectable absorption for a given X-ray photon energy.

Near Edge XAFS (NEXAFS) applies to the region within 50eV of the absorption edge onset and is attributed to localised atomic spacing. The region post 50eV is due to long range delocalised order and is referred to as Extended XAFS (EXAFS).

XAFS effects are therefore absent from isolated atomic systems (gases) and become more pronounced with increasing numbers of atomic neighbours about the absorption site (solids).

2.3 Relaxation Events

X-ray photon absorption results in electron holes being created in the valence (pre-edge) or core (post-edge) states. In order for the atomic system to return to thermal equilibrium, these vacant holes must relax through recombination with electrons in higher energy states. There are three crucial processes involved in atomic relaxation pertinent to XAS experimental techniques, which are diagrammatically represented in

figures 2.4, 2.5 and 2.7. It is worth noting that a single photon absorption may give rise to a cascade of relaxation events.

2.3.1 Fluorescent X-ray emission

Fluorescent X-ray emission is the simplest relaxation event, as depicted in figure 2.4. A core hole is filled by an electron from a higher energy state, this recombination results in the electron relinquishing its energy as a fluorescent X-ray.

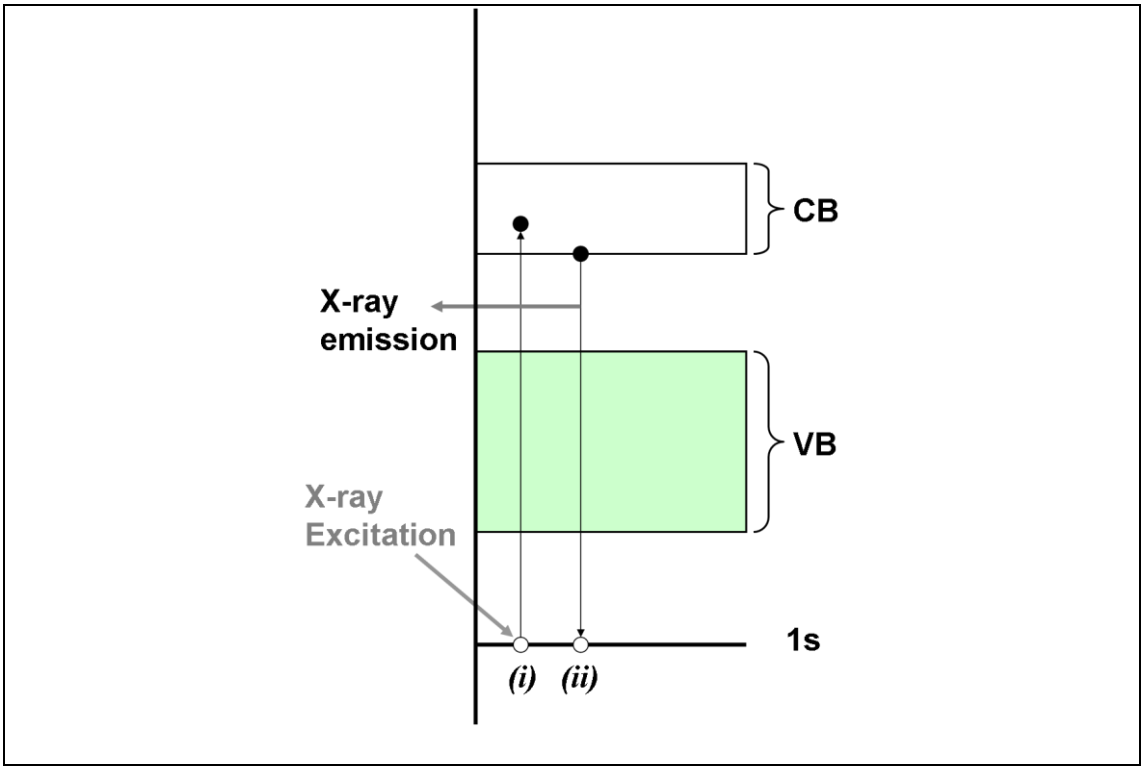

Figure 2.4 – Schematic representation of fluorescent X-ray emission following core state X-ray absorption. The shaded area indicates occupied states in the valence band. (i) X-ray absorption - exciting electron from core 1s to conduction band state. (ii) X-ray emission from recombination of electron in conduction state with 1s core hole.

2.3.2 Auger electron emission

An electron recombines with a vacant core hole by dropping down from a higher energy state. The energy relinquished by this first electron is transferred to a second within the same atom which is then subsequently emitted. Auger electrons are therefore of fixed kinetic energy regardless of the excitation X-ray energy.

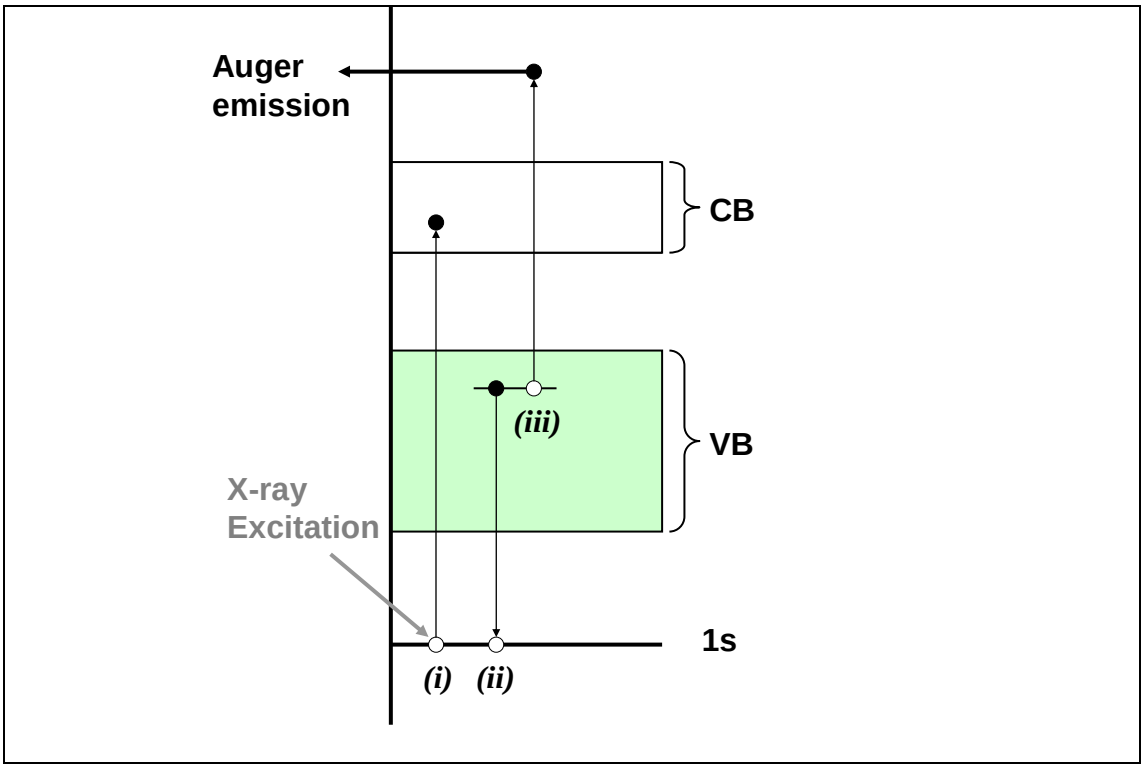

Figure 2.5 – Schematic representation of Auger electron emission due to core state X-ray absorption. The shaded area indicates occupied states in the valence band. (i) X-ray absorption - exciting electron from core 1s to conduction band state. (ii) Recombination of core hole with electron from occupied state (iii) Energy released during (ii) transferred to second electron which is then subsequently emitted from the sample.

2.3.3 Charge transfer and luminescent emission

The mobility and lifetime of charge carriers dictates the physical distance from an absorption site subsequent charge can propagate before recombining. The electron and electron hole are charge carriers having negative and positive charge respectively. Excited electrons move within the continuum and conduction states with kinetic energy absorbed from the incident X-rays. An electron's mobility within a material is governed by the inelastic mean free path, which statistically describes the physical distance an electron can travel before being inelastically scattered, figure 2.6.

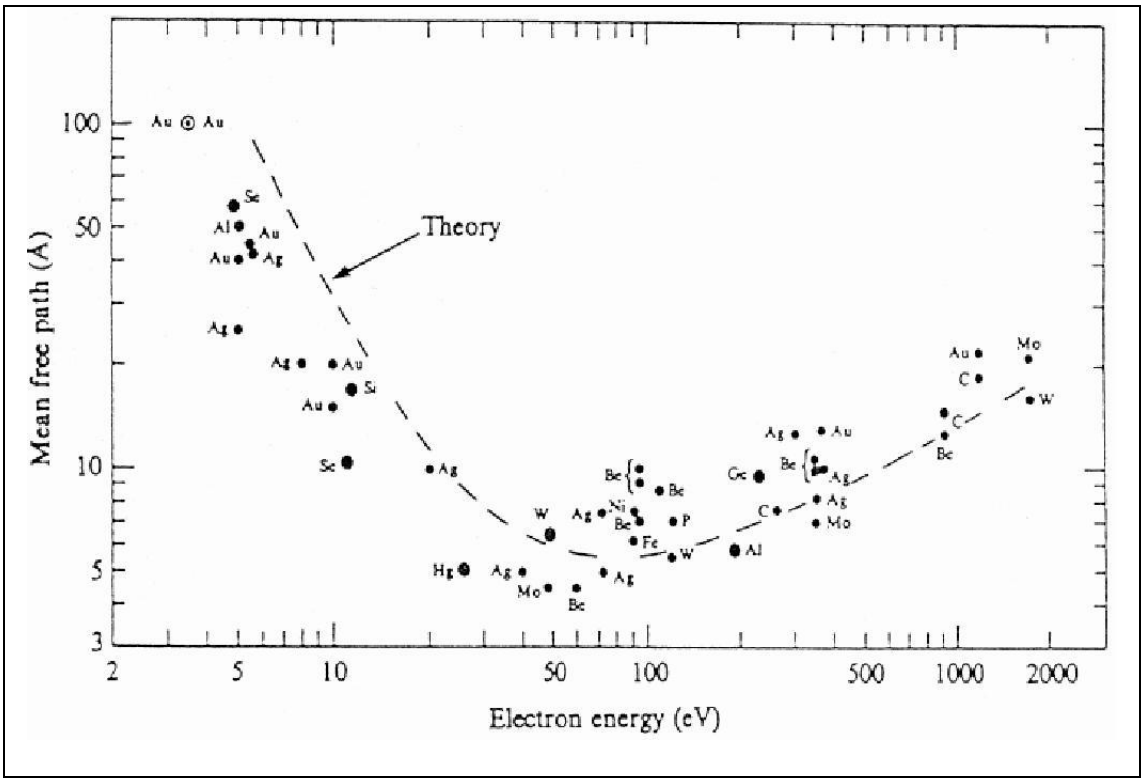

Figure 2.6 – The experimental inelastic mean free path of electrons in Angstroms [11].

The electron energy dissipation causes a cascade of electrons from higher states filling holes to restore thermal equilibrium. The cascade of electrons results in electrons and

holes populating the lowest conduction and highest valence states respectively, either side of the band gap. Electrons recombine with holes across the band gap emitting the associated energy for the separation between states.

Optical luminescence (OL) is the emission of low energy photons (UV/VIS/IR) due to the recombination of electrons across optical transitions within the band gap. Materials can contain numerous optical transitions which contribute to a total yield luminescent signal, many of which are due to defect states [12]. Luminescent emission can be wavelength analysed at fixed excitation energy to resolve between separate optical transitions. Lasers are often used as excitation sources for most materials, however for wide band gap materials such as BN (~6eV) fixed energy X-rays are utilised in a technique known as X-ray excited optical luminescence (XEOL) [3-5, 13, 14].

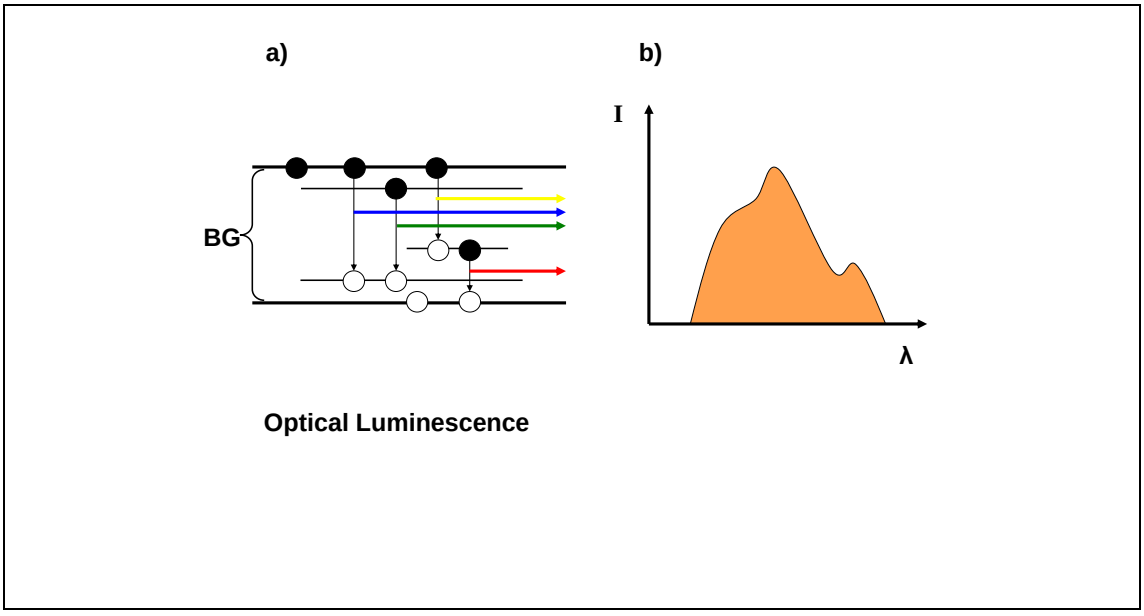

Figure 2.7 – a) Schematic representation of defect related luminescent emission from optical transitions within the band gap. b) A representation of a typical wavelength resolved OL emission intensity graph (colour indication of wavelength).

2.4 Thermal quenching of OL

Thermal increase has a quenching effect upon the luminescent intensity of crystalline solids. This is due to non-radiative decay transitions becoming active as temperature increases (phonons). In order to derive the thermal relationship between radiative and non-radiative luminescent yield, it is necessary to define a simple two level luminescent electron decay system, with a higher energy excited state and lower energy ground state [15]. The rate of change in population of the higher energy state can be described as $\left(\frac{dN_2}{dt}\right)$;

$$\left(\frac{dN_2}{dt}\right) = G - \frac{N_2}{\tau_{radiative}} - \frac{N_2}{\tau_{non-radiative}} \qquad (2.12)$$

Where N_2 is the population of the upper state (proportional to the intensity of luminescence) and G is the rate of excitation. The recombination relaxation times of radiative and non-radiative luminescent decay are denoted by $\tau_{radiative}$ and $\tau_{non-radiative}$ respectively. If G and $\tau_{radiative}$ are independent of temperature it can be assumed that they remain constant. Therefore the temperature dependence of luminescent emission is dependent upon $\tau_{non-radiative}$, which decreases with temperature rise (2.13).

$$\frac{1}{\tau_{non-radiative}} = Ae^{-\frac{E_A}{k_B T}} \qquad (2.13)$$

Where A is the rate of non-radiative decay due to temperature and E_A is the minimum activation energy. The thermal quenching relationship can be attained by substituting equation (2.13) into equation (2.12) and solving for the steady state condition where $\left(\frac{dN_2}{dt}\right) = 0$, this results in equation (2.14)

$$Intensity: I = \frac{I_0}{1 + Be^{-\frac{E_A}{k_B T}}} \tag{2.14}$$

Where $I_0 = G.\tau_{radiative}$ and B is the ratio of $\tau_{radiative}$ to $\tau_{non-radiative}$

Lowering the temperature of a crystal removes thermal energy from the system thus reducing the effect of non-radiative transitions. At temperatures about absolute zero electrons are more likely to recombine via luminescent rather than non-radiative channels. Therefore in order to maximise luminescent intensity, experiments are conducted with samples cryogenically cooled to ~10K. The minimum activation energy E_A can be measured experimentally by monitoring the luminescent emission intensity as a function of sample temperature.

2.5 Methods of XAS detection

Having explained the key principles of XAS, detection of the X-ray absorption will now be considered.

For transparent materials, absorption can be directly measured by detection of the incident X-rays through the material itself. However for fully absorbing materials, such as those considered in this study, absorption is measured indirectly as a function of secondary emission due to relaxation processes, either photo-electron (Auger and

general photo-electron emission), fluorescent X-ray emission or luminescent emission.

Photo-electron detection is achieved either by placing a retarding voltage detector facing the sample (partial yield) or measuring the drain current as electrons are emitted from the surface (total yield). Fluorescent emission detectors are placed in front of the sample in the same manner as partial yield electron detectors. Both electron and fluorescent X-ray collection are well established experimental techniques, however that of luminescent emission is still very much in its infancy. The detection of luminescent emission is in principle as straight forward as that of fluorescence but the response at the absorption edge needs further explanation.

2.6 OD-XAS

Optically detected XAS (OD-XAS) is a specialised technique which records the absorption of the incident X-ray flux as a function of luminescent emission [4, 5, 13, 14, 16, 17]. OD-XAS probes the chemical origin of optical emission by measuring the luminescent yield whilst irradiating at absorption edge energies. A qualitative explanation of the underlying physics governing OD-XAS is presented, although it is worth noting there have been theoretical discussions of the technique [4, 18, 19].

In order to explain the concept of OD-XAS we must again consider an atomic system pre-edge and at the absorption edge energy, but this time concentrate upon the luminescent response, figure 2.8.

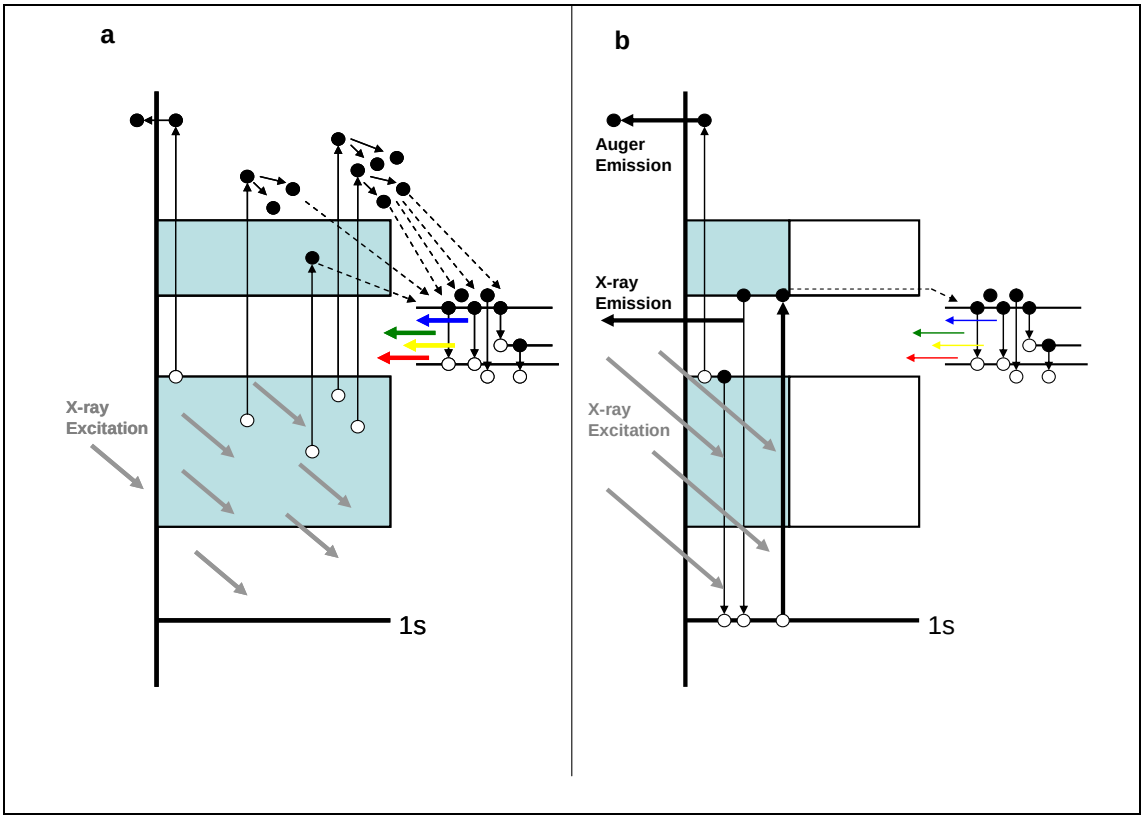

Figure 2.8 – Schematic representation of total luminescent yield in a thick sample due to X-ray absorption a) pre-edge non-resonant and b) at absorption edge resonance. The X-ray penetration depth is indicated by the shaded area. The sum of the luminescent centres is shown as a series of defect states which exist within the band gap.

Pre-edge - electrons are being excited from valence to conduction/continuum states throughout the X-ray sampling depth, delocalised to the atomic centres. Electrons are effectively being pumped into the conduction band populating the upper band gap due to the subsequent electron cascade. Assuming luminescent centres exist within the band gap, luminescent emission will occur as electrons recombine via these channels. This process creates a background **non-resonant** luminescent signal for the entire system which linearly increases with X-ray excitation energy [20].

At the absorption edge – **resonant** localised electron excitation occurs between the core 1s and the lowest conduction state, creating a dominant transport channel at the

atomic absorption centres. This causes a measurable jump in the luminescent response which can be positive or negative with respect to the non-resonant background.

2.6.1 OD-XAS luminescent response

There are several factors which affect the response of the luminescent emission at the absorption edge which include charge mobility, sample thickness and localised chemical environment.

2.6.1.1 Charge mobility and chemical environment effects

Low temperature conditions create a ground state system in which all states below the Fermi level are filled and all those above vacant. When a core state absorption occurs, a cloud of charge is created due to the creation of a highly energetic core hole. Charge propagates radially from the site of absorption with a maxima proportional to the sample temperature [20]. The charge cloud's physical size is greatly reduced at lower temperatures due to reduced phonon contribution, therefore core absorption is localised to the atomic centres. Only if this charge cloud reaches a luminescent centre will a photon result from a core absorption event. This effect has been experimentally verified by monitoring the luminescent yield with temperature of separate emission bands in high purity quartz (SiO_2) [8]. Observations of positive absorption edge jumps becoming negative with reduced sample temperature have also been witnessed [8, 18, 21].

2.6.1.2 Sample thickness effects

The background non-resonant signal is proportional to the amount of material being irradiated [18, 19]. Therefore a thicker sample in which all the incident radiation is absorbed will have a greater background signal than one of the same material with a thickness smaller than the X-ray penetration depth.

For the case of a thick sample, the effective penetration depth reduces significantly at the absorption edge energy as the incident X-ray energy is scanned [22]. This decreases the total volume in which all the X-ray flux is absorbed, thus reducing the non-resonant background signal causing a negative jump in luminescence at the edge [18, 19].

For the case of a thin sample (of thickness less than the penetration depth at the edge) the X-ray penetration depth remains constant. With a reduced thickness the background non-resonant signal is relatively small, therefore at the absorption edge energy an increase in luminescent yield results in a positive jump relative to the background [4].

The depth from which a luminescent photon can be emitted is dependent upon self absorption within the material. The effect of self absorption acts to enhance the sample thickness dependence of the absorption edge jump. This is due to the probability of self absorption being proportional to the amount of material through which the luminescent photon must travel. Therefore, a luminescent photon has a greater probability of being emitted and subsequently detected from a thin sample than one from deep within a thick sample [23]

Experimental studies of sample thickness effects upon OD-XAS have been reported, with signals being shown to be both positive and negative for the same materials. It is

important to note that localised luminescent yield generally increases at the absorption edge but sample thickness is the prominent factor which dictates the type of edge jump observed.

2.6.2 Partial Yield OD-XAS

In order to investigate the chemical origin of specific luminescent bands, as per XEOL, partial yield OD-XAS can be employed [20, 24-26]. Monochromators can be used to selectively filter the OD-XAS signal at specific wavelengths creating a partial yield spectrum. Correlation of the XEOL emission to the PY OD-XAS directly links luminescent emission to its chemical origin. Studies have been conducted using this method to evaluate bonding differences between bulk and surface states in mixed phase materials [10, 20].

2.7 Pump Probe Spectroscopy

Pump probe spectroscopy (PP) is a common technique for the investigation of transient charge trapping dynamics in semi-conducting materials [27]. Two fixed energy photon excitation sources are utilised, one as a pump and the other a probe. The pump source excites electrons across the band gap inducing non-resonant luminescence (XEOL). The probe source (of energy less than the band gap) is applied in conjunction with the pump and the effect upon the XEOL measured. Measurements are made cyclically by controllably pulsing the probe source whilst continually irradiating with the pump, an annotated example of a typical PP scan is shown in figure 2.9.

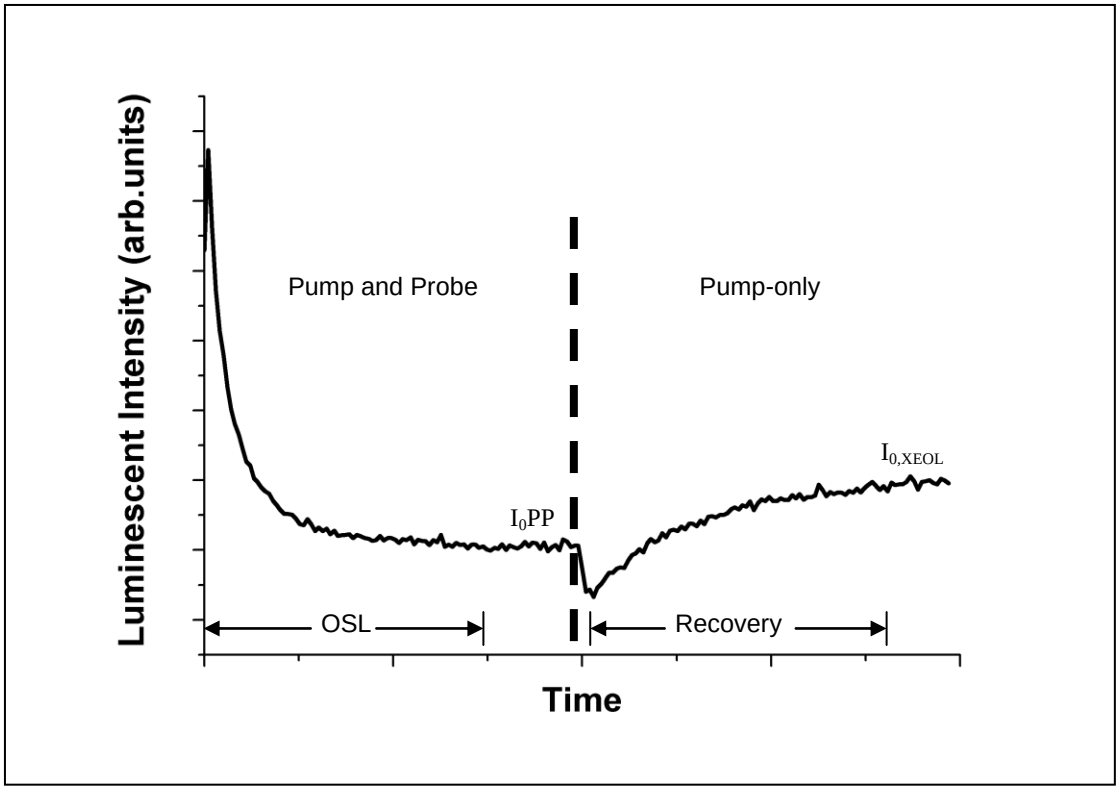

Figure 2.9 – Annotated pump probe scan showing regions of pump probe and pump-only interactions.

Generally lasers are used for both excitation sources. However, for wide band gap materials pump sources must have sufficient energy to excite between the valence and conduction/continuum states, therefore higher energy sources must be implemented (e.g. synchrotron radiation or Deutrium lamp).

In reference to figure 2.9, there is a clear distinction between the pump probe and pump-only regions, both of which must be considered separately.

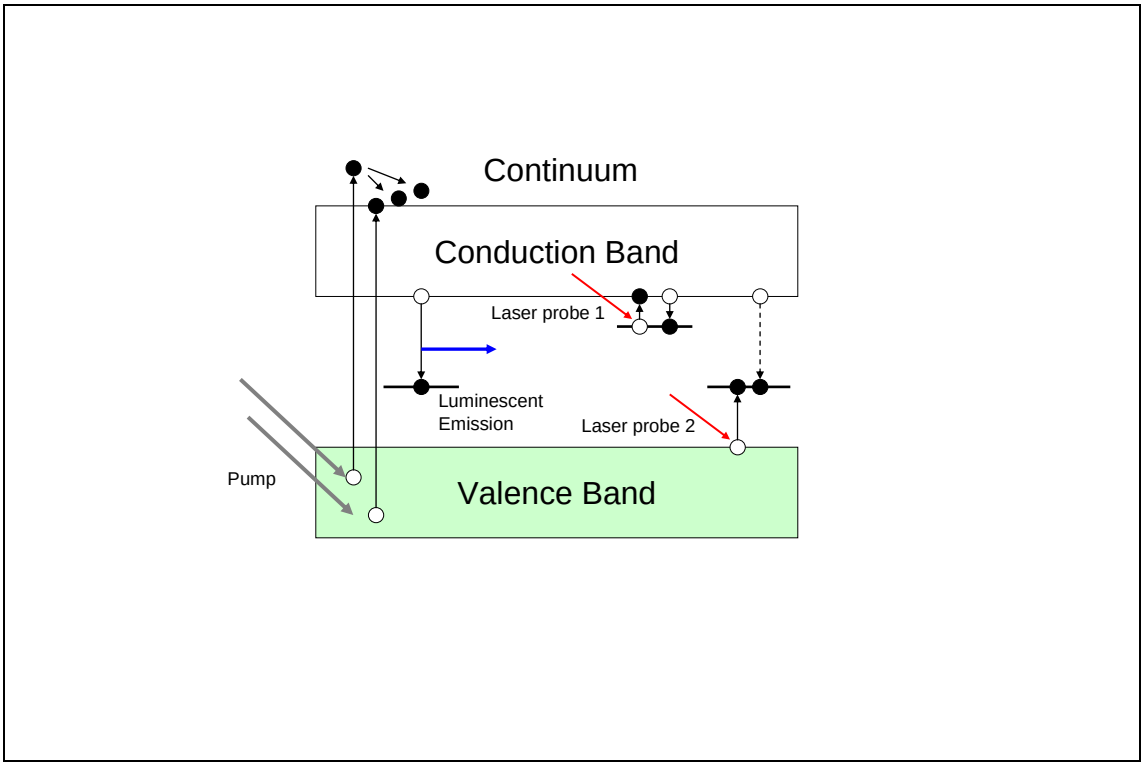

Figure 2.10 – Schematic representation of the pump probe processes as referred to in the text.

For the case of the pump probe condition, the probe can have two effects upon the system as depicted in figure 2.10. The first labelled as laser probe 1 resonates with deep lying electron traps removing their charge into the conduction band and effectively blocking the trap from becoming populated while the probe is active. This causes an initial burst of optically stimulated luminescence (OSL) at the commencement of the laser probe being switched on, which then decays rapidly as the trap becomes depleted of charge. These deep lying states are often referred to as OSL traps, being non-radiative they also have populations proportional to the amount of radiation received by a sample and can be used as a method of material dating [28]. The second interaction, labelled as laser probe 2, excites electrons from the valence band into defect states within the band gap. If the defect is an acceptor centre for

luminescent recombination the annihilation of holes reduces the quantum yield of the centre and thus quenches the luminescence.

As shown in figure 2.9, the pump probe signal evolves from initial probe commencement to a steady state equilibrium (I_0PP). The position of I_0PP in respect to the pump-only equilibrium ($I_{0,XEOL}$) can be either enhanced or quenched dependent upon which interactions are present. Thus, if a system has only OSL electron trapping defects the pump and probe signal will display an initial luminescent enhancement and decay to an I_0PP above that of $I_{0,XEOL}$, due to there being more charge available to luminescent recombination. If the system has only luminescent acceptor defects a quenching of the signal would occur with no observable initial enhancement, as the luminescent yield of the centre diminishes. However, if the system has both OSL electron trapping states and acceptor defects with which the probe interacts, the pump probe signal will be a superposition of the two outcomes, displaying an initial luminescent enhancement which will decay to an I_0PP below that of $I_{0,XEOL}$.

For the case of the pump-only region the signal recovers from the pump probe interaction back to $I_{0,XEOL}$. The recovery is not instantaneous, attributed to the refilling of the electron traps over time. At the point of laser probe switch off a transient can be identified as the XEOL signal quenches from that of I_0PP. This initial quenching effect is due to the electron traps suddenly becoming active and removing charge from the luminescent recombination. From this starting point the pump-only XEOL signal recovers to $I_{0,XEOL}$ as the traps become fully occupied again.

Further discussion upon these charge trapping dynamics are included with reference to the materials studied as part of this thesis in chapter 5.

1. E. Fermi. *Notes on Quantum Mechanics,* 1995: The University of Chicago Press.

2. J. Stohr. *NEXAFS Spectroscopy,* 1996: Springer.

3. P. Tola, A. Retournard, J. Dexpert-Ghys, M. Lemonnier, M. Pagel and J. Goulon. *On the use of x-ray-excited optical luminescence (XEOL) for the analysis of multisite rare-earth systems,* Chemical Physics, 1983. **78**(3): 339.

4. L. Soderholm, G.K. Liu, M.R. Antonio and F.W. Lytle. *X-ray excited optical luminescence (XEOL) detection of x-ray absorption fine structure (XAFS),* Journal of Chemical Physics, 1998. **109**(16): 6745-6752.

5. T.K. Sham, R. Sammynaiken, Y.J. Zhu, P. Zhang, I. Coulthard and S.J. Naftel. *X-ray excited optical luminescence (XEOL): a potential tool for OELD studies,* Thin Solid Films, 2000. **363**(1-2): 318.

6. N.R.J. Poolton, L. Botter-Jensen and O. Johnsen. *On the relationship between luminescence excitation spectra and feldspar mineralogy,* Radiation Measurements, 1996. **26**(1): 93.

7. N.R.J. Poolton, B.M. Towlson, B. Hamilton and D.A. Evans. *New instrumentation for micro-imaging X-ray absorption spectroscopy using optical detection methods,* Nuclear Instruments and Methods in Physics Research Section B: Beam Interactions with Materials and Atoms, 2006. **246**(2): 445-451.

8. N.R.J. Poolton, L. Botter-Jensen, P.M. Denby, T. Nakamura, B. Hamilton and E. Pantos. *High-sensitivity instrumentation for spectrally-resolved optically detected X-ray absorption spectroscopy,* Nuclear Instruments and Methods in Physics Research Section B: Beam Interactions with Materials and Atoms, 2004. **225**(4): 590.

9. G. van der Laan and I.W. Kirkman. *The 2p absorption spectra of 3d transition metal compounds in tetrahedral and octahedral symmetry,* Journal of Physics: Condensed Matter, 1992. **4**: 4189-4204.

10. D.A. Evans, A.R. Vearey-Roberts and N.R.J. Poolton. *Locating hexagonal and cubic phases in boron nitride using wavelength-selective optically detected x-ray absorption spectroscopy,* Applied Physics Letters, 2006. **89**(16): 161107.

11. A. Zangwill. *Physics at surfaces,* 1988: Cambridge University Press.

12. D.A. Evans, A.G. McGlynn, B.M. Towlson, M. Gunn, D. Jones, T.E. Jenkins, R. Winter and N.R.J. Poolton. *Determination of the optical band-gap energy of cubic and hexagonal boron nitride using luminescence excitation spectroscopy,* Journal of Physics: Condensed Matter, 2008. **20**: 075233.

13. Y.F. Hu, K.H. Tan, P.S. Kim, P. Zhang, S.J. Naftel, T.K. Sham, I. Coulthard and B.W. Yates. *Soft x-ray excited optical luminescence: Some recent applications,* Review of Scientific Instruments, 2002. **73**(3): 1379-1381.

14. G. Dalba, P. Fornasini, R. Grisenti, N. Daldosso and F. Rocca. *On the sensitivity of the x-ray excited optical luminescence to the local structure of the luminescent Si sites of porous silicon,* Applied Physics Letters, 1999. **74**(10): 1454-1456.

15. D.L. Dexter, C.C. Klick and G.A. Russell. *Criterion for the Occurrence of Luminescence,* Physical Review, 1955. **100**(2): 603-605.

16. S. Gardelis, U. Bangert, B. Hamilton, R.F. Pettifer, D.A. Hill, R. Keyse and D. Teehan. *Chemical nature of the luminescent centre in fresh and aged porous silicon layers,* Applied Surface Science, 1996. **102**: 408-412.

17. N. Daldosso and F. Rocca. *New EXAFS Measurements by XEOL and TEY on Porous Silicon,* Journal of Porous Materials, 2000. **7**: 169-172.

18. S. Emura, T. Moriga, J. Takizawa, M. Nomura, K.R. Bauchspiess, T. Murata, K. Harada and H. Maeda. *Optical-Luminescence Yield Spectra Produced By X-Ray-Excitation,* Physical Review B, 1993. **47**(12): 6918-6930.

19. J. Goulon, P. Tola, M. Lemonnier and J. Dexpert-Ghys. *On a site-selective exafs experiment using optical emission,* Chemical Physics, 1983. **78**(3): 347.

20. N.R.J. Poolton, E. Pantos, B. Hamilton, P.M. Denby and O. Johnsen. *Application of wavelength-resolved optically-detected XAS methods to phase-segregated silicates,* Physica Status Solidi B-Basic Solid State Physics, 2004. **241**(15): 3656-3663.

21. T. Nakamura, N. Takahashi, N.R.J. Poolton and A.E.R. Malins. *Optical and structural properties of CVD-grown single crystal SiO_2 using optically detected XAS,* Applied Surface Science, 2005. **244**(1-4): 318-321.

22. N.R.J. Poolton, B.M. Towlson, D.A. Evans and B. Hamilton. *Synchrotron-laser interactions in hexagonal boron nitride: an examination of charge trapping dynamics at the boron K-edge,* New Journal of Physics, 2006. **8**: 76.

23. S.J. Naftel, Y.M. Yiu, T.K. Sham and B.W. Yates. *X-ray excited optical luminescence (XEOL) studies of CaF_2 at the Ca L3,2-edge,* Journal of Electron Spectroscopy and Related Phenomena, 2001. **119**(2-3): 215.

24. J. Roque, N.R.J. Poolton, J. Molera, A.D. Smith, E. Pantos and M. Vendrell-Saz. *X-ray absorption and luminescence properties of metallic copper nanoparticles embedded in a glass matrix,* Physica Status Solidi B-Basic Solid State Physics, 2006. **243**(6): 1337-1346.

25. N.R.J. Poolton, L. Botter-Jensen, P.M. Denby, T. Nakamura, B. Hamilton and E. Pantos. *High-sensitivity instrumentation for spectrally-resolved optically detected X-ray absorption spectroscopy,* Nuclear Instruments & Methods in Physics Research Section B-Beam Interactions with Materials and Atoms, 2004. **225**(4): 590-598.

26. G. Dalba, N. Daldosso, P. Fornasini, M. Grimaldi, R. Grisenti and F. Rocca. *Evidence of x-ray absorption-edge shift as a function of luminescence wavelength in porous silicon,* Physical Review B, 2000. **62**(15): 9911-9914.

27. A. Othonos. *Probing ultrafast carriers and phonon dynamics in semiconductors,* Applied Physics Reviews, 1998. **83**: 1789.

28. S.W.S. McKeever and M.F. Morris. *Computer simulations of optical bleaching of TL and OSL signals,* Radiation Measurements, 1994. **23**(2-3): 301.

Chapter 3

Instrumentation

This chapter introduces the experimental apparatus and modes of operation used to collect the data presented in this thesis. Each piece of apparatus is presented individually with key operational parameters explained in detail. Firstly section 3.1 introduces photon excitation sources, including lasers and synchrotron radiation (SR). Section 3.2 concerns detection of luminescent emission describing the two synchrotron beamline end stations used, MoLES and CLASSIX1. Finally, in section 3.3, Atomic force microscopy (AFM) is introduced. AFM was used to investigate the surface morphology of materials deposited by ESD (Chapters 4 and 6).

3.1 Photon excitation sources

Photon excitation sources can be either of tuneable or fixed energy, both of which were employed within this thesis. The brightest and most versatile sources are synchrotrons which produce tuneable radiation used to conduct both static energy (XEOL) and scanning energy experiments (XAS). Fixed energy sources on the other hand, such as lasers, can only be used to conduct static energy experiments (OL). Lasers are generally simple devices which produce monochromatic emission at narrow bandwidths. Based on a stimulated lasing material (gaseous or solid state) most lasers rely upon enhancement within a cavity to produce a bright directional and coherent beam of light. The lasers used to produce the PL results contained within this

thesis were all solid state laboratory sources as described within the relevant experimental sections, with the exception of the quasi-tuneable source used to conduct the pump probe experiments (Chapter 5).

3.1.1 Synchrotron Radiation Source (SRS)

Synchrotrons are used as photon excitation sources for a myriad of experimental techniques. For surface science applications synchrotron radiation (SR) has some major advantages over laboratory excitation sources, which are generally of fixed energy. SR is extremely bright (high flux density) yielding coherent plane polarised "white light" radiation, as shown in figure 3.1.

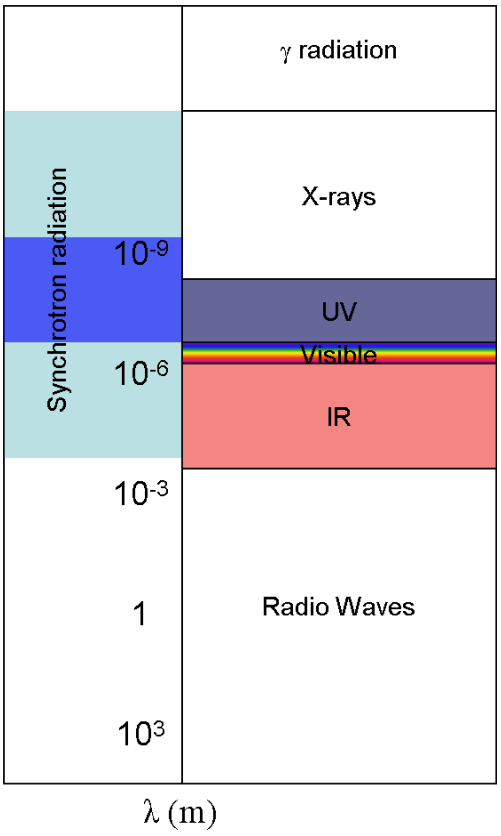

Figure 3.1 – Representation of SR within the electromagnetic spectrum, Blue region indcates wavelengths used in this study (VUV-soft X-ray)

White light SR is produced by manipulating charged particles at close to the speed of light. When the path of a relativistic charged particle is changed it causes in a change of acceleration which results in the emission of electromagnetic radiation. For the case of a relativistic particle travelling in a circular trajectory the acceleration is centripetal, directed towards the centre of the orbit and the radiation is emitted at a tangent to its path. The maximum energy of the radiation is dependent upon the velocity of the particle; hence SR is described as "white" being from the infrared to hard X-ray.

In a synchrotron storage ring relativistic electrons are maintained in a circular orbit from which the emitted SR produced as a continuous distribution of electromagnetic radiation, polarised in the plane of the orbit.

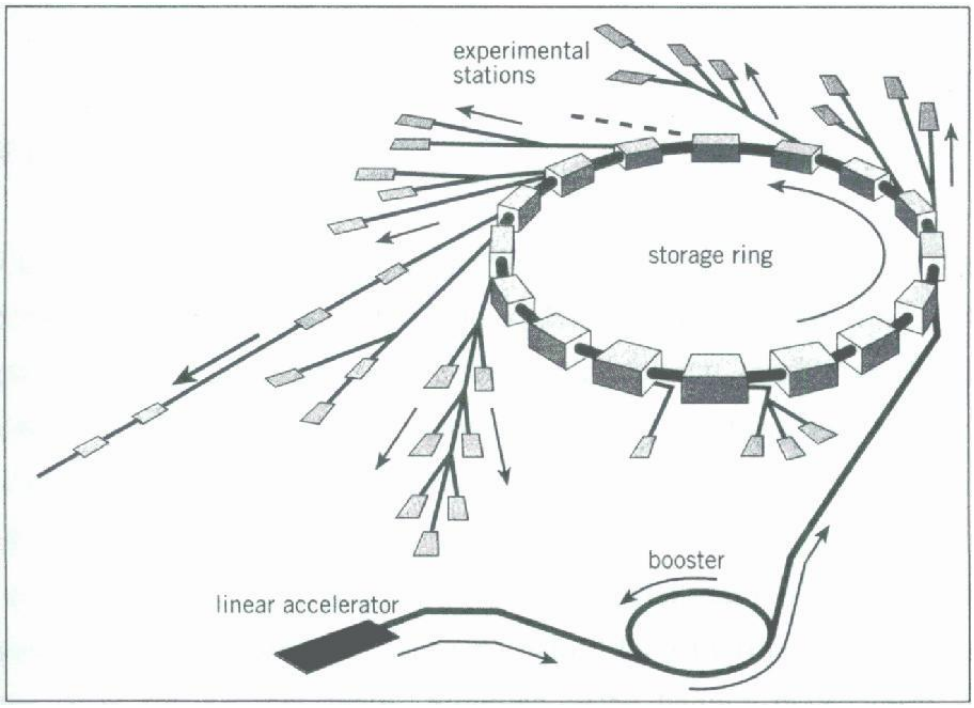

Figure 3.2 – Schematic representation of a synchrotron radiation source, analogous to the SRS, Daresbury [1]

3.1.1.1 SRS Daresbury

The SRS Daresbury is an electron based 2nd generation synchrotron, analogous to that shown in figure 3.2. The operation of a synchrotron can be regarded as a three stage process. A linear accelerator (LINAC) initially accelerates electrons to 12MeV before injecting them into the booster synchrotron ring. Within the booster ring electrons are accelerated further by radio frequency (RF) and maintained in a circulatory orbit by bending magnets. Electrons of 600MeV are fed in bunches from the booster into the main synchrotron storage ring and further accelerated to 2GeV in synchronisation with the maintaining RF. When the synchrotron is operating in "multi-bunch" mode one hundred and sixty bunches of electrons are each separated by 2ns within the storage ring. The path of the electrons within the storage ring is controlled by bending magnets; these create a polygonal path due to the magnets being separated by straights. At points of beam path directional change SR is produced tangentially, polarised in the plane of the orbit.

Insertion devices (undulators and wigglers) are used to produce SR in the straight sections of the storage ring. Both employ multiple magnets with alternate polarity (in the direction of the electron path) to cause the electrons to oscillate as they pass through. The oscillatory path of the electrons increases the total SR flux from that produced at a dipole bending magnet, with each oscillation and subsequent change in acceleration superimposing SR to the total device yield. The power of SR is proportional to the magnetic field experienced by the electrons. Insertion devices have a magnetic field of greater magnitude (5-6T) than that of bending magnets (1.2T) [2, 3], thus the cut-off photon energy and flux is significantly higher than that produced at the bending magnets.

The entire storage ring is kept under UHV to minimise energetic losses due to collisions. However losses do occur and the electron beam current degrades with time, usually dropping sufficiently to necessitate refilling every 24 hours. New 3rd generation synchrotrons (e.g. Diamond Light Source at Oxford, UK) have overcome this issue by continually injecting into the storage ring to achieve a continuous stable beam.

At bending magnets and insertion devices SR is passed through the storage ring wall and delivered to experimental end stations by beamlines. Soft X-ray (under 2000eV) beamlines manipulate white radiation with focussing optics and Bragg style diffraction gratings to deliver tuneable monochromatic photons to experiments. Beamlines are optimised to deliver photons within specific ranges of energy.

3.1.1.2 Beamlines 3.2 and MPW6.1

Two beam lines at the SRS Daresbury were used during this study, namely beamline 3.2 and MPW6.1 which are discussed individually below.

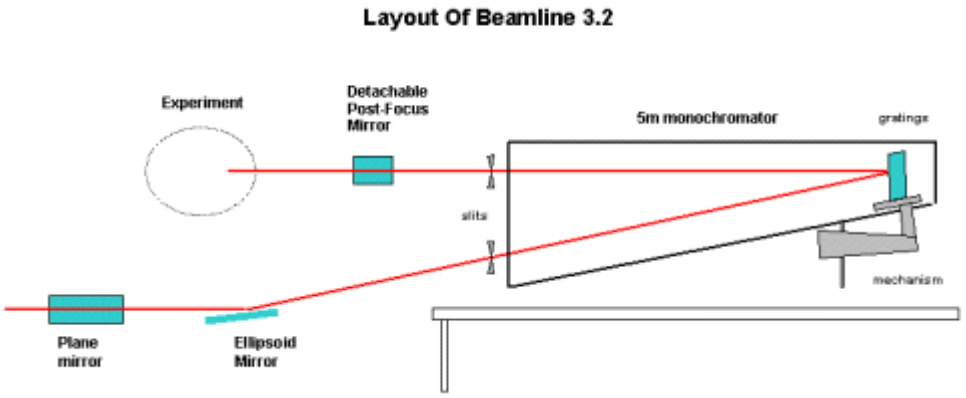

Figure 3.3– Schematic representation of beamline 3.2 reproduced from [4]

Beamline 3.2 has a relatively basic orientation, as depicted in figure 3.3. Situated at a dipole bending magnet, the beam is focused using mirrors through a monochromator that selectively filters the SR to deliver VUV radiation in the energy range 4 - 41eV (300-30nm) to the sample. Beamline 3.2 was used to study the band gap energies of boron nitride samples as part of this thesis (section 5.4.2).

Beamline MPW6.1 is located upon a multi pole wiggler (MPW), specifically designed to accommodate a range of end chambers in the XUV energy range 40 - 450eV (31-2.75nm).

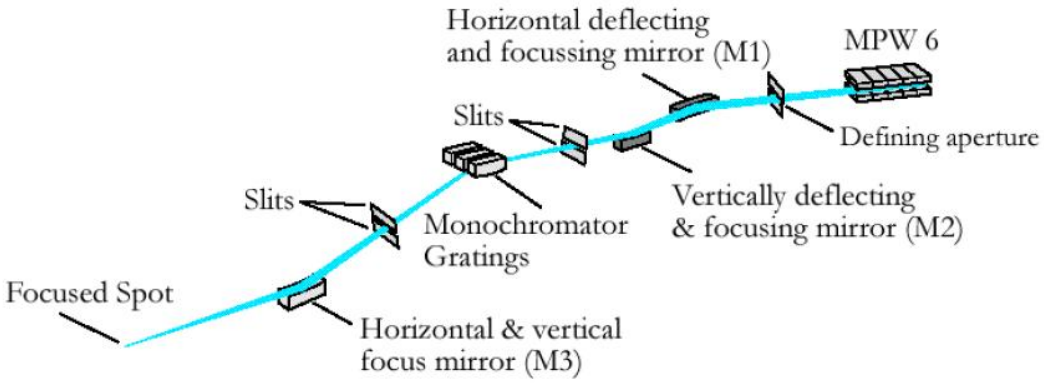

Figure 3.4 – Schematic representation of beamline MPW6.1 reproduced from [4]

The orientation of MPW6.1, as shown in figure 3.4, is more complex than that of beamline 3.2 due to the enhanced SR flux of the wiggler (ten times that of a bending magnet) and increased distance from the storage ring. The beam is again selectively filtered using a monochromator, although in this case the geometry requires additional focussing mirrors and entrance and exit slits to deliver a focused beam of small cross section to the sample. Additionally integrated baffles can be used to shape the beam at the sample which is of importance for spatially resolved techniques. Beamline MPW6.1 was employed to conduct the XEOL and NEXAFS experiments contained within this thesis using mobile end stations as described below.

It is worth noting that for the work contained within this thesis, SR was used in the energy range 4-450eV; mostly in UV, VUV and XUV regions rather than X-ray.

3.2 Luminescent detection

Detection of luminescent emission is not trivial due to low signal intensities and the presence of erroneous background. Luminescence experiments therefore require specialised apparatus in order to attain meaningful results. Two specifically designed luminescence detection chambers were used during this study, MoLES and CLASSIX1, both of which are discussed in greater detail in the following section.

3.2.1 Introduction to MoLES

Mobile **L**uminescence **E**nd **S**tation (MoLES) [5] is a designated chamber for the detection of volume-integrated luminescence, as depicted in figure 3.5. Designed as a synchrotron beamline chamber MoLES can also be used offline with laboratory excitation sources such as lasers and X-ray sources.

Briefly, MoLES consists of a spherical UHV chamber into which a cryogenically cooled cold finger sample stage and focussing optics are integrated. Several optical ports are orientated towards the sample stage to allow for detection from and interaction with the sample. Detection of luminescence is made by two external photomultiplier tubes (PMT) (Hamamatsu). The first, positioned directly onto the chamber can be used to collect OD-XAS signal. The second records wavelength selective emission through a monochromator (Jobin-Yvon), recording XEOL and OL.

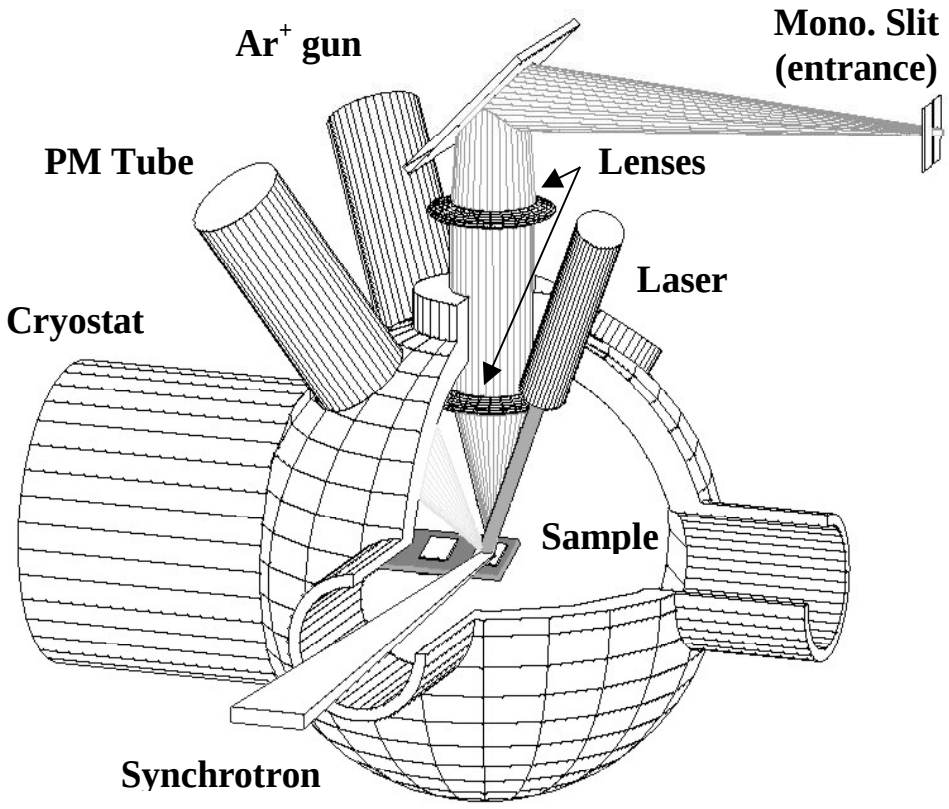

Figure 3.5 - Schematic of MoLES reproduced from the literature, showing geometry pertinent to its operation [5].

3.2.1.1 Sample manipulation and cooling

An adiabatic helium cryostat cools the copper cold finger (8-330K) on a partially recirculated system, all of which is driven on a linear drive perpendicular to the excitation beam, in such a way as to allow several samples to be loaded in a single experimental run.

3.2.1.2 The monochromator

The monochromator (190 Triax, Jobin-Yvon) (200-1000nm) is positioned on the uppermost central port, through which the luminescent emission is focused. Three Bragg type diffraction gratings are located within the monochromator which can be individually selected for optimal response at the wavelength range desired. The nominal optical resolution of the monochromator is dependent upon its entrance slit size (3nm resolution per 1mm slit size), which can be optimised for luminescent transmission. Detection is made via a PMT on the exit slits of the monochromator. Several PMTs are available to MoLES which are selected for optical response in the spectral range desired.

3.2.1.3 Computer control

MoLES is remotely controlled via a custom LabVIEW interface through which the scan data and parameters can be collected and nominated. Parameters include excitation energy (SRS beamline), monochromator wavelength, data collection frequency, grating and entrance slit size.

3.2.1.4 Experimental procedure

MoLES can be used to perform static energy and scanning energy experiments; the key operational considerations of both are described in the following section.

3.2.1.4.1 XEOL and OL

To conduct a XEOL experiment, a fixed excitation energy must be selected (usually just below the absorption edge) in order to maximise luminescent emission. For OL experiments a laser is used with an excitation energy greater than the band gap of the sample. The monochromator is then scanned over a nominated range between 200-1000nm with the appropriate grating in place, as specified by the user. Data is collected as emission intensity against wavelength.

3.2.1.4.2 OD-XAS

OD-XAS experiments are conducted using a PMT to record the luminescent yield as a function of the incident SR excitation energy. The PMT positioned directly onto the chamber is used to collect data in either total luminescent yield (TLY) or when filtered partial luminescent yield (PLY). It is also noted that PLY OD-XAS can also be collected through the monochromator whilst it is set to idle at a particular emission wavelength. However this can only be implemented for highly luminescent samples due to the reduction in signal intensity due to passage through the monochromator. Subsequent data is collected as luminescent intensity against excitation energy.

MoLES can also accommodate additional laser sources in order to conduct synchrotron based pump probe (PP) experiments [6, 7].

3.2.2 Introduction to CLASSIX1

Chemistry, **L**uminescence **A**nd **S**tructure of **S**urface by mirco-**I**maging **X**-ray absorption, CLASSIX1 [8, 9], is a synchrotron end station chamber used to study spatially resolved optical luminescence, as shown in figure 3.6. CLASSIX1 exploits the fact that luminescent emission is in the UV/VIS/IR region of the spectrum, utilising standard optics to image samples in emission.

Briefly, the instrument consists of a small UHV chamber into which a cryogenically cooled cold finger sample stage is mounted. Windows onto the chamber allow for excitation and luminescent detection. 2D luminescent imagery is collected by a CCD through external focusing optics and a purpose built filter wheel. Each component of the machine is discussed in greater detail below.

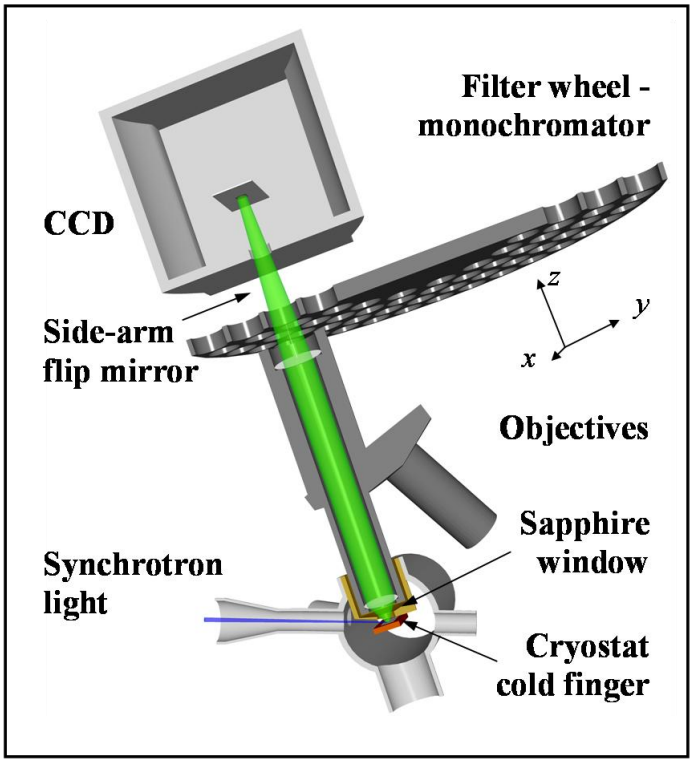

Figure 3.6 - Schematic representation of CLASSIX1 reproduced from the literature [9].

3.2.2.1 Cryostat and sample manipulation

Samples are held within CLASSIX1 upon a copper cold finger cooled in the range 30-300K by an integrated cryostat (ARES technology). The cryostat is operated through an external pump on a continuous liquid helium flow in order to minimise vibration to the sample. SR enters CLASSIX1 through a radial port impinging upon the sample which held at 19^{o} to the horizontal. The luminescence detection is made perpendicular to the sample. This geometry ensures only emitted light is collected and any reflected light is omitted. UHV bellows allow the entire cryostat to be remotely manipulated within chamber, such that a sample can be spatially probed.

3.2.2.2 System optics

CLASSIX1 utilises commercially available optics to focus and filter luminescent emission prior to its detection by the CCD. The optical system consists of a UHV sapphire window, focusing objectives and a filter wheel, each of which are described individually.

The sapphire window is recessed within the chamber such that the sample is only 5mm from its surface. This orientation allows for maximum transmission and focussing of the objectives within the recess.

The focusing objectives are interchangeable and are held upon a turret on which four can be accommodated at any one time. There are five objectives available to CLASSIX1 at present which differ in their transmission and focussing power, as summarised in table 3.1. The x2, x10 and x50 objectives are of visible and IR transmission (380-1000nm), whereas those of x20 and x80 have increased sensitivity

in the UV (200-1000nm). This leads to the distinction between two groups of objectives, with those of x2, x10 and x50 being referred to as visible and those of x20 and x80 as UV.

Magnification	Transmission (nm)	Working distance (mm)	Depth of field (μm)	CCD pixel resolution (μm^2)
x2	380-1000	34	91	7.8
x10	380-1000	33.5	3.5	1.6
x50	380-1000	13	0.9	0.3
x20	200-1000	15	2.1	0.8
x80	200-1000	10	0.9	0.2

Table 3.1 – Summary of CLASSIX1 objectives

The filter wheel, situated above the objectives accommodates up to 107 individual 25mm diameter circular filters. These are arranged in sequential groups of type including narrowband (10nm), broadband (50nm), interference and long pass. However any filter can be fitted within the wheel for specific requirements.

Luminescence is detected by either a charge coupled device, CCD, (yielding micro-imagery) or PMT with selection between the two made by a flip mirror above the filter wheel.

The CCD detector (Andor Technology iXon DV887) is made up of a 512x512 pixel array of area $8mm^2$. This yields a sample detection area of between $4mm^2$ and $0.1mm^2$ for the x2 and x80 objectives respectively. It is electronically cooled during operation to improve the sensitivity, able to detect a single photon in the region 200-1000nm with a 10MHz refresh rate.

3.2.2.3 Computer control and experimental procedure

CLASSIX1 is remotely controlled with a LabVIEW interface through which all scanning parameters are selected and the data collected.

CLASSIX1 is capable of conducting spatially resolved OD-XAS and XEOL experiments. In all cases an objective must be selected and focused to achieve the best resolution and depth of field prior to experimental commencement.

3.2.2.4 XEOL

In order to carry out a XEOL experiment the beamline excitation energy is fixed to give a strong luminescent yield (usually below the absorption edge energy). A series of filters are selected to give the desired transmission and resolution (for example a narrowband filter).

During the scan the filter wheel moves to each filter in turn within the selected series and records images of the sample in partial luminescent yield. Once the scan has finished data is presented as a graph of volume-integrated luminescent signal against emission wavelength. Each point is represented by an image of the sample in partial luminescent yield, thus this data illustrates lateral differences in luminescent emission across a sample.

3.2.2.5 OD-XAS

To conduct an OD-XAS experiment either no filter (total yield) or a specific filter (partial yield) must be selected which will remain in place for the duration of the experiment. The beamline is scanned across an absorption edge within an energy range and resolution selected by the user. CLASSIX1 records an image at each energy step within the range and displays the result as a graph of volume-integrated luminescence against excitation energy.

3.2.2.6 Data processing

For all CLASSIX1 experiments the luminescence signal is volume-integrated over the whole image but can be selectively filtered to yield data from specific regions. This creates spatially resolved XEOL and OD-XAS results, from which it is possible to compare regions of the sample within a single scan [9].

3.3 Atomic force microscopy

Optical microscopic techniques are limited in resolution by the wavelength of visible light (350-750nm), therefore in order to visualise surfaces on an atomic scale (0.1nm) different microscopy techniques must be employed.

Atomic force microscopy (AFM) is an extremely versatile microscopic technique able to measure the topography of surfaces on an atomic scale in varied environments including UHV, atmospheric, clean gas and liquid.

The first AFM was developed by Binnig *et al* in the 1980's as an alternative to existing scanning tunnelling microscopy (STM) methods [10]. AFM utilises the electrostatic forces between a chemically sharpened cantilever and the atoms of a sample's surface. The force is either attractive or repulsive depending upon the proximity of the cantilever tip to the surface as illustrated in figure 3.7.

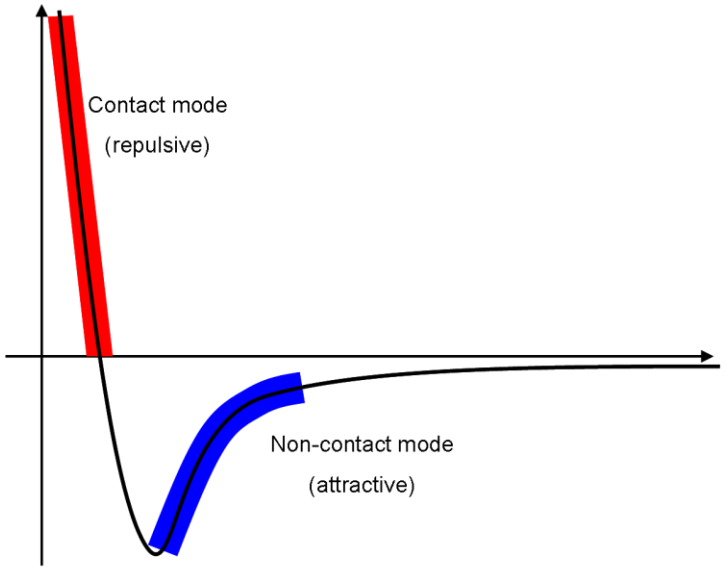

Figure 3.7 - The dependence of attractive and repulsive atomic forces with distance and the associated AFM mode.

The basic operational considerations are illustrated in figure 3.8. A laser focused upon the back of the cantilever is used to measure its deflection as it interacts with the sample surface. The laser signal, reflected from the cantilever, is focused upon a CCD which measures its deflection from a set point in two dimensions.

The sample surface is scanned beneath the cantilever whilst maintaining a constant tip to surface distance. This is achieved by means of a feedback loop, which controls the z-scanner onto which the cantilever is mounted.

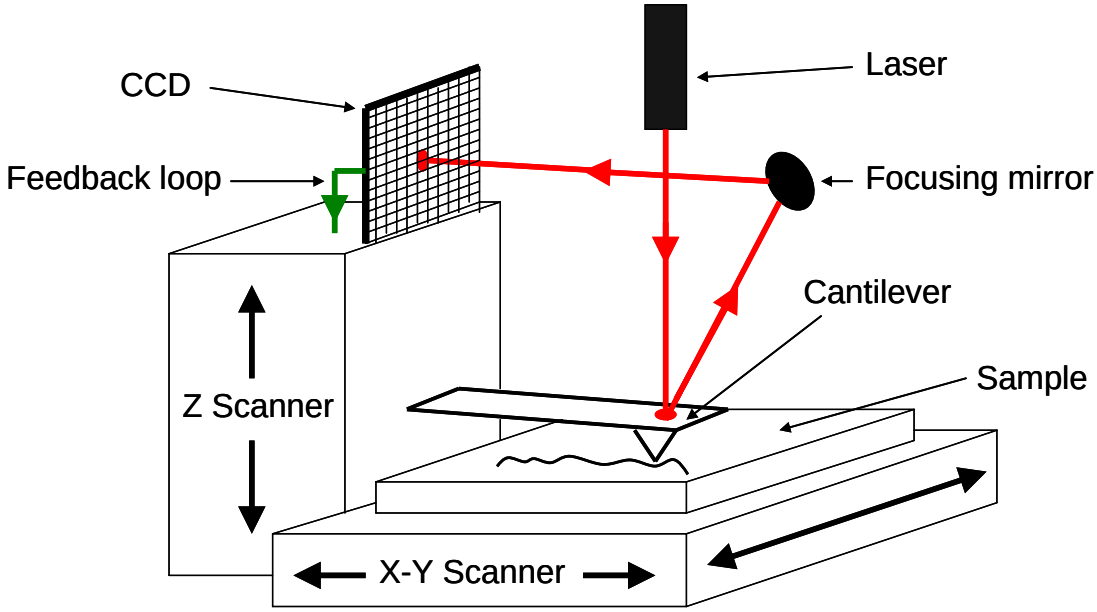

Figure 3.8 - Schematic representing the operation of the PSIA-100 AFM.

The machine used in this thesis, PSIA XE-100, utilises a combination of sample and cantilever control, as depicted in figure 3.8 [11]. The sample is manipulated in the horizontal plane (x,y) beneath the cantilever by piezo-electric motors. The vertical cantilever control, z scanner, is mounted in the probe head and controls the height of the cantilever in relation to the sample surface. This orientation of sample manipulation reduces the data processing required to produce a flat image when

compared to three dimensional sample manipulation, allowing for fast scanning without loss of resolution.

The PSIA XE-100 can operate in three discrete modes, contact (C-AFM), non-contact (NC-AFM) and dynamic force (DF-AFM). The best mode of operation is largely dependent upon the physical properties of a sample and generally chosen in order to acquire the greatest resolution. Contact and dynamic force modes are suited to harder materials where the cantilever cannot damage or be damaged by the sample. Non-contact as its name suggests does not physically touch the sample surface, thus is suited to analysis of softer materials. Cantilevers are chemically sharpened in order to acquire a sharp tip a few atoms wide, this allows for extremely high resolution on the atomic scale in some cases.

3.3.1 Contact AFM (C-AFM)

C-AFM describes the method of physically drawing a cantilever across a surface, the tip held at repulsive proximity under a small (1-10nN) pressure. Therefore C-AFM cantilevers are relatively stiff with small spring constants ($0.1\text{-}3 Nm^{-1}$). The laser position at the CCD is kept constant as the z-scanner compensates by means of a feedback loop. The topographic measurement at each point is made by reference to the z-scanner position. C-AFM can only be used in cases where the cantilever will not damage the sample surface and therefore lends itself to the measurement of hard samples.

3.3.2 Non-Contact AFM (NC-AFM)

In non-contact mode the cantilever is forcibly oscillated a small fraction above its natural frequency. As the tip is bought towards the surface the attractive van der waals forces affect the phase and amplitude of oscillation, effectively increasing the cantilever spring constant. The phase and amplitude of the oscillations are monitored by the CCD. The AFM continually maintains the oscillatory amplitude by maintaining a constant tip sample distance. Information of sample topography is again measured with reference the z-scanner as it adjusts the tip sample distance whilst scanning the surface.

3.3.3 Dynamic Force AFM (DF-AFM)

Dynamic force mode is similar to NC-AFM in that the cantilever is forcibly oscillated, but unlike NC-AFM the cantilever is driven at a frequency just below resonance. This creates a situation whereby the cantilever amplitude is increased by the attractive van der waals forces as it approaches the surface. The tip is then controllably tapped on the surface. The tip is then retracted before re-approaching at the next point in the scan. Therefore the sample tip distance is constantly changing unlike in contact and non-contact modes. The topography is attained by measuring the tip amplitude under the repulsion of the surface, also by simultaneously measuring the phase the surface elasticity can be acquired. This is a very useful technique when examining samples with rough topography or irregular features which can damage tips in other modes of operation.

1. D.N. Gnoth. *NEWI*, University of Wales (Wrexham), 1998.

2. G.N. Greaves, R. Bennett, P.J. Duke, R. Holt and V.P. Suller. *X-ray optics and spectral brightness of the superconducting SRS wiggler*, Nuclear Instruments and Methods in Physics Research, 1983. **208**(1-3): 139.

3. N. Marks, G.N. Greaves, M.W. Poole, V.P. Suller and R.P. Walker. *Initial operation of a 5 T superconducting wiggler magnet in the SRS*, Nuclear Instruments and Methods in Physics Research, 1983. **208**(1-3): 97.

4. http://srs.dl.ac.uk/XUV-VUV/science.html.

5. N.R.J. Poolton, L. Botter-Jensen, P.M. Denby, T. Nakamura, B. Hamilton and E. Pantos. *High-sensitivity instrumentation for spectrally-resolved optically detected X-ray absorption spectroscopy*, Nuclear Instruments and Methods in Physics Research Section B: Beam Interactions with Materials and Atoms, 2004. **225**(4): 590.

6. N.R.J. Poolton, B. Hamilton and D.A. Evans. *Synchrotron-laser pump-probe luminescence spectroscopy: Correlation of electronic defect states with x-ray absorption in wide-gap solids*, Journal of Physics D-Applied Physics, 2005. **38**(9): 1478-1484.

7. N.R.J. Poolton, B.M. Towlson, D.A. Evans and B. Hamilton. *Synchrotron-laser interactions in hexagonal boron nitride: an examination of charge trapping dynamics at the boron K-edge*, New Journal of Physics, 2006. **8**: 76.

8. N.R.J. Poolton, B.M. Towlson, B. Hamilton, J. Wallinga and A. Lang. *Micro-imaging synchrotron-laser interactions in wide band-gap luminescent materials*, Journal of Physics D-Applied Physics, 2007. **40**(12): 3557-3562.

9. N.R.J. Poolton, B.M. Towlson, B. Hamilton and D.A. Evans. *New instrumentation for micro-imaging X-ray absorption spectroscopy using optical detection methods*, Nuclear Instruments and Methods in Physics Research Section B: Beam Interactions with Materials and Atoms, 2006. **246**(2): 445-451.

10. G. Binnig, C.F. Quate and C. Gerber. *Atomic Force Microscope*, Physical Review Letters, 1986. **56**(9): 930-933.

11. PSIA. XE-100 user manual version 1.0.

Chapter 4

Electrospray Deposition

This chapter introduces the electrospray process and its application as a scientific deposition method. It will then describe the design and manufacture of the Aberystwyth electrospray deposition system (ESD), highlighting the key parameters involved in each stage of the build process.

4.1 Electrospray Ionisation (ESI)

Electrospray ionisation describes the fission of liquid droplets under the influence of electrical pressure. Two systems generate the conditions of electrospray; droplets can either have their own charge such as those passing through a high voltage capillary or be acted on by an external field. For the purposes of this thesis only the former will be considered although the dynamics of droplet behaviour between the two systems is similar.

4.1.1 History

The term electrospray (ES) was not coined until the 1960's but the first known reports of the phenomena date back to the mid 18th century. Letters written by French clergyman and scientist Abbe Nollet to fellow academics at the royal academy of sciences, described the altered dynamics of liquid flow from electrified vessels [1].

Nollet's observations included descriptions of spray from electrified capillary tubes being accelerated and ray like. He also noted that for a small bore capillary, electrifying the tube enabled spray which could not occur under pressure alone.

Lord Rayleigh was the first to postulate a theory for the break up of a charged droplet in his ground breaking 1882 theoretical paper [2]. Rayleigh's theory introduced a relationship between the electrostatic charge *q*, droplet radius *D*, surface tension γ and the permittivity of air ε_0 (equation 4.1).

$$q^2 = 8\pi^2 \varepsilon_0 \gamma D^3 \qquad (4.1)$$

This simple relationship described the maximum possible charge (Rayleigh limit) a droplet of given size and surface tension could support. At or above the Rayleigh limit a spherical droplet was shown to restore equilibrium by ejecting mass. Jet emission was shown to occur at the polar regions of a prolate spheroid, thus the shape of the droplet was modified. This was an extremely important development, as quantitative research of ES was now made possible.

In the early 20th century an understanding of electrical storms drove research interest into ES, with scientists attempting to describe the behaviour of water droplets being acted on by external electrical fields.

In 1917 Zeleny *et al* [3], experimentally demonstrated the emission jet and subsequent plume formed by glycerol and water droplets issuing from high voltage capillary tube terminations. By measuring the potential at which the droplet became unstable, this work calculated an experimental criterion of stability.

Rigorous experimental work by Wilson and Taylor in 1925 [4] demonstrated the same field dependent phenomena with soap bubbles held over tubes and by Macky in 1931 [5] with isolated water droplets in external fields.

Research up to this point had taken Rayleigh's postulate of droplet deformation to be correct, assuming that the spherical droplet changed to a spheroid shape when the emission jet formed.

However in 1964, G. Taylor published his theory of the ES phenomena [6, 7]. Taylor's work demonstrated that the shape of the droplet about the emission jet was better described by a cone (Taylor cone) rather than a spheroid. This was clearly substantiated by experimentation, indicating the Taylor cone's theoretical angle (49.3^{o}) to be correct. Although not fully understood, rapid development of commercial ES painting and plating techniques ensued, reports on which were published [8, 9] and by the middle of the 20^{th} century ES was an accepted industrial deposition method but had yet to find a scientific application.

In 1968 Dole *et al* pioneered a basic mass spectrometry technique, electrospraying polystyrene/solvent solutions, introducing polystyrene ions into vacuum for analysis [10]. A series of differentially pumped stages separated by skimmer apertures achieved a vacuum gradient through which the ES droplet plume could propagate. This was the first attempt to introduce ES ions into vacuum and displayed its potential as a scientifically important process.

However it was not until 21 years later in 1989 that Fenn and his co-workers developed Dole's original concept into a scientific technique; electrospray ionisation mass spectrometry (ES-MS), for which Fenn received the Nobel prize in 2002 [11-14]. Today ES-MS is a widely used research technique yielding many thousands of publications over the past 20 years, however ES has not been developed as a

deposition technique and is largely unknown to the surface science community. The recent increased interest in large delicate molecules as semi-conducting materials has necessitated the need for methods of non-destructive UHV deposition. The process of controllably delivering molecules into vacuum via ES is the principle on which the electrospray deposition system (ESD) was designed.

4.1.2 The Electrospray Process

The ES phenomena has been the subject of many theoretical studies with complex dynamics having been modelled extensively [13-21]. However for the purposes of this study a qualitative explanation is given, as the ES process is implemented rather than being studied.

Continuous inline ES is essential for its implementation as a deposition method. This is achieved by creating a steady-state process at the termination of a high voltage capillary, through which a constant flow of molecule/solvent solution is passed.

At the capillary termination the solution is ionised and drawn out into a symmetrical Taylor cone, from which an emission jet issues at the apex. The dynamics within the emission jet are complex; solution surface tension is overcome by the charge (repulsive force) breaking up the solution into a plume of charged droplets in an event referred to as Coulombic fission. Detailed photographic studies of the charge induced fission of ES droplets have been conducted by Gomez and Tang [19].

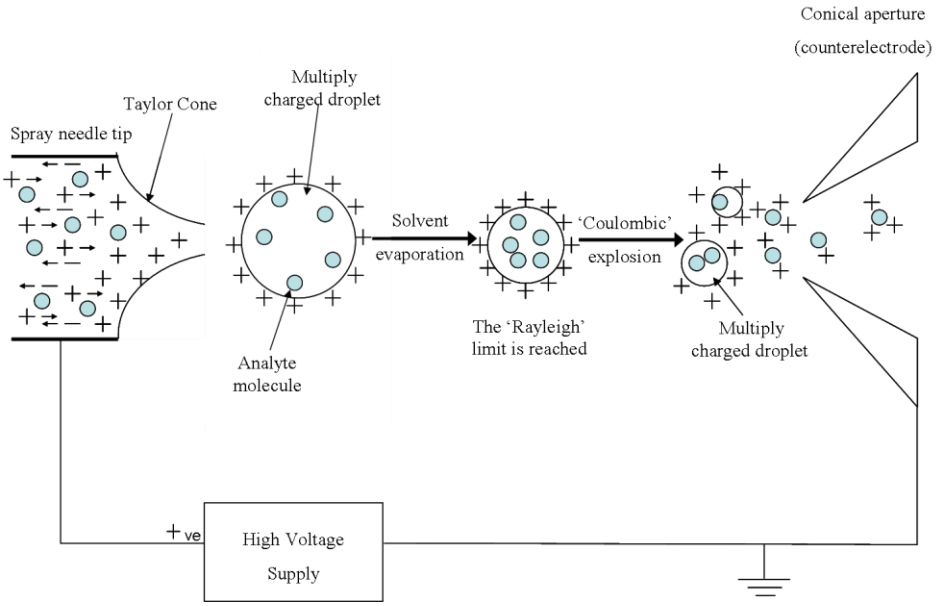

Figure 4.1 – Diagram of the ES process. The high voltage at the emitter tip ionises the solution drawing it out into a Taylor cone. From the subsequent jet charged droplets are emitted which undergo solvent evaporation and columbic fission yielding a beam of ionised molecules.

The charged droplets travel away from the capillary towards electrical ground undergoing further fission and solvent evaporation, eventually yielding a beam of molecular ions suitable for deposition.

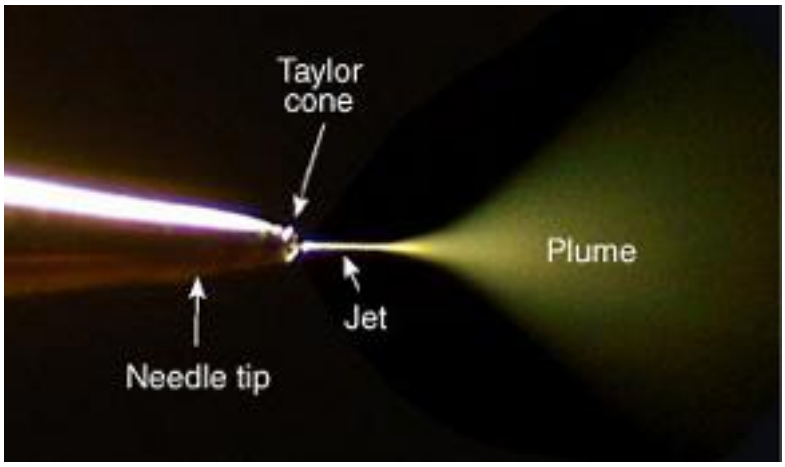

Figure 4.2 – Annotated image of ES emission from the tip of a high voltage capillary, taken from [22]

The Taylor cone and subsequent spray characteristics are highly sensitive to initial conditions, as such many separate modes of jet emission can be observed when the system is operating off resonance. In studies conducted by Cloupeau and Prunetfoch qualitative identification of the various jet formations were investigated [16, 23] with dripping effects being observed below stable Taylor cone voltages and multiple Taylor cone and jet emissions above.

4.2 Electrospray Deposition ESD

As a scientific deposition method ES is a relatively modern technique. ESD has been investigated as an alternative method for creating thin films of solute molecules over the past 10 years with numerous studies having been reviewed by Jaworek [24]. The new importance of organic molecules, in particular polymers, as semi-conducting materials has led to increased interest from the surface science community in ES as a potential deposition method. The following section reviews ESD reported in the literature.

4.2.1 Atmospheric pressure ESD

Several studies have investigated the ESD of proteins for biological research [25-27], where deposited protein molecules were shown to be intact post ESD, indicating the non-destructive nature of the technique.

The ESD of nanoparticles has shown potential in recent years as a way of selectively seeding substrates [28-33]. Nanoparticles can be electrostatically manipulated in-flight using the charge of the ES droplets. Patterned arrays of Au created by ESD

were first reported by Suh *et al* in 2005 [28] and of SiO_2 by Lenggoro *et al* in 2006 [33]. Publications since have developed methodology using different nanoparticles with good success [29-32].

Thin films of polymers have been created using ESD in air and under clean gas atmospheres [34-40], film morphologies have been studied with various microscopy techniques.

Morota *et al* produced ESD films of poly(ethyleneoxide) (PEO), investigating the effect of solution properties and spray conditions on surface morphologies [36]. Spheres and long fibres were observed, whilst fibrous features were enhanced by lower solution surface tension. Experiments were conducted in a dry air environment and morphologies evaluated with SEM.

Matsumoto *et al* implemented ESD to produce "fiber fabrics" of synthetic polymers [38]. A SEM was used to investigate films, indicating ESD successfully deposited polymers without degradation.

Rietveld *et al*, also studied the morphology of ESD polymer films, demonstrating a large variation of film uniformity with initial solution and ES conditions [37], concluding that ESD could be tuned for specific polymers.

4.2.2 Vacuum ESD

Initial studies of in vacuum ESD used modified existing ES-MS systems, placing samples within mass analysis chambers [41, 42]. These publications proved the concept but had little application at the time.

Recent increased interest in large molecules as semi-conducting materials has generated a suitable application for *in situ* UHV deposition methods. Two other university based research groups have built their own UHV ESD systems [43-54].

O'Shea *et al*, University of Nottingham, have developed an ESD capable of delivering solute molecules into a vacuum of 10^{-8} mBar. Based upon a modular differential pumping system, ES droplets travel directly from the emitter into UHV. Studies have included the comparison of ESD PEO samples prepared in air to those in vacuum, indicating an increased uniformity of UHV samples [43] and the successful deposition of nanotubes and fullerines from suspension [44-46].

Schlaf *et al*, University of South Florida, have developed a simple UHV ESD based upon a two stage differential pumping system coupled to a load lock [51]. The system is capable of depositing into a vacuum of 10^{-5} mBar, thus samples are deposited prior to analysis in a separate chamber. Publications to date have assessed polymer samples with photo-electron spectroscopy, conducting experiments on the prepared films between depositions without having to break vacuum [47-54].

4.3 Aberystwyth ESD system

Portability was of major importance in the design of the ESD apparatus, with the intension of transporting it to research facilities (synchrotrons). As such, the system needed to be easily integrated into existing analysis chambers, all of which are based on inherent UHV technology with access via standardised conflate knife edge flanges. The ideal size for this application was 70mm, popular and small enough for weight considerations but large enough for implementation of system requirements. Most UHV analysis chambers are orientated with sample manipulation in the vertical plane

from a central top flange, therefore the deposition system would have to be able to utilise available ports and would need to be operational invariant of position. The entire system would have to be self supporting in both vertical and horizontal orientations without the need for additional infrastructure. Vacuum welds are very strong but it is inadvisable to subject these to significant strain as a failure could be catastrophic, therefore a maximum apparatus weight of 10kg was set**.**

The choice of materials available was limited due to UHV compatibility, stainless steel was chosen due to its ease of machining and availability. Bespoke components made for the project were produced by Scanwel Ltd and Aberystwyth University.

The initial ESD was designed to spray directly into a vacuum, but preliminary tests indicated this caused several detrimental issues; Firstly, emitters could only have a relatively small inner diameter (tens of microns) in order to prevent the liquid being drawn out by low pressure, thus necessitating the need for extra flow control. Secondly, emitters in vacuum block readily due to adiabatic freezing as liquid rapidly expands at the tip, which is a particular problem with the use of small inner diameter emitters. Thirdly, establishment of stable ES and its alignment relative to the incident skimmer are extremely difficult with the emitter housed within a closed volume. Finally, solvent evaporation is aided by the presence of a gaseous atmosphere at the emitter tip and although it has been proven that an entirely UHV based ESD system is possible [44], this does result in significant solvent presence at the sample site and would therefore render the desired UHV levels necessary for direct deposition into analysis chambers unattainable**.**

The ESD system was developed upon mass spectrometry methodology, with the emitter spraying into atmosphere and the resulting droplets travelling through a series of differentially pumped stages impinging upon the sample held in UHV, as shown in figure 4.3.

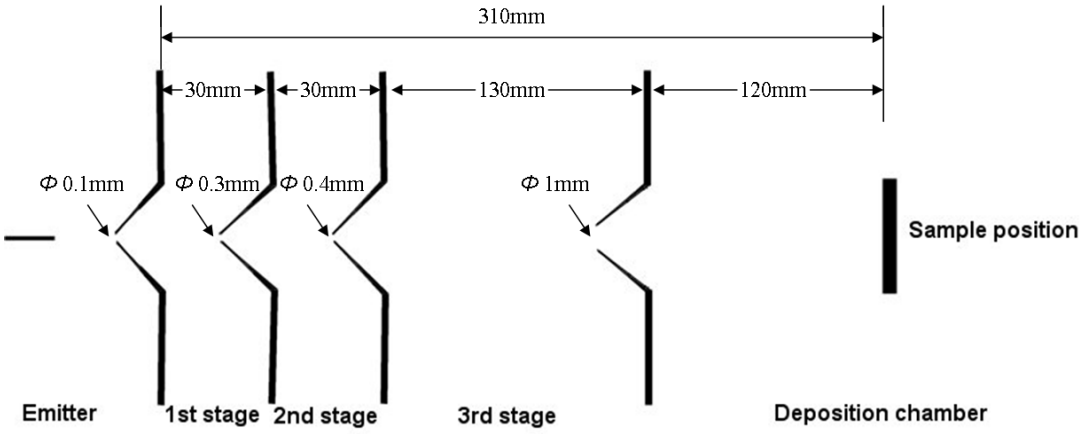

Figure 4.3 – Schematic representation of the Aberystwyth ESD system. Size of apertures as per final optimised system orientation (section 4.4.2).

For clarity the ESD system is discussed in sections describing each function involved in its operation.

4.3.1 Liquid delivery system

The molecules held in solution need to be delivered to the emitter at controlled flow rates (10-100μlmin^{-1}). A schematic representation of the liquid delivery system is shown in figure 4.4. Due to the inner diameters of ES emitters, liquid delivery has to be applied under considerable pressure. Options available for such a system were limited to only two, either a pumped syringe or a pressurised vessel. Due to safety considerations, the decision sided with the mechanically pumped syringe.

From the syringe the liquid is delivered through a 300µm inner diameter PEEK tube via an inline 2µm filter prior to the emitter.

The emitter is held in a conducting fitting with a high voltage connection concealed within a gimbal housing. The gimbal angularly aligns the emitter, compensating for any emitter distortion, a problem observed when using those with a small outer diameter (360µm). The gimbal consists of a truncated copper ball into which the conductive fitting is seated. The ball is held in an acrylic casing in which an electrode is held against it under tension by means of a small spring. The gimbal housing is attached to a small XYZ manipulator stage allowing for accurate alignment of the emitter and adjustment whilst spraying.

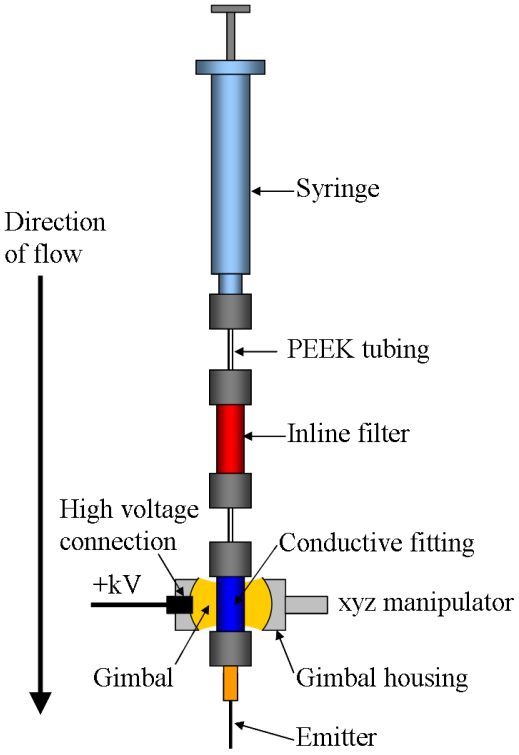

Figure 4.4 – Schematic representation of the ESD liquid delivery system.

4.3.2 Fittings

Fittings used throughout the liquid delivery system are zero dead volume PEEK micro tight fittings (Upchurch Scientific). Easy connection is achieved by finger tightening, causing ferrules to "swage" lock against the tubing forming a union which is rated to 10,000PSI operating pressure [55].

4.3.3 The syringe pump

Liquid is forced through the capillary tubing and emitter under significant pressure. In order to supply the liquid at constant flow rates a syringe pump was built in-house, powered by a low geared electric stepper motor. Syringe size and plunger speed can be used to control liquid flow rates. The syringe pump is able to accommodate syringe sizes up to 20mm outer diameter. A maximum continuous spray of 10ml of solution can be achieved before refilling using the larger 20mm syringes. At the highest pumping speeds this equates to a continuous deposition of approximately one hour duration.

4.3.4 Syringes

During this study PEEK Luer terminated medical syringes were used, with rubber plunger seals in volume sizes of 1ml and 10ml depending upon the flow rate and deposition period required. Although any type of syringe could be used the Luer microtight fitting allowed for the simplest connection between the syringe and the rest of the liquid delivery system.

4.3.5 Emitters

Electrospray emitters are available in many sizes and materials. ES-MS emitters are designed specifically for spraying solute molecules at very low flow rates and are therefore suited to application in the ESD system.

Emitters are categorised as either on-line or off-line. On-line emitters are designed to be connected to a flow rig allowing for continuous spraying over many hours. Off-line emitters are designed to hold finite amounts of solution and are used to control the amount of solution sprayed. Because the ESD system needed to deposit for varying time intervals only on-line emitters were considered, as these would allow for the deposition to be turned on and off at will. Many emitters are made for specific ES-MS commercial systems rendering most unsuitable. Also due to the way in which high voltage is applied to the conducting fitting, only emitters which are fully conductive are suitable.

Durability was a major consideration in the choice of emitter, as the ability to clean the emitters after use is essential. Stainless steel emitters can be cleaned by sonification and were considered to be the best choice due to their durability and conductivity.

Two sizes of stainless steel emitters were used during this study, the relatively small 30μm inner diameter (Proxeon [56]) and larger 100μm inner diameter (New Objective [22]). The ES droplet size was found to be directly proportional to the inner diameter of an emitter (section 4.5). The Emitters have tapered profiles reducing the wall thickness at the tip which aids in the formation and stability of the Taylor cone.

4.3.6 The high voltage supply

The voltage required for stable ES using the emitters described above is between 2 and 5 kilovolts, and needed to be a stable floating high voltage with respect to ground. It was decided this should be positive as this was demonstrated to have the most applications and choice of suitable solvents [24].

The high voltage supply was built in-house based upon a capacitance and diode voltage multiplier circuit. This was integrated into the same control unit as that of the syringe pump saving space, thus aiding in the portability of the machine.

4.3.7 Differential pumping system

In order to achieve the desired UHV sample conditions, a series of differentially pumped stages separated by small apertures was designed, aligned with a clear line of sight through the system to deliver molecules from atmosphere directly into UHV.

After consideration of the available pumps, the apparatus size and the ultimate vacuum level required, it was decided the differential pumping stages should be modular, such that extra stages could be added if necessary as shown in figure 4.5.

The design was based upon three pumping stages prior to a deposition chamber, the first two stages are pumped by rotary pumps and the third by a turbo molecular pump.

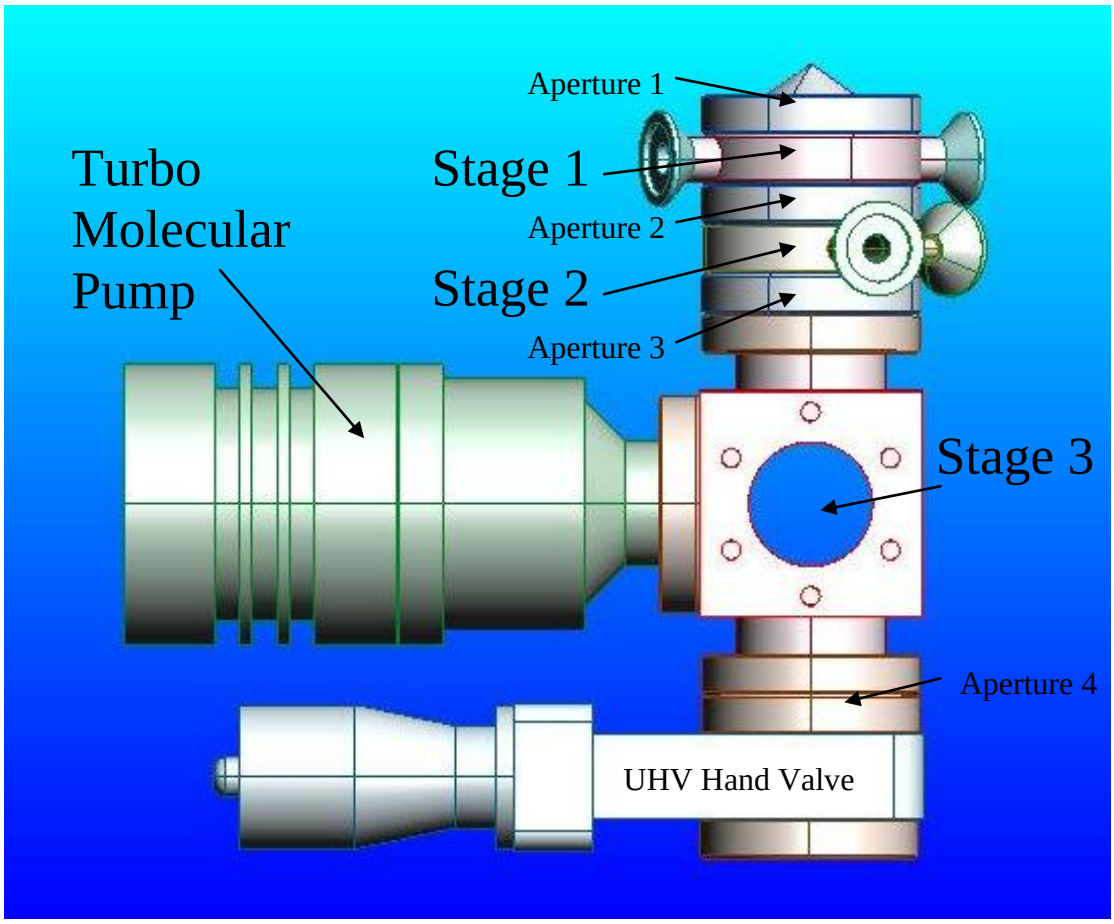

Figure 4.5 – Schematic representation of the ESD differential pumping system, consisting of three stages separated by apertures with UHV hand valve for connection to deposition chamber. The quartz crystal assembly is removed from stage 3 for clarity.

4.3.8 Apertures

Apertures are a critical component of the differential pumping system allowing the propagation of the sprayed droplets and restricting the gas flow.

The original apertures were machined into 70mm blank flanges, manufactured by drilling through and cutting a conical shape to the under side. The conical recess aided transmission through the aperture reducing the wall length and allowing for expansion on the higher vacuum side. However transmission through these apertures was poor as the large surface area presented to the incident spray caused random electrostatic deflections. Evaluation of this issue suggested that the conical shape to the underside

of the apertures did aid transmission, but presenting the spray with a large surface area was less than ideal.

In order to reduce the surface area at the aperture inlet it was necessary to change the aperture design to a projected cone, creating a skimmer akin to those used extensively throughout ES-MS. The conical apertures were produced with an outer angle of 57^{o} and inner angle of 59^{o} creating a sharp edge at the inlet to the aperture (minimising the wall thickness). Angular dimensions were theoretically calculated from work by Kantrowitz and Grey, optimising post orifice turbulence effects [57].

The apertures are made as insert components which can be fitted to a generic recess in specially machined 70mm blanks, thus apertures can be interchanged easily without compromising the infrastructure of the pumping system.

The orifice size of the apertures directly influences the vacuum achievable within the system and the transmission rate of ES molecules, therefore there is a compromise between the two factors. Experimentation indicated the first aperture to be the critical factor in the ultimate vacuum levels achievable within each stage of the system, optimisation of the aperture orifice sizes resulted in a deposition chamber vacuum level of 10^{-8} mBar (section 4.4.2).

4.3.9 Stage design

Each stage of the differential pumping system was designed and manufactured as a purpose built component based on 70mm UHV flange terminations. Alignment of the apertures separating each pumping stage was imperative in order to allow the transmission of ES molecules to the sample position. Workbench laser alignment ensured the system was set up correctly, all stages then had three of their six clamping

holes reamed, such that when assembled the stages and apertures would be accurately doweled in position.

The first two stages are identical spacer sections with two access ports for pumping and vacuum monitoring, as shown in figure 4.6. Rotary pumps can cope with large gas loads and are therefore well suited to these initial stages. Solvent is removed from the droplets by evaporation whilst in air and the low vacuum of the first two stages. This process occurs very quickly due to the size of the ES droplets (μm), therefore the first two stages are of minimum length to increase pumping efficiency.

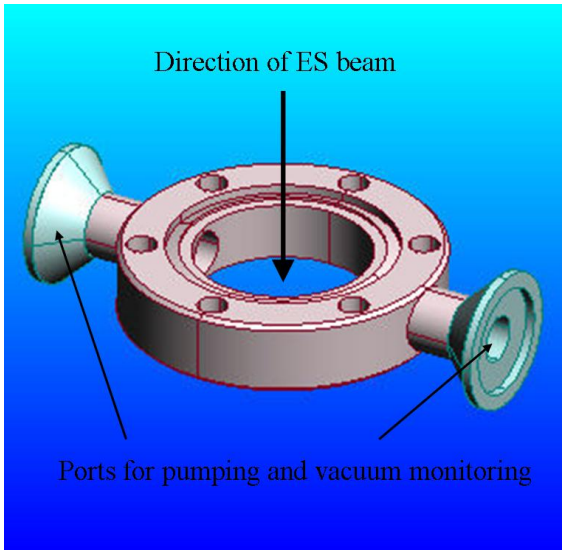

Figure 4.6 – Schematic representation of the 1st and 2nd differential pumping stages.

The third stage is the first to be pumped by a rotary backed turbo molecular pump. The initial aperture vacuum level tests were conducted using a generic UHV 70mm T-piece. This was adequate for the vacuum tests but alignment between the flanges was out by a considerable margin, thus rendering it unsuitable for the ESD system. This misalignment is caused by the manufacturing welding processes causing heat stress within the metal and warping of the tube from straight. Therefore a new third stage had to be manufactured to ensure perfect alignment in the orientation of ES molecule

propagation. The third stage was manufactured from a single billet of stainless steel, as shown in figure 4.7, it was based upon a cube with bored holes orientated centrally along each axis. The six terminations were allocated as follows, two directly opposing for connection to the system through which the molecular beam propagates and the remaining as orthogonal access ports.

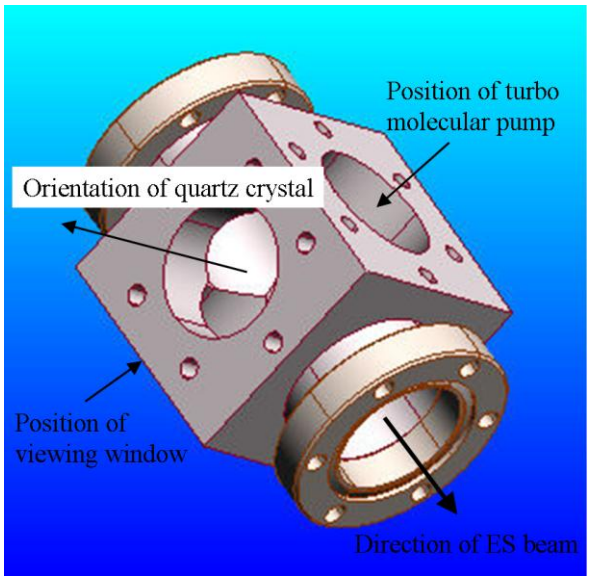

Figure 4.7 – Schematic representation of the 3rd differential pumping stage. The orientation of the quartz crystal is indicated but the assembly has been removed from the image for clarity.

The third stage was designed to be able to house instrumentation so the ES beam could be dissected by a quartz crystal resonator. Therefore the four ports are allocated as; one viewing window, one for pumping and the remaining two for the quartz crystal manipulator, associated electrical feed through and ion gauge. The turbo pump was connected directly on to the third stage to maximise its pumping efficiency.

The quartz crystal manipulator is based upon those used in scanning electron microscope (SEM) with linear movement, thus the quartz crystal can be moved into

the ES beam to assess its presence and deposition rate. The electrical connection for the crystal balance is supplied via a Kapton insulated copper wire.

The third stage is separated from the deposition chamber by a hand valve situated below the final aperture, allowing the deposition chamber to be kept under UHV whilst the ESD is non-operational or whilst establishing the desired deposition rate.

4.3.10 The Deposition Chamber

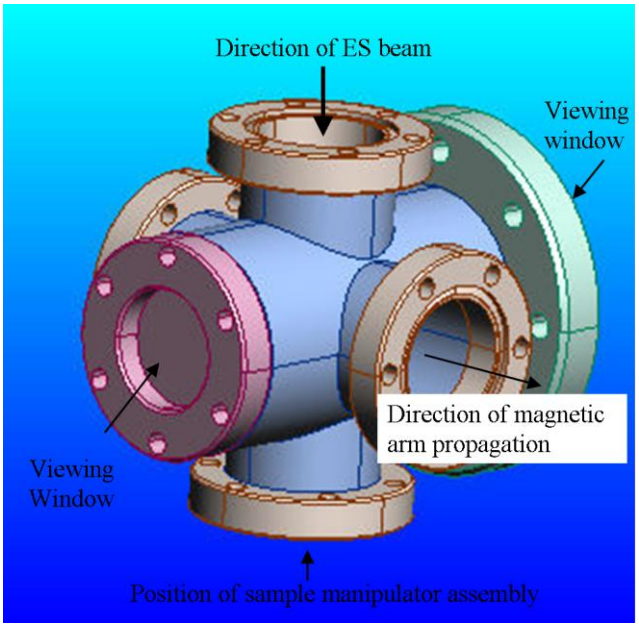

Figure 4.8 – Schematic representation of the ES deposition chamber. The positions of the magnetic transfer arm and sample manipulator are indicated but not shown for clarity.

The deposition chamber is a purpose built unit of six-way cross orientation, with two opposing ports on each axis, as shown in figure 4.8. The deposition chamber serves as a load lock delivering samples from the ESD system to analysis chambers by a magnetic arm orthogonally orientated to the ES beam. A retractable sample stage is built on to a high temperature (1200^{o}C) button heater (HeatWave Labs Inc) [58] positioned directly in the path of the ES beam. The sample stage is electrically

isolated from the chamber such that a drain current can be taken to indicate the ES beam presence.

The deposition chamber is pumped by a turbo molecular pump connected directly to the chamber and an ion pump situated on the magnetic arm which can be isolated from the chamber by a second hand valve. The ion pump acts as a supplementary pump whilst the ESD is non-operational and also allows samples to be withdrawn from the chamber and kept under UHV for transportation.

4.4 ESD commissioning

The ESD system once built required a series of experiments in order to characterise its functionality.

4.4.1 UHV heater calibration

The sample stage heater (x-369 Heatwave Labs Inc) incorporated into the deposition chamber required calibration in order to establish its lower temperature operation, as shown in figure 4.9.

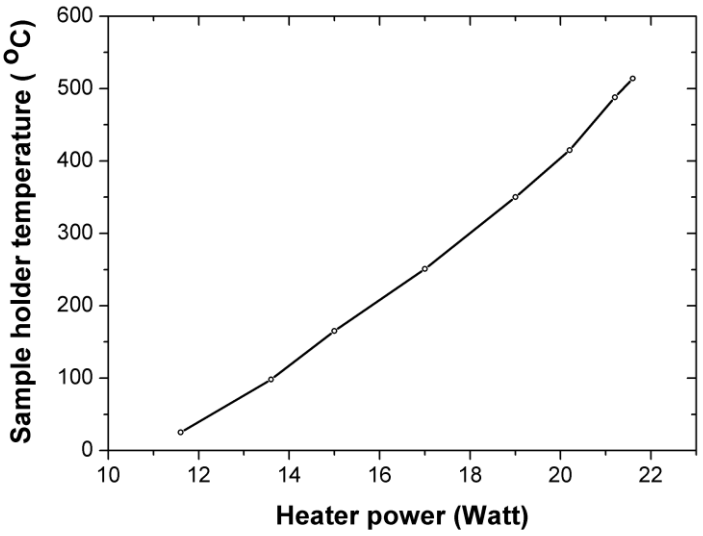

Figure 4.9 – Calibration of ESD sample stage, temperature taken using k-type thermocouple at sample position.

The deposition chamber had an initial base pressure of $2x10^{-8}$mBar which was observed to rise with increasing heater temperature due to out-gassing of the sample stage. Temperature measurements were made by k-type thermocouple attached to the sample stage.

4.4.2 Differential pumping system

The differential pumping system of the ESD was optimised in order to improve the ultimate achievable UHV level within the deposition chamber. The pumping of the initial two stages was improved by maximising the size of the pipes joining the rotary pumps to each stage. The pumping efficiency of the third stage was maximised by orientating the turbo molecular pump directly onto the chamber.

The parameter shown to have the largest influence upon the vacuum levels within the system was the size of the apertures. A series of tests were conducted to investigate the vacuum levels within the differential pumping system, as summarised in tables 4.1-4.4.

The tests summarised in tables 4.1-4.4 describe the aperture sizes between the stages and the vacuum level achieved under operation. The first two tests (tables 4.1 and 4.2) were only conducted over the first three stages, as the vacuum level of the third stage did not achieve adequate levels for the turbo molecular pump to be started.

As demonstrated by tests 3 and 4 the ultimate vacuum level of the deposition chamber is dependent upon the size of the initial inlet aperture of stage 1. Therefore the sequence of apertures described in test 4 was used to acquire the necessary vacuum levels for UHV ESD.

Test 1

	Aperture size (mm)							
Stage	0.1	0.2	0.3	0.4	0.5	1.0	Vacuum level (mBar)	Pump
1					X		16.8	Rotary
2					X		<1	Rotary
3					X		$5x10^{-1}$	Rotary

Test 2

	Aperture size (mm)							
Stage	0.1	0.2	0.3	0.4	0.5	1.0	Vacuum level (mBar)	Pump
1			X				9.6	Rotary
2				X			$4x10^{-1}$	Rotary
3					X		$1.2x10^{-2}$	Rotary

Test 3

	Aperture size (mm)							
Stage	0.1	0.2	0.3	0.4	0.5	1.0	Vacuum level (mBar)	Pump
1		X					1.8	Rotary
2			X				$8x10^{-2}$	Rotary
3				X			$5x10^{-5}$	Turbo
4						X	$2x10^{-7}$	Turbo

Test 4

	Aperture size (mm)							
Stage	0.1	0.2	0.3	0.4	0.5	1.0	Vacuum level (mBar)	Pump
1	X						<1	Rotary
2			X				$4x10^{-2}$	Rotary
3				X			$5x10^{-6}$	Turbo
4						X	$7x10^{-8}$	Turbo

Tables 4.1-4.4 – ESD differential pumping system aperture size optimisation tests. Pressures recorded as the base pressure of each stage in the absence of ES.

4.4.3 The liquid delivery system

Initial experiments were conducted to test the liquid delivery system using blank 50:50 water methanol solution. The system was set up as described in section 4.3.

These tests enabled experimental verification of the minimum and maximum proximity of the emitter to electrical ground, found to be 1 and 20mm respectively. At distances below 1mm arcing at the emitter can cause irreversible welding damage to the emitter tip. At distances greater than 20mm, the solution produced large droplets at the tip failing to form a Taylor cone even at maximum voltage (5kV).

The spray was found to be easily tuned with the variable high voltage supply to achieve stable ES. Below adequate voltage resulted in a "dripping" effect at the tip, the frequency of which increased with voltage until the Taylor cone was established. At higher voltages the formation of multiple jets was observed in agreement with those reported in the literature [16, 23].

4.5 Electrospray deposition of PEO

Poly(ethyleneoxide) (PEO) (Chapter 6) was chosen as a suitable molecule to test the ESD system as comparisons could be drawn to other ESD results reported in the literature. Solutions of PEO were made in 50:50 methanol/water at concentrations of $0.5gl^{-1}$.

Initial experiments were conducted to investigate deposition rates of the ESD by measurement with the quartz crystal analyser situated within the third stage.

The differential pumping system (with the deposition chamber isolated) was started prior to spraying allowing the third stage turbo molecular pump to operate and the vacuum level to stabilise. The emitter was held at a 1mm proximately to the inlet aperture of the first stage, continuous ES was tuned at the emitter to establish continuous spray. Within stage three the quartz crystal dissected the ES beam to record a deposition rate, an example of which is shown in figure 4.10.

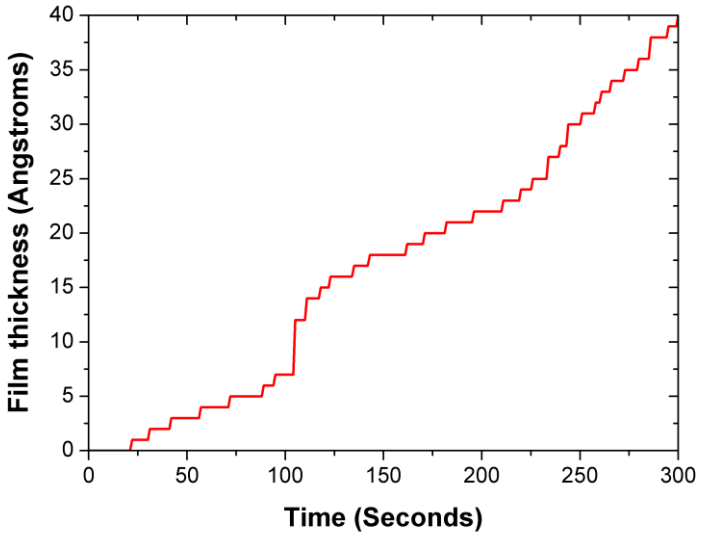

Figure 4.10 – Quartz crystal monitoring of ES PEO film deposition.

The recorded deposition rate has a stepped nature, this is attributed to intermittent blocking of the emitter tip with aggregated PEO. Therefore the deposition is a discontinuous process, as clearly illustrated by the large step at ~100 seconds.

Quartz crystal analysers are extremely sensitive instruments able to detect monolayers of material by recording the deflection of the quartz from its natural frequency [59], as described by the Sauerbrey equation (4.2).

$$A_F = \frac{N_q D_q}{\pi D_f Z F_C} \arctan\left(Z \cdot \tan\left(\frac{\pi\left(F_q - F_C\right)}{F_q} \right) \right) \qquad (4.2)$$

Where, A_F is the film thickness, N_q is the frequency constant for the crystal used ($1.668 \cdot 10^{13} Hz / Ang$), D_q is the density of the quartz ($2.648 g / cm^3$), F_q the eigen frequency of the quartz crystal before deposition, F_C the eigen frequency of the loaded sensor quartz crystal and D_f the density of the film material ($1 gcm^{-3}$). The component Z represents the square root of the ratio of density multiplied by the shear modulus of the quartz to that of the deposited material, as shown in equation 4.3.

$$Z = \sqrt{\frac{D_q \mu_q}{D_f \mu_f}} \qquad (4.3)$$

Where μ_q and μ_f represent the shear modulus of the quartz and the deposited material respectively.

4.5.1 Vacuum level effects

PEO samples were produced at vacuum levels corresponding to the tests described in tables 4.1-4.4, as summarised in table 4.5. The stated film thicknesses were calculated from the deposition rates taken before and after deposition.

Sample	Emitter I.D (μm)	Emitter Voltage (kV)	Solution concentration (gl^{-1})	Film thickness (nm)	Vacuum level (mBar)	Deposition time (mins)
A	30	2.5	0.5	100	10^{-2}	94
B	30	2.7	0.5	100	10^{-5}	94
C	100	3.6	0.5	100	10^{-7}	63

Table 4.5 - PEO ESD sample summary

The samples were deposited at steady rates of ~11 $Åmin^{-1}$ for samples A and B and ~16$Åmin^{-1}$ for sample C. The discrepancy between the deposition rates of the samples is attributed to the difference in emitter sizes used as indicated in table 4.5. The high voltage of the emitter tip was tuned to establish steady state ES in all cases. In the case of samples A and B the same 30μm inner diameter emitters were used resulting in only a relatively small voltage difference between the tests, whereas for the case of sample C the 100μm inner diameter emitter used required a significantly higher voltage in order to establish stable ES at the tip.

AFM imagery was used to study the surface topography of all three samples as shown in figure 4.11. The root mean square (rms) average roughness of the samples over a 10x10μm area was found to be 80nm, 60nm and 35nm for samples A, B and C respectively.

(i)

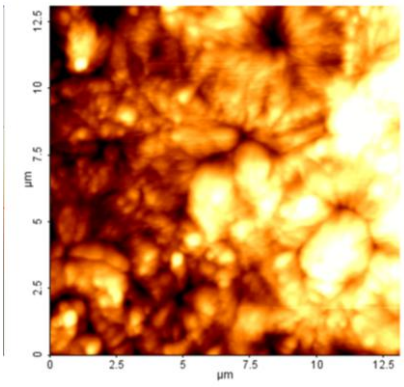

(ii)

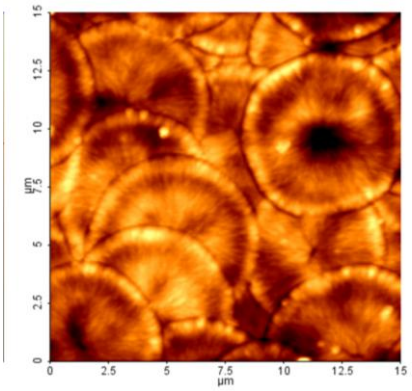

(iii)

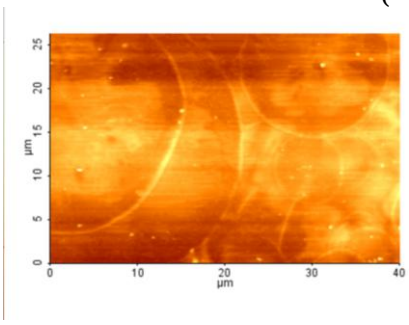

Figure 4.11 – AFM images of 50nm PEO surfaces taken using C-AFM (i) Deposition pressure of 10^{-2}mBar (ii) Deposition pressure of 10^{-5}mBar and (iii) Deposition pressure of 10^{-7}mBar.

Sample A displayed an amorphous structure, whereas samples B and C displayed clearly defined discs of polymer. This indicates the droplets are still wet on contact with the substrate and thus must be of significant solvent content in all cases. The definition of individual discs suggests the droplets dried quickly upon contact with the substrate as the solvent was removed into the gas phase and pumped away. The disc size difference between samples B and C is attributed to the different emitters used. The improved planarity of the films deposited in high vacuum allowed for more detailed AFM analysis of growth mechanisms, as described in section 4.5.2.

4.5.2 Investigations of PEO films grown in UHV

Three PEO samples of varied thickness were grown in a vacuum of 10^{-7}mBar, in order to investigate film morphology differences. The samples are summarised in table 4.6 stated with film thicknesses calculated from the deposition rates taken before and after deposition (~16Åmin^{-1}).

Sample	Emitter I.D (μm)	Emitter Voltage (kV)	Solution concentration (gl-1)	Film thickness (nm)	Deposition time (mins)
D	100	3.3	0.5	10	6
E	100	3.5	0.5	50	32
F	100	3.1	0.5	100	63

Table 4.6 – Summary of PEO samples grown by ESD in vacuum of 10^{-7}mBar

NC-AFM was used to investigate surface topographies of the samples, the results of which are presented in figure 4.12.

For sample D, image *(i)* shows bead like and chain structures within areas of low coverage (<10nm). The chain growth mechanism can be seen to disappear as the film thickness increases, therefore surface interaction must influence the polymer structure for low sample coverage.

For sample E, the increased film thickness causes the beads to become islands of aggregated polymer. The height of the islands in image *(ii)* (>100nm) are more than fives times greater than those observed for sample D (~20nm). The feature shown in *(iii)* is a dendrite structure observed at the extremity of the island features of sample E. These features do not have the same chain like structure observed for sample D, as there is greater mobility of the polymer when deposited in thicker films.

For sample F, higher polymer coverage was observed to yield fibrous growth as shown in images *(iv)* and *(v)*. These features are akin to those reported for electrospinning [60], attributed to relatively high solution concentrations. This type of growth is caused by clustering of the polymer within the solution prior to deposition.

All of the morphologies shown here are in close agreement with those reported for vacuum ESD in the literature [43].

In summary, the ESD system was demonstrated to successfully deposit solute molecules into a high vacuum environment of 10^{-7}mBar. AFM analysis of the PEO samples displayed varied morphologies similar to those reported in the literature. The ESD system was used to produce organic thin films for luminescent analysis, the results of which are presented in Chapter 6.

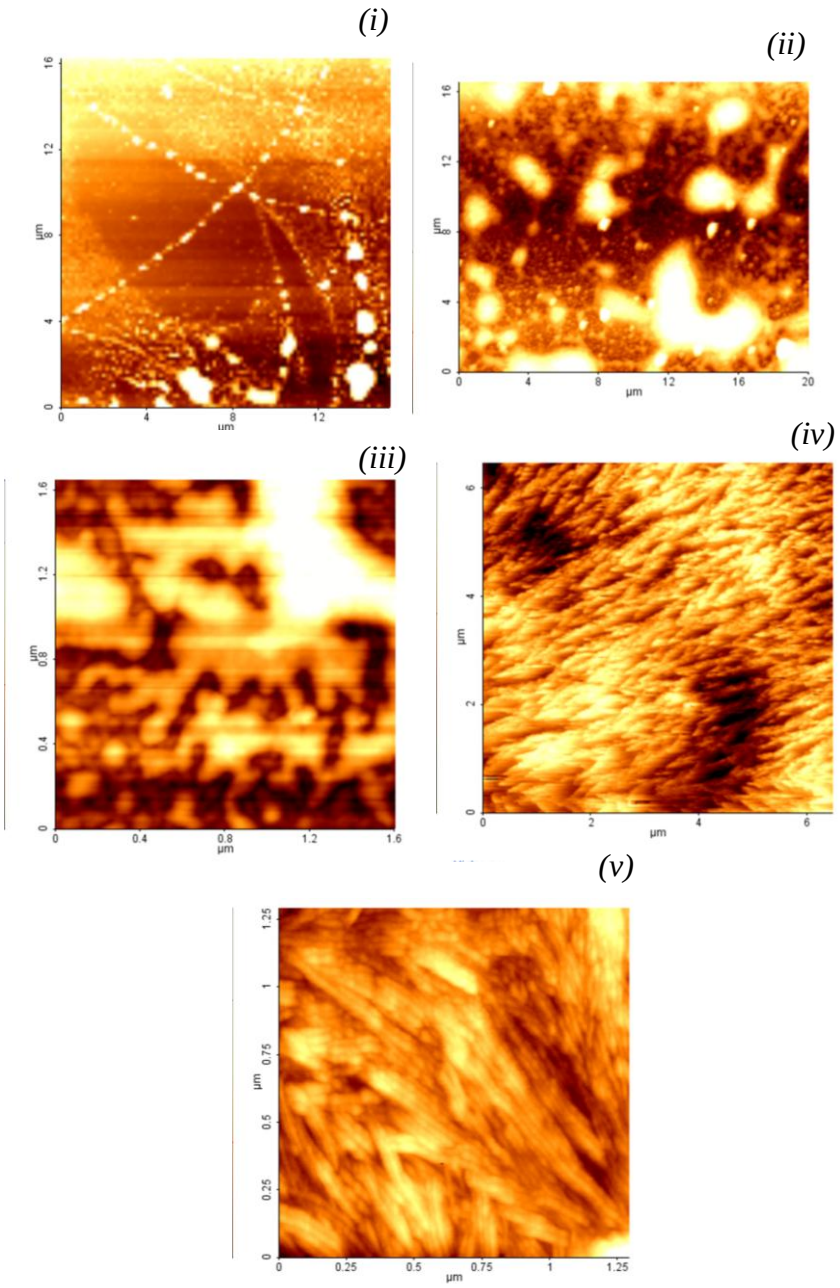

Figure 4.12 – High resolution NC-AFM images of PEO samples grown at 10^{-7}mBar. Image (i) sample D, images (ii)-(iii) sample E and images (iv) and (v) sample F. Several morphologies were identified including (i) bead and chain, (ii) aggregated bead-like structures, (iii) dendrites and (iv)-(v) fibrous growth.

1. A. Nollet and T. Stack. *Part of a letter from Abbe Nollet, of the Royal Academy of Sciences at Paris, and F.R.S to Martin Folkes Esq; Presisident of the Same, concerning Electricity*, Philosophical Transactions, 1748. **45**: 187-194.

2. L. Rayleigh. *On the equilibrium of liquid conducting masses charged with electricity*, Philosophical Magazine, 1882. **14**: 184-186.

3. J. Zeleny. *Instability of Electrified Liquid Surfaces*, The Physical Review, 1917. **10**(1): 1-7.

4. C.T.R. Wilson and G.I. Taylor. *The bursting of soap-bubbles in a uniform electric field*, Proceedings of the Cambridge Philosophical Society, 1925. **22**: 728-730.

5. W.A. Macky. *Some Investigations on the Deformation and Breaking of Water Drops in Strong Electric Fields*, Proceedings of the Royal Society of London Series A-Mathematical and Physical Sciences, 1931. **133**(822): 565-587.

6. G. Taylor. *Disintegration of water drops in an electric field*, Proceedings of the Royal Society of London Series A-Mathematical and Physical Sciences, 1964. **280**(1382): 383-397.

7. G. Taylor, A.D. McEwan and L.N.J. De Jong. *Studies in electrohydrodynamics I: The circulation produced in a drop by an electric field*, Proceedings of the Royal Society of London Series A-Mathematical and Physical Sciences, 1965. **291**: 159-166.

8. R.L. Hines. *Electrostatic Atomization and Spray Painting*, Journal of Applied Physics, 1966. **37**: 2730-2736.

9. R. Tilney and H.W. Peabody. *Electrostatic coating processes*, British Journal of Applied Physics, 1953. **S2**: 51-54.

10. M. Dole, L.L. Mack and R.L. Hines. *Molecular Beams Of Macroions*, Journal of Chemical Physics, 1968. **49**(5): 2240.

11. S.F. Wong, C.K. Meng and J.B. Fenn. *Multiple Charging in Electrospray Ionization of Poly(ethylene glycols)*, Journal of Physical Chemistry, 1988. **92**(2): 546-550.

12. J.B. Fenn, M. Mann, C.K. Meng, S.F. Wong and C.M. Whitehouse. *Electrospray Ionization for Mass Spectrometry of Large Biomolecules*, Science, 1989. **246**: 64-71.

13. M. Yamashita and J.B. Fenn. *Negative Ion Production with the Electrospray Ion Source*, Journal of Physical Chemistry, 1984. **88**(20): 4671-4675.

14. M. Yamashita and J.B. Fenn. *Electrospray Ion Source. Another Variation on the Free-Jet Theme*, Journal of Physical Chemistry, 1984. **88**(20): 4451-4459.

15. P.M. Adornato and R.A. Brown. *Shape and stability of electrostatically levitated drops*, Proceedings of the Royal Society of London Series A-Mathematical and Physical Sciences, 1983. **389**: 101-117.

16. M. Cloupeau and B. Prunetfoch. *Electrostatic spraying of liquids in cone-jet mode.*, Journal of Electrostatics, 1989. **22**(2): 135-159.

17. C.B. Richardson, A.L. Pigg and R.L. Hightower. *On the stability limit of charged droplets*, Proceedings of the Royal Society of London Series A-Mathematical and Physical Sciences, 1989. **422**: 319-328.

18. M. Cloupeau and B. Prunetfoch. *Electrohydrodynamic spraying functioning modes - a critical review*, Journal of Aerosol Science, 1994. **25**(6): 1021-1036.

19. A. Gomez and K. Tang. *Charge and fission of droplets in electrostatic sprays*, Physics of Fluids, 1994. **6**(1): 404-414.

20. A.M. Ganan-Calvo. *Cone-Jet Analytical Extension of Taylor's Electrostatic Solution and the Asymptotic Universal Scaling Laws in Electrospraying.*, Physical Review Letters, 1997. **79**(2): 217-220.

21. D. Duft, T. Achtzehn, R. Muller, B.A. Huber and T. Leisner. *Rayleigh jets from levitated microdroplets*, Nature, 2003. **421**: 128.

22. http://newobjective.com/electrospray.

23. M. Cloupeau and B. Prunetfoch. *Electrostatic spraying of liquids - main functioning modes*, Journal of Electrostatics, 1990. **25**(2): 165-184.

24. A. Jaworek. *Electrospray droplet sources for thin film deposition*, Journal of Materials Science, 2007. **42**(1): 266-297.

25. A.Lloyd. *Electrospray deposition of protein films: Surface engineering*, Materials Today, 2004. **7**(2): 19.

26. I. Uematsu, H. Matsumoto, K. Morota, M. Minagawa, A. Tanioka, Y. Yamagata and K. Inoue. *Surface morphology and biological activity of protein thin films produced by electrospray deposition*, Journal of Colloid and Interface Science, 2004. **269**(2): 336.

27. B. Lee, N. Kamiya, S. Machida, Y. Yamagata, K. Horie and T. Nagamune. *Fabrication of a protein film by electrospray deposition method and investigation of photochemical properties by persistent spectral hole burning*, Biomaterials, 2003. **24**(12): 2045.

28. J. Suh, B. Han, K. Okuyama and M. Choi. *Highly charging of nanoparticles through electrospray of nanoparticle suspension,* Journal of Colloid and Interface Science, 2005. **287**(1): 135.

29. F. Bagheri-Tar, M. Sahimi and T.T. Tsotsis. *Preparation of polyetherimide nanoparticles by an electrospray technique,* Industrial & Engineering Chemistry Research, 2007. **46**(10): 3348-3357.

30. H.M. Lee, S.G. Kim, I. Matsui, T. Iwaki, F. Iskandar, I.W. Lenggoro and K. Okuyama. *Monolayer deposition of L1(0) FePt nanoparticles via electrospray route,* Journal of Magnetism and Magnetic Materials, 2007. **313**(1): 62-68.

31. J. Therrien, A. Dindar and D. Smith. *AFM studies of nanoparticle deposition via electrospray ionization,* Microscopy Research and Technique, 2007. **70**(6): 530-533.

32. P.H.M. Bottger, Z. Bi, D. Adolph, K.A. Dick, L.S. Karlsson, M.N.A. Karlsson, B.A. Wacaser and K. Deppert. *Electrospraying of colloidal nanoparticles for seeding of nanostructure growth,* Nanotechnology, 2007. **18**(10): 105304.

33. I.W. Lenggoro, H.M. Lee and K. Okuyama. *Nanoparticle assembly on patterned "plus/minus" surfaces from electrospray of colloidal dispersion,* Journal of Colloid and Interface Science, 2006. **303**(1): 124.

34. S. Sarkar, N. Levit and G. Tepper. *Deposition of polymer coatings onto SAW resonators using AC electrospray,* Sensors and Actuators B: Chemical, 2004. **114**(2): 756-761.

35. H. Matsumoto, T. Mizukoshi, K. Nitta, M. Minagawa, A. Tanioka and Y. Yamagata. *Organic/inorganic hybrid nano-microstructured coatings on insulated substrates by electrospray deposition,* Journal of Colloid and Interface Science, 2005. **286**(1): 414.

36. K. Morota, H. Matsumoto, T. Mizukoshi, Y. Konosu, M. Minagawa, A. Tanioka, Y. Yamagata and K. Inoue. *Poly(ethylene oxide) thin films produced by electrospray deposition: morphology control and additive effects of alcohols on nanostructure,* Journal of Colloid and Interface Science, 2004. **279**(2): 484.

37. I.B. Rietveld, K. Kobayashi, H. Yamada and K. Matsushige. *Morphology control of poly(vinylidene fluoride) thin film made with electrospray,* Journal of Colloid and Interface Science, 2006. **298**(2): 639.

38. H. Matsumoto, Y. Wakamatsu, M. Minagawa and A. Tanioka. *Preparation of ion-exchange fiber fabrics by electrospray deposition,* Journal of Colloid and Interface Science, 2006. **293**(1): 143.

39. M.D. Paine, M.S. Alexander, K.L. Smith, M. Wang and J.P.W. Stark. *Controlled electrospray pulsation for deposition of femtoliter fluid droplets onto surfaces,* Journal of Aerosol Science, 2007. **38**(3): 315-324.

40. E. Burkarter, C.K. Saul, F. Thomazi, N.C. Cruz, L.S. Roman and W.H. Schreiner. *Superhydrophobic electrosprayed PTFE,* Surface & Coatings Technology, 2007. **202**: 194-198.

41. K.J. Kitching, H.-N. Lee, W.T. Elam, H. Johnston, H. MacGregor, R.J. Miller, F. Turecek and B.D. Ratner. *Development of an electrospray approach to deposit complex molecules on plasma modified surfaces.,* Review of Scientific Instruments, 2003. **74**(11): 4832-4839.

42. M. Danek, K.F. Jensen, C.B. Murray and M.G. Bawendi. *Electrospray organometallic chemical vapor deposition-A novel technique for preparation of II-VI quantum dot composites,* Applied Physics Letters, 1994. **65**(22): 2795-2797.

43. J.C. Swarbrick, J.B. Taylor and J.N. O'Shea. *Electrospray deposition in vacuum,* Applied Surface Science, 2005. **252**(15): 5622-5626.

44. J.N. O'Shea, J.B. Taylor, J.C. Swarbrick, G. Magnano, L.C. Mayor and K. Schulte. *Electrospray deposition of carbon nanotubes in vacuum,* Nanotechnology, 2007. **18**(3): 035707.

45. A. Saywell, G. Magnano, C.J. Satterley, L.M.A. Perdigao, N.R. Champness, P.H. Beton and J.N. O'Shea. *Electrospray deposition of C-60 on a hydrogen-bonded supramolecular network,* Journal of Physical Chemistry C, 2008. **112**(20): 7706-7709.

46. C.J. Satterley, L.M.A. Perdigao, A. Saywell, G. Magnano, A. Rienzo, L.C. Mayor, V.R. Dhanak, P.H. Beton and J.N. O'Shea. *Electrospray deposition of fullerenes in ultra-high vacuum: in situ scanning tunneling microscopy and photoemission spectroscopy,* Nanotechnology, 2007. **18**: 455304.

47. A.J. Cascio, J.E. Lyon, M.M. Beerbom, R. Schlaf, Y. Zhu and S.A. Jenekhe. *Investigation of a polythiophene interface using photoemission spectroscopy in combination with electrospray thin-film deposition,* Applied Physics Letters, 2006. **88**(6): 062104.

48. J.E. Lyon, A.J. Cascio, M.M. Beerbom, R. Schlaf, Y. Zhu and S.A. Jenekhe. *Photoemission study of the poly(3-hexylthiophene)/Au interface,* Applied Physics Letters, 2006. **88**(22): 222109.

49. J. Magulick, M.M. Beerbom, B. Lagel and R. Schlaf. *Ionization energy and electronic structure of polycytidine,* Journal of Physical Chemistry B, 2006. **110**(6): 2692-2699.

50. B. Lagel, M.M. Beerbom, B.V. Doran, M. Lagel, A. Cascio and R. Schlaf. *Investigation of the poly[2-methoxy-5-(2 '-ethyl-hexyloxy)-1,4-phenylene vinylene]/indium tin oxide interface using photoemission spectroscopy,* Journal of Applied Physics, 2005. **98**(2): 023512.

51. N. Dam, M.M. Beerbom, J.C. Braunagel and R. Schlaf. *Photoelectron spectroscopic investigation of in-vacuum-prepared luminescent polymer thin films directly from solution,* Journal of Applied Physics, 2005. **97**(2): 024909.

52. J. Magulick, M.M. Beerbom and R. Schlaf. *Investigation of adenine, uracil, and ribose phosphate thin films prepared by electrospray in vacuum deposition using photoemission spectroscopy,* Thin Solid Films, 2008. **516**(9): 2396-2400.

53. J. Magulick, M.M. Beerbom and R. Schlaf. *Comparison of ribonucleic acid homopolymer ionization energies and charge injection barriers,* Journal of Physical Chemistry B, 2006. **110**: 15973-15981.

54. N. Dam, B.V. Doran, J.C. Braunagel and R. Schlaf. *Charge injection barriers at a ribonucleic acid/inorganic material contact determined by photoemission spectroscopy,* Journal of Physical Chemistry B, 2005. **109**(2): 748-756.

55. www.upchurchscientific.com.

56. Proxeon-Biosystems. *Nano-Electrospray Emitters,* 2006.

57. A. Kantrowitz and J. Grey. *A High Intensity Source For The Molecular Beam.1. Theoretical,* Review of Scientific Instruments, 1951. **22**(5): 328-332.

58. www.cathode.com.

59. G. Sauerbrey. *Verwendung von Schwingquarzen zur Wagung dunner Schichten und zur Mikrowagung,* Zeitschrift fur Physik A Hadrons and Nuclei, 1959. **155**(2): 206-222.

60. S. Tang, C. Shao, Y. Liu, S. Li and R. Mu. *Electrospun nanofibres of poly(ethylene oxide)/teraamino-phthalocyanine copper(II) hybrids and its photoluminescence properties.,* Journal of Physics and Chemistry of Solids, 2007. **68**: 2337-2340.

Chapter 5

Luminescent Investigation of Boron Nitride

In this Chapter the results of luminescent investigations of hexagonal and cubic boron nitride are presented. Following an introduction to boron nitride (BN) the results are ordered as follows; In section 5.3 investigations of the luminescent emission of both phases are made using XEOL. In section 5.4.1 volume-integrated and spatially resolved OD-XANES is used to investigate structural defects of the cubic phase. In section 5.4.2 the XEOL emission of BN is used to determine the band gap energies of the two phases. Finally in section 5.5 pump probe measurements are used to resolve defect states within the band gaps of both phases.

5.1 Introduction to Boron Nitride

First synthesised in 1842 by Balmain *et al* [1], boron nitride (BN) is a synthetic inorganic III-V material consisting of equal atomic quantities of boron and nitrogen. The bonding of BN is isostructural to that of carbon materials having both sp^2 and sp^3 bonded phases. Several polytypes of BN exist, which can be considered in terms of phase bonded groups. These are the soft sp^2 bonded polytypes of hexagonal (h-BN), rhombohedral (r-BN), turbostratic (t-BN) and amorphous (a-BN) and the super hard sp^3 bonded polytypes of cubic (c-BN) and wurtzite (w-BN) [2, 3]. It has also been shown that BN can form fullerene cage and nanotube structures, both of which have been reported in the literature [4-6].

The simplest sp^2 polytype, a-BN, is synthesized at ambient pressure from either boric acid or boron trioxide at relatively low temperatures (<1000K) usually in the presence of a catalyst. From this disordered material higher order sp^2 bonded polytypes can be produced by annealing at high temperatures (~1500-2000K) [7]. The transitions between sp^2 polytypes are temperature dependent, ascending in degree of crystallographic order a-BN → t-BN → r-BN → h-BN [8, 9]. The manufacture of sp^3 bonded BN is usually made from conversion of sp^2 phase materials under conditions of high temperature and high pressure (typically T ~2000K and P ~ 5GPa) [2].

Historically, high temperature high pressure (HTHP) synthesis has been shown to yield the purest sp^3 crystals, as the other modes of growth tend to introduce unwanted sp^2 domains and impurities [10]. However, in recent years CVD epitaxial growth of c-BN on diamond has been shown to yield highly ordered pure materials at relatively low temperatures (~1100K) [11-13].

Several other modes of growth exist for the procurement of thin BN films, including plasma enhanced chemical vapour deposition (PECVD) [14-16], ion sputtering [17-20], radio frequency sputtering [21] and ion-assisted pulsed laser deposition [22-24]. Methods of BN thin film growth are still very much in their infancy but some significant and promising progress has been made recently.

The most common sp^2 and sp^3 polytypes of crystalline BN are h-BN and c-BN respectively. These materials were studied as part of this thesis and will be discussed in greater detail. The c-BN samples, supplied by Element Six Ltd, were produced by HPHT methods and the h-BN was supplied as powder from BDH Chemicals Ltd.

BN is the lightest of the III-V compounds, exhibiting global intrinsic properties of high thermal conductivity, high melting point, low thermal expansion, low electrical conductivity and chemical inertness [25, 26]. This has led to its use in a wide range of

industrial applications. Soft laminar h-BN is used as an industrial lubricant and chemically stable ceramic material for vacuum technology [10], whereas extremely hard c-BN (second only to diamond [27]) is used as a cutting grit in ferrous metal environments as an alternative to the more reactive diamond [28].

Since the first synthesis of c-BN in 1957 by Wentorf *et al* [29], BN has been investigated for its potential use as an optoelectronic material, due to its durability and optical response in the deep ultra violet (DUV) region of the spectrum [30-32]. However, much like diamond, both h-BN and c-BN are intrinsic insulators with wide band gap energies (~6eV), thus only in doped forms can BN be considered as semi-conducting. In 1962 it was shown that BN could be readily doped during synthesis with Be, S and Si yielding both n- and p-type materials [33]. Refinements have since been made to BN doping procedures although they remain largely the same in terms of dopant species utilised, with Be and Mg used to yield p-type and S, Si and C compounds used to produce n-type materials [33-36]. The ease of BN n-type doping is of particular interest as it overcomes the limitations of diamond in this respect [36-38].

Although alluded to in the 1960s the first functioning c-BN p-n junction was not realised until 1987 by Mishima *et al* [34, 39]. Subsequent development of BN as an optoelectronic material has been relatively slow compared to that of diamond, although there have been some promising new devices reported in recent years [40, 41]. The main reason for the lack of development in BN electronics is due to the debate surrounding many of its fundamental electronic properties; including the band gap energy, band structure and its optical response.

5.1.1 Physical structure

The structure of h-BN and c-BN are analogous to that of graphite and diamond respectively, as shown in figure 5.1. Only L-shell electrons are involved in BN bonding with the core K-shell 1s states remaining localised to the atomic nuclei. The bonding characteristics of both phases are described individually with reference to their carbon counterparts.

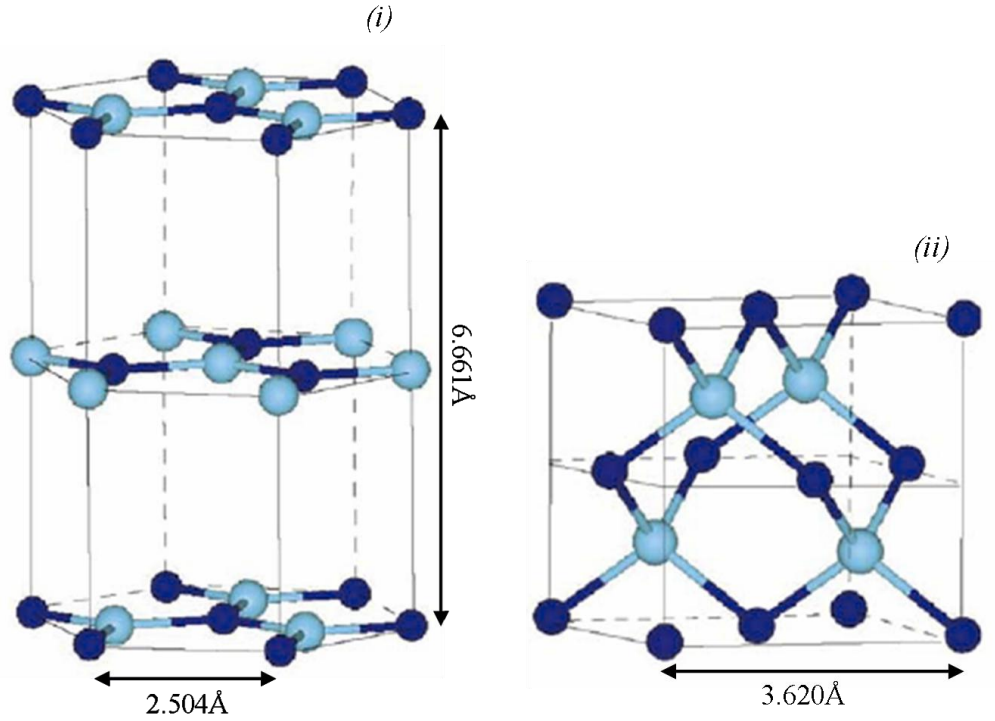

Figure 5.1 – Structural representation of the unit cells of (i) h-BN and (ii) c-BN reproduced from the literature [42]. B atoms are denoted by turquoise and those of N by dark blue.

h-BN is a laminar sp^2 bonded material similar in structure to that of graphite, thus having similar mechanical properties. Flat B_3N_3 hexagons are covalently bonded in atomic layers separated by weak interlayer bonds (van der Waals) [43]. However, the interlayer registry of h-BN differs from that of graphite. In h-BN atomic hexagons of neighbouring layers lie directly over one another with alternating boron over nitrogen orientation, whereas in graphite the adjacent atomic layers are stepped out of phase

with half the atoms of adjacent layers not lying directly over one another. The bonding of h-BN and graphite is described in terms of hybridized sp^2 bonding, which occurs in the plane of the hexagonal lattice (x,y), with each atom equivalently bonded to three others creating in plane σ bonds. The $2p_z$ orbitals, unsubscribed in sp^2 bonding, stand perpendicular to the lattice plane above and below each atomic centre. These $2p_z$ orbitals overlap to form delocalised π bonds parallel to the lattice plane.

c-BN on the other hand is sp^3 bonded in a zinc-blende tetrahedral structure, isostructural to that of diamond [27, 44], with a unit cell of face centred cubic orientation [45]. The bonding of c-BN and diamond is described in terms of hybridised bonds, where four equivalent hybridized sp^3 bonds about each atom mix all three orientations of the 2p with the 2s orbitals forming only σ bonds [2]. The bond lengths of c-BN (1.446Å) are comparable to those of diamond (1.420Å), hence c-BN is also a dense and super hard material.

For clarity a representation of hybridised bonding in both phases is displayed in figure 5.2

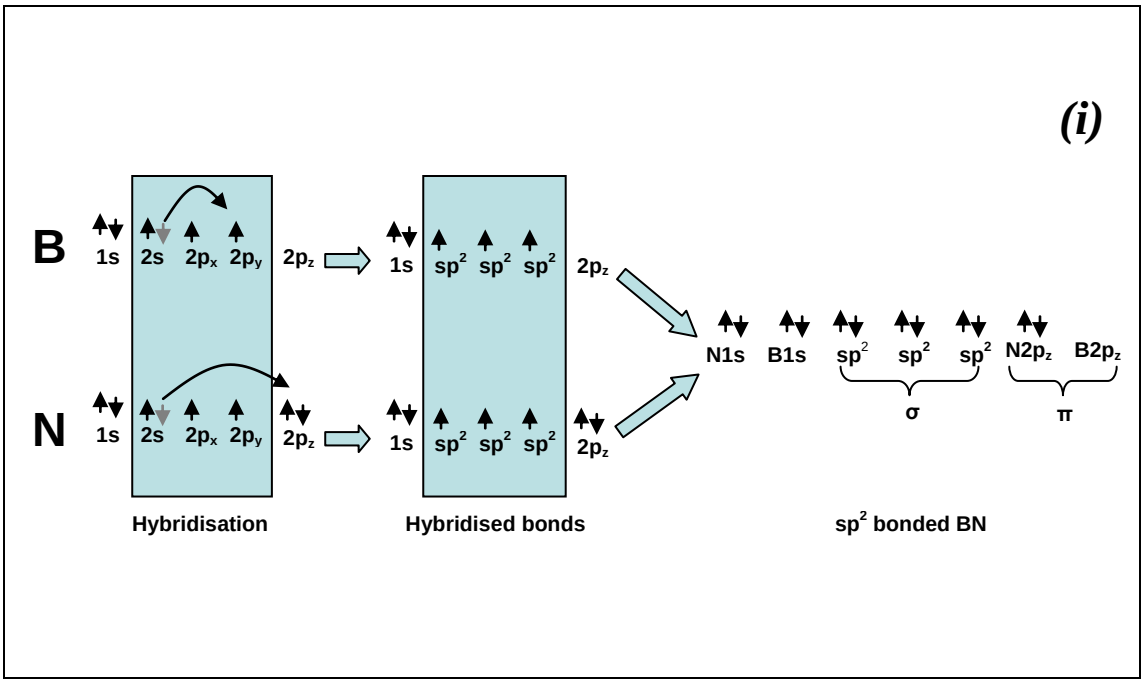

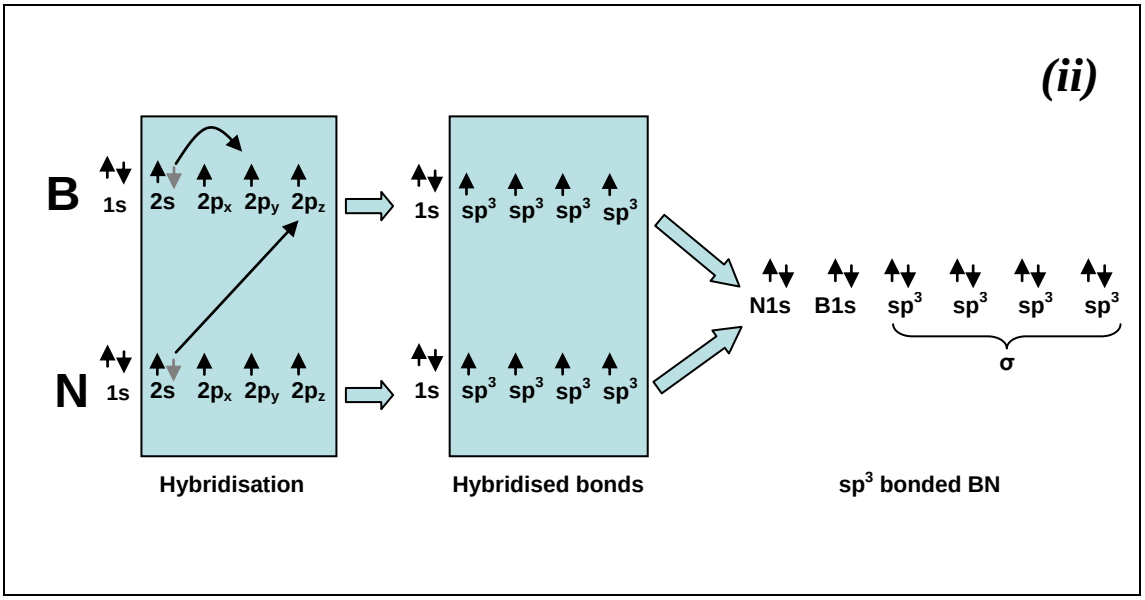

Figure 5.2 – Hybridised bonding of BN, small arrows indicate the presence of an electron and its direction of spin.
(i) sp^2 bonding – Prior to hybridisation electrons are promoted from the B2s to B2p_y and from the N2s to N2p_z as indicated. Hybridisation mixes the 2s with the 2p_x and 2p_y in both B and N creating three equivalent sp^2 orbitals. The resultant sp^2 bonded BN is shown with σ and π orbitals as indicated.
(ii) sp^3 bonding – Prior to hybridisation electrons are promoted from the B2s to B2p_y and donated by the N2s to the B2p_z, thus all L-shell orbitals in both B and N are singularly occupied. Hybridisation mixes the 2s with all three orientations of the 2p, forming four equivalent sp^3 bonds. Resultant sp^3 bonded BN is shown with σ bonds as indicated.

5.1.2 Electronic Structure

All B-N bonds exhibit polarity due to the charge difference between the boron and nitrogen atomic nuclei [2]. This polarity causes a large separation in energy between the bonding and anti-bonding states, creating a wide band gap in both h-BN and c-BN (~ 6eV).

The electrical conduction of h-BN is poor in contrast to that of graphite which has quasi-metallic response. This is attributed to the difference between the π bonds of graphite and h-BN. In graphite the 2p_z orbitals are all singularly occupied creating

unpolarised π bonds, the bonding and anti-bonding states of the π bonds overlap giving high conduction in the direction of the lattice. Whereas for h-BN, the $2p_z$ orbitals of nitrogen are doubly occupied while those of boron are vacant, this causes π bond polarity and a large separation between the bonding and anti-bonding states. Electrical conduction in h-BN is therefore poor due to the low mobility of electrons trapped at the nitrogen centres.

The electrical conductivity of c-BN is akin to that of diamond. Having only strong covalent σ bonds yields no weakly bound electrons for conduction, culminating in a large separation between the bonding and anti-bonding states. Also, much like diamond c-BN has been reported to have a negative electron affinity (NEA) [10, 36, 46], where the energy of the vacuum level exists below the conduction band minima, thus an electron excited above the Fermi level can escape from the material's surface unimpeded.

5.1.3 Band structure

Electronic band structure describes the directional variation of electronic structure with reference to the crystallographic lattice. It is calculated by three dimensional modification of the Schrödinger equation to include the anisotropic nature of charge distribution within the lattice, thus electron bands can no longer be considered as simply parabolic in distribution. This modified condition is described by the Bloch equation, expressing the forbidden and allowed electron states in terms of momentum (k) and energy (E).

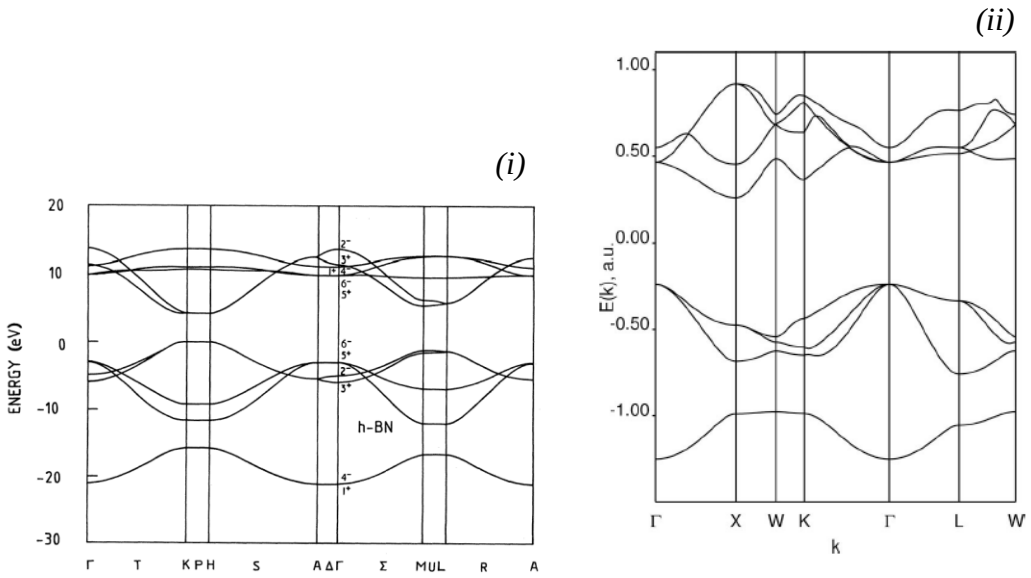

Figure 5.3 – Theoretical band structure of (i) h-BN) and (ii) c-BN reproduced from the literature[45, 47]

The typical band structures of both h-BN and c-BN are reproduced from the literature in figure 5.3. h-BN is described has having a quasi-direct band gap at either H or K [48], whereas c-BN has an indirect band gap between Γ and X [44]. As the structure of c-BN is highly ordered and periodic there is little variation in the band structure reported. However for the case of h-BN, there is a lack of common agreement as to the nature of the band structure, with reports of both indirect and direct band gaps [49, 50]. Studies have also reported a variation of the h-BN band structure with applied external pressure, due to its laminar mechanical structure [51].

UV and X-ray absorption techniques can probe the density of states (DOS) within the valence and conduction bands respectively, viewing the band structure in one dimension. However, band structure only accounts for the absorption and emission of light above 6eV, it does not indicate the anisotropic defect states existing within the band gap responsible for lower energy luminescent emission. Therefore detection of the luminescent emission can be used to probe defect states within BN.

Luminescent emission can be utilised as a probe into a material's structural and electronic quality (Chapter 2). Several luminescent techniques were employed to study both h-BN and c-BN in this thesis, the results for which are displayed and discussed in this Chapter. Experimentally obtained results of the band gap energy, defect state energies and structural variation are presented for both phases.

5.2 Introduction to the Boron Nitride samples

The BN samples studied as part of this thesis are summarised in table 5.1. The c-BN samples were supplied as extremely high purity (99.9%) HPHT materials by Element Six Ltd in two size selected crystal sizes of 10-20μm and 100μm. The h-BN powder also of high purity (99%) was obtained commercially from BDH Chemicals Ltd.

Sample phase	Crystal size	Source
h-BN	>nm powder	BDH Chemicals Ltd
c-BN	10-20μm	Element Six Ltd
c-BN	~100μm	Element Six Ltd
Mixed phase (h-BN and c-BN)	>1μm	Element Six Ltd

Table 5.1 – Summary of BN samples

The 10-20μm c-BN and mixed phase BN samples were investigated using scanning electron microscopy (SEM), the results of which are shown in figure 5.4 [1]

[1] SEM results courtesy of Biological Sciences, Aberystwyth.

(i)

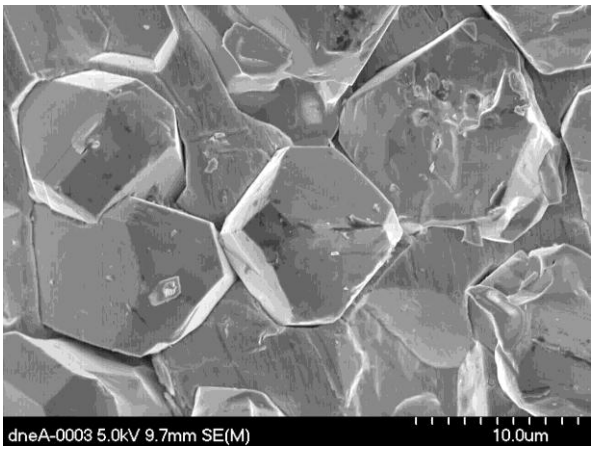

(ii)

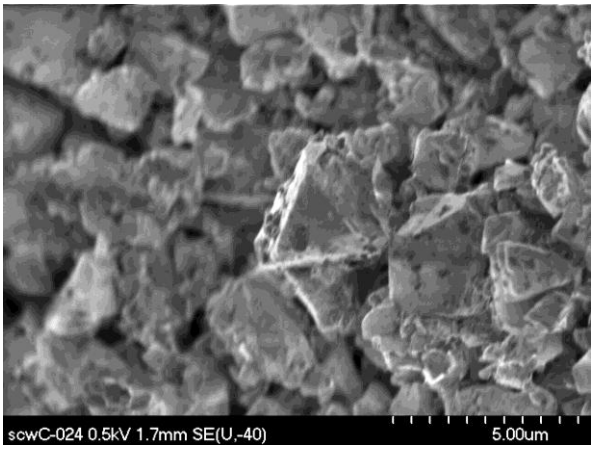

Figure 5.4 – SEM images of (i) 10-20μm c-BN and (ii) mixed phase BN samples.

The 10-20μm c-BN sample consists of crystals displaying uniform octahedral morphology, as shown in figure 5.4*(i)*; this suggests an extremely high crystalline quality [52].

The mixed phase sample is made up of small c-BN crystals with surface h-BN growth, as clearly shown in figure 5.4*(ii)*, thus it is of relatively poor crystalline quality.

The 100μm c-BN sample, not studied with SEM, also displayed octahedral morphology, although of less uniform content (section 5.4.1.3.2.1).

5.3 Optical properties – X-ray excited optical luminescence (XEOL)

The most efficient optical transitions result from a change of electron energy without a change of momentum, thus they are depicted as vertical transitions in terms of the band structure. Indirect electron transitions also exist but require the additional interaction of phonons to satisfy momentum change.

Both h-BN and c-BN, as already mentioned, are optically active materials displaying absorption in the UV and emission in the UV and visible regions. This section will introduce the XEOL and Raman spectroscopic results for the h-BN powder and 10-20μm c-BN samples after a review of the relevant literature.

5.3.1 Previous research

The luminescence of h-BN consists of several clearly defined deep ultra violet (DUV) bands and a single broad convoluted UV/VIS emission. The DUV bands have been studied extensively both theoretically and experimentally. The most commonly reported DUV emission bands are centred at 5.77eV and 5.46eV (215nm and 227nm respectively). Additional DUV bands have also been identified with energies of 5.35eV (231nm), 5.64eV (220nm) and 5.88eV (210nm) [53]. All of the DUV bands of h-BN have been attributed to band to band excitonic recombination, however there are subtle differences between the individual bands. For example, the second highest reported energy band (5.77eV) has been ascribed to the recombination of a single free exciton, whereas those of lower energy are ascribed to bound excitons and vibrational replicas [54].

Theoretical studies have reported the DUV emission of h-BN as being of Frenkel-type excitonic recombination (with binding energies of about 0.7eV) rather than the usual Wannier-type attributed to most III-V semi-conducting materials [48, 53, 55, 56].

An exciton is an electron and associated electron hole which behave as a neutral particle within the atomic lattice. The energy required to dissociate the charges of an exciton is referred to as its binding energy. Frenkel-type excitons have a strong electron-hole interaction having high binding energies (~0.5eV), whereas the electron-hole interaction of Wannier-type excitons is weak resulting in low binding energies (meV).

Spatially resolved cathodoluminescence (CL) has been used to investigate the DUV emission bands of h-BN; Spatially resolved investigations of a relatively large (5μm) single crystals, proved the origin of the lower energy bands (5.64eV and 5.46eV) to be structural defects (grain boundaries and dislocations) [55]. This conclusion was also shared by Watanabe *et al* [54] in a separate study, where h-BN samples were analysed before and after mechanical deformation. This work compared the emission of the 5.77eV and 5.46eV bands before and after deformation. Before deformation both bands were present with the 5.77eV emission dominant. However, after deformation the emission was exclusively due to the 5.46eV band, proving its dependence upon structural stacking defects. Further evidence of the difference between the excitonic emission of the 5.77eV and 5.46eV bands was shown by time-resolved PL decay analysis [57], comparing the lifetimes of the associated luminescence. The lifetime of the 5.46eV band was shown to be an order of magnitude longer than that of the 5.77eV band (3ns compared to 70ps) suggesting quite separate charge dynamics are involved with each.

The broad UV/VIS emission bands of h-BN have been ascribed to defect related recombination. Common agreement of the likely candidates for such defects exists within the literature, however the identity of individual bands still remain a subject of debate. Museur *et al* [58], initially ascribed the emission to singular and multiple nitrogen vacancies as well as band-impurity transitions, however in a later publication [56] higher resolution PL results led to localised C and O donor acceptor pairs (DAPs) being cited as the likely origin. Other experimental studies have also assigned structural defects as well as C and O impurities to the broad UV/VIS emission of h-BN, drawing comparisons from the luminescent emission observed in Gallium Nitride (GaN) [53].

The luminescent emission of c-BN is observed as a broad convoluted band in the UV/VIS region [39, 59]. c-BN unlike h-BN displays no DUV emission indicating an absence of near band to band excitonic recombination. The luminescent emission of c-BN is thus solely attributed to defect related transitions, however there does remain little common agreement in the positions of individual emission bands within the luminescent spectra.

Trinkler *et al* [59], reported four broad emission peaks within the luminescence of c-BN, centred in the UV, blue, green and red regions of the spectra. Ageing samples were also shown to have increased red emission. However, the samples were reported to be mostly cubic phase suggesting they may have been of inferior quality.

Zhang *et al* [60], attributed the broad emission of c-BN to multi-vacancy complexes of boron and nitrogen in pure cubic phase samples. Two main emission bands were identified with energies of 2.48eV and 3.12eV.

Ca and Mg doped c-BN samples have also been shown to display common distinct luminescent bands centred at 2.07eV, 3.12eV and 3.77eV, with Ca doping yielding an additional band at 1.77eV [32]. The relative band intensities between samples indicated potential correlation with doping species. However the report did not define the defects responsible for each individual luminescent band.

In summary, the luminescence of h-BN and c-BN are similar in terms of their broad UV/VIS emission but differ with relation to the near band to band transitions (DUV), which are observed exclusively in the hexagonal phase. There are several defects common to both phases which are attributed to the broad UV/VIS emission but there is no definitive proof linking individual bands to their origin. However, recently a correlation between the atomic concentrations of C and O with luminescent emission has been reported, indicating impurity as the origin of broad UV/VIS emission in both phases [61].

Numerous Raman and Fourier transform infra red (FTIR) spectroscopic studies of BN have been undertaken. Both techniques monitor the inelastic phonon related scattering of low energy monochromatic light. Spectra are resolved in terms of wavenumber (cm^{-1}) difference from that of the excitation source. Materials with optical phonon structure generally yield sharp lines corresponding to separate phonon contributions within the lattice. Optical phonons (those probed by Raman) are described in terms of their propagation through the crystallographic lattice in either transverse (transverse optical - TO) or longitudinal (longitudinal optical - LO) orientations.

For the case of h-BN, there are two Raman active lines reported at wavenumbers of $51.8cm^{-1}$ and $1366cm^{-1}$ which are attributed to in plane low and high energy phonons

respectively [43, 62]. The origin of the phonons is centrally orientated to the Brillouin zone at Γ symmetry. Interestingly both lines exhibit no longitudinal-transverse (LO-TO) splitting, this has been attributed to the opposing motion of nitrogen and boron atoms within the lattice. The two planes of displacement are combined symmetrically cancelling each other out, thus yielding a single phonon line. FTIR studies yield an additional line at 780cm^{-1} caused by an out of plane sp^2 bending mode, however this response is dependent upon the amount of material present as the line is completely absent for samples of thickness less than 50nm [62, 63].

For the case of c-BN, there is one optical phonon originating from the centre of the Brillouin zone at Γ. This degenerative phonon splits giving rise to the TO and LO Raman active lines at 1056cm^{-1} and 1306cm^{-1} respectively [52, 62].

In summary, both phases have optically active phonon structure, with that of c-BN more clearly defined. The Raman spectroscopic results for the BN samples studied as part of this thesis are presented below and discussed in relation to the XEOL emission.

5.3.2 Results

The XEOL spectra of the h-BN powder and 10-20μm c-BN are shown in figure 5.5. The data was collected at ~10K using MoLES on beamline MPW6.1 at the SRS, Daresbury. Both materials were irradiated with continuous monochromatic X-rays at 185eV just below the B K-egde absorption energy.

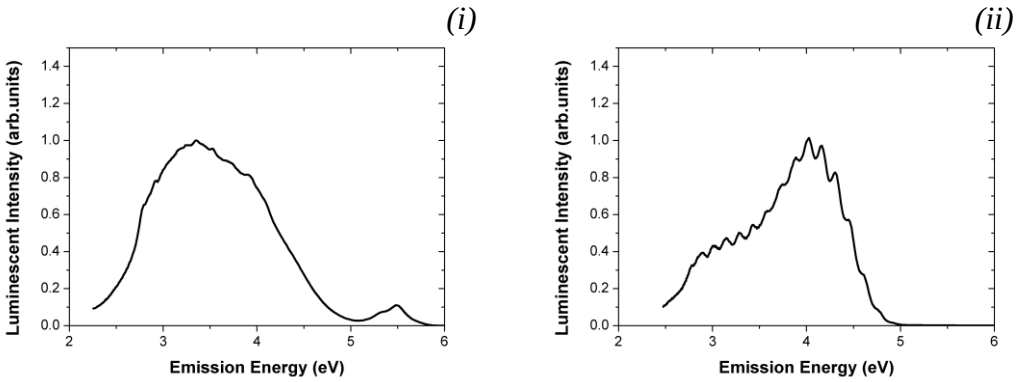

Figure 5.5 - XEOL emission at 185eV of (i) h-BN and (ii) c-BN corrected for background and normalised.

Both phases as expected display UV/VIS emission in the form of a large convoluted band, h-BN also has additional emission in the DUV region. The fitting of the h-BN and c-BN XEOL is shown in figures 5.6 and 5.7 respectively.

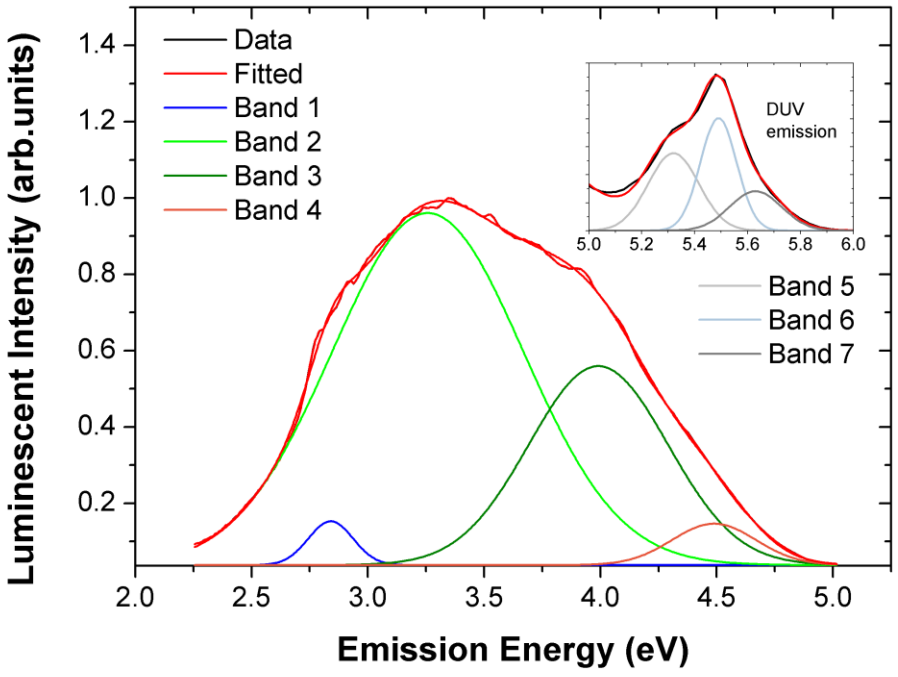

Figure 5.6 – Fitted h-BN XEOL spectra of convoluted UV/VIS emission (main) and DUV bands (inset).

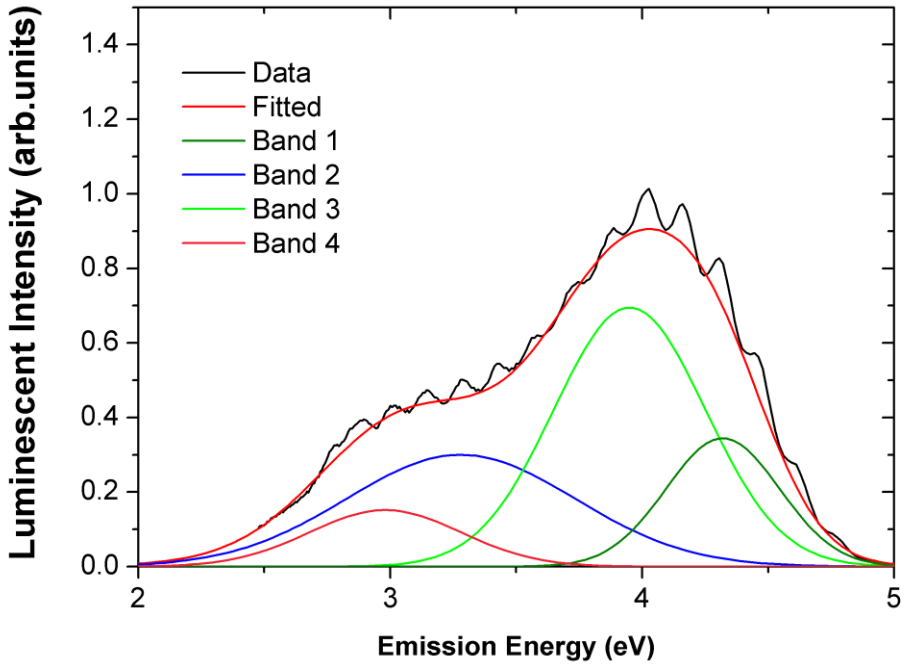

Figure 5.7 – Fitted c-BN XEOL spectra of convoluted UV/VIS emission.

5.3.3 Discussion

For the case of h-BN four Gaussian bands can be fitted to the UV/VIS emission centred at 2.84eV, 3.25eV, 3.99eV and 4.49eV as shown in figure 5.6 labelled 1 to 4 respectively. Previously reported results have indicated only two bands are responsible for this emission [64-66], however by consideration of the pump probe results (section 5.5) this updated fitting procedure can be applied. There remain two dominant broad bands at 3.25eV and 3.99eV (labelled as band 2 and 3). The lowest and highest energy emission bands, that of 2.84eV and 4.49eV (labelled as band 1 and band 4) exist as lower intensity emissions with the presence of band 1 marked by a shoulder upon the low energy side of band 2, whereas that of band 4 is observed as a deviation in the emission towards the high energy tail of band 3.

The DUV emission of h-BN can be fitted by three narrow Gaussian bands centred at 5.32eV, 5.49eV and 5.62eV as shown in the inset figure 5.6. These bands are of similar energy to that reported in the literature, however the free exciton emission (5.77eV) is absent. This would suggest the DUV bands indicated are exclusively due to bound exciton emission.

For the case of c-BN four Gaussian bands centred at 2.98eV, 3.28eV, 3.95eV and 4.32eV are fitted within the broad UV/VIS emission as shown in figure 5.7, labelled as 1 to 4 respectively. All the bands overlap one another and are consistent with those reported in the literature. The relative intensities of the bands have been reported to differ between sample batches and as such the dominant bands observed here may not be representative of all c-BN samples [64]. For the case of this sample (10-20μm c-BN) the two dominant bands are at 3.28eV and 3.95eV (2 and 3).

5.3.3.1 Raman spectroscopy and phonon structure

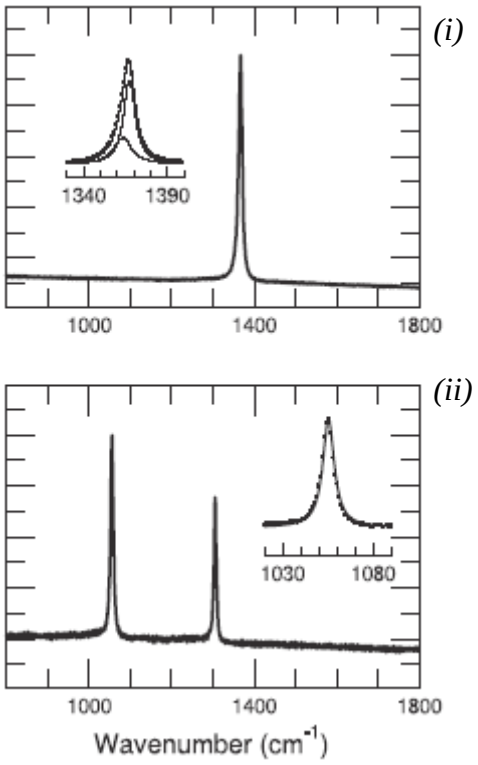

Figure 5.8 – The raman spectroscopy results of the (i) h-BN powder and (ii) 10-20μm c-BN samples.

The Raman spectra for both samples are shown in figure 5.8. Data was collected using an anti-stokes Raman spectrometer (Horiba Jobin Yvon, Labram) at HeNe laser wavelength 632.8nm. The h-BN was found to have a single Raman active line at 1366cm^{-1}, whereas c-BN had lines at 1056cm^{-1} and 1306cm^{-1}. For c-BN the two lines were fitted by single Lorentzian functions with narrow FWHM of 7cm^{-1}, indicating the material of be of extremely high bulk purity. However, for the case of h-BN, the Raman line had an anisotropic structure with a tail extending to low energies. This was fitted with two Lorentzian functions at 1363.5cm^{-1} and 1367.2cm^{-1}. The presence of low energy tails within Raman lines has been attributed to a superposition of contributions from bulk and microcrystalline materials.

The positions of the Raman active lines for both phases were in excellent agreement with those reported in the literature (section 5.3.1).

The presence of phonon structure within the XEOL spectra of a material is an indication of high purity. The XEOL emission of both phases exhibit phonon structure as shown in figures 5.9 and 5.10 for h-BN and c-BN respectively. The phonon peaks can be resolved for average energy separation and considered with relation to the presented Raman spectra and FTIR spectra reported in the literature. Only LO phonons strongly interact with light emission, due to the electo-optical effect [67], thus the TO contributions will not considered.

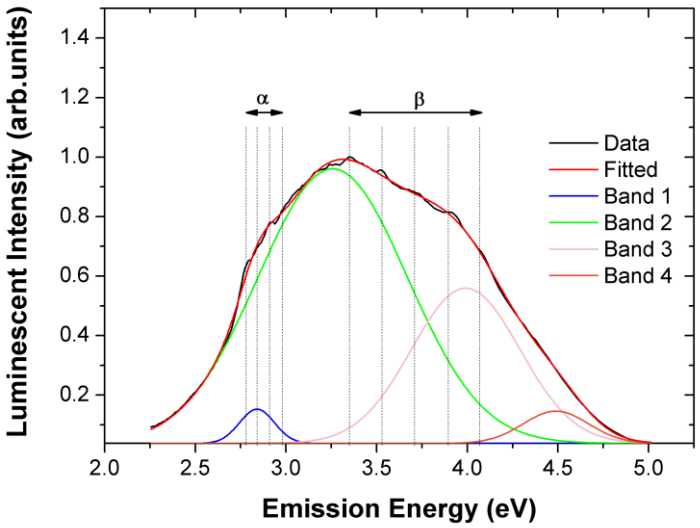

Figure 5.9 – XEOL emission spectra of h-BN indicating phonon positions within regions labelled α and β.

As shown in figure 5.9 the XEOL phonon structure of h-BN can be resolved as two regions of distinct energy separation, labelled as α and β. Region α has an energy separation of 70meV and is ascribed to the 2.84eV band (band 1). Region β has an energy separation of 182meV and is ascribed to the 3.25eV band (band 2). As would be expected the phonon structure is observed on the high energy side of the respective bands, however the zero phonon energy cannot be identified in either instance. The

higher energy bands of 3.99eV and 4.49eV (3 and 4) do not display any clear phonon contribution. Considering the phonon structure with reference to the Raman spectroscopy, the 1366cm^{-1} line corresponds to an energy separation of 169meV which is in reasonable agreement to region β. However, the phonon structure of region α does not have a corresponding Raman line. The reported FTIR active line at 780cm^{-1} corresponds to an energy separation of 90meV, which would suggest a greater separation than that observed. However, it is possible that the phonon contribution responsible for region α is due to this out of plane IR active phonon.

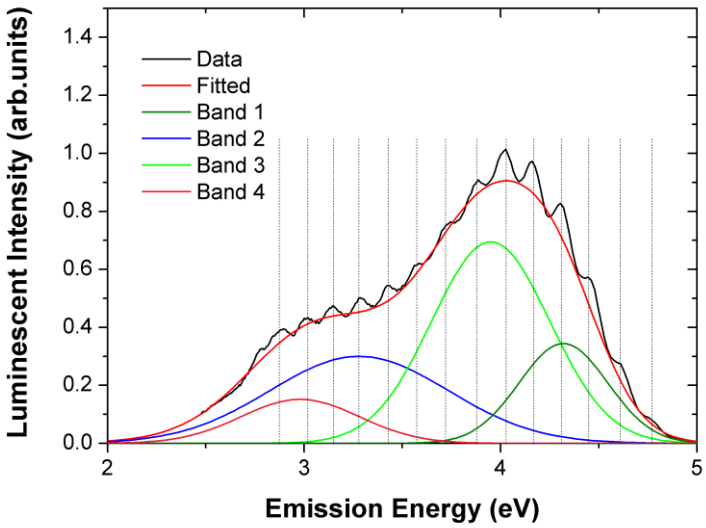

Figure 5.10 – XEOL emission spectra of c-BN with phonon positions indicated

For the case of c-BN, strong phonon contribution exists across the entire XEOL emission as shown in figure 5.10. The average energy separation of the phonon structure is 152meV which is in agreement to that previously reported. However there is also additional contribution of lower energy phonons (125meV) leading to increased broadening of replicas away from the zero order emission (high energy tail of band) [64]. The LO Raman line at 1306cm^{-1} corresponds to an energy of 162meV,

in close agreement with the energy separation observed, although it does not account for the lower energy contributions. The observed phonon structure is likely to be due to the superposition of phonons from each overlapping emission band, thus giving rise to the relatively broad peaks (~150meV).

5.3.4 Summary

The XEOL emission reported here is typical for that of both phases, however the resolution is much improved such that extra phonon related contribution can be identified. The convoluted UV/VIS emission of both phases is similar, although at this time it cannot be concluded that the defects responsible are the same.

The XEOL phonon structure is observed in both phases, with that of the cubic phase being more pronounced due to its greater crystallographic order. For both phases this phonon structure within the light emission is unusual, with very few previously reported cases [60].

The prime candidates for the UV/VIS luminescent emission are nitrogen vacancy and impurity. The DUV bands of h-BN identified at near band gap energies are due to the recombination of bound excitons.

Correlation of the Raman and FTIR lines to the XEOL was successful in ascribing the observed phonon structures.

5.4 Optically detected X-ray absorption studies

5.4.1 K-edge OD-XAS of Boron Nitride

XAS is an experimental method sensitive to bonding differences in materials of identical atomic constituents. Therefore, it can be utilised to identify the bonding differences between h-BN and c-BN. Optically detected XAS (OD-XAS) as described in chapter 2 monitors the luminescent yield of a material (XEOL) as a function of photon excitation energy. The area of greatest interest to this study is the initial absorption edge onset (XANES region), in which the core 1s to lowest unoccupied state resonance occurs. For the case of h-BN this is the anti-bonding π^* orbital, whereas for c-BN it is the anti-bonding σ^* orbital. In this section the OD-XANES of the BN samples are presented. CLASSIX1 was utilised to spatially investigate the luminescent emission of c-BN crystals, linking abnormalities in the emission to structural defects.

5.4.1.1 Previous research

The B and N K-edge XANES of BN has been the subject of several experimental studies, although those using optical detection (OD-XAS) are relatively few. The results of electron and fluorescent experimentation are still valid as reference to this study, as it is only the detection mode which differs.

Due to only the B K-edge being studied as part of this thesis, the following literature review will only concentrate upon its features. However, features of the B K-edge do have equivalent N K-edge resonances, although these are less well defined.

The B K-edge features of h-BN and c-BN are markedly different. For the case of h-BN, there is a prominent π* resonance at 192eV prior to a doubly split σ* resonance peaking at 198eV and 199eV [2, 38, 65, 66, 68]. Additional π* resonances have also been reported, attributed to N vacancy and interstitial states around the B atoms. Monitoring of the relative π* peak intensities whilst inducing increasing amounts of N vacancy within the lattice provided evidence as to the origin of each resonance. N vacancy peaks were identified at lower binding energies than the stoichiometric π* resonance (192eV), whereas a single peak at higher binding energy was attributed to an additional N bond (interstitial states) [2].

For the case of c-BN, the B K-edge features are solely due to σ* resonances. In the XANES region there are two convoluted peaks present, an initial sharp peak at 194eV superimposed upon a much broader peak centred at 198eV. The initial sharp σ* resonance (194eV) has been ascribed to excitonic contribution (effectively increasing the absorption), interestingly it is only present in the cubic polytype being entirely absent from the similarly sp^3 bonded wurtzite polytype. Unlike h-BN, the peaks of c-BN have not been ascribed to separate defects within the lattice, this is due to the overlap of resonances making up the continuum conduction states which the B1s-σ* resonances represent [2, 38, 66, 68, 69].

Additional B1s-σ* resonances are reported to exist beyond 200eV for both phases, however these are not of relevance to the present study.

Several studies have utilised B K-edge XAS to establish phase contributions in BN materials, a selection from which are described below;

Berns *et al* [69], used NEXAFS to study CVD grown BN films, establishing h-BN bonded contamination in otherwise c-BN bonded materials. Zhou *et al* [38], utilised

the linear polarisation of synchrotron light to investigate the orientation of sp^2 bonded interface layers of c-BN films grown on Si and diamond coated Si surfaces. The sp^2 basal layers were found to be normally orientated to the substrates, however the contribution was greatly reduced on the diamond coated Si. Thus, c-BN was proven to grow epitaxially on diamond. Hemraj-Benny *et al* [68], used NEXAFS to characterise BN nanotubes showing them to be of high sp^2 bonded crystallographic order (h-BN) with low levels of defects.

All of these studies used electron and fluorescent detection methods. These methods whilst established, are limited in application due to their fixed sampling depth; electron yield probes only the surface (~5nm) of a sample, whereas fluorescent yield is a bulk sensitive technique (~200nm). Thus both methods of detection need to be employed simultaneously to effectively probe the chemistry of an entire sample. OD-XAS on the other hand provides a workable solution, being able to differentiate between surface and bulk contributions within the same data set. Evans *et al* [66], used OD-XANES as a method of phase identification in mixed phase BN samples. The h-BN luminescent contribution was shown to originate from the surface states; Partial luminescent yield (PLY) OD-XAS was utilised to resolve separate emission contributions from the crystals. The OD-XANES signal generated from the emission in the DUV (226nm) displayed a purely positive h-BN signal, indicative of luminescence from surface states.

5.4.1.2 Experimental details

All experiments were carried out on beamline MPW6.1 at the SRS Daresbury with CLASSIX1 used as the end chamber. The samples studied are summarised in table 5.1 (section 5.2).

The B K-edge was studied exclusively as the beamline flux over the N K-edge (~400eV) was too weak for any detail to be resolved from the data. CLASSIX1 was operated in CCD collection mode and the optics varied as described for the individual results. The samples, adhered to the cold finger holder by conductive tape, were cooled to ~30K and held in a vacuum of 10^{-8}mBar. All experiments were conducted for each sample with the beam position remaining constant, such that the same crystals responsible for the emission were studied throughout.

The data was corrected for background and fluctuations to the beamline flux. The background signal was recorded as an average CCD pixel intensity with the beamline closed. A SiO_2 sample was used to generate beamline flux measurements as a material of linear response in the relevant energy range. XEOL measurements made with CLASSIX1 were corrected for relative filter transmission response by the operating software.

The results are organised as follows; The total area integrated results are presented first, where the signal was taken to be the average CCD pixel intensity for each energy step. Following this the spatially resolved XEOL and OD-XANES results are presented, where the CCD signal was selectively filtered to investigate the luminescent emission of individual crystals and areas of interest.

5.4.1.3 Boron K-edge OD-XANES results

5.4.1.3.1 Volume-integrated OD-XANES

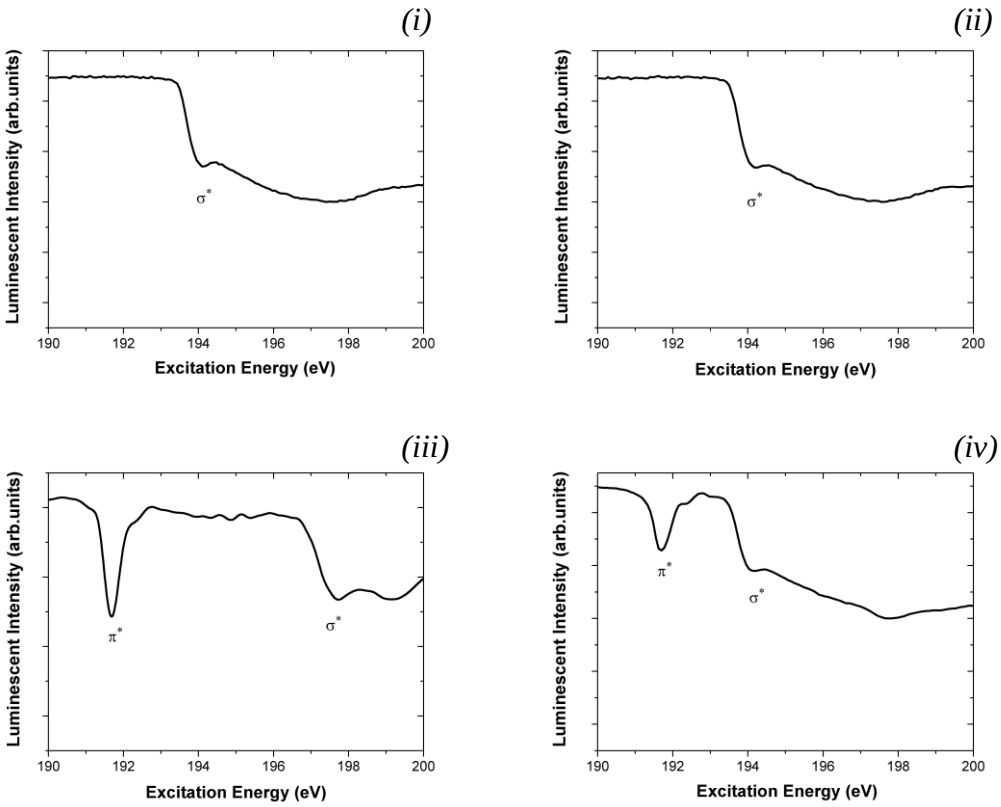

Figure 5.11 – B K-edge OD-XANES of (i) 100μm c-BN (ii) 10-20μm c-BN (iii) h-BN powder and (iv) mixed phase BN. The anti-bonding B1s-π* and B1s-σ* resonances are indicated.

The boron K-edge OD-XANES of all the BN samples are shown in figure 5.11. All the results were conducted in total luminescent yield (TLY) using the x10 visible objective.

For the case of both c-BN samples the only contribution is that of B1s-σ* resonances with the two peaks at 194eV and ~198eV. For h-BN, there is a strong B1s-π* resonance at 191.71eV prior to the B1s-σ* resonances, which peak at 197.8eV and 199.2eV. The positions of the anti-bonding resonances of the pure phase materials are

in excellent agreement with that reported in the literature as already described. The mixed phase sample consists of small (>1μm) c-BN crystals with high levels of hexagonal phase contamination. Therefore features of the mixed phase OD-XANES are a superposition of h-BN and c-BN signals. The B1s-π* and B1s-σ* peaks are positioned identically to that of h-BN (191.71eV) and c-BN (194eV, 198eV) respectively. However, the relative intensities of the resonances are different to that of the pure samples as would be expected.

On closer inspection, the B1s-π* resonances of h-BN and the mixed phase sample contain additional peaks. Shown in figure 5.12 the inverted results indicate separate B1s-π* resonances of both samples, which are fitted by a series of Gaussian peaks (α,β,γ and ζ). Peak α represents the stoichiometric B1s-π* (191.71eV) resonance, as already described. Those of β and γ are located at higher energy (lower binding energy) than α and are ascribed to the 1N and 2N vacancy defects respectively. Peak ζ is located at lower energy than α and is ascribed to an additional N bond due to interstitial defects.

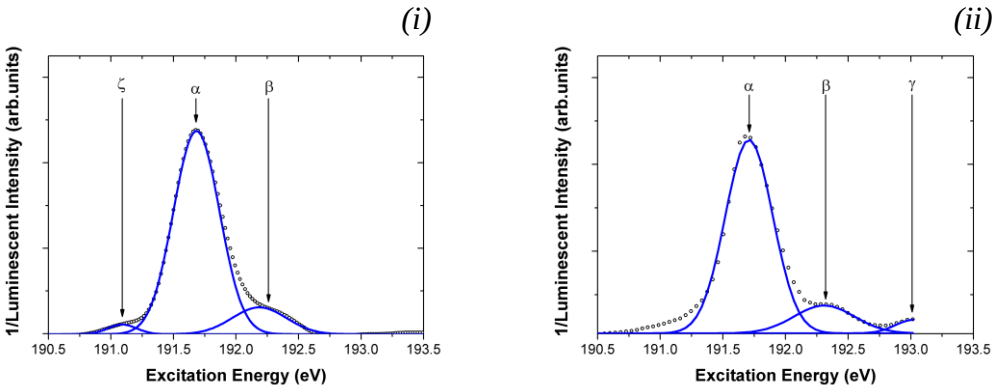

Figure 5.12 – The fitted B K-Edge π* resonances of (i) h-BN and (ii) mixed phase samples. The inverted data points (open circles) are fitted with Gaussian peaks (solid lines).

The energy positions of the B1s-π* resonances of both samples are summarised in table 5.2.

	ζ	α	β	γ
h-BN	191.09	191.71	192.28	
Mixed phase		191.71	192.32	193.01

Table 5.2 – Energy positions of the B1s-π* resonances of h-BN and the mixed phase BN samples.

The position of the 1N vacancy defect (β) is of excellent agreement between the two samples with the 2N (γ) vacancy resonance present only in the mixed phase sample. Thus, the sp^2 bonded material of the mixed phase sample must be of inferior crystallographic quality to that of h-BN. This is in agreement with the conclusion of sp^2 bonded material on the surface terminations of the c-BN crystals as already reported for this sample [66]. The average separation between these N vacancy peaks is 0.62eV, which is in close agreement to that previously reported (0.63eV) [2, 38, 68].

The lower energy resonance (ζ) is only resolved within the h-BN results, 0.62eV below the stoichiometric peak. This peak has been ascribed to an additional N bond (B bonded to four N) within the hexagonal lattice [2], however without appropriate chemical analysis it is not possible to prove a higher N concentration for this sample.

In summary both samples have a prominent stoichiometric resonance centred at 191.71eV and are thus predominantly h-BN as oppose to other sp^2 bonded polytypes.

The ability for OD-XANES to identify defects in materials is of little surprise as the emission is defect related, however this is the first reported incidence.

5.4.1.3.2 Spatially resolved XEOL and OD-XANES results

Spatial analysis of the luminescence was made, selectively investigating regions of the samples' surface. Regional selection returns average pixel intensity for a given area. For the case of both c-BN samples, significant spatial variation of the luminescent yield was observed. However, analysis of the h-BN and mixed phase samples revealed no discernable variation in the luminescent signal across the surface. Therefore, only the spatially resolved c-BN results are presented.

5.4.1.3.2.1 100μm c-BN results

Data was collected using the visible (x2, x10, x50) and UV (x80) transmitting objectives. The x10 results displayed the best combination of depth of field (3.5μm), pixel resolution (1.6μm^2) and optical transmission and are therefore presented. An image of the sample taken at 185eV in TLY is shown in figure 5.13, with the sampling region within the beam line footprint indicated at x2 magnification. At x10 magnification individual ~100μm crystals can be clearly resolved. Image collection times were adjusted to avoid CCD saturation. The crystals are of octahedral morphology having dark colour and irregularities in size and shape [52].

(i) *(ii)*

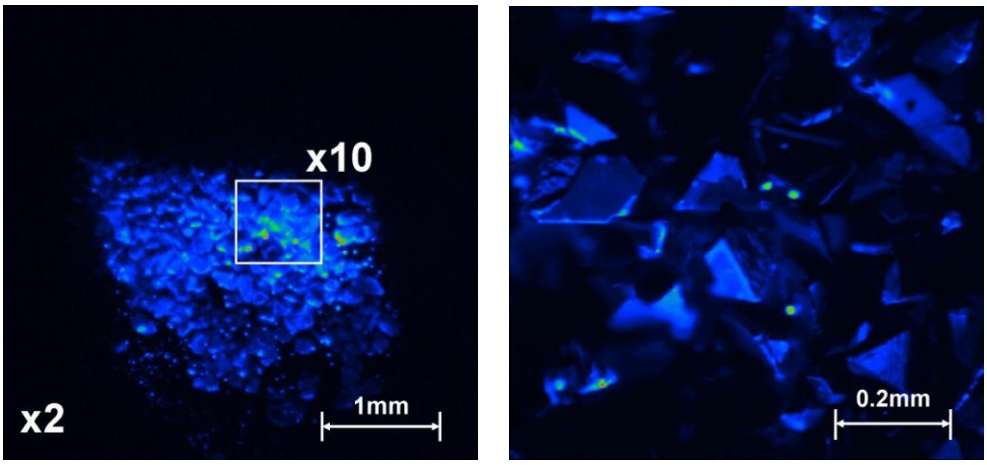

Figure 5.13 – CCD images of 100µm c-BN taken at 185eV in TLY (intensity graph indicated in fake colour). (i) Image at x2 magnification showing the beamline footprint (~ 2 x 2 mm) and sampling area at x10 magnification (ii) Image at x10 magnification..

Narrowband (10nm) XEOL measurements are shown in figure 5.14. On review an additional IR emission band can be resolved centred at 1.54eV of width 0.42eV. The CLASSIX1 CCD detector is sensitive in the IR, more so than MoLES, thus IR is available within the same scan as the UV and visible spectrum. The bands within the broad UV/VIS emission cannot be definitively resolved, however the same bands as reported for the 10-20µm (section 5.3) are likely to be present although with different relative ratios.

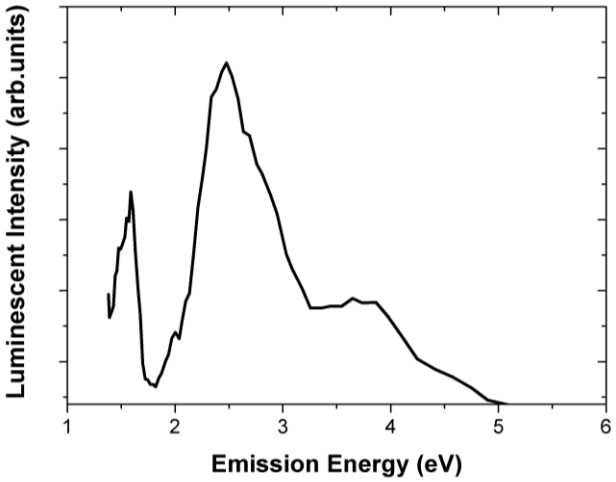

Figure 5.14 – Narrowband XEOL of 100µm c-BN crystals at 185eV showing emission in the UV, visible and IR using x80 UV objective.

The origin of the luminescent emission can be visually assessed by filtering the emission, probing individual emission bands. Filtered image results are shown in figure 5.15. Images were taken using broadband (FWHM 50nm) 2.805eV (442nm) and 1.540eV (805nm) filters whilst exciting at 185eV. By merging the two images, areas of separate emission can be identified as shown in figure 5.15*(iii)*.

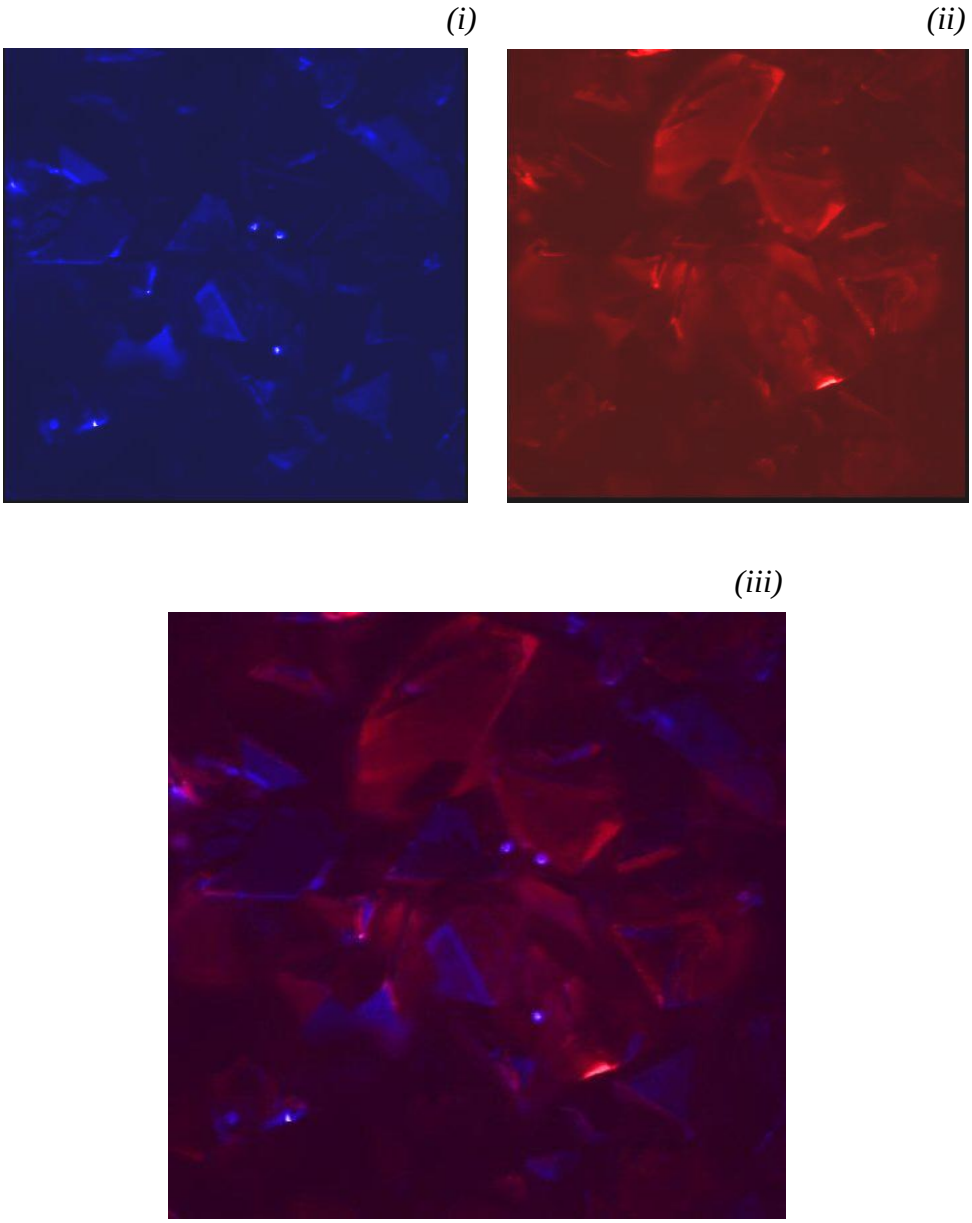

Figure 5.15 – Images of 100µm c-BN crystals in partial luminescent yield (PLY) at 185eV (i) 2.805eV (442nm) and (ii) 1.540eV (805nm). Image (iii) displays a merger of (i) and (ii). Blue colour indicates 2.805eV emission and red 1.540eV.

At this juncture it is necessary to introduce a coherent labelling system describing individual regions of interest within the results. Figure 5.16 displays four regions (labelled A-D) and points within each. Points will hence be referred to with the nomenclature of region then point, i.e. region B point *(i)* will be denoted as B*(i)*.

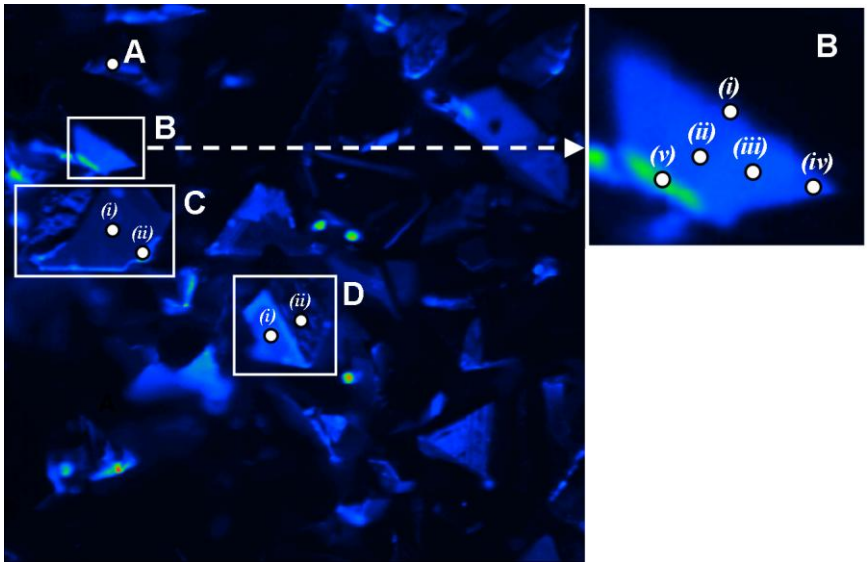

Figure 5.16 – Labelling of specific regions of interest (A-D) and points therein.

The XEOL emission (figure 5.14) was spatially filtered to compare the emission from different regions across the sample. Two facets D*(i)* and D*(ii)* of the same crystal D were of typical response for the 2.805eV and 1.540eV emissions respectively. The same luminescent bands are responsible for the emission from both facets. However, the ratio between the visible and IR emission is markedly different, as shown in figure 5.17.

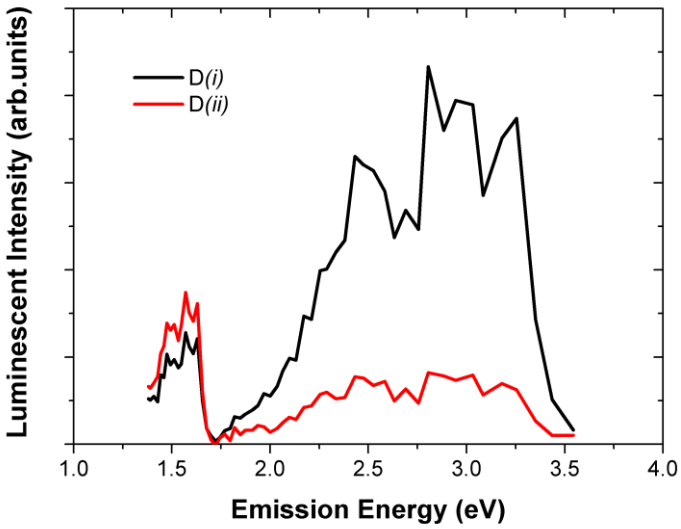

Figure 5.17 – Spatially resolved XEOL comparison between D(i) and D(ii). The XEOL emission ratio (visible:IR) of D(i) is 3.4:1 whereas that of D(ii) is 1:2

The spatially resolved XEOL results would suggest structural differences between individual crystals and in some cases facets of the same crystals (region D). Thus, spatially resolved B K-edge OD-XANES was employed to investigate the origins of the visible and IR luminescent bands and any structural differences therein.

The OD-XANES results are presented and discussed for each region in turn. For regions B and C only PLY OD-XANES at 2.805eV (442nm) could be attained due to a lack of signal at 1.540eV (805nm). Point scans represent an average pixel intensity over an area of 9 x 9 pixels (14.06μm x 14.06μm).

Region A

For the case of region A, a thin facet boundary could be observed displaying emission at both 2.805eV and 1.540eV. The B K-edge OD-XANES results for region A are shown in figure 5.18.

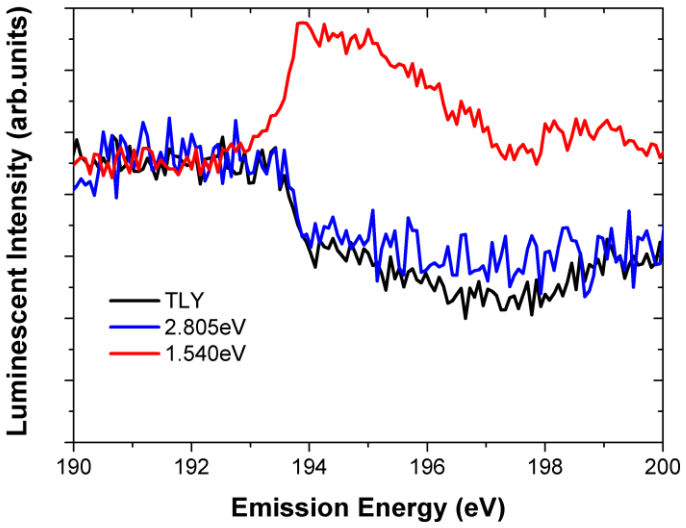

Figure 5.18 – TLY and PLY B K-edge OD-XANES results for region A.

The TLY displays a typical c-BN signal with a quenching response at the absorption edge, indicative of an optically thick sample. There is no B1s-π* contribution pre edge, thus this region must be considered purely sp^3 bonded. In PLY the OD-XAS varies between the 2.805eV and 1.540eV emission. For 2.805eV, the signal is exactly that of the TLY, however at 1.540eV the signal has a positive edge response. The 1.540eV signal is still that of c-BN although convoluted due to partial inversion, this suggests that the IR contribution originates from surface states in this region.

Region B

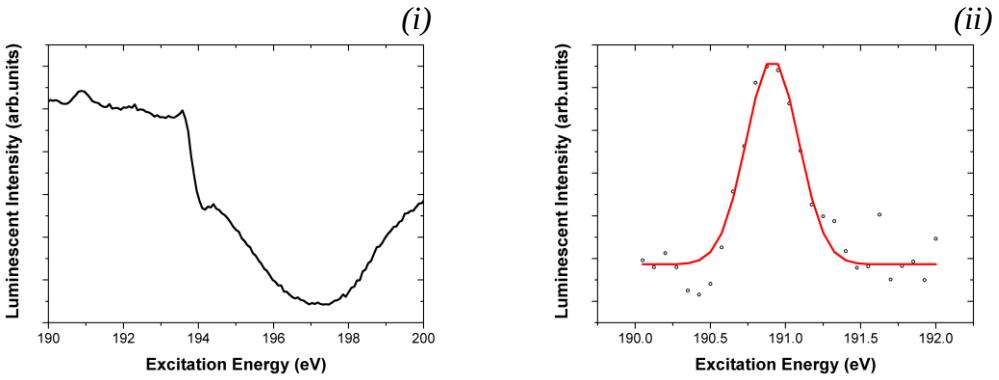

Figure 5.19 – The volume integrated TLY OD-XANES, (i) of region B and (ii) fitting of pre-edge resonance.

For the case of region B, a single crystal facet is observed, however it is unclear whether this is part of a larger crystal or a shard. The TLY of the entire region is shown in figure 5.19*(i)*. Prior to the edge there is a small positive B1s-π* resonance indicative of sp^2 contribution, this is fitted by a Gaussian curve in figure 5.19*(ii)* centred at 190.9eV FWHM 0.35eV. This resonance is of higher binding energy than that due to the hexagonal phase (191.7eV) or any of the additional N bonded B π* states. With reference to the literature, carbon states within boron carbon nitride (BCN) have been shown to exhibit B1s-π* resonances of this energy [70]. Therefore due to its positive response and energy it can be ascribed to sp^2 bonded C states located at the crystal surface.

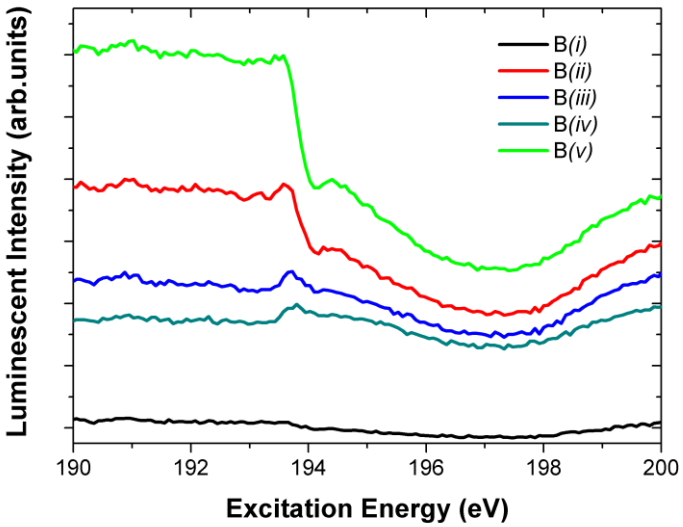

Figure 5.20 – TLY of region B points (i) to (v)

The TLY OD-XANES of points B*(i)* to B*(v)* are summarised in figure 5.20. There is clearly large spatial variation in the OD-XANES response across the region. The C bonded sp^2 peak is present for all points indicating unilateral contribution. Background luminescent emission is dependent upon the thickness of a sample, i.e. the amount of luminescent material present. The background signal can be seen to vary significantly within region B, B*(v)* displays the greatest background signal, therefore this is the point of greatest optical density and therefore thickness. The signal decays towards the extremities of the facet clearly indicating a decrease in sample thickness. The signal of points B*(ii)*, B*(iii)* and B*(iv)* have increasingly positive edge response again indicative of a thin sample. Previous studies have reported sample thickness effects, however none have shown variation within a single crystal [71]. Region B is therefore a shard rather than a thick crystal.

Region C

Region C is a relatively large (~ 200 x 100μm) crystal having a single observable facet. Two points are investigated within region C; C*(i)* is centrally located within the facet and C*(ii)* is at its extremity.

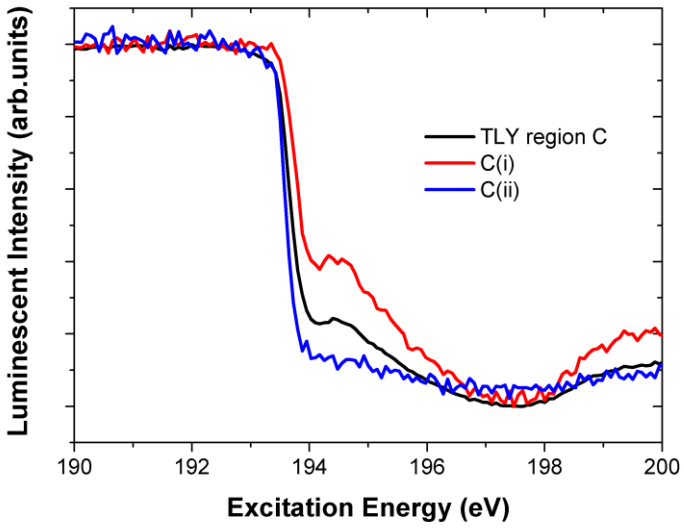

Figure 5.21 – TLY OD-XAS of region C and points therein.

The TLY OD-XANES of the entire region and points C*(i)* and C*(ii)* is shown in figure 5.21, the 2.805eV PLY mirrored TLY results, hence only the TLY are shown here. There are no sp^2 contributions prior to the absorption edge, thus region C must be of high sp^3 purity. Additionally the OD-XANES results are all of negative absorption edge response indicative of an optically thick material. The OD-XANES of points C*(i)* and C*(ii)* differ in their post edge response; For point C*(i)*, the characteristic 1s-σ* resonances are present, however these are absent from C*(ii)*. Therefore there are less structural effects contributing to the C*(ii)* signal, this is due to the surface states of the facet termination being of poor crystallographic order. The TLY of the entire

region is dominated by the emission of the facet as indicated by C*(i)*. This is to be expected due to the relative area difference between the facet and its termination.

Region D

Region D is a single crystal of excellent octahedral morphology. As described above the luminescent emission from both the observed facets differs, with that of D*(i)* dominant in the visible and that of D*(ii)* dominant in the IR.

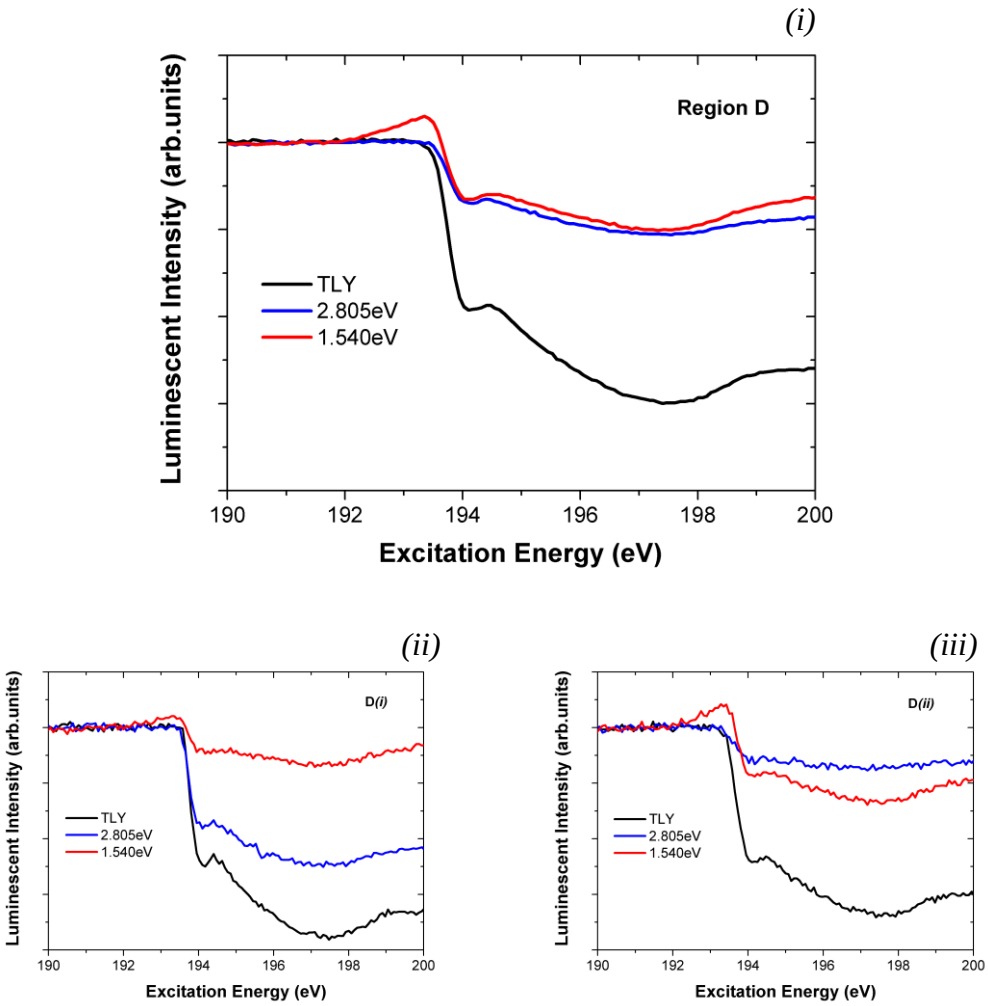

Figure 5.22 – TLY and PLY OD-XAS of region D, (i) results taken over the whole region (ii) results from facet D(i) and (iii) results from facet D(ii).

The TLY and PLY OD-XAS of region D is summarised in figure 5.22. There are no sp^2 contributions within the OD-XAS indicating a purely sp^3 bonded crystal. The TLY and 2.805eV PLY were negative in response at the edge, however the 1.540eV PLY has a small positive response prior to the edge. This would suggest the visible emission is due to bulk states, whereas the IR emission is due to surface states. The TLY OD-XANES of both facets are identical and indicative of an optically thick sample. However, the PLY does differ in relative intensity between D*(i)* and D*(ii)* as would be expected with reference to the XEOL.

5.4.1.3.2.2 10-20µm c-BN results

Experiments were conducted using the x80 objective, as it gave the best possible pixel resolution ($0.2\mu m^2$), although for this case individual crystals could not be easily resolved. The image shown as an inset to figure 5.23 indicates the region under investigation in TLY.

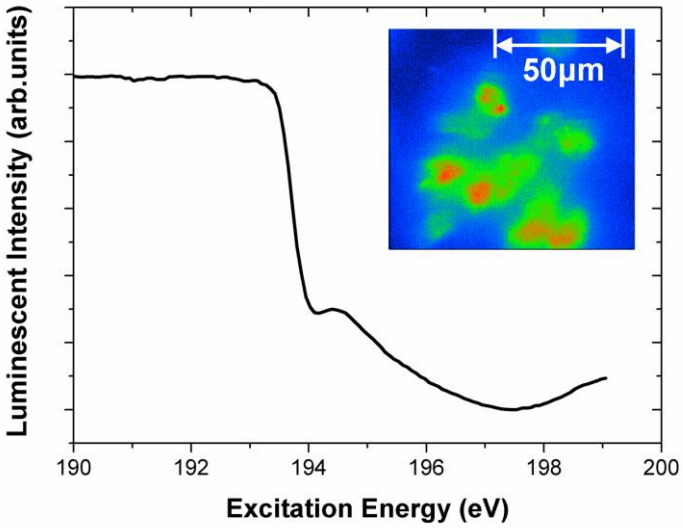

Figure 5.23 – OD-XAS of 10-20µm c-BN in TLY, corresponding luminescent image of sample taken at 185eV shown as inset.

Narrowband XEOL analysis of the 10-20µm c-BN as shown in figure 5.24, agreed with that obtained via MoLES (section 5.3) with additional IR emission centred at 1.57eV (FWHM 0.24eV), of similar position to that observed for the 100µm crystals.

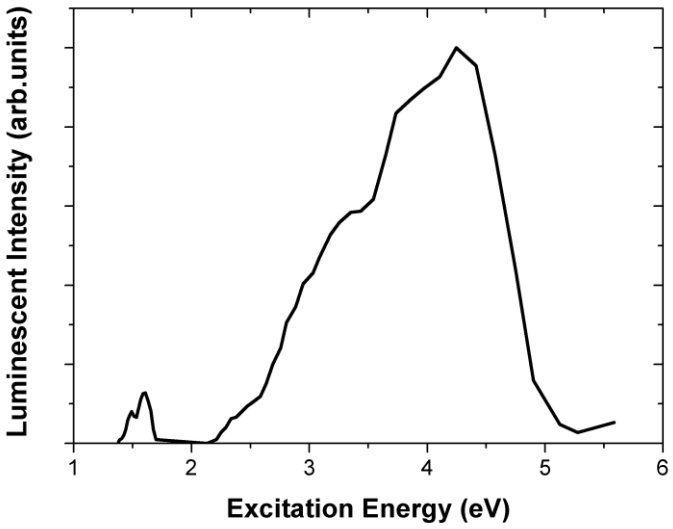

Figure 5.24 – Narrowband XEOL of 10-20μm c-BN at 185eV

Spatially resolved PLY OD-XANES was conducted at energies of 4.079eV (304nm), 2.465eV (503nm) and 1.540eV (805nm) using broadband filters (FWHM 50nm) as shown in figure 5.25. Included as an inset to each result is the corresponding image of the sample taken in partial luminescent yield.

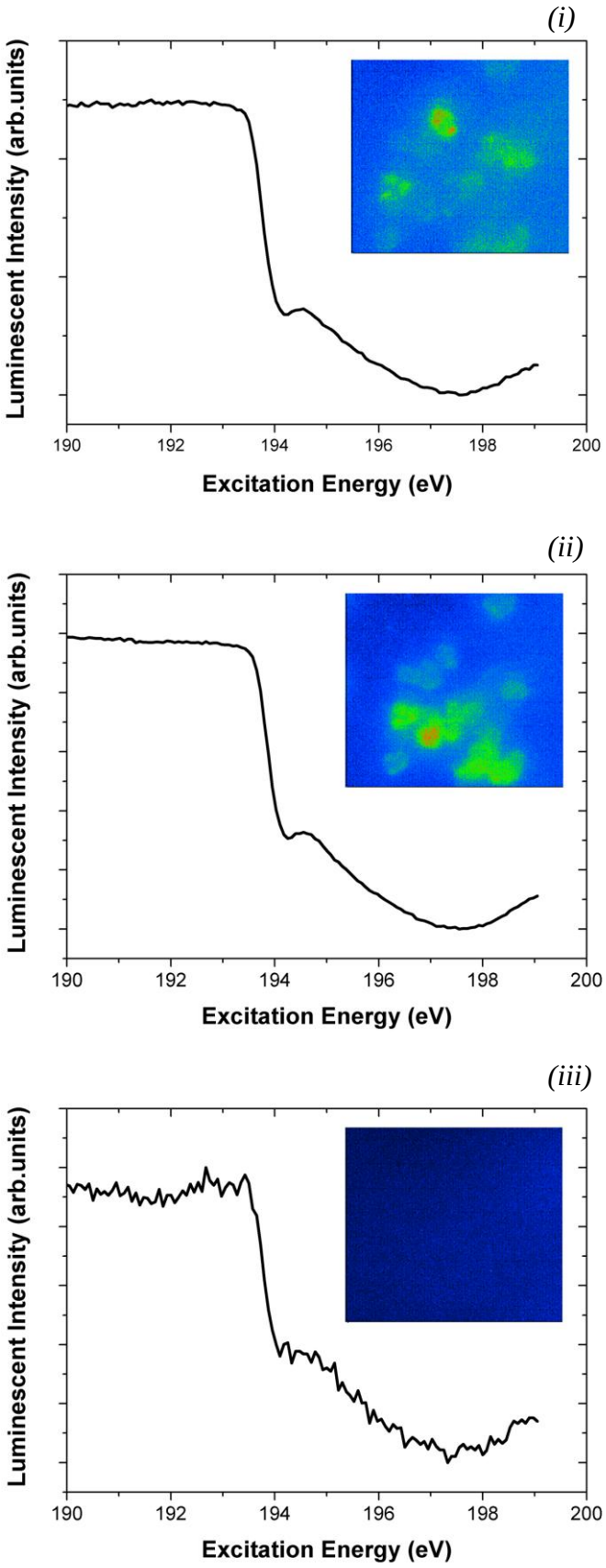

Figure 5.25 – PLY OD-XANES of the 10-20µm c-BN (i) 4.079eV (304nm), (ii) 2.465eV (503nm) and (iii) 1.540eV (805nm)

It can be observed from the images that the 4.079eV and 2.465eV emission bands have distinctly separate origins, whereas the emission from the 1.540eV band cannot be resolved due to a lack of signal. This would suggest the luminescent emission of individual crystals and possibly facets of the same crystals differ quite significantly. The PLY OD-XANES are invariant of emission, all displaying the typical edge response observed in TLY. Thus the 10-20μm BN crystals are of extremely high sp^3 purity with no surface related contributions present at any emission energy.

5.4.1.4 Discussion of spatially resolved OD-XANES results of c-BN samples

The spatially resolved XEOL and OD-XANES have shown significant variation in the luminescent emission and structure for which the total volume-integrated signal gave no indication. The IR emission previously unknown for either c-BN sample was shown to be an indication of poor crystal quality, being mainly located at surface terminations in the 100μm sample. The relative intensities of the IR emission between the 100μm and 10-20μm samples (UV/VIS:IR) were calculated to be 1.5:1 and 7.7:1 respectively, indicating a much higher concentration within the 100μm sample. The energy position of the IR emission ~1.6eV is in close agreement to that reported for spurious Ca catalyst doping during in synthesis [32]. Thus, the difference in IR emission between the samples suggested the 10-20μm to be of higher purity than the 100μm sample.

For the case of the 100μm c-BN, carbon surface contamination was exclusively identified in one crystal (region B), demonstrating the power of spatially resolved OD-XANES to identify relatively small areas of difference within samples of high

purity. Thickness effects due to optically thin regions were shown to exist, however these become diluted by the dominant bulk signal in total emission.

For the case of the 10-20μm c-BN, variation in the emission band origins was observed. However the sample displayed unilateral OD-XANES response indicating optically thick crystals of extremely high sp^3 purity.

5.4.2 Luminescent determination of the band gap energies of h-BN and c-BN

As described earlier (section 5.1) the band gap energies of both phases are of some dispute. In this study OD-XAS was implemented to investigate the band gap energies of h-BN and c-BN whilst exciting with VUV radiation (5-20eV).

5.4.2.1 Previous research

Experimental Technique	**E_g hBN (eV)**		**E_g cBN (eV)**	
X-ray photo-electron spectroscopy	3.6 3.85 ± 0.5	[72] [73]	6.2	[44]
Optical reflectivity	5.2 ± 0.2	[74]	5.2 > 6.4	[75] [76]
Optical absorption spectra	3.9 4.3 5.79 ± 0.1 5.83	[77] [78] [51] [79]	6.1 ± 0.2 6.27 ± 0.02	[80] [81]
Optical emission spectra	4.02 ± 0.01 ≥ 5.5 5.89 5.971	[49] [82] [83] [30]	6.25	[84]
Photo-conductivity spectra	5.8	[85]		
Inelastic electron scattering	5.9	[86]		
Temperature dependent electrical resistivity	7.1 ± 0.1	[87]		

Table 5.3 – Experimental values for the band gap energies of h-BN and c-BN taken from the literature.

The band gap energies of both h-BN and c-BN are of some dispute with experimentally obtained values varying substantially for both phases, as summarised in table 5.3.

The band gap energies of h-BN are spread dramatically from a minimum of 3.6eV to a maximum of 7.1eV. Whereas, with the omission of the smallest value (5.2eV), the band gap energies of c-BN are in reasonable agreement, all reporting magnitudes in the 6.1eV to 6.4eV range. This variation of the band gap energies in both phases can be attributed to a combination of effects, including differences in sample quality and experimental technique.

Sample quality differences can be marked, with the presence of phase anisotropy and atomic contamination in both h-BN and c-BN commonplace [3, 88]. In the case of h-BN the synthesis of sp^2 bonded polytypes is thermally dependent, thus structural changes can be transitional and samples may not be purely a single polytype. For the case of c-BN, unwanted sp^2 bonded regions are common. HPHT c-BN materials are usually of the purest crystalline order with sp^2 regions having a tendency to be located mainly at surface terminations, grain boundaries and thin film substrate interfaces [38, 69]. Thus techniques which only probe surface states could lead to erroneous conclusions with regards to c-BN electronic structure.

Atomic sample contamination introduced during synthesis is also common in BN. Species, such as those used as dopants and catalysts can cause donor or acceptor states to exist within the band gap, thus any interaction with unknown defects could result in an underestimation of the band gap energy.

5.4.2.2 Experimental details

Experiments were carried out on beamline 3.2 at the SRS Daresbury using CLASSIX1 as the end chamber. The 10-20μm c-BN and h-BN powder were investigated, having been proven to be the purest materials by OD-XANES. All the samples were adhered to the cold finger with conductive tape and were of thickness far greater than the radiation penetration depth. The samples were cooled to ~30K and held in a vacuum of 10^{-8}mBar. In order to cut out any reflected synchrotron light, the luminescent signal was filtered using UG11 and BG11 (Schott) filters, defining a narrow detection window of bandwidth 0.74eV centred at 3.44eV. CLASSIX1 was operated in CCD collection mode, the beam aligned to the samples using reflected light.

The data was corrected for background signal and beamline flux. The background emission levels were recorded with the beamline closed and beamline flux measurement made from a sodium silicate (Na_2SiO_3) sample.

The luminescent signal was too weak to obtain images of the substrates whilst scanning. Thus results presented are obtained from volume-integration over the whole CCD area.

5.4.2.3 Results

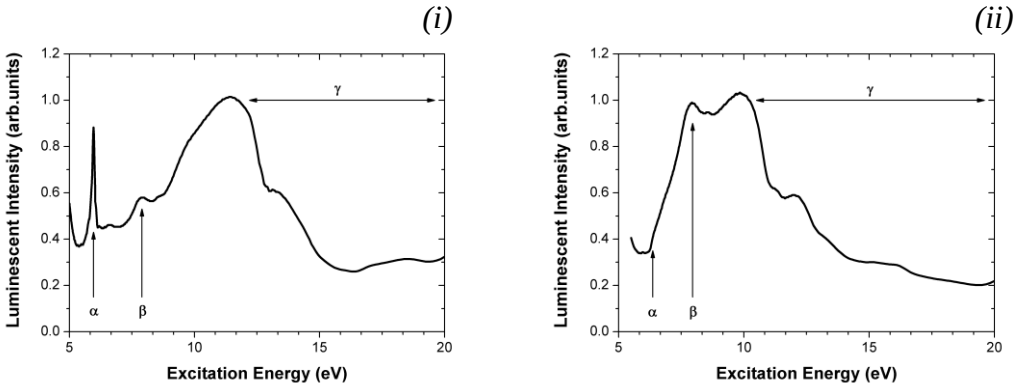

Figure 5.26 – Band edge OD-XAS of (i) h-BN and (ii) c-BN in the excitation energy range 5-20eV whilst detecting at 3.44eV ± 0.37eV.

The wide scan results are shown in figure 5.26. There are three distinct features labelled α, β and γ which correlate to separate electronic processes. The luminescent efficiency of both phases reduces significantly in the post 10eV region (denoted by γ), as expected with reference to the dielectric constant and subsequent energy losses. BN as already mentioned has an ionic structure, thus its dielectric constant is anisotropic leading to strong energy losses in the energy range 8-20eV [10, 89]. Additionally for the case of c-BN the absorption coefficient has been reported to increase significantly post 10eV which would also cause a drop in the luminescent efficiency [80].

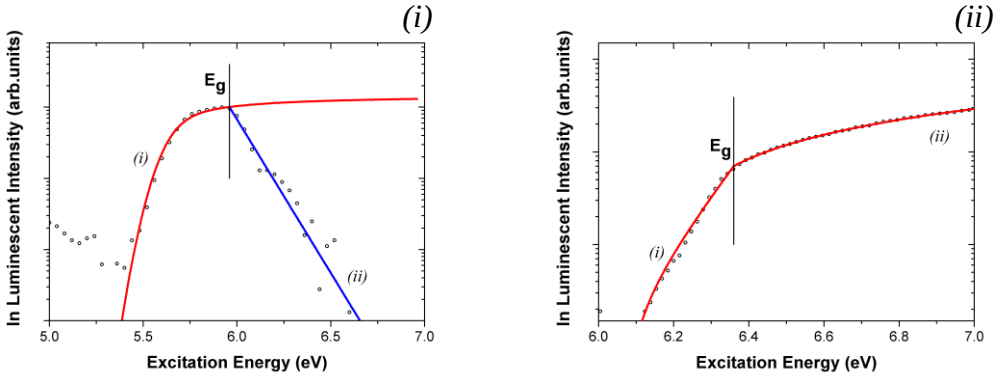

Figure 5.27 – Band edge OD-XAS of (a) h-BN and (b) c-BN showing determination of band gap energy (E_g) and associated fitted curves for each.

The features labelled α denote the band gap energy, the structures of which are analysed in greater detail in the energy range 5-7eV as shown in figure 5.27. There is clearly a marked difference in the band edge luminescence of the two phases, hence they must be considered separately.

For the case of h-BN, the band edge has the form of a peak superimposed upon a rising background continuum. Once this background is removed the data can be fitted by consideration of the luminescent emission spectra, as presented in section 5.3. If it is assumed that h-BN has an acceptor centre at 5.62eV below the conduction band edge (responsible for the DUV emission) and if this state is partially occupied an increase in the charge available to the lower energy luminescent recombination would be expected as the excitation energy is scanned across it. Therefore the energy dependent coefficient of absorption $\alpha(E)$, will vary by excitation between a Gaussian distributed state 5.62eV (FWHM 0.2eV) below a parabolic conduction band ($\sqrt{(E-E_g)}$) in terms of density of states (DOS). In this instance the luminescent intensity $L(E)$ is described as a function of photons absorbed where;

$$L(E) \propto (1-\exp(-\alpha d)) \qquad (5.1)$$

The value d represents the sample thickness, which in this case is much greater than the penetration depth of the incident VUV radiation. This is plotted as curve *(i)* figure 5.27*(i)*, clearly fitting the onset of the peak to 5.96eV after which it plateaus. Above 5.96eV the luminescent signal exponentially decays, fitted as curve *(ii)*. This point of intersection is indicative of the band edge, as the absorption efficiency is significantly increased due to the fundamental band to band absorption, akin in character to the

response observed at the K-edge absorption energy. Thus the band gap energy is identified as the convergence of these two fitted curves at 5.96eV ± 0.04eV.

For the case of c-BN, the band gap determination is relatively straightforward due to the absence of shallow acceptor centres. Sub band gap the luminescent signal increases exponentially, fitted as curve *(i)* figure 5.27*(ii)*. This is indicative of an Urbach tail, where anisotropic bond perturbations create a low density of sub band gap transitions [90, 91]. The band gap energy is observed as the deviation of the Urbach tail at 6.36eV ± 0.03eV, where the fundamental band to band absorption dominates the spectra. Above the band gap energy the luminescent emission can be linearly fitted by curve *(ii)*, as shown in figure 5.27*(ii)*.

5.4.2.4 Discussion

The optical band gap energies for both phases can be considered with reference to the theoretical band structure (section 5.1.3).

For h-BN, the band gap energy of 5.96eV corresponds to the direct (or quasi-direct) transition, reported to be at either H or K [89]. A second direct transition of ~8.9eV is predicted at Γ, the feature labelled as β in figure 5.26*(i)* has an energy of 7.9eV which could correlate to this transition.

For c-BN, the band gap energy of 6.36eV corresponds to the indirect Γ-X transition [45]. Due to the indirect nature of the band gap phonon contribution must occur, however no evidence of this can be ascertained from the results presented here. A second direct ~8.7eV transition is predicted at Γ, which could correspond to the luminescent yield reduction at 7.9eV labelled β in figure 5.26*(ii)*.

The band energies of both phases can be considered with reference to the literature. As summarised in table 5.3, the nearest values of the band gap energies of h-BN and c-BN are 5.971eV [30] and 6.25eV [84] respectively. These values correspond to minimum energy differences between those reported in this thesis to those in the literature of 0.011eV and 0.110eV for h-BN and c-BN respectively. Interestingly these closest values were both determined from the threshold of OL and are therefore estimations subject to considerable conjecture. The quality of the materials investigated in the literature is also of question as many of the articles date from more than two decades ago.

The band gap energies reported in this thesis are the first using VUV OD-XAS, thus probing the fundamental band to band absorption by scanning the excitation energy across it. Taking into consideration the quality of the materials under investigation, the resolution of the data and the nature of the luminescent signal at the band gap energy the values reported represent definitive measurements.

In summary, the optical band gap energies of h-BN and c-BN were determined to be 5.96 ± 0.04eV and 6.36eV ± 0.04eV respectively using synchrotron based OD-XAS techniques.

5.5 Pump probe measurement of optically stimulated defect states

As described in Chapter 2 pump probe (PP) spectroscopy is an experimental method of investigation into the charge trapping dynamics of luminescent materials. Due to the wide band gap of BN the usual method of laser-laser PP is inadequate. In this instance synchrotron radiation can be utilised as the pump excitation source. The results presented here investigate the charge trapping dynamics of the 10-20μm c-BN and h-BN powder samples.

5.5.1 Previous research

Previous PP studies of BN have shown interesting results relating to the charge trapping dynamics of BN.

In 2005, Poolton *et al* [92] demonstrated the potential of PP measurements upon c-BN and other wide band gap materials in an initial study of the technique using SR as the pump excitation source. Using a laser probe of energy 2.33eV (532nm) the non-resonant synchrotron induced XEOL was shown to be significantly quenched by the probe.

Following this work the same author studied the PP interaction of laser probes upon the XEOL and OD-XAS of h-BN [65]. Three laser probes of energies of 3.069eV (404nm), 2.331eV (532nm) and 1.494eV (830nm) were utilised. Results successfully defined the dynamics of the transient PP interactions and recovery to equilibrium following laser removal.

The following experimental results build upon these previous studies utilising a quasi-tuneable laser source in conjunction with SR, mapping the PP-XEOL interaction as a

function of probe energy. Results are used to define the energy of the intra-band gap defect level above the valence band maxima.

5.5.2 Experimental details

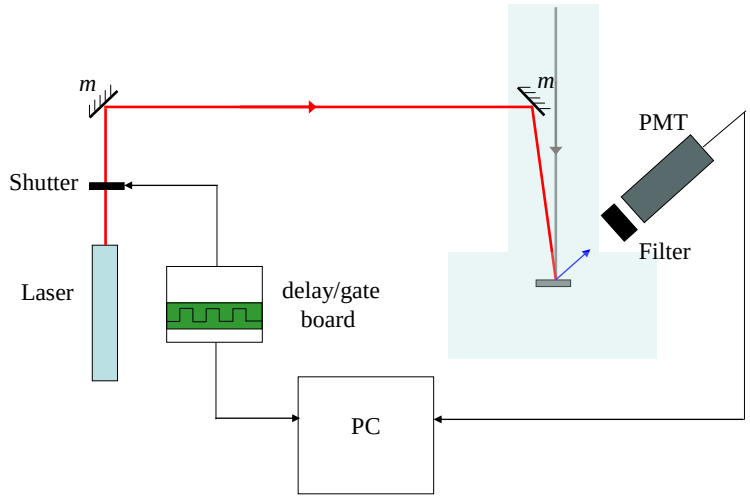

Figure 5.28 – Diagram of the Pump probe experimental set-up, depicting the control paths of the system.

The experiments contained within this section were conducted on beamline MPW6.1 at the SRS Daresbury. The experimental set-up is diagrammatically represented in figure 5.28. CLASSIX1 was used as the end chamber orientated to the synchrotron beam in the usual manner. The class 4 quasi-tuneable laser source (SRS/Manchester University) was used as the probe for all experiments contained within this section. The source based upon a Ti:sapphire laser, allows a user to select energies within regions spanning the UV (240-333nm), visible (360-520nm) and near IR (690-1080nm) regions of the spectrum at constant power, polarisation and coherence, thus having major advantages over single wavelength lasers. Shutter controlled, the laser

source entered the beam line upstream of CLASSIX1 through a UHV sapphire window impinging upon a focussing mirror. Both the synchrotron and laser beams were focussed at the sample with the laser overfilling the synchrotron footprint (1x0.4mm) completely. In order to optimise luminescent detection, CLASSIX1 was operated in PMT collection mode (Hamamatsu R758-10). The luminescent emission was filtered to remove laser probe breakthrough from the data, as indicated in figure 5.29.

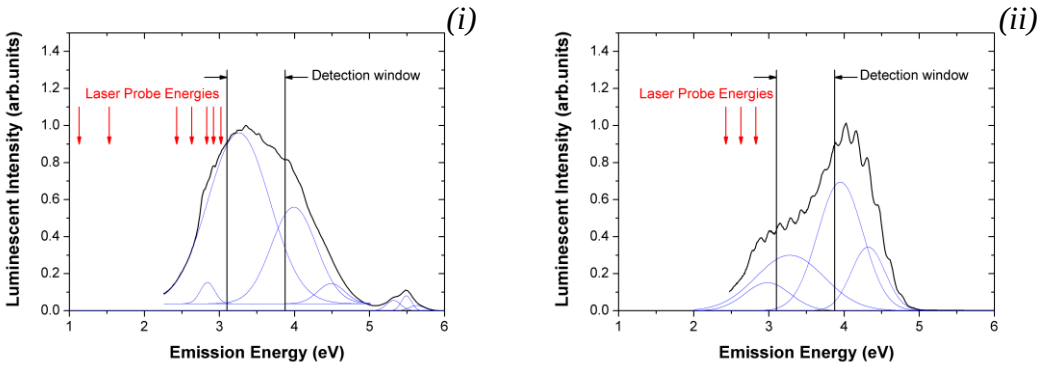

Figure 5.29 – Annotated XEOL spectra for (i) h-BN and (ii) c-BN excited at fixed photon energy of 185eV at ~ 10K. The pump probe detection window is indicated together with the laser probe energies.

A detection window of bandwidth 0.74eV centred at 3.44eV was defined by colour glass filters UG11 and BG39 (Schott) applied in combination. The position of the detection window is critical as it must be at lower energy than the band edge (~6eV) but higher than that of the laser probes. This orientation ensures the signal recorded is due to the interaction of the probe with the charge generated by the pump and not solely the result of probe interactions. Data recording and laser shutter control was maintained by delay/gate boards (Becker and Hickl DDG-200 and PMS-400A) operated with a square wave of 2 second periodicity. The data was recorded at a

sampling rate of 10ms triggered by the laser shutter signal at the start of each sweep, thus ensuring the same collection window for each laser cycle. Collection was made over five hundred laser cycle iterations and averaged for each time step to generate the experimental signal. Laser probe energies were selected within obtainable regions as summarised in table 5.4.

Laser Region	Energy (eV)	Wavelength (nm)	Power (mW)
Visible	3.024	410	200
360-500nm	2.918	425	205
	2.825	439	200
	2.627	472	200
	2.427	511	70
Near IR	1.529	811	202
690-1100nm	1.127	1100	164

Table 5.4 – Summary of laser probe energies

The samples, adhered to the sample stage with conductive tape, were of greater thickness than the X-ray penetration depth of the synchrotron beam (~0.2mm), thus ensuring conditions of total photon absorption. The orientation of the crystals was deliberately disordered to negate any angular dependence due to the linear polarisation of the synchrotron and laser sources, therefore the results are the consequence of average interactions over all directional orientations. Samples were cooled to ~30K and positioned in the combined beam with use of CLASSIX1 integrated optics and CCD detector. All experiments were conducted for each sample with its position maintained relative to the beam throughout the entire run.

5.5.3 Results

The entire scan results for both h-BN and c-BN are shown in figures 5.30 and 5.31 respectively. The data was corrected to the initial pump only equilibrium intensity $I_{0,XEOL}$ in terms of percentage change. The results are considered in two regions, that of pump probe and pump-only as indicated. Both regions have distinctive characteristics as described in Chapter 2.

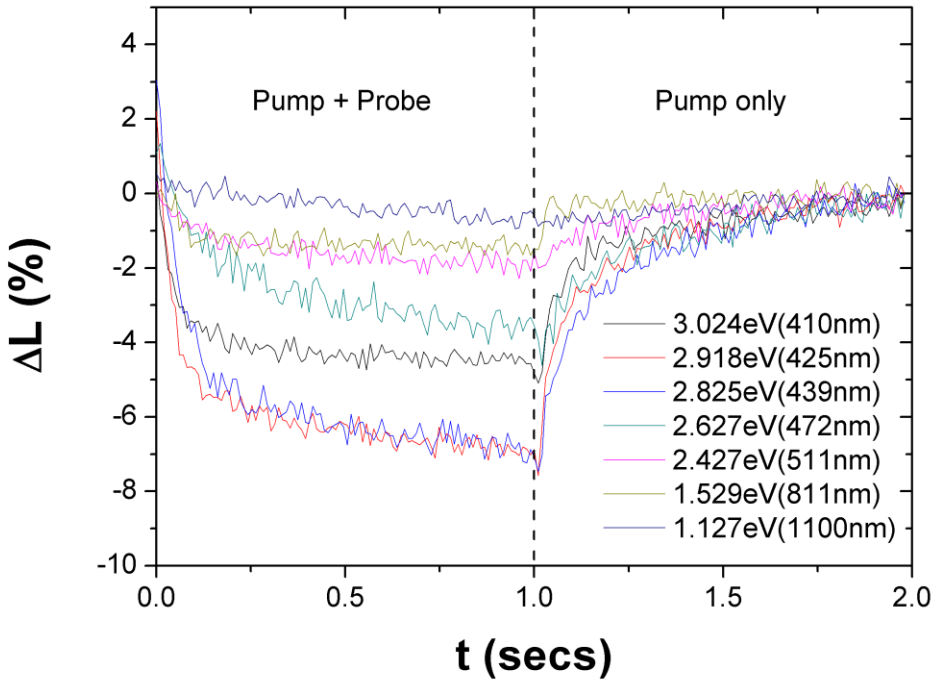

Figure 5.30 – Summary of hBN pump probe results, displaying full scan data at each laser probe energy. Pump probe and pump only regions indicated either side of the laser off position (dashed line) situated at time equal to 1 second.

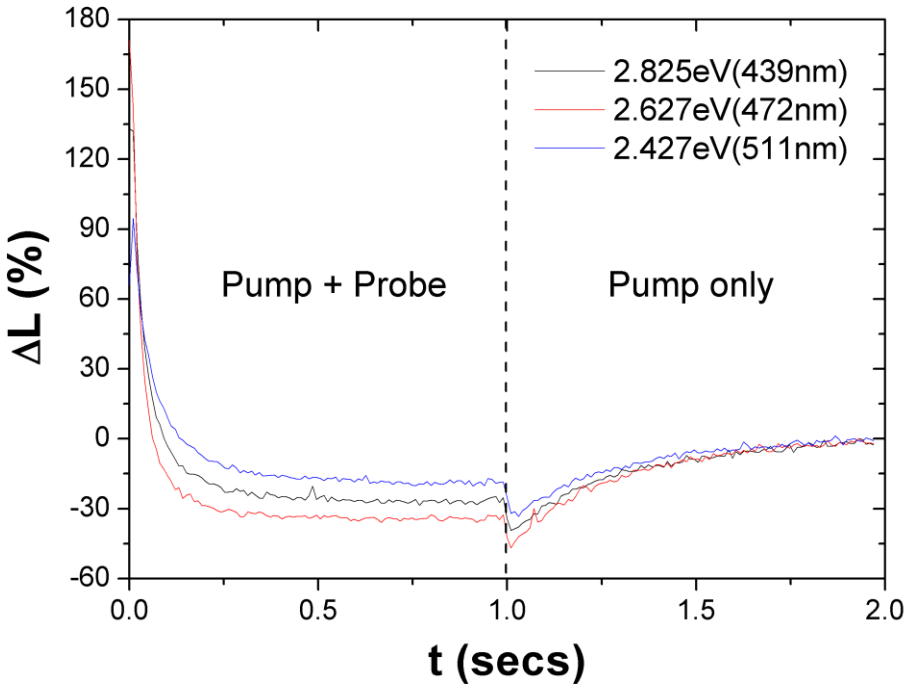

Figure 5.31 – Summary of c-BN pump probe results, displaying full scan data at each laser probe energy. Pump probe and pump only regions indicated either side of the laser off position (dashed line) situated at time equal to 1 second.

5.5.3.1 Pump probe interaction

The value of I_0PP was taken to be the point of equilibrium following the initial OSL decay, and was recorded as percentage difference from that of $I_{0,XEOL}$.

The determination of I_0PP for each laser probe is shown in figures 5.32 and 5.33 for h-BN and c-BN respectively.

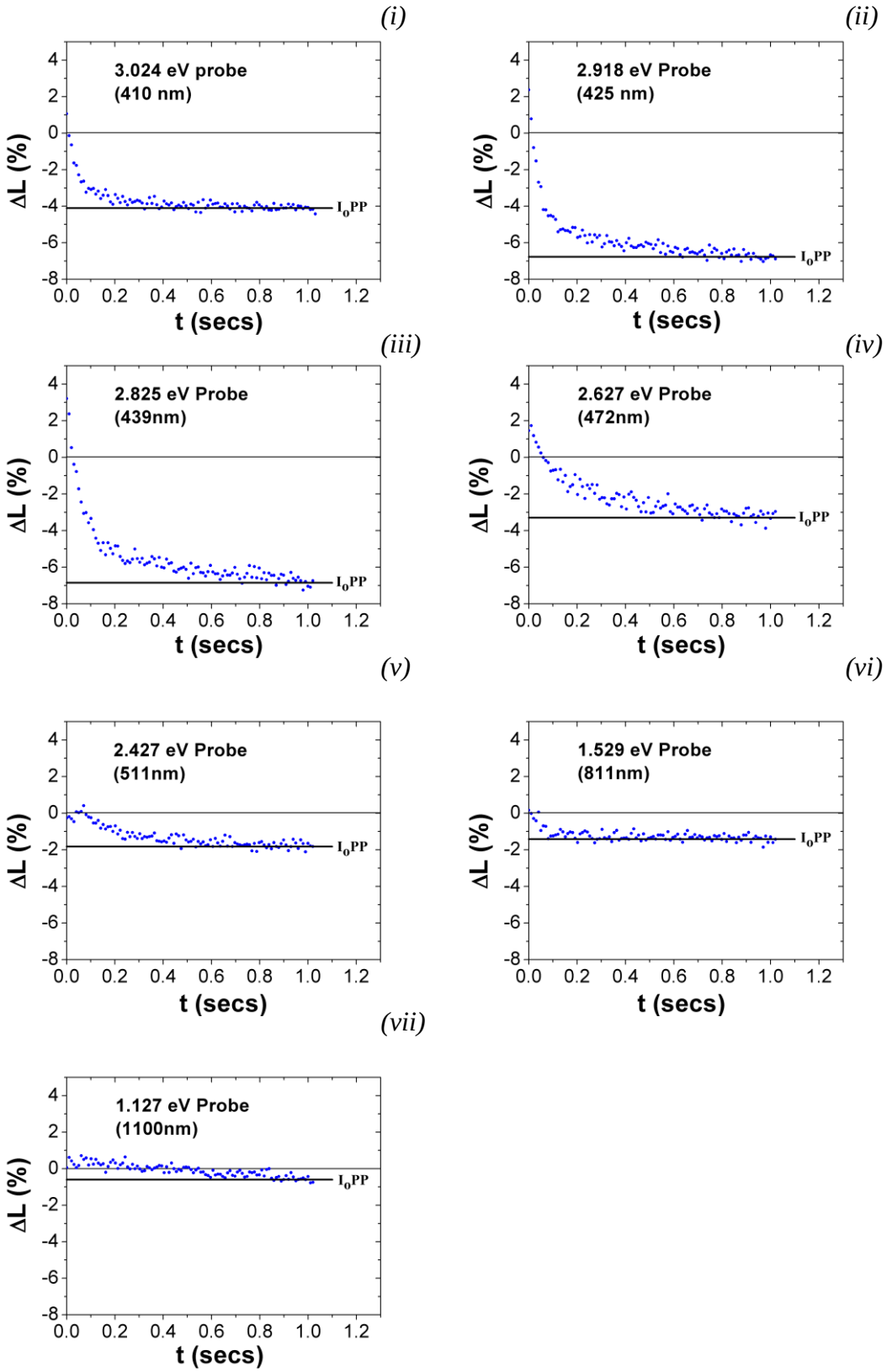

Figure 5.32 – h-BN pump probe results; plots (i) to (vii) display the determination of pump and probe equilibrium (I_0PP), expressed as percentage change in luminescence from that of pump only equilibrium (set as zero).

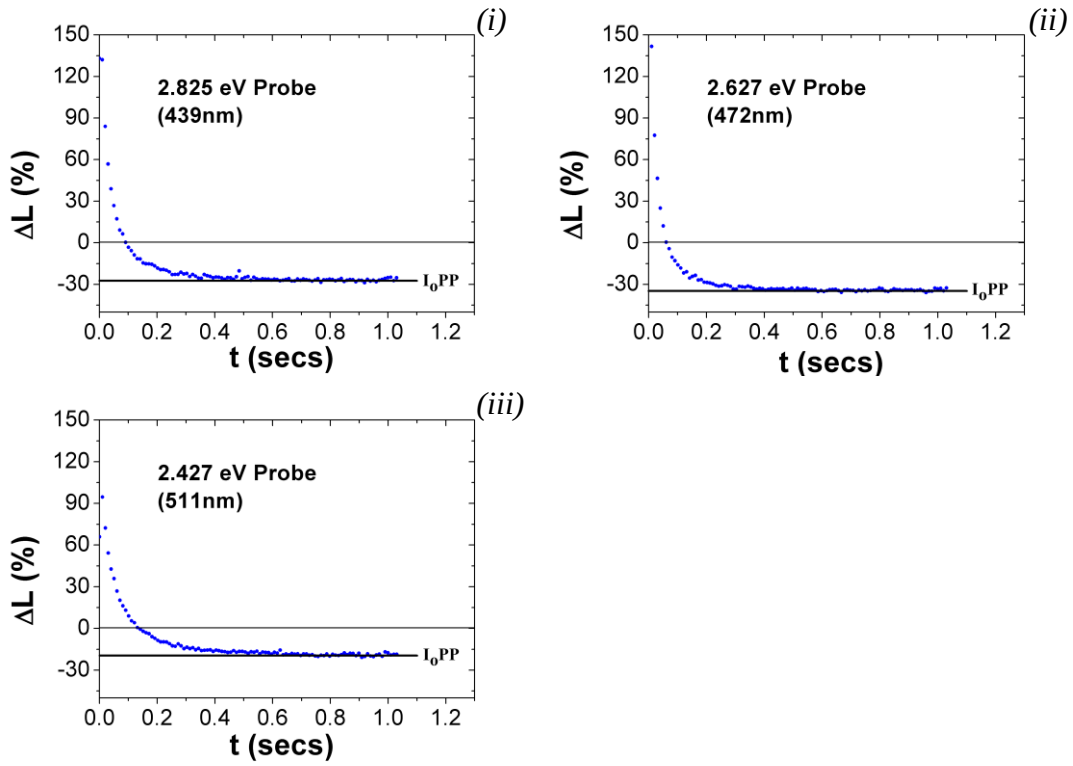

Figure 5.33 – c-BN pump probe results; plots (i) to (iii) display the determination of pump and probe equilibrium (I_0PP), expressed as percentage change in luminescence from that of pump only equilibrium (set as zero).

5.5.3.2 Pump only recovery

The pump-only recovery results are plotted in figures 5.34 and 5.35 for h-BN and c-BN respectively. Data was plotted with time set to zero at the start of the pump-only region.

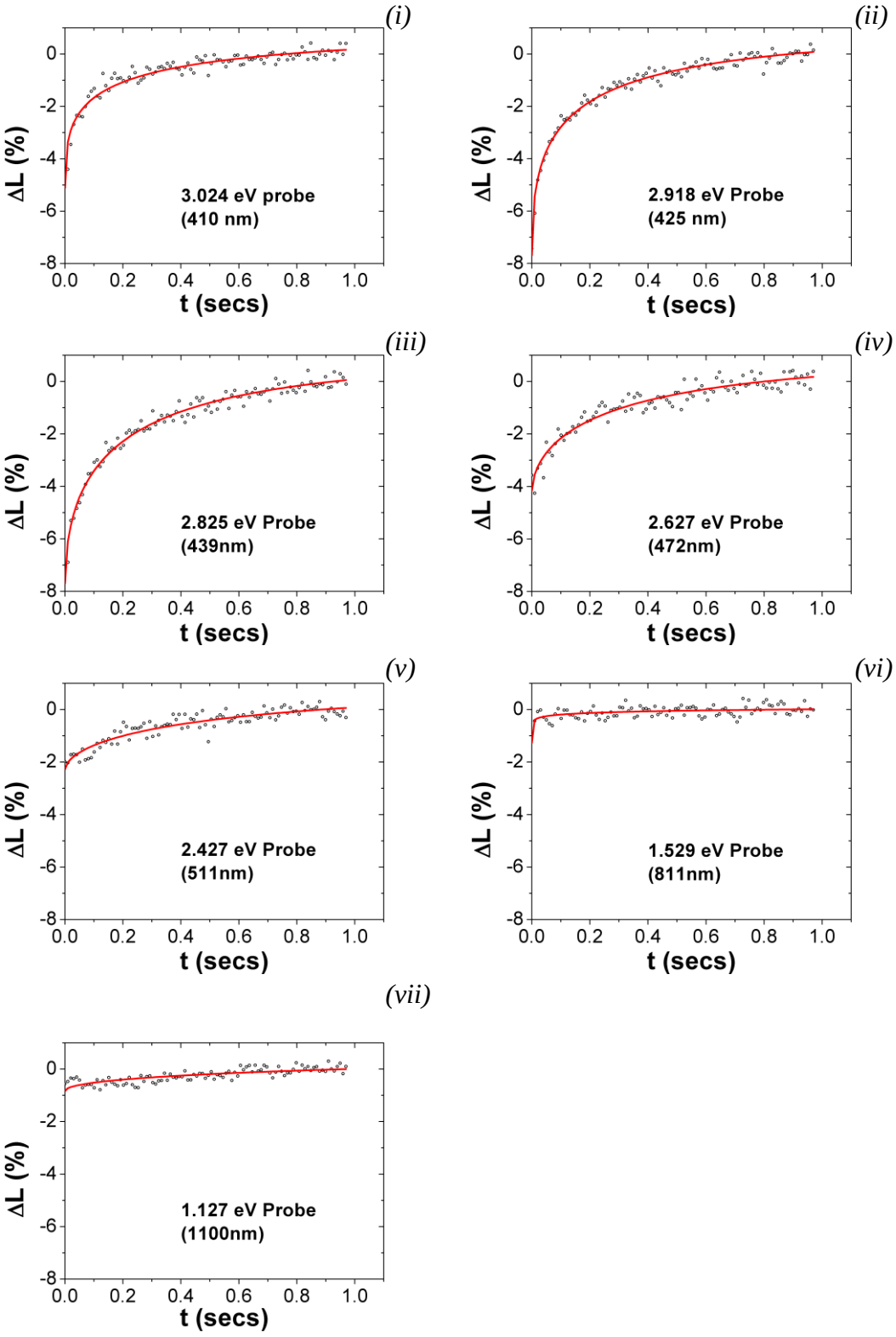

Figure 5.34 – Recovery of h-BN luminescent signal to pump only equilibrium following laser probe switch off. Solid lines indicate fitting.

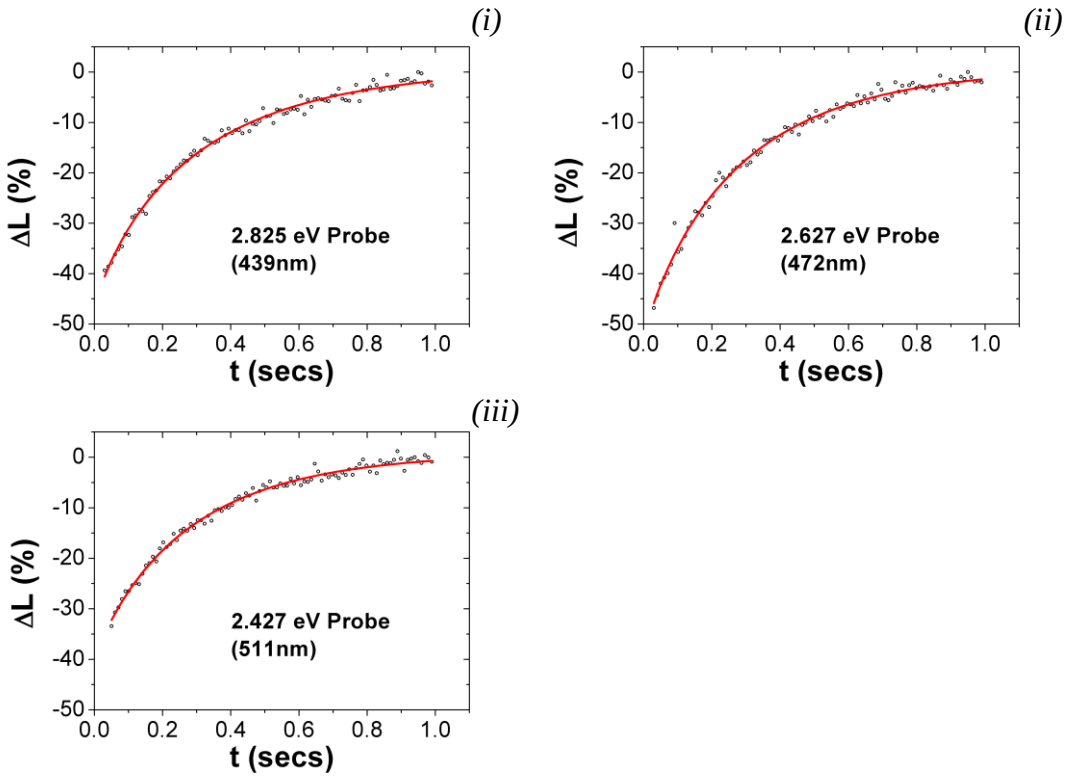

Figure 5.35 – Recovery of c-BN luminescent signal to pump only equilibrium following laser probe switch off. Solid lines indicate fitting.

5.5.4 Discussion

The results are considered in the two regions of pump probe and pump only and will be discussed separately.

5.5.4.1 Pump probe discussion

From comparison between the data sets of the two samples it can clearly be seen that c-BN has a much greater OSL contribution than that of h-BN. There is therefore more charge located in the OSL traps of c-BN with which the probe interacts. This implies that the trapping sites within c-BN are better defined and isotropic than those of h-BN. It is noted that the pump probe OSL decay can be fitted, but as it is a measure of

trap absorption cross section having little relevance to this study. The position of I_0PP is due to two competing conditions; the first being the continual resonance of the OSL traps (increasing luminescent emission) and the second due to the excitation of electrons from the valence band states to acceptor defect states located within the band gap (quenching luminescent emission). The values of I_0PP are determined as the position of equilibrium for each laser energy as shown in figures 5.32 and 5.33 for h-BN and c-BN respectively. By mapping the position of I_0PP as a function of probe energy it is possible to define the energy of the defect state in relation to the valence band maxima as the point of maximum quenching, as shown in figure 5.36*(i)* and 5.36*(ii)* for h-BN and c-BN respectively.

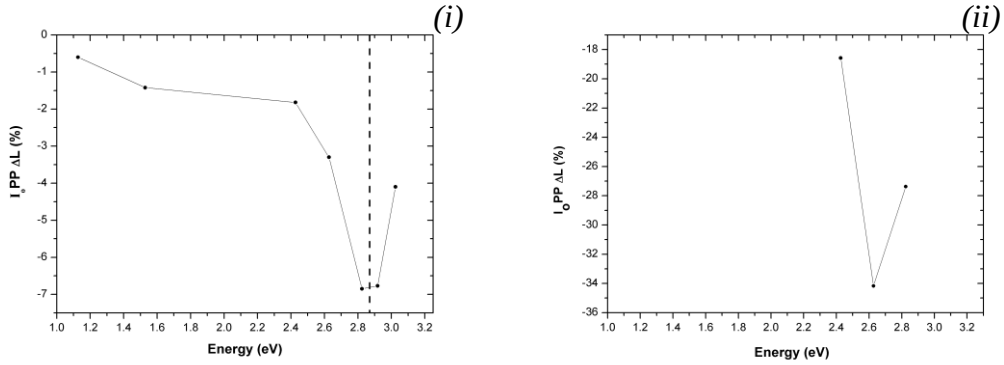

Figure 5.36 – I_0PP against laser probe energy (i) h-BN and (ii) c-BN.

The energy of the defect state in h-BN was determined to be 2.87eV ± 0.05eV above the valence band. The energy of the defect state in c-BN was determined to be centred at 2.63eV ± 0.20eV above the valence band. The larger error associated with the c-BN result is due to there being less data points across the resonance. By subtracting the defect energy from the band gap energy (Eg as determined in section 5.4.2) it is possible to establish the resultant energy of the associated luminescent band, as summarised in table 5.5.

	h-BN	c-BN
Band gap E_g	5.96	6.36
Defect state	2.87	2.63
Emission band	3.09	3.73

Table 5.5 – Determination of luminescent emission band energy due to defect acceptor state as per PP results.

The emission energy calculated from the PP results is correlated with the XEOL spectra of both h-BN and c-BN in figures 5.37 and 5.38 respectively.

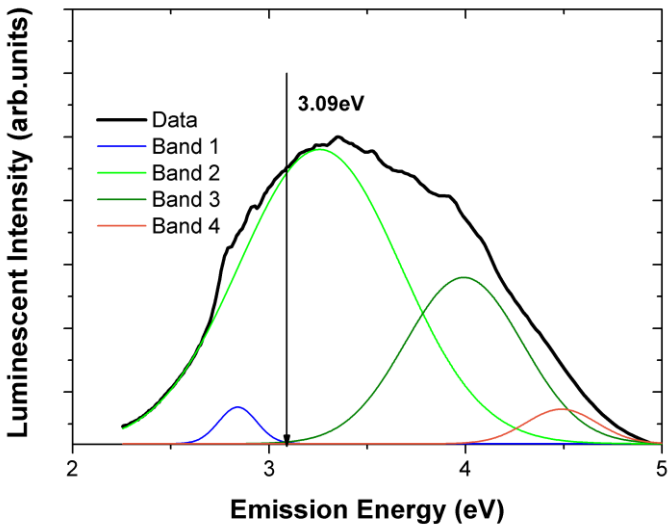

Figure 5.37 – XEOL of h-BN with energy of emission due to PP defect indicated.

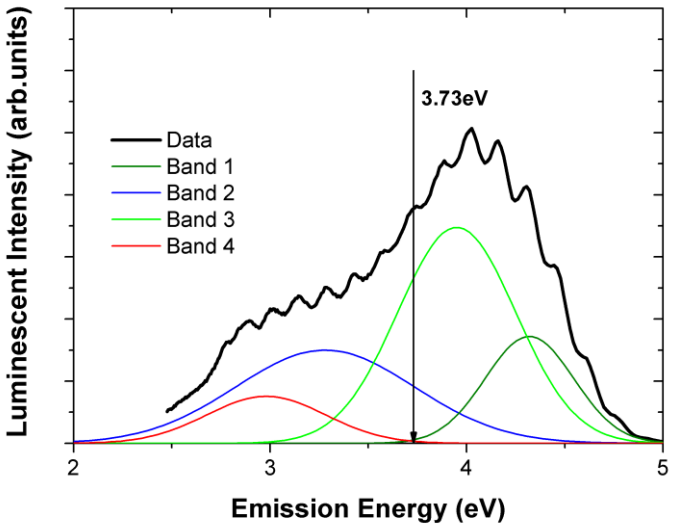

Figure 5.38 – XEOL of c-BN with energy of emission due to PP defect indicated.

For the case of h-BN the emission energy of 3.09eV falls close to the high energy tail of the first emission band centred at 2.84eV. The resonant quenching of luminescent emission was measured as between the laser probe energies of 2.918eV and 2.825eV as shown in figure 5.36*(i)*, where the value of I_0PP remained relatively constant for both. The defect state has therefore a convoluted form which can be fitted by a Gaussian peak of centre 2.87eV and FWHM of 0.31eV. It is concluded that this defect state is responsible for the lowest energy emission band of h-BN (band 1, figure 5.37). The phonon structure (section 5.3) can be used to predict higher energy phonon positions. If it is assumed that the defect state energy refers to the zero phonon of the first emission band, then the value 3.09eV is within 0.01eV of that predicted.

For the case of c-BN, there is a marked resonance at the laser probe energy of 2.627eV as shown in figure 5.36*(ii)*, this yields an emission energy of 3.73eV when subtracted from the band gap energy (6.36eV). When correlated with the XEOL of c-BN the emission energy due to this defect lies at the high energy tail of the low

energy emission band at 2.98eV (band 1, figure 5.38). This is the interaction of the laser with the zero phonon state of the defect, which is predicted to be located at 3.717eV in the same manner as that described for h-BN.

The likely candidate for the defect states of both phases is nitrogen vacancy, as this has been theoretically shown to yield partially occupied mid band gap states in both h-BN and c-BN [26]. However as already mentioned the defect states of BN are as yet not definitively known. Unfortunately this work can only speculate upon the origins of the luminescent emission.

When compared to one another the PP results of h-BN and c-BN are quite different. For c-BN the defect state is easily resolved with a large resonance, whereas the resonance is less well defined for h-BN. This could be due to the difference in the crystallographic order of the materials; c-BN displays stronger phonon contribution in its XEOL emission. This would suggest that the defect states of c-BN are more clearly defined than those of h-BN. The PP quenching of c-BN was almost an order of magnitude greater than that of h-BN, there was therefore a greater interaction with the detected luminescent emission for c-BN compared to that of h-BN. Comparison of the emission bands being probed to the detection window reveals the reason for this discrepancy. The window of detection simultaneously monitors all of the overlapping emission bands of c-BN, whereas it almost completely omits that of the first emission band in h-BN. As the interaction has been attributed to the first emission band in both phases it is clear that the detection window for h-BN was the cause of the weaker signal.

5.5.4.2 Pump only discussion

The pump-only region describes the system's recovery to steady state XEOL equilibrium, $I_{0,XEOL}$. The recovery is essentially exponential in shape due to the re-trapping of electrons at the OSL centres, thus electrons are becoming increasingly available to the XEOL process as the traps refill. It must be noted that the initial burst of luminescent emission when the laser probe is activated is directly dependent upon the length of time the traps are given to refill. Therefore, if the laser is activated before the XEOL signal has fully recovered the initial burst will be of less magnitude than if allowed to recover fully [65].

If there is only a single OSL trap present the pump-only region could be described by an exponential recovery to equilibrium, whereas if more than one OSL trap is active the recovery could be described as a sum of exponentials. However, the real case is more complex due to the variation of synchrotron radiation power with sampling depth, thus even the distribution of a single trap would be anisotropic. It is therefore necessary to implement a stretched exponential function [93] to model the recovery satisfactorily as described by the equation;

$$I(t) = I_{0,XEOL}(1 - \eta(\exp - (\varepsilon.t)^{\mu})) \tag{5.2}$$

Where η and ε represent the constants of re-trapping dynamics; η is the number of relative traps available and ε is the re-trapping rate. The value μ represents a distribution of exponentials.

This equation was fitted to the pump-only recoveries of h-BN and c-BN as shown in figures 5.34 and 5.35 respectively. The fitting parameters are summarised in tables 5.6 and 5.7 for h-BN and c-BN respectively.

Laser Probe	**Recovery kinetics – pump only**		
	η	**ε**	**μ**
3.024eV (410nm)	0.0612	6.18	0.39
2.918eV (425nm)	0.0869	6.57	0.44
2.825eV (439nm)	0.0869	4.76	0.52
2.627eV (472nm)	0.0516	2.94	0.58
2.427eV (511nm)	0.0327	1.51	0.59
1.529eV (811nm)	0.0282	1.83	0.54
1.127eV (1100nm)	0.0183	0.79	0.51

Table 5.6 – Summary of fitting parameters for hBN luminescent recovery post laser switch off, as plotted in figure 5.31.

Laser Probe	Recovery kinetics – pump only		
	η	**ε**	**μ**
2.825eV (439nm)	0.482	3.467	0.847
2.627eV (472nm)	0.540	3.630	0.883
2.427eV (511nm)	0.413	3.655	0.903

Table 5.7 – Summary of fitting parameters for cBN luminescent recovery post laser switch off, as plotted in figure 5.32.

The value of η is merely the initial position of the signal immediately following the laser switch off transient. The transient is the instantaneous quenching of the XEOL signal as the laser is removed, due to the reactivation of the electron traps. For h-BN the transient is observed as a further ~2% reduction whereas for c-BN it is ~20%. If these values are compared to the position of I_0PP this represents a relative transient of 27% for h-BN and 58% for c-BN. This large difference is further proof of the increased proportion of deep trapping centres in the cubic phase.

The re-trapping rates (ε) vary due to the initial positions of η and are of little physical relevance, however the values of μ are important. The values of μ are relatively invariant of the preceding laser probe for both phases. This suggests that in each case the same traps are responsible for the recovery regardless of probe energy.

1. W.H. Balmain and J. Prakt. *Observations on the formation of compounds of boron and silicon with nitrogen and certain metals,* Philosophical Magazine, 1842. **21**(138): 270-277.

2. I. Jimenez, A.F. Jankowski, L.J. Terminello, D.G.J. Sutherland, J.A. Carlisle, G.L. Doll, W.M. Tong, D.K. Shuh and F.J. Himpsel. *Core-level photoabsorption study of defects and metastable bonding configurations in boron nitride,* Physical Review B, 1997. **55**(18): 12025-12037.

3. L. Liu, Y.P. Feng and Z.X. Shen. *Structural and electronic properties of h-BN,* Physical Review B, 2003. **68**(10): 104102.

4. N.G. Chopra, R.J. Luyken, K. Cherrey, V.H. Crespi, M.L. Cohen, S.G. Louie and A. Zettl. *Boron Nitride Nanotubes,* Science, 1995. **269**(5226): 966.

5. A. Loiseau, F. Willaime, N. Demoncy, G. Hug and H. Pascard. *Boron Nitride Nanotubes with Reduced Numbers of Layers Synthesized by Arc Discharge,* Physical Review Letters, 1996. **76**(25): 4737.

6. Z.H. Zhang, W.L. Guo and Y.T. Dai. *Stability and electronic properties of small boron nitride nanotubes,* Journal of Applied Physics, 2009. **105**(8): 084312.

7. B. Yao, L. Liu, W.H. Su, Z.X. Shen, L. Liu, W.X. Sun and J. Ding. *Effects of degree of three-dimensional order and Fe impurities on photoluminescence of boron nitride,* Journal of Applied Physics, 2004. **96**(4): 1947-1952.

8. J. Thomas, N.E. Weston and T.E. O'Connor. *Turbostratic Boron Nitride, Thermal Transformation to Ordered-layer-lattice Boron Nitride,* Journal of the American Chemical Society, 2002. **84**(24): 4619.

9. S. Alkoy, C. Toy, T. Gonul and A. Tekin. *Crystallization behavior and characterization of turbostratic boron nitride,* Journal of the European Ceramic Society, 1997. **17**(12): 1415-1422.

10. G. Cappellini, G. Satta, M. Palummo and G. Onida. *Optical properties of BN in cubic and layered hexagonal phases,* Physical Review B, 2001. **64**(3): 035104.

11. W.J. Zhang, I. Bello, Y. Lifshitz, K.M. Chan, Y. Wu, C.Y. Chan, X.M. Meng and S.T. Lee. *Thick and adherent cubic boron nitride films grown on diamond interlayers by fluorine-assisted chemical vapor deposition,* Applied Physics Letters, 2004. **85**(8): 1344-1346.

12. X.W. Zhang, H.G. Boyen, P. Ziemann and F. Banhart. *Heteroepitaxial growth of cubic boron nitride films on single-crystalline (001) diamond substrates,* Applied Physics A, 2005. **80**(4): 735-738.

13. X.W. Zhang, H.G. Boyen, D. N., P. Ziemann, F. Banhart and M. Schreck. *Epitaxy of cubic boron nitride on (001)-orientated diamond,* Nature Materials, 2003. **2**(870): 312-315.

14. H. Saitoh and W.A. Yarbrough. *Growth of cubic boron nitride on diamond particles by microwave plasma enhanced chemical vapor deposition,* Applied Physics Letters, 1991. **58**(22): 2482.

15. T.K. Paul, P. Bhattacharya and D.N. Bose. *Characterization of pulsed laser deposited boron nitride thin films on InP,* Applied Physics Letters, 1990. **56**(26): 2648.

16. X. Jiang, J. Philip, W.J. Zhang, P. Hess and S. Matsumoto. *Hardness and Young's modulus of high-quality cubic boron nitride films grown by chemical vapor deposition,* Journal of Applied Physics, 2003. **93**(3): 1515-1519.

17. H. Hoffsass, C. Ronning, U. Griesmeier, M. Gross, S. Reinke and M. Kuhr. *Cubic boron nitride films grown by low energy B+ and N+ ion beam deposition,* Applied Physics Letters, 1995. **67**(1): 46.

18. J.T. Yim, M.L. Falk and I.D. Boyd. *Modeling low energy sputtering of hexagonal boron nitride by xenon ions,* Journal of Applied Physics, 2008. **104**(12): 123507.

19. K. Teii, R. Yamao, T. Yamamura and S. Matsumoto. *Synthesis of cubic boron nitride films with mean ion energies of a few eV,* Journal of Applied Physics, 2007. **101**(3): 033301.

20. H. Feldermann, C. Ronning, H. Hofsass, Y.L. Huang and M. Seibt. *Cubic boron nitride thin film heteroepitaxy,* Journal of Applied Physics, 2001. **90**(7): 3248-3254.

21. M. Mieno and T. Yoshida. *Preparation of Cubic Boron Nitride Films by RF Sputtering,* Japanese Journal of Applied Physics, 1990. **29**: L1175.

22. A.K. Ballal, L. Salamanca-Riba, G.L. Doll, C.A. Taylor and R. Clarke. *Ion-assisted pulsed laser deposition of cubic BN films on Si (001) substrates,* Journal of Materials Research, 1992. **7**(7): 1618-1620.

23. G.L. Doll, J.A. Sell, L. Salamanca-Riba and A.K. Ballal. *Laser deposited cubic boron nitride films,* Carbon, 1990. **28**(6): 805.

24. S. Komatsu, Y. Shimizu, Y. Moriyoshi, K. Okada and M. Mitomo. *Preparation of boron nitride nanocapsules by plasma-assisted pulsed laser deposition,* Journal of Applied Physics, 2002. **91**(9): 6181-6184.

25. B. Yao, Z.X. Shen, L. Liu and W.H. Su. *Strong deep-blue photoluminescence of mesographite boron nitride,* Journal of Physics-Condensed Matter, 2004. **16**(12): 2181-2186.

26. J.L.P. Castineira, J.R. Leite, L.M.R. Scolfaro, R. Enderlein, J.L.A. Alves and H.W. Leite Alves. *First principles studies of point defects and impurities in cubic boron nitride,* Materials Science & Engineering, 1998. **B51**: 53-57.

27. S. Shin, A. Agui, M. Fujisawa, Y. Tezuka, T. Ishii, Y. Minagawa, Y. Suda, A. Ebina, O. Mishima and K. Era. *Resonant photoemission study on the boron 1s exciton of the wide-band-gap semiconductor c-BN,* Physical Review B, 1995. **52**(16): 11853.

28. R.H. Wentorf, R.C. DeVries and F.P. Bundy. *Sintered Superhard Materials,* Science, 1980. **208**(4446): 873.

29. R.H. Wentorf. *Cubic Form Of Boron Nitride,* Journal of Chemical Physics, 1957. **26**(4): 956-956.

30. K. Watanabe, T. Taniguchi and H. Kanda. *Direct-bandgap properties and evidence for ultraviolet lasing of hexagonal boron nitride single crystal,* Nature Materials, 2004. **3**(6): 404-409.

31. Y. Kubota, K. Watanabe, O. Tsuda and T. Taniguchi. *Deep ultraviolet light-emitting hexagonal boron nitride synthesized at atmospheric pressure,* Science, 2007. **317**(5840): 932-934.

32. C. Manfredotti, E. Vittone, A. Lo Giudice, C. Paolini, F. Fizzotti, G. Dinca, V. Ralchenko and S.V. Nistor. *Ionoluminescence in CVD diamond and in cubic boron nitride,* Diamond and Related Materials, 2001. **10**(3-7): 568-573.

33. R.H. Wentorf. *Preparation Of Semiconducting Cubic Boron Nitride,* Journal of Chemical Physics, 1962. **36**(8): 1990.

34. O. Mishima, J. Tanaka, S. Yamaoka and O. Fukunaga. *High-Temperature Cubic Boron Nitride P-N Junction Diode Made at High Pressure,* Science, 1987. **238**(4824): 181.

35. T. Taniguchi, S. Koizumi, K. Watanabe, I. Sakaguchi, T. Sekiguchi and S. Yamaoka. *High pressure synthesis of UV-light emitting cubic boron nitride single crystals,* Diamond and Related Materials, 2003. **12**(3-7): 1098-1102.

36. S. Noor Mohammad. *Electrical characteristics of thin film cubic boron nitride,* Solid-State Electronics, 2002. **46**(2): 203.

37. R. Kalish. *Doping of diamond,* Carbon, 1999. **37**(5): 781.

38. X.T. Zhou, T.K. Sham, W.J. Zhang, C.Y. Chan, I. Bello, S.T. Lee and H. Hofsass. *X-ray absorption studies on cubic boron nitride thin films,* Journal of Applied Physics, 2007. **101**(1): 013710.

39. O. Mishima, K. Era, J. Tanaka and S. Yamaoka. *Ultraviolet light-emitting diode of a cubic boron nitride pn junction made at high pressure,* Applied Physics Letters, 1988. **53**(11): 962.

40. A. Soltani, H.A. Barkad, M. Mattalah, B. Benbakhti, J.C. De Jaeger, Y.M. Chong, Y.S. Zou, W.J. Zhang, S.T. Lee, A. BenMoussa, B. Giordanengo and J.F. Hochedez. *193 nm deep-ultraviolet solar-blind cubic boron nitride based photodetectors,* Applied Physics Letters, 2008. **92**(5): 053501.

41. J.H. Kaneko, T. Taniguchi, S. Kawamura, K. Satou, F. Fujita, A. Homma and M. Furusaka. *Development of a radiation detector made of a cubic boron nitride polycrystal,* Nuclear Instruments and Methods in Physics Research Section A: Accelerators, Spectrometers, Detectors and Associated Equipment, 2007. **576**(2-3): 417.

42. Y.F. Zhukovskii, S. Piskunov, N. Pugno, B. Berzina, L. Trinkler and S. Bellucci. *Ab initio simulations on the atomic and electronic structure of single-walled BN nanotubes and nanoarches,* Journal of Physics and Chemistry of Solids, 2009. **70**(5): 796-803.

43. R. Geick, C.H. Perry and Rupprech.G. *Normal Modes In Hexagonal Boron Nitride,* Physical Review, 1966. **146**(2): 543.

44. A. Agui, S. Shin, M. Fujisawa, Y. Tezuka, T. Ishii, O. Mishima, K. Era, E. Shigemasa and A. Yagishita. *Soft X-ray emission spectra and band structure in cubic boron nitride,* Journal of Electron Spectroscopy and Related Phenomena, 1996. **79**(96): 191-194.

45. A. Stoyanova, L. Hozoi, P. Fulde and H. Stoll. *Correlation-induced corrections to the band structure of boron nitride: A wave-function-based approach,* Journal of Chemical Physics, 2009. **131**(4): 044119.

46. C. Ronning, H. Feldermann and H. Hofsass. *Growth, doping and applications of cubic boron nitride thin films,* Diamond and Related Materials, 2000. **9**(3-6): 1767-1773.

47. J. Robertson. *Electronic-Structure And Core Exciton Of Hexagonal Boron-Nitride,* Physical Review B, 1984. **29**(4): 2131-2137.

48. B. Arnaud, S. Lebegue, P. Rabiller and M. Alouani. *Huge Excitonic Effects in Layered Hexagonal Boron Nitride,* Physical Review Letters, 2006. **96**(2): 026402.

49. V.L. Solozhenko, A.G. Lazarenko, J.P. Petitet and A.V. Kanaev. *Bandgap energy of graphite-like hexagonal boron nitride,* Journal of Physics and Chemistry of Solids, 2001. **62**(7): 1331-1334.

50. J. Li, G. Gui and J.X. Zhong. *Tunable bandgap structures of two-dimensional boron nitride,* Journal of Applied Physics, 2008. **104**(9): 094311.

51. H. Akamura, A. Onodera, T. Endo and O. Mishima. *Pressure dependence of the optical-absorption edge of AIN and graphite-type BN,* Journal of Physics and Chemistry of Solids, 2002. **63**(5): 887-894.

52. H. Sachdev. *Influence of impurities on the morphology and Raman spectra of cubic boron nitride,* Diamond and Related Materials, 2003. **12**(8): 1275-1286.

53. M.G. Silly, P. Jaffrennou, J. Barjon, J.S. Lauret, F. Ducastelle, A. Loiseau, E. Obraztsova, B. Attal-Tretout and E. Rosencher. *Luminescence properties of hexagonal boron nitride: Cathodoluminescence and photoluminescence spectroscopy measurements,* Physical Review B, 2007. **75**(8): 085205.

54. K. Watanabe, T. Taniguchi, T. Kuroda and H. Kanda. *Band-edge luminescence of deformed hexagonal boron nitride single crystals,* Diamond and Related Materials, 2006. **15**(11-12): 1891-1893.

55. P. Jaffrennou, J. Barjon, J.S. Lauret, B. Attal-Tretout, F. Ducastelle and A. Loiseau. *Origin of the excitonic recombinations in hexagonal boron nitride by spatially resolved cathodoluminescence spectroscopy,* Journal of Applied Physics, 2007. **102**(11): 116102.

56. L. Museur, E. Feldbach and A. Kanaev. *Defect-related photoluminescence of hexagonal boron nitride,* Physical Review B, 2008. **78**(15): 155204.

57. K. Watanabe, T. Taniguchi, T. Kuroda, O. Tsuda and H. Kanda. *Time-resolved photoluminescence in band-edge region of hexagonal boron nitride single crystals,* Diamond and Related Materials, 2008. **17**(4-5): 830-832.

58. L. Museur, D. Anglos, J.P. Petitet, J.P. Michel and A.V. Kanaev. *Photoluminescence of hexagonal boron nitride: Effect of surface oxidation under UV-laser irradiation,* Journal of Luminescence, 2007. **127**(2): 595-600.

59. L. Trinkler, B. Berzina, M. Benabdesselam, P. Lacconi, L. Botter-Jensen and K. Atobe. *Radiation induced luminescence processes in c-BN,* Radiation Measurements, 2004. **38**(4-6): 615-618.

60. W.J. Zhang, H. Kanda and S. Matsumoto. *Cathodoluminescence of cubic boron nitride films deposited by chemical vapor deposition,* Applied Physics Letters, 2002. **81**(18): 3356-3358.

61. T. Taniguchi and K. Watanabe. *Synthesis of high-purity boron nitride single crystals under high pressure by using Ba-BN solvent,* Journal of Crystal Growth, 2007. **303**(2): 525-529.

62. M.G. Beghi, C.E. Bottani, A. Miotello and P.M. Ossi. *Vibrational spectroscopy of mixed hexagonal-cubic boron nitride thin films,* Thin Solid Films, 1997. **308-309**: 107-112.

63. K.-L. Barth, W. Fukarek, H.-P. Maucher, M.F. Plass and A. Lunk. *In situ characterization of cubic boron nitride film growth in the IR spectral region,* Thin Solid Films, 1998. **313-314**: 697-703.

64. D.A. Evans, A.G. McGlynn, B.M. Towlson, M. Gunn, D. Jones, T.E. Jenkins, R. Winter and N.R.J. Poolton. *Determination of the optical band-gap energy of cubic and hexagonal boron nitride using luminescence excitation spectroscopy,* Journal of Physics: Condensed Matter, 2008. **20**(7): 075233.

65. N.R.J. Poolton, B.M. Towlson, D.A. Evans and B. Hamilton. *Synchrotron-laser interactions in hexagonal boron nitride: an examination of charge trapping dynamics at the boron K-edge,* New Journal of Physics, 2006. **8**: 76.

66. D.A. Evans, A.R. Vearey-Roberts and N.R.J. Poolton. *Locating hexagonal and cubic phases in boron nitride using wavelength-selective optically detected x-ray absorption spectroscopy,* Applied Physics Letters, 2006. **89**(16): 161107.

67. S. Reich, A.C. Ferrari, R. Arenal, A. Loiseau, I. Bello and J. Robertson. *Resonant Raman scattering in cubic and hexagonal boron nitride,* Physical Review B, 2005. **71**(20): 205201.

68. T. Hemraj-Benny, S. Banerjee, S. Sambasivan, D.A. Fischer, W.Q. Han, J.A. Misewich and S.S. Wong. *Investigating the structure of boron nitride nanotubes by near-edge X-ray absorption fine structure (NEXAFS) spectroscopy,* Physical Chemistry Chemical Physics, 2005. **7**(6): 1103-1106.

69. D.H. Berns, M.A. Cappelli and D.K. Shuh. *Near-edge X-ray absorption fine structure spectroscopy of arcjet-deposited cubic boron nitride,* Diamond and Related Materials, 1997. **6**(12): 1883.

70. M.A. Mannan, M. Nagano, T. Kida, N. Hirao and Y. Baba. *Characterization of BCN films synthesized by radiofrequency plasma enhanced chemical vapor deposition,* Journal of Physics and Chemistry of Solids, 2009. **70**(1): 20-25.

71. S. Emura, T. Moriga, J. Takizawa, M. Nomura, K.R. Bauchspiess, T. Murata, K. Harada and H. Maeda. *Optical-Luminescence Yield Spectra Produced By X-Ray-Excitation,* Physical Review B, 1993. **47**(12): 6918-6930.

72. V.A. Fomichev. Fizika Tverdogo Tela, 1971. **13**: 907.

73. Khusidma.M.B. Fizika Tverdogo Tela, 1972. **14**: 3287.

74. D.M. Hoffman, G.L. Doll and P.C. Eklund. *Optical-Properties Of Pyrolytic Boron-Nitride In The Energy-Range 0.05-10 eV,* Physical Review B, 1984. **30**(10): 6051-6056.

75. V.G. Aleshin. Soviet Physics-Solid State, 1968. **10**: 2284.

76. R.M. Chrenko. *Ultraviolet And Infrared-Spectra Of Cubic Boron-Nitride,* Solid State Communications, 1974. **14**(6): 511-515.

77. M.J. Rand and J.F. Roberts. *Preparation And Properties Of Thin Film Boron Nitride,* Journal of the Electrochemical Society, 1968. **115**(4): 423.

78. J. Zupan and D. Kolar. *Optical Properties Of Graphite And Boron Nitride,* Journal of Physics Part C Solid State Physics, 1972. **5**(21): 3097.

79. W. Baronian. *Optical Properties Of Thin Boron Nitride Films,* Materials Research Bulletin, 1972. **7**(2): 119.

80. N. Miyata, K. Moriki, O. Mishima, M. Fujisawa and T. Hattori. *Optical-Constants Of Cubic Boron-Nitride,* Physical Review B, 1989. **40**(17): 12028-12029.

81. A. Onodera, M. Nakatani, M. Kobayashi, Y. Nisida and O. Mishima. *Pressure-Dependence Of The Optical-Absorption Edge Of Cubic Boron-Nitride,* Physical Review B, 1993. **48**(4): 2777-2780.

82. S. Larach and R.E. Shrader. *Multiband Luminescence In Boron Nitride,* Physical Review, 1956. **104**(1): 68-73.

83. A.I. Lukomskii, V.B. Shipilo and L.M. Gameza. *Luminescence properties of graphite-like boron nitride,* Journal of Applied Spectroscopy, 1993. **57**(1-2): 607-610.

84. K. Watanabe, T. Taniguchi and H. Kanda. *Ultraviolet luminescence spectra of boron nitride single crystals grown under high pressure and high temperature,* Physica Status Solidi, 2004. **201**(11): 2561-2565.

85. A. Katzir, A. Zunger and A. Halperin. *Optical-Properties Of Hexagonal Boron-Nitride,* Bulletin of the American Physical Society, 1976. **21**(3): 246-246.

86. C. Tarrio and S.E. Schnatterly. *Interband-Transitions, Plasmons, And Dispersion In Hexagonal Boron-Nitride,* Physical Review B, 1989. **40**(11): 7852-7859.

87. L.G. Carpenter and P.J. Kirby. *The Electrical-Resistivity Of Boron-Nitride Over The Temperature-Range 700-Degrees-C To 1400-Degrees-C,* Journal of Physics D-Applied Physics, 1982. **15**(7): 1143-1151.

88. X.T. Zhou, T.K. Sham, W.J. Zhang, C.Y. Chan, I. Bello, S.T. Lee and H. Hofsass. *Cubic phase content and structure of BN films from an X-ray absorption study,* Analytical Chemistry, 2006. **78**(18): 6314-6319.

89. Y.N. Xu and W.Y. Ching. *Calculation Of Ground-State And Optical-Properties Of Boron Nitrides In The Hexagonal, Cubic, And Wurtzite Structures,* Physical Review B, 1991. **44**(15): 7787-7798.

90. R. Akimoto, M. Kobayashi and T. Suzuki. *The urbach tail of absorption and photoluminescence spectra in EuSe,* Journal of Physics-Condensed Matter, 1996. **8**(1): 105-110.

91. F. Urbach. *The Long-Wavelength Edge of Photographic Sensitivity and of the Electronic Absorption of Solids,* Physical Review, 1953. **92**(5): 1324.

92. N.R.J. Poolton, B. Hamilton and D.A. Evans. *Synchrotron-laser pump-probe luminescence spectroscopy: Correlation of electronic defect states with x-ray absorption in wide-gap solids,* Journal of Physics D-Applied Physics, 2005. **38**(9): 1478-1484.

93. R. Chen and P.L. Leung. *The decay of OSL signals as stretched-exponential functions,* Radiation Measurements, 2003. **37**(4-5): 519-526.

Chapter 6

Organic Thin Films

Investigations of organic thin films were made using NEXAFS and photo-luminescent (PL) techniques. Following an introduction to organic semi-conducting materials the results are ordered as follows; In section 6.2 the angular resolved NEXAFS, PL and OD-NEXAFS of spin coated polymers are presented. In section 6.3 the PL and OD-NEXAFS of electrospray deposited organic thin films are presented.

6.1 Organic semi-conducting materials

With the discovery of conducting polymers in the 1970s by Macdiarmid, Heeger and Shirakawa [1], organic materials suddenly became regarded as a potential alternative to inorganic semi-conducting materials. Further investigations throughout the 1980s defined the characteristics of numerous conducting polymers, accelerating the interest in polymer based electronics [2-4]. A testament to the importance of conductive polymers was made in 2000, when the trio of Macdiarmid, Heeger and Shirakawa were awarded the Nobel Prize for chemistry [5].

Localised and polarisation phenomena dominate the physics of charged excitation and transport in organic materials [6]. Conducting organic materials all share a common bonding characteristic, that of conjugation, where alternate single and double carbon bonds are contained within the structure, usually indicated by the presence of aromatic rings. Double carbon bonds within conjugated organic materials donate

delocalised p_z electrons to inter-atomic π bonds which form above and below the molecular plane. The bonding and antibonding states of the π bonds create the highest occupied molecular orbital (HOMO) and lowest unoccupied molecular orbital (LUMO) defining a band gap within the material [7]. It is through these delocalised π bonds that charge transfer takes place, although the mechanisms are markedly different to that of inorganic materials. Organic molecules can be considered as self contained entities which when deposited in a film interact weakly with one another. Therefore, charge carrier conduction relies upon the hopping of charges between molecules or along the chain in the case of polymers [8]. The nature of charge transport has been described as polar (polarons) where a charged particle is transferred with an associated charge cloud of opposite polarity [9].

Visible light emission (1.5-3eV) occurs when charges recombine across an optical transition, which for organic materials is localised to the π-π* transitions. Therefore the light emission of organic molecules is an intrinsic property rather than a defect related property as in many inorganic materials. A representation of the dynamics of electroluminescence in an organic LED (OLED) is shown in figure 6.1.

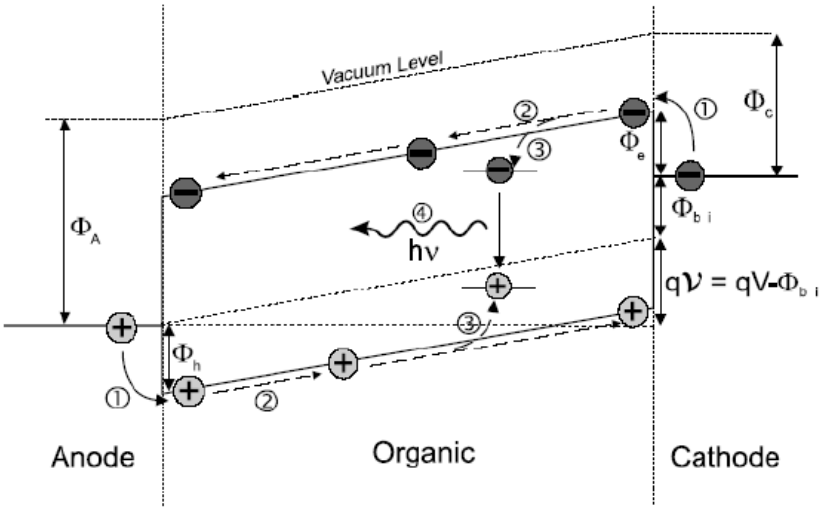

Figure 6.1 – The system of electroluminescence in organic materials, reproduced from [10]; (1) charge carrier injection (2) charge carrier transport (3) formation of excitons (4) radiative recombination of exciton at optical transition. (ΦA – anode work function, ΦC – cathode work function, Φh – hole injection barrier, Φe – electron injection barrier, Φbi – built-in potential, v – effective applied voltage, V – applied voltage, q – elementary charge)

The first light emission from an organic material was reported in the early 1960s by Pope *et al* [11]. Although the quantum efficiency was extremely low (0.01%) this result did demonstrate the potential of organic light emitting materials. The interest in OLEDs was re-ignited in 1987 when the first functioning device, based upon small molecules, was reported to work at low voltages (>10V) [12]. At this time many fluorescent organic materials were known to exist but required high voltages of ~100V in order to work [13-16]. Despite having low efficiency (1%), the OLED described in [12] demonstrated the simplicity of OLED architecture and relative ease with which organic light emitting materials could be incorporated, as shown in figure 6.2. Subsequently in 1990, the first working polymer based LED (PLED) was reported by Burroughes *et al* [17].

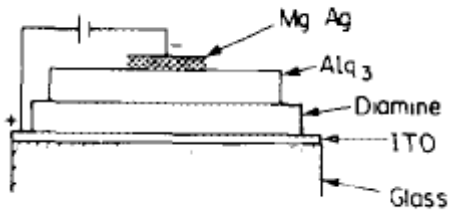

Figure 6.2 – OLED device architecture reported by Tang et al in 1987, reproduced from the literature [12]

The light emission of organic materials is due to the recombination of neutral electron hole pairs, which are known as excitons. The nature of exciton formation and propagation within organic materials is still of some debate [18-20].

A study by De Jong *et al* [18] used electric fields to dissociate excitons formed by photoluminescence (PL) within films of poly(phenylene-vinylene) (PPV). Results indicated a significant drop in luminescent yield, proving the excitons to be strongly bound (Frenkel-type), a conclusion shared by Hill *et al* [9] in a separate study of the same material. It should be noted that exciton binding energies of organic materials are of much greater magnitude (~0.5eV) than those of inorganic materials (~meV) [9]. This results in longer lifetimes of excitons within organics, as thermal energy is insufficient to dissociate the charges (as is the case for inorganic materials).

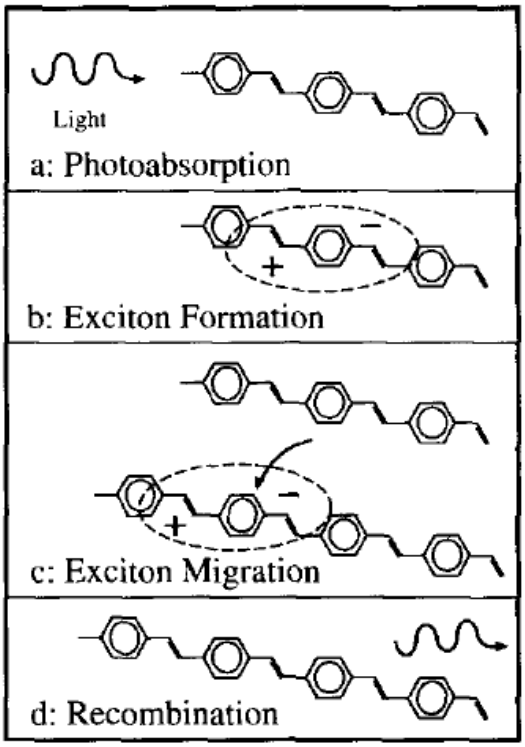

Figure 6.3 – Schematic representation of PL in PPV reproduced from [18], (a) the excitation of charge on a polymer following the absorption of a photon, (b) the formation of an exciton, (c) cross-chain exciton migration (d) exciton recombination resulting in the emission of a photon.

It has also been reported that the migration of excitons (figure 6.3) within molecules results in their recombination across the smallest available transitions [19], causing a red shift between the absorption and emission spectra of many organic materials [21]. Thus the wavelength of light emission from organic materials is dependent upon the minimum separation between the HOMO and LUMO. However inter molecular migration is not thought to occur over any great distance, as the formation and recombination of excitons is described as being localised to individual molecules [20, 22].

The nature of light emission from organic materials is different to that of inorganic semi-conductors due to complexities of the excited states. Spin coupling of excitons results in the creation of either singlet or triplet states. Optical transitions are the result

of singlet to singlet transitions whereas triplet relaxation usually results in non-radiative decay [23]. Singlet to triplet crossing can occur but is less energetically favourable than transitions in which spin is conserved [22]. For photo-stimulated luminescence (PL) only singlet states are activated which generally decay radiatively, thus the quantum efficiency can approach 100%. However for electrically excited luminescence (EL) the triplet states become active with a triplet to singlet ratio of 3:1, this results in a drop of quantum efficiency to a maximum of only 25% [24]. It must be noted that it is the same emission channels which are responsible for the emission of PL and EL in organic materials [25].

Several other modes of non-radiative decay exist including multiphonon excitation, exciton-exciton anhilation and exciton migration to quenching sites (defects) [25]. These additional processes result in the EL efficiencies of real devices being significantly lower than the theoretical maximum of 25%, the best being reported at around 12% [26].

The performance and life-times of organic materials is dependent upon defect states within the structure [27]. Defects are mainly caused by oxidation within the conjugated bonds, for example a single carbonyl state (C=O) in four hundred conjugated bonds can lead to a drop of 50% in EL emission [28]. Oxidised states in organic materials act as electron trapping states, which cause a blue shift in optical emission as the high electron affinities of the oxidised states dissociate charge from the lowest energy excitons (π-π^*) [4, 18].

Oxidation can be caused by exposure of organic films to air and moisture [29]. Encapsulation of OLEDs is therefore essential, usually with indium tin oxide (ITO) coated glass, such that it also forms a transparent upper electrode of the device through which emitted light can escape. OLEDs constructed in this manner have been

reported as having high efficiencies (>10%) and operational life-times of 20,000hrs [30]. Further processes of oxidation include operational photo- and electro-chemical reactions [18, 31-33]. One method of increasing OLED life-times is to introduce electron and hole transport materials between the light emitting layer and the electrodes [34]. These materials act as the anode and cathode to the light emitting layer but with much reduced potential barriers, thus lowering the required operating voltages and improving device efficiency.

Photo stimulated luminescence was used as a method of characterisation for the thin films studied as part of this thesis.

6.2 Experimental studies of poly(arylamine) thin films

6.2.1 Introduction to Poly(arylamines)

Poly(arylamines) (PAAs) are a group of polymers used as hole transport materials (HTM) in many in PLEDs [27, 34, 35]. The nomenclature arylamine describes its molecular constituents, aryl being an aromatic ring with one removed hydrogen and amine, a triple bonded nitrogen, analogous to ammonia (NH_3). PAAs are characterised by the monomeric structure of a central nitrogen atom bonded to three substituents of which at least one is an aromatic ring. The PAA films studied as part of this thesis are poly(phenylamines) (PPAs) in which the aryl rings are benzene-like phenyl groups (C_6H_5).

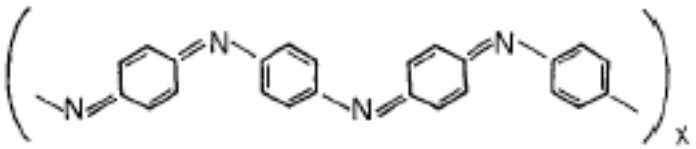

Figure 6.4 – Taken from [36], schematic representation of the conductive base form of poly(aniline).

The most commonly reported PPA is poly(aniline) (PANI), one of the first reported conducting polymers, which has a monomer structure consisting of a single phenyl ring per nitrogen atom [36]. The polymerised structure of PANI, as shown in figure 6.4, incorporates the phenyl rings into the backbone creating a conjugated pathway along the chain. Several authors have studied the electrical conduction of PANI and reported on the ease with which its structure can be altered and doped [36, 37].

Many other (*higher*) PPAs exist which are considered in groups of di- or tri-phenylamine derivative structures. There are also small molecules which fall into the same phenylamine groups existing as either monomeric or dimerised structures, an example of which is tri-phenlyamine (TPA) [22, 38]. All PPA structures exhibit the similar conjugated bonding structure to PANI, however not all the phenyl rings are involved in forming the backbone. This structural orientation causes considerable change to the electrical conduction of these polymers when compared to PANI, with conduction requiring significant overlap of LUMO states between phenyl rings of the chain and at cross linkages. The conduction between TPA moieties within the polymer structure has a hopping character localised to the phenyl rings [38].

The optical properties of phenylamine materials have been studied in several publications. The absorption spectra of phenylamines have been shown to be dependent upon the number of phenyl rings present within the monomer, where the

absorption energies of the π-π* are shifted to lower energies for tri-phenylamine (297nm) as compared to di-phenylamine (285nm) and aniline (280nm) [4]. In polymerised forms the absorption energies are additionally shifted to lower energies, studies have reported a shift in the principle absorption of poly(tri-phenylamine) structures to 350nm [21, 39].

The luminescent emission of PPA materials is accepted to be mainly centred in the blue region (400-420nm) of the spectrum due to π-π* exciton recombination at lower energies than the absorption [29].

Bushby *et al* [40], studied the luminescent emission from PPAs of di- and tri-phenyl monomeric structures. Emission was shown to be in the blue region of the spectrum for the poly(tri-phenylamine) and in both the blue and red regions of the spectrum for the poly(di-phenylamine) material. Antonel *et al* [41], studied the electro-luminescent emission of PANI as a function of film thickness and electrical potential, reporting an emission of 412nm in its conducting emraldine form. Yano *et al* [21], investigated the absorption and emission of phenylamine small molecule solutions, again an emission of 420nm was stated for higher order materials.

The PPA studied as part of this thesis was characterised using NEXAFS and photo-luminescent emission, results of which are presented in sections 6.2.3 and 6.2.4 respectively, following an introduction to the PPA samples studied.

6.2.2 Sample details

The PPA samples studied were supplied to the Aberystwyth University Materials Research Group by Bangor University. The PPA was deposited from solution via spin-coating, producing thin films (~200nm) of polymer on Au/glass substrates. Individual samples (5mm x 8mm) were produced from portions of a single slide yielding several chemically identical samples. The samples were shipped under a nitrogen atmosphere, which was broken immediately prior to experimentation.

The PPA was of unknown monomeric structure, therefore X-ray photo-electron spectroscopy (XPS) was employed to establish relative carbon to nitrogen ratios within the material, the results of which are displayed in figure 6.5.

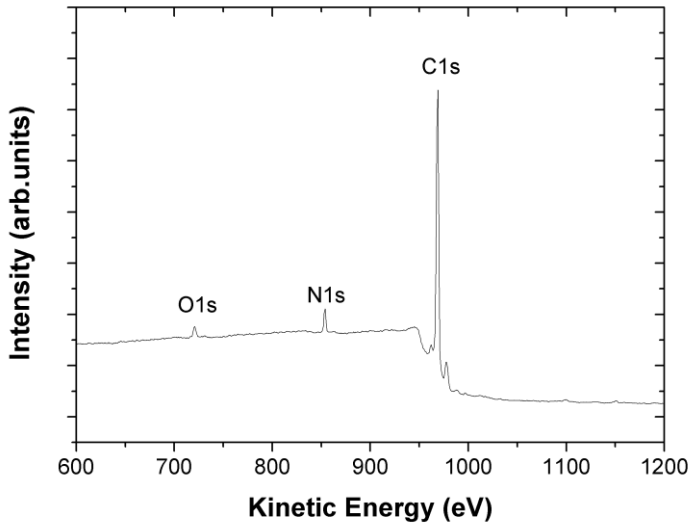

Figure 6.5 – Wide scan XPS of PPA thin film. X-ray excitation source Mg kα 1253.6eV with data taken at 100eV pass energy.

Calculated from the relative peak areas, the ratio of carbon to nitrogen was 15:1 and that of carbon to oxygen 30:1 (nitrogen to oxygen 2:1). The relative ratio of carbon to nitrogen was used to predict the TPA bonded monomer structure shown in figure 6.6.

Luminescent investigation (section 6.2.4) of the PPA film proved the oxygen contribution to be due to surface oxidation and was therefore omitted from the monomeric structure.

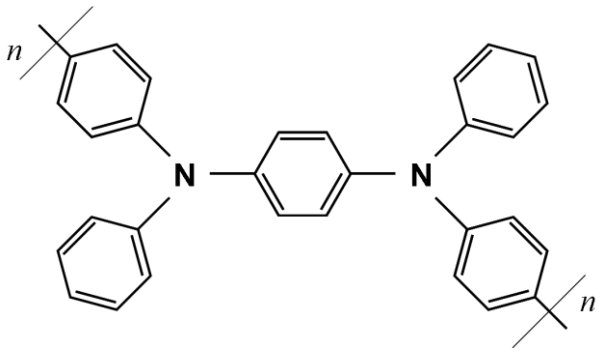

Figure 6.6 – Proposed poly(tri-phenylamine) monomer structure consisting of two tri-phenylamine moieties sharing a central phenyl ring with a 15:1 carbon:nitrogen ratio.

6.2.3 Angular resolved NEXAFS of PPA

6.2.3.1 NEXAFS experimental procedure

Total electron yield (TEY) NEXAFS experiments were carried out on beamline MPW6.1 at the SRS Daresbury using a modified angular resolved ultra-violet photo-electron spectroscopy (ARUPS) chamber. The internal detector of the ARUPS chamber, not used as part of this work, was parked beneath the sample stage throughout the experimental run. A custom sample manipulation system (Aberystwyth University Materials Research Group) was placed into the chamber allowing for linear horizontal and vertical movement as well as rotation about the vertical axis relative to the incident beam (sample surface plane normal set as 0˚ position to the beam). The sample stage was electrically isolated with a ceramic break

and an insulated copper wire was attached to the sample stage to enable drain current measurement to be taken. The beamline response was recorded from an Au mesh placed in the beam upstream of the sample chamber and both the sample and Au mesh drain currents were monitored via external pico ammeters. The data was recorded using the beamline control computer, where three channels simultaneously recorded the SR beam energy, TEY sample drain current and TEY Au mesh drain current. For the angular resolved experiments TEY measurements were taken at incremental angular steps of the incident beam with manual adjustment performed to the manipulator. Corrections to the results for beamline flux fluctuations were made by normalising the sample and Au signals to the pre-edge intensity at 280eV and then dividing the sample data with that of the Au mesh.

6.2.3.2 Results

The carbon K-edge NEXAFS of PPA contains several resonant peaks (A-F) as shown in figure 6.7. The initial peak at 284.34eV can be confidently ascribed to the C1s-π^* resonance of the phenyl ring C=C bonds [42]. However the other peaks at lower binding energies (B-F), are due to combinations of C1s-π^* and C1s-σ^* resonances and cannot be ascribed without appropriate density functional theory (DFT) calculation, which is not available at the present time.

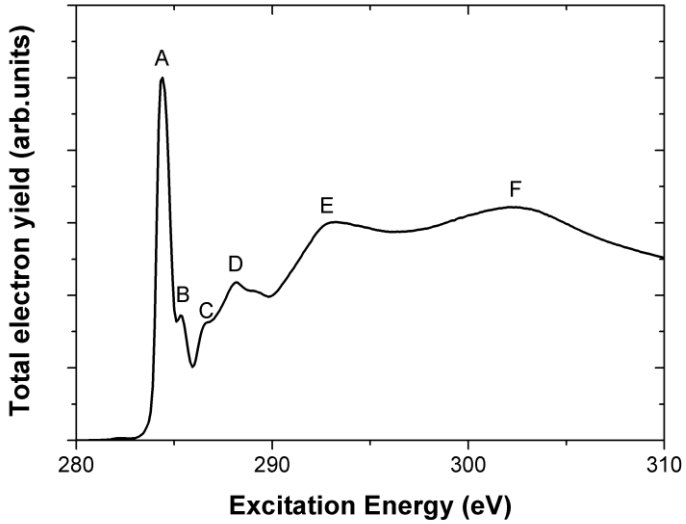

Resonance Peak	Position (eV)
A	284.34
B	285.33
C	286.52
D	288.14
E	292.93
F	302.44

Figure 6.7 – Total electron yield NEXAFS of PPA taken at 0˚X-ray incidence to the sample plane normal and resonant peak positions denoted in the spectra.

The angular dependence of the XANES region (280-290eV) is shown in figure 6.8. The results were collected at increments of SR angular incidence to the normal of the sample plane (set as 0˚), corrected for beamline flux, set to a common pre-edge intensity and normalised to 290eV. The variation in the intensity immediately prior to the absorption edge onset is due to the relative intensity differences of each result to the background signal. There is clearly opposing angular dependence between the resonances at 284.34eV and 288.14eV, labelled π* and σ* respectively. A cross over

energy of 286.43eV was identified as the transition between the π* and σ*-like resonances as indicated in figure 6.8 by a dashed line.

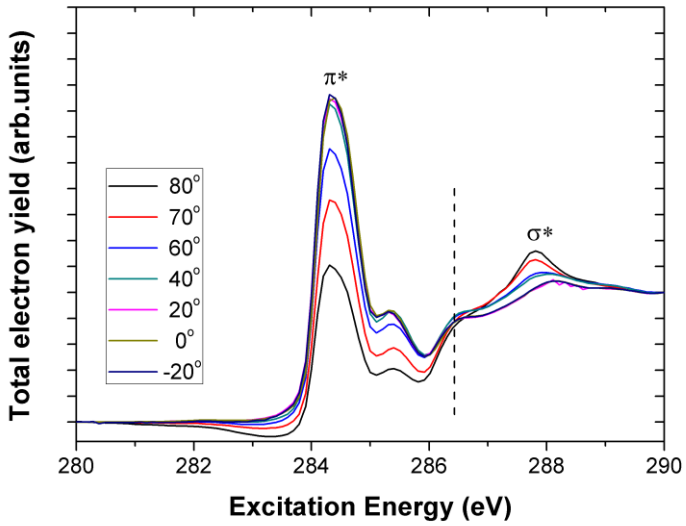

Figure 6.8 – Angular dependence of the π* and σ*-like resonances of poly(tri-phenylamine) at angular positions of the sample plane normal (z) to synchrotron beam (90^{o}-θ), thus the electric field vector of the incident X-rays is parallel to the sample surface at 0˚. Dashed line indicates transition between π* and σ*-like resonances.

Angular orientation considerations

Angular resolved NEXAFS is a useful tool in establishing molecular orientation in organic thin films. The basic principle of coupling between the electric field vector of the plane polarised incident X-ray and molecular orbital vector governs the resonant intensity of the peaks observed. Therefore by measuring the relative intensity of defined resonances as a function of the X-ray incidence angle, the orientation of molecules on a surface can be estimated.

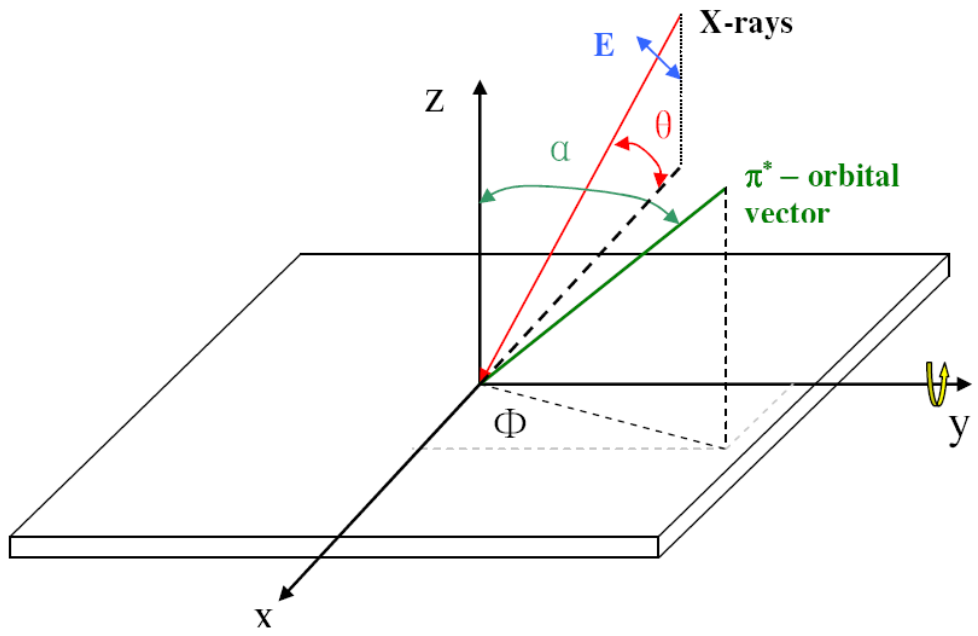

Figure 6.9 – The coordinate system of angular resolved NEXAFS reproduced from the literature [43]. The sample surface, normal to which is z, lies in the xy plane. SR incident in the direction of x at an angle relative to the surface plane θ, is plane polarised in the xz plane as indicated by the vector E. For beamline MPW6.1 the direction y is the samples' vertical orientation about which it is rotated to vary θ. The direction of the π* orbital vector is defined by the polar angle α and azimuthal angle Φ.

The geometry of angular resolved NEXAFS experiments is shown in figure 6.9.

For the case of beamline MPW6.1, the SR is polarised in the plane of the storage ring orbit (xz). The vertical orientation of the sample is in the y direction about which the angle of X-ray incidence θ can be varied.

If it is assumed that the molecular plane has threefold or higher symmetry then the angular vector of the π* orbital can be swept around the azimuth creating a cone onto which the molecule is orientated. In this case the tilt angle of the molecular plane is described by the polar angle α.

The X-ray absorption cross section (chapter 2) of the π* molecular orbital changes with incident angle θ of the SR beam, due to coupling between the two vector

components of π* and E; strong interaction when the two vectors are in close parallel alignment leads to enhanced resonance, whereas weak interactions result from vector misalignment.

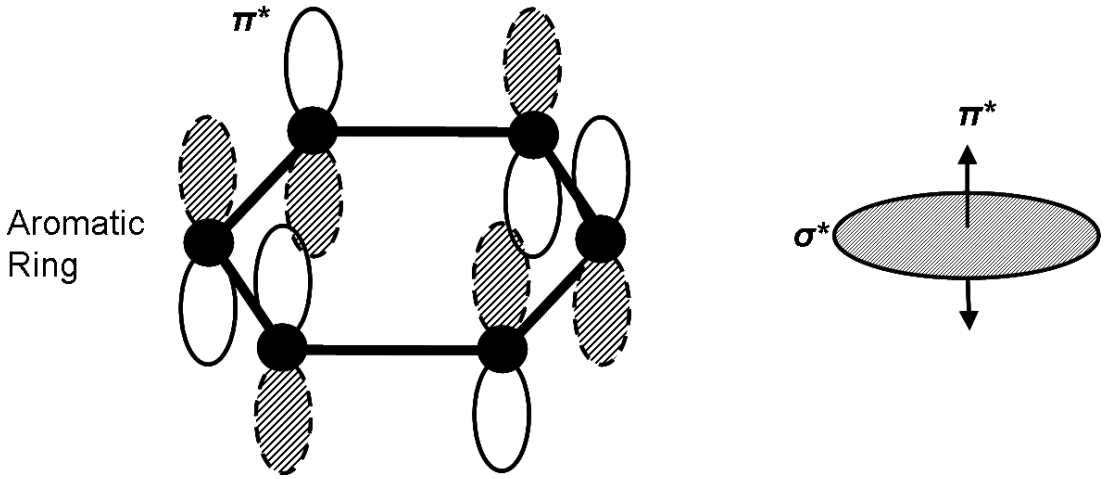

Figure 6.10 – Schematic representation of the π* and σ* resonances of a benzene ring. The vector component of the π* is normal to the molecular plane, whereas that of the σ* is quasi- in plane.

The angular dependence of the C1s-π* resonance intensity can be used as an indication of net phenyl ring orientation within a film using angular resolved NEXAFS.

With reference to the angular resolved NEXAFS of PPA shown in figure 6.8, the initial C1s-π* (284.34eV) is indicative of the phenyl ring, its directional π* vector perpendicular to its planer orientation. The resonance at 287.82eV is attributed to in plane σ* resonances of the phenyl rings due to its opposing angular dependence to that of the π* resonance. The use of the first π* resonance to establish molecular orientation is valid in this instance, as its intensity is less influenced by neighbouring/overlapping contributions and its background easier to ascertain.

The change of intensity (I) with X-ray incidence angle (θ) of the π^* resonance can be modelled by the equation $I \propto \cos^2(\theta)$, as shown in figure 6.11*(i)*, where the excellent linear fit strongly indicates molecular orientation within the film. This simplified relationship is used as a first approximation of an angular dependence [44].

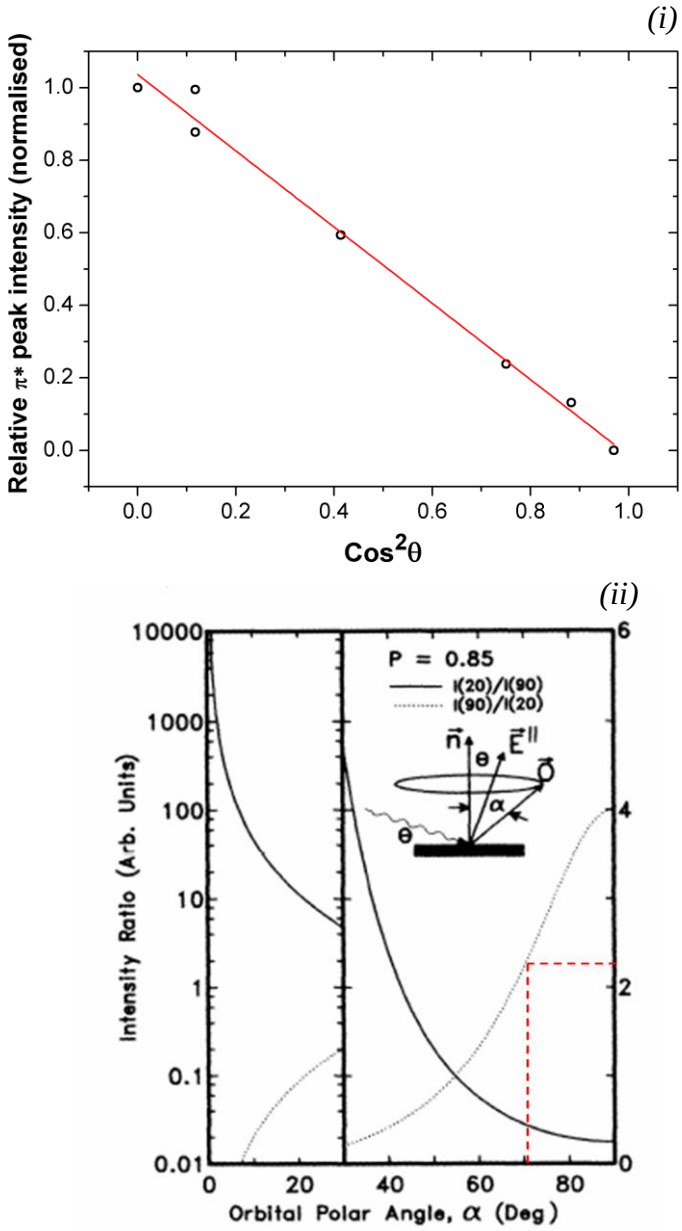

Figure 6.11 – The considerations used to assess the tilt angle of the PPA film (i) The relative peak intensity angular dependence modelled by $I \propto \cos^2(\theta)$***. The linear fit is an indication of molecular orientation. (ii) The intensity dependence of the normal to grazing angle incidence taken from [45] used to estimate the tilt angle of the phenyl rings of the PPA films (dashed red line) as described in the text. Where P represents the polarisation of the beamline.***

For a more detailed analysis the ratio of π* resonance intensity between normal (θ_{90°) and grazing (θ_{20°) X-ray incidence can be used to estimate the tilt angle of the molecules with respect to the substrate plane normal [45] assuming three fold or higher symmetry, as shown in figure 6.11*(ii)*. For this case the PPA π* ($I\theta_{90^\circ}/I\theta_{20^\circ}$) intensity ratio is 2.20 which indicates the phenyl rings are tilted by less than 20˚ (dashed red line figure 6.11*(ii)*) from the substrate plane normal and are standing up from the surface, as represented by figure 6.12. (This result assumes a beamline polarisation of 85%).

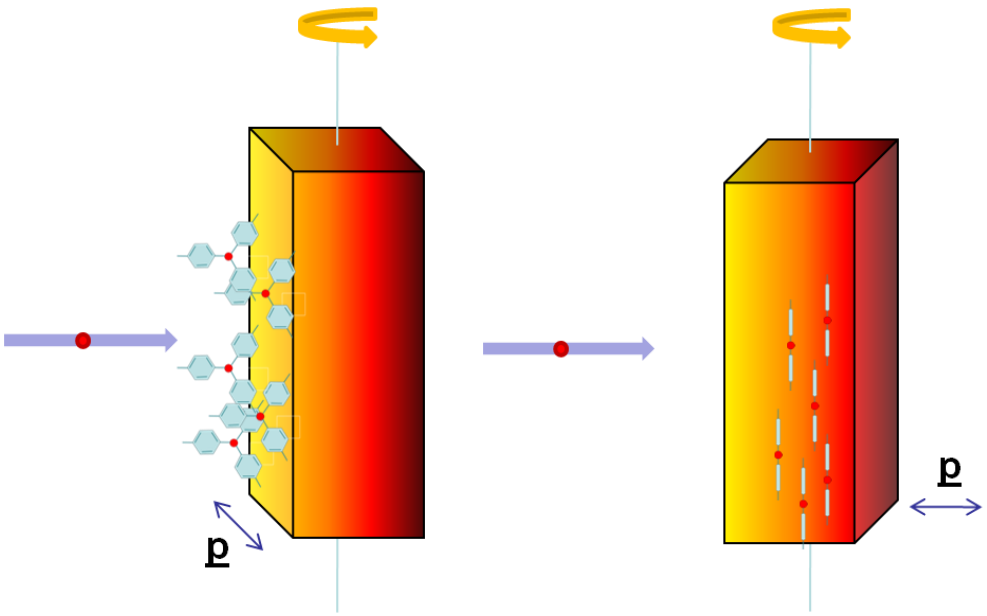

Figure 6.12 – Schematic representation of the molecular orientation of PPA to the substrate plane. Incident SR is indicated by the blue arrow with its polarised electric field vector E into the page (red dot). The π* orbital vector is indicated by p, normal to the molecular plane.

6.2.3.3 Discussion

The results presented here are the first observed occurrence of preferred orientation for a poly(tri-phenylamine) thin film using angular resolved NEXAFS. The orientation of the phenyl rings of PPA are shown to be standing up from the surface such that the π* vector is parallel to the surface plane.

The potential mechanisms of polymer self organisation are governed by π stacking and planarity within the chains [8, 38]. For the case of phenylamines the planarity of the monomer structure has been theoretically studied, proving its dependence upon the number of phenyl rings, the TPA moiety being shown to be flat in the plane of the nitrogen bonds. For the proposed PPA structure only the central shared phenyl ring would be planer to the nitrogen atoms with the outer rings able to rotate about their bond axis [38].

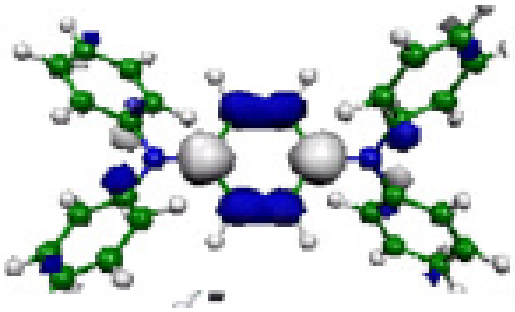

Figure 6.13 – Taken from [38] the calculated LUMO distribution (blue) of poly(tri-phenylamine) using density functional theory (DFT) is localised to the shared central phenyl ring.

As shown in figure 6.13 the LUMO states of the PPA monomer are localised to the shared central phenyl ring, therefore the orientation observed by NEXAFS is a measurement of these states, suggesting that the monomers are aligned within the polymer chains regardless of potential rotations between adjoining phenyl groups. However care must be taken in this assumption as other closely lying LUMO states,

not necessarily localised upon the central phenyl ring, may be measured within the same experimental resolution of the NEXAFS experiment. Unfortunately at present further DFT calculation of other LUMO states is unavailable within the literature.

The asymmetry of molecular PPA structures has also been shown to hinder self organisation of thin films during deposition [46], this would suggest that the symmetrical monomer structure of the PPA film here would readily self-organise.

Preferred orientation has been previously observed in other organic materials, however these reports mostly concern small molecule systems [47-49]. Only one other polymer has been reported to exhibit preferred orientation NEXAFS, the organo-metallic polymer Pt-DEBP, which was shown to orientate itself to metal substrates with a tilt angle of 40˚ to the substrate plane normal [44, 50].

Most polymer thin films are described as being of amorphous structure [51], however some studies have described localised order as a potential mechanism for charge transfer [3, 46, 52].

The self organisation of small molecules is used to create devices with definitive electronic characteristics, however most require in-vacuo sublimation as contact with atmosphere can cause aggregation [52, 53]. The self organisation of spin coated polymer films could therefore be of great technological importance.

6.2.4 Luminescent studies of PPA films

Although PPA is generally regarded as a HTM it is also a luminescent material. Therefore its photo-induced emission can be used to characterise its electronic structure using PL and OD-NEXAFS, the results of which are contained within this section.

6.2.4.1 Photoluminescence (PL)

6.2.4.1.1 Experimental procedure

The PL investigation of PPA was conducted offline using MoLES as the luminescence detection chamber. The sample was mounted on the sample stage using carbon tape. Measurements were conducted in air at ambient temperature ~300K using a 3.069eV (404nm) laser as an excitation source. All data was collected using a PMT (Hamamatsu R758P) in conjunction with the high energy grating of the monochromator (range 350-650nm at 1nm resolution).

6.2.4.1.2 Results

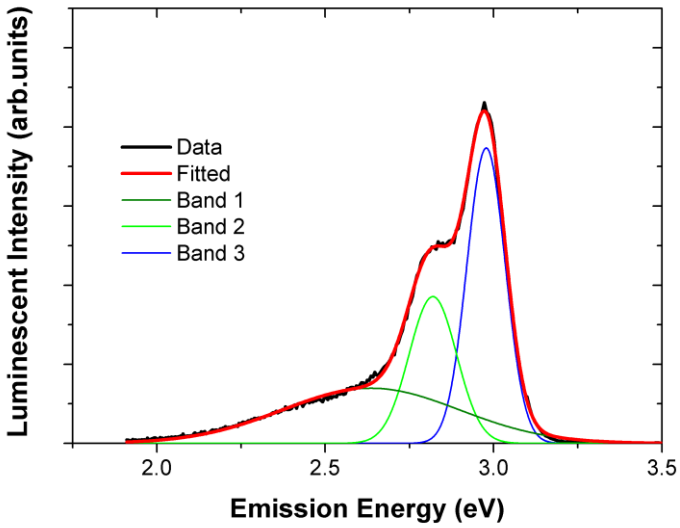

Figure 6.14 – Fitted PL spectra of poly(arylamine) recorded with excitation energy 3.069eV (404nm) at 300K.

The PL of PPA is shown in figure 6.14. Three Gaussian bands can be fitted to the emission centred at 2.635eV (470nm), 2.820eV (439nm) and 2.978eV (416nm) labelled 1 to 3 respectively. The entire emission of PPA is relatively narrow with the highest intensity in the blue region of the spectrum.

The emission bands vary in their intensity and broadening. The 2.635eV band (Band 1) is of a relatively broad FWHM 0.53eV spanning the entire emission. The two higher energy bands of 2.820eV and 2.978eV (bands 2 and 3), have greater intensity than band 1 exhibiting similar FWHM values of 0.14eV and 0.11eV respectively.

6.2.4.1.3 Discussion

The narrow emissions bands of 2 and 3 are indicative of excitonic π-π^* transitions which must be located upon the phenyl rings of the polymer [18]. The small energy separation of the two excitons, 0.158eV, would suggest the origins are from the conjugated bonds of C-C and C-N bonded constituents of the phenyl rings. The lack of red emission from the PPA provides further evidence of a poly(tri-phenylamine) structure [40].

For the case of the broad emission of band 1, the origin is less clear, although it is likely to be defect related. The broadening observed in the emission of band 1 would suggest a dilute system with considerable vibration contribution. Oxidation of the aromatic rings has been reported in many polymer thin films due to the presence of molecular oxygen [18, 25]. The XPS results (figure 6.5) of the PPA film suggest some oxygen content was present, consistent with partial oxidation. Oxidation is known to interrupt conjugation causing carbonyl groups (C=O) within organic materials. This leads to defect states which act as electron traps resulting in a quenching of

luminescent emission. Therefore the intense luminescence observed from this PPA material would suggest the oxidated states are located only on the surface and not within the bulk.

6.2.4.2 Spatially resolved OD-NEXAFS

6.2.4.2.1 Experimental procedure

Experiments were conducted on beamline MPW6.1 at the SRS Daresbury using CLASSIX1 as the end station. The sample was mounted on to the sample stage with conductive tape and held in a vacuum of $1x10^{-9}$mBar. A SiO_2 sample was loaded in addition to the polymer to measure the beamline flux as a correction factor. The luminescent emission was found to be invariant of temperature change therefore measurements were carried out at ambient temperature (300K). Measurements were conducted in total luminescent yield (no filter), using the x2 visible objective (pixel resolution of $7.8\mu m^2$).

6.2.4.2.2 Results

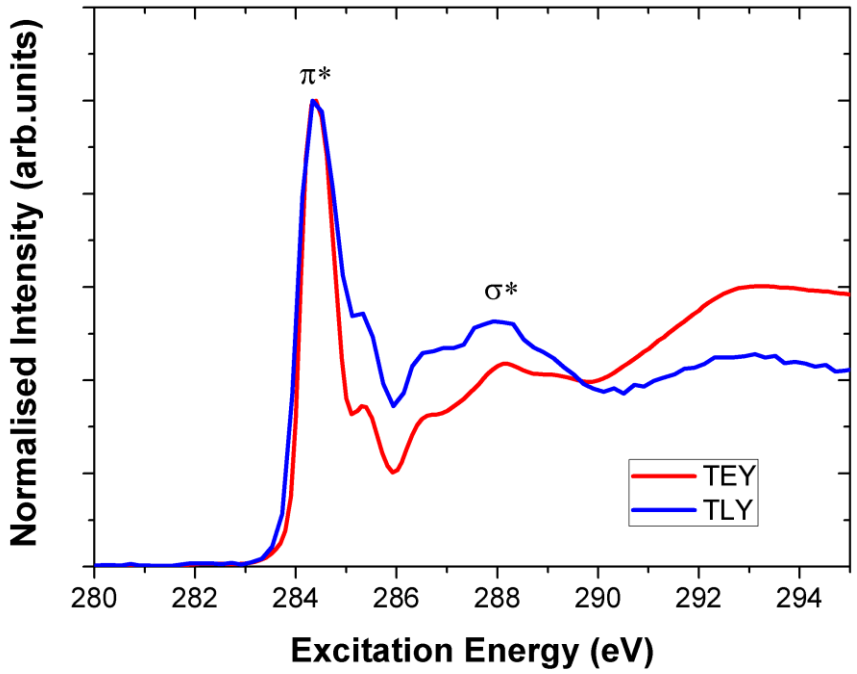

Figure 6.15 – Comparison plot of the total electron yield TEY and volume-integrated total luminescent yield TLY NEXAFS.

As shown in figure 6.15 the same π* and σ* resonances are present for in both the electron and luminescent yield NEXAFS, although of varied relative intensity between the two data sets. This result also indicates that the luminescent centres are localised to the absorption centres as the K-edge jump of the total luminescent yield (TLY) is positive with respect to the pre-edge signal. If considered with reference to the luminescent emission of PPA, this result is expected as the strongest emission bands are the π-π* transitions which are excited by the K-edge absorption.

An image of the PPA film taken in total luminescent emission is shown in figure 6.16*(i)* at a fixed excitation energy of 293eV (the point of maximum luminescent intensity). The volume-integrated TLY NEXAFS is shown in figure 6.15. However when the surface is imaged in emission, there are two distinctly different regions

labelled as 1 and 2 in figure 6.16*(i)*. If the emission is spatially resolved at different excitation energies (284.34eV and 285.34eV) the difference between the two regions is revealed as shown in figure 6.16*(ii)* and 6.16*(iii)*.

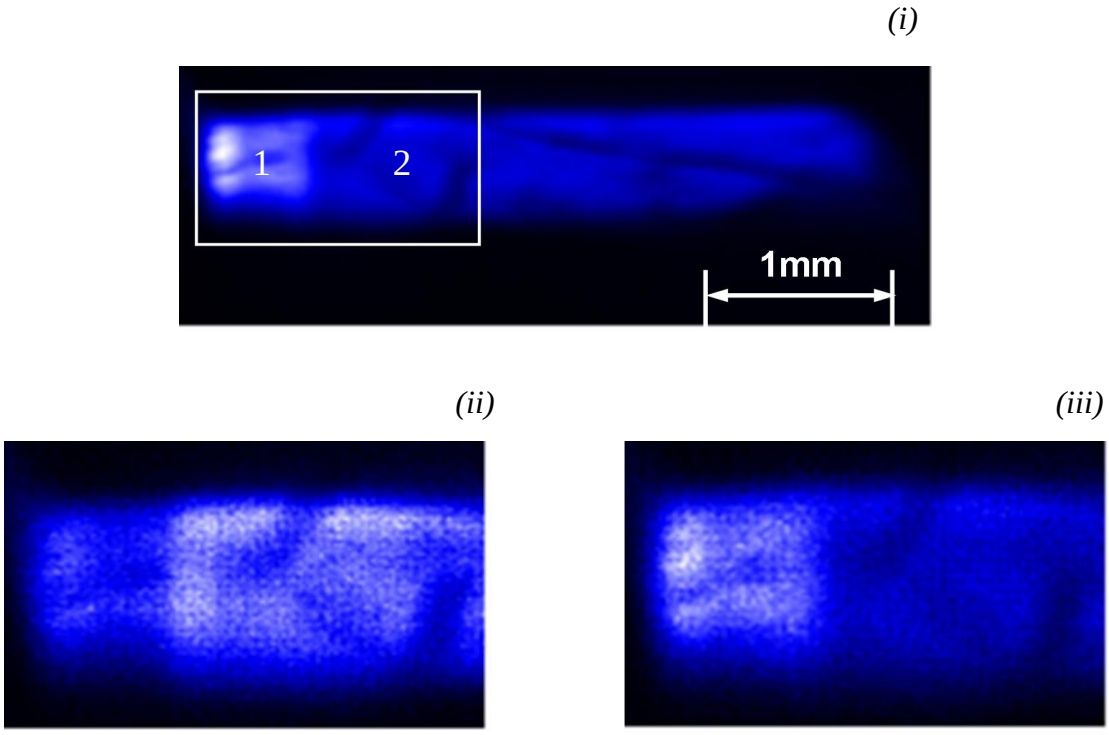

Figure 6.16 – Image of PPA film in (i) total luminescent yield at 293eV excitation energy, indicated area of 1.5x1mm from which images (ii) and (iii) are taken. (ii) Image taken at excitation energy 284.34eV. (iii) Image taken at excitation energy 285.34eV.

The spatially resolved OD-NEXAFS of regions 1 and 2 are shown in figure 6.17. The spectra are normalised to the pre-edge intensity and corrected for background and beamline flux. The difference spectra calculated from the subtraction of region 1 from 2 is also displayed. There is clearly a significant suppression in the initial C1s-π* resonance (284.34eV) in region 1, therefore it can be stated that the resonances of region 1 are σ*-like compared to those of region 2 and is therefore an indication of orientation difference.

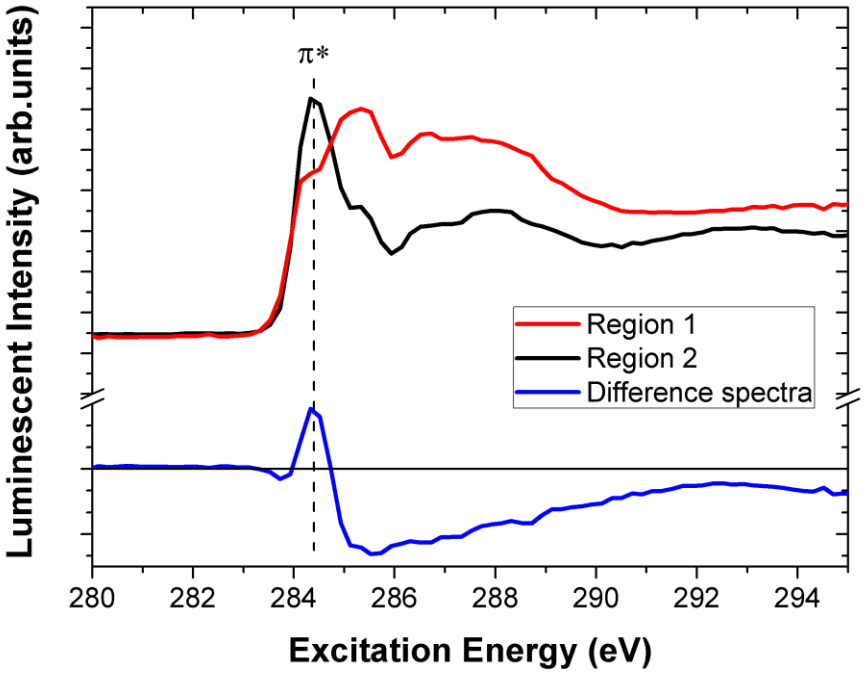

Figure 6.17 – The PPA OD-NEXAFS of regions 1 and 2 and the resultant difference spectra. The initial C1s-π* resonance is indicated at an excitation energy of 284.34eV.

If the angular resolved NEXAFS of the PPA film is taken as a template, the phenyl ring orientation of region 1 must be parallel to the sample surface and those of region 2 standing up as diagrammatically shown in figure 6.18. As OD-NEXAFS is a bulk probe, the effect of surface states will be suppressed, signifying orientation throughout the material and not only on the surface of the film.

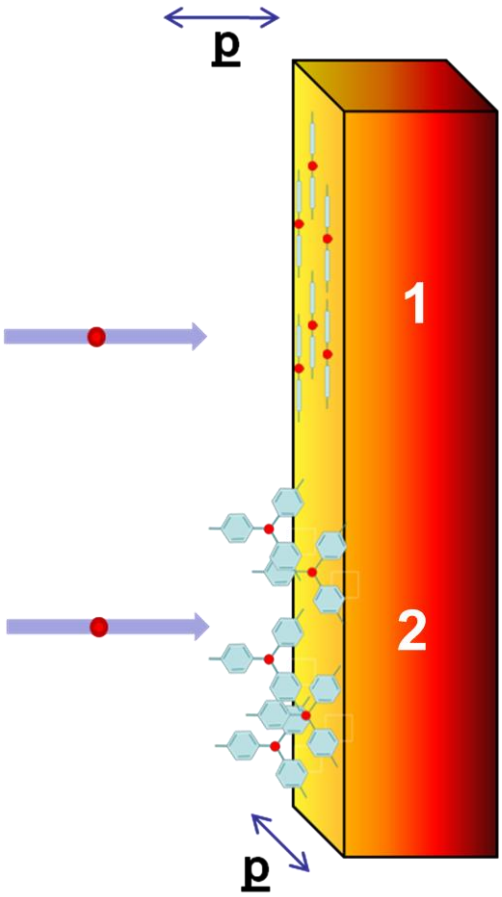

Figure 6.18 – Schematic representation of the orientation differences observed for PPA using spatially resolved OD-NEXAFS. The phenyl rings of region 1 are lying parallel to the surface plane whereas those of region 2 are standing up.

6.2.4.2.3 Discussion

The spatially resolved OD-NEXAFS indicates significant orientation differences between regional areas within the same PPA film. This suggests segmented growth in bound regions and weak interactions with the substrate. Therefore the materials orientation must be dominated by intermolecular forces.

It is important to note with reference to the TEY angular resolved NEXAFS that the regional growth may have resulted in a superposition of signals from areas of different molecular orientation as seen in TLY. Therefore unknown C1s-π* suppression may have caused an error in the estimation of the molecular tilt angle.

Film crystallisation has been cited as a possible mechanism of bonding change in PPAs [39]. However for this case the PPA film can be seen to be of regular morphology across the entire footprint of the synchrotron beam, therefore crystallisation is not the cause of the observed structural variation.

Another potential cause of regional growth is non-uniform film thickness effects due to the spin coating process. The PPA films having been spin coated displayed an undulating surface morphology as can be observed in the imagery, thus the structural differences between the regions could be due to overlying polymer layers causing an amorphous structure. This suggests that self-assembly of the PPA is dependent upon the film thickness.

6.3 Luminescent studies of electrospray deposited organic thin films

The experimental investigations described in this section utilised the Aberystwyth University Materials Research Group ESD system (Chapter 4) to create films for luminescent analysis.

Copper phthalocyanine (CuPc) is an optically active organic material, with weak optical emission reported in the IR region of the spectrum [54, 55], however in its monomeric form it has been shown to emit at higher energies. This effect is due to the increased efficiency of non-radiative triplet states in multi-molecular systems.

CuPc has a tendency to aggregate when deposited as a thin film due to intermolecular forces [56]. However it has been proven that the addition of poly(ethyleneoxide) (PEO) to CuPc solution will effectively disstack the phthalocyanine creating dimerised PEO/CuPc structures [57, 58].

The experiments reported in this section describe investigations of electrospray deposited thin films of CuPc, PEO and CuPc/PEO hybrid materials from solution and subsequent characterisation using AFM, PL and OD-NEXAFS.

6.3.1 Introduction to Copper Phthalocyanine (CuPc)

Phthalocyanines (Pc) are small dye molecules closely related to porphyrins. They are known to have some exceptional intrinsic properties including high chemical stability, high thermal stability and extremely low defect populations (10^{14}-10^{16} traps per cm^3). Phthalocyanines are known to display crystallographic growth when deposited by in-vacuum sublimation leading to highly ordered films ideal for electronic applications

[47] and are therefore of significant scientific interest. Phthalocyanines are centro-symmetrical molecules made up of four isoindole units, as shown in figure 6.19 [59].

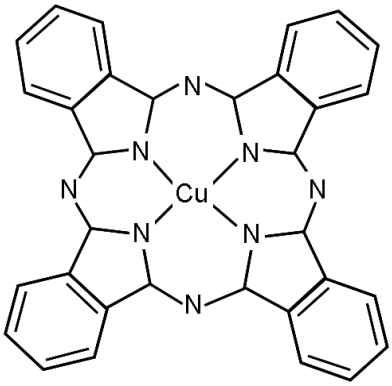

Figure 6.19 – Schematic representation of the molecular structure of Copper Phthalocyanine.

The central atom of a Pc is usually occupied by a metal which causes a non planer structure, where the metal atom is pronounced from the molecular plane. The presence of aromatic rings within the Pc structure leads to delocalised π bonds above and below the molecular plane, forming the HOMO and LUMO states of the molecule and these are responsible for its optical properties.

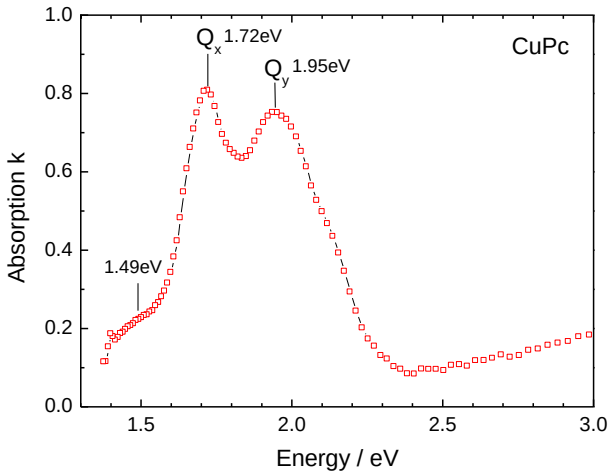

Figure 6.20 – The absorption spectra of CuPc taken by the Aberystwyth University Materials Research Group.

All phthalocyanines have strong absorption bands around 700nm giving them a characteristic deep blue colour. The absorption spectra of CuPc has two dominant bands at 1.72eV (720nm) and 1.95eV (635nm), as shown in figure 6.20. All of the absorption bands of CuPc are due to the fundamental π-π* transition (Q band). The energy difference between the two bands is a result of bond symmetry, where the distribution of the π bonds leads to separate resonant modes [60]. The light emission of solid state CuPc is of weak intensity and significantly red shifted from its absorption, centred in the infrared at 1.13eV (1100nm) [54, 55, 61]. This emission band is a phosphorescent decay of the triplet state. However in monomeric form (solutions) CuPc emits at significantly higher energies, due to suppression of intersystem crossing between the singlet and triplet. Therefore, triplet decay is enhanced in the solid state where stacking of the Pcs create efficient non-radiative pathways.

In order to dissolve CuPc in solution it must be sulfonated, where at least one of its benzene rings has the chemical group SO_3 added to it. The sulfonated CuPc investigated in this thesis was tetra-sulfonated (tsCuPc) the structure of which is shown in figure 6.21 [62, 63].

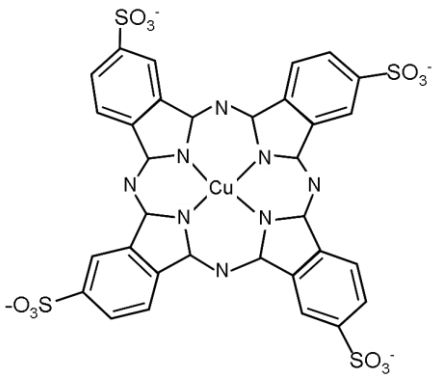

Figure 6.21 – Schematic representation of tetra sulfonated Copper Phthalocyanine (tsCuPc).

6.3.2 Introduction to poly(ethyleneoxide) (PEO)

Poly(ethylenes) (PEs) are insulating polymers commonly used as packaging materials. The simplest PE polymer structure is $(-CH_2-)_n$, where each carbon atom within the backbone is singly bonded (σ) to two other carbons and two hydrogens. Therefore the carbon bonding of PE is saturated (sp^3) yielding no delocalised π states for conduction. This molecular orientation makes PE extremely flexible, as the single bonds within the backbone allow significant movement of the atoms. All PEs are long chain polymers which create an amorphous physical structure in the solid phase.

Poly(ethyleneoxide) (PEO) is an oxidised variation of the group having substituted oxygen for every third carbon within the backbone, its chemical structure is depicted in figure 6.22. [64]

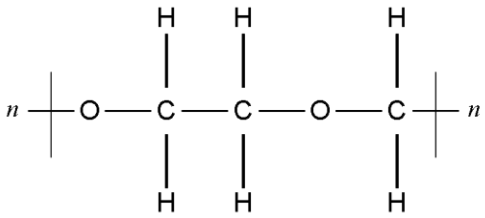

Figure 6.22 – Schematic representation of the chemical structure of PEO.

The presence of oxygen does not give rise to π bonding as the carbons remain saturated, resulting in an electrically insulting material. PEO does have unsaturated oxygen bonds and is therefore negatively charged, however this is asymmetrically distributed resulting in a polar material [65]. The intrinsic charge of PEO has been shown to act as an excellent matrix for carbon based electrolytes in which ionic salts are mobile, a subject for which detailed review articles are found in the literature [66].

PEO is also of pharmaceutical importance used in a variety of medicines including blood clotting agents [67].

In a solid PEO tends to create an amorphous structure, where the long chains lie over one another in a random orientation. However within a thin film segmented crystalline structure has been reported but is usually inferred as a measure of degradation [66].

PEO has also been used to modify the physical structure of light emitting polymers [65, 68]. For example Tang *et al* [68] adjoined PEO to the light emitting polymer PHP creating a copolymerised tri-block structure. The resulting film was shown have intense light emission and much greater flexibility than the pure PHP material.

6.3.3 ESD thin film production

Molecular thin films were deposited onto silicon (Si) 110 substrates, all of which were cut from the same wafer. Si was chosen as a suitable non-emissive substrate in the luminescent detection window of this investigation (200-1000nm). The Si substrate was cleaned prior to deposition via ultrasonic isopropanol bath and plasma to remove surface contaminants.

The PEO powdered material of molecular weight 100,000au was acquired commercially from Sigma-Adrich. The tsCuPc material was supplied in water solution of $2.4\mu Ml^{-1}$ concentration by Bangor University. The PEO was dissolved in 50:50 methanol/water solution with a $5.1\mu M/l^{-1}$ concentration. The hybrid tsCuPc/PEO solution was mixed with a relative ratio of 4.2:1 PEO to tsCuPc by adding the appropriate amount of the tsCuPc solution to the PEO solution and compensating for the extra water content with additional methanol to yield 50:50

water/methanol. All of the prepared solutions were stirred for 24 hours within sealed containers prior to deposition.

The cleaned Si substrate was mounted onto a glass slide within the third stage chamber of the ESD just below the quartz crystal position. Solution was sprayed using a 30μm inner diameter emitter (proxeon) at voltages of 3.1kV, 2.8kV and 2.9kV for the PEO, tsCuPc and tsCuPc/PEO solutions respectively at continuous flow rates of ~10μlmin^{-1}. The pressure of the third stage was observed to rise to a pressure of 7x10^{-4}mBar from its base of 5x10^{-5}mBar whilst spraying. A quartz crystal analyser was used to establish deposition rates for each of the materials before deposition on to the substrate (section 4.5). Deposition rates were calculated assuming material densities of 1gcm^{-3} [69] for the PEO and 1.67gcm^{-3} for the tsCuPc and tsCuPc/PEO materials. The films were all grown to estimated thicknesses of 100nm with typical deposition rates of ~16 Angstroms/min.

6.3.3.1 AFM analysis of ESD films

The resulting films were examined using AFM the results of which are displayed in figures 6.23 – 6.29. The AFM was operated in both contact and non-contact mode with all measurements being made in atmosphere.

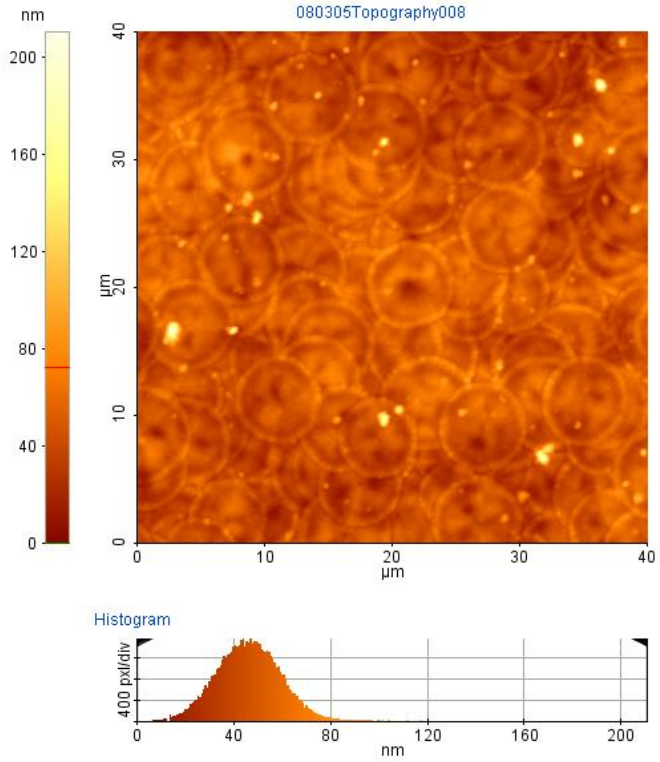

Figure 6.23 – Contact AFM topography (40µmx40µm) of 100nm PEO film prepared by in vacuum ESD on a Si substrate. Histogram displaying the rms average roughness of the surface to be 50nm.

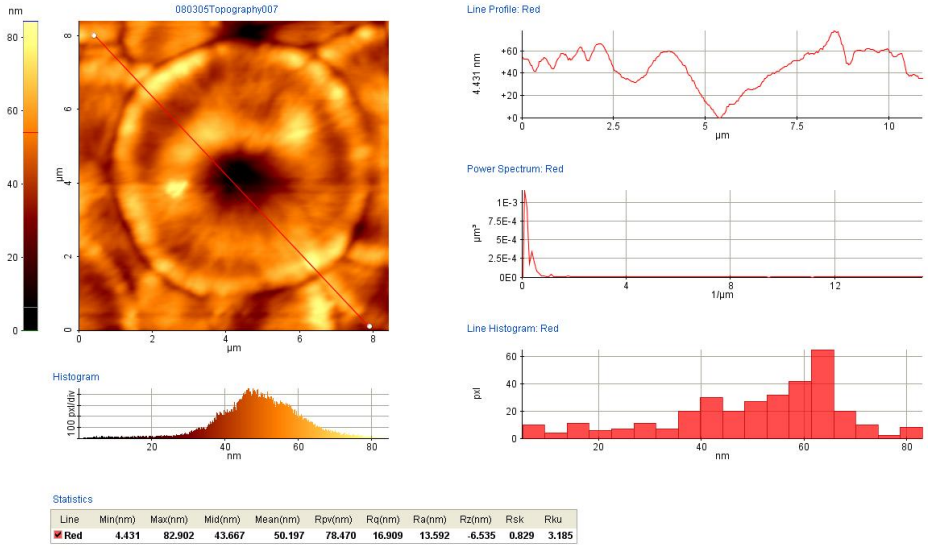

Figure 6.24 – High resolution AFM image of PEO film (9µmx9µm). Line profile drawn through the centre of the disc revealing cross section shown in red on image and relevant statistics therein.

Figure 6.23 shows the PEO sample to be made up from a matrix of overlapping ~5µm discs, creating a thin film, with an average roughness of 50nm over a 40µmx40µm area. On closer inspection the main contribution to the surface roughness was localised to the centres of the discs, where the PEO had spread from the centre outwards creating a cratered morphology, as shown in figure 6.24. This morphology suggests that the ES droplets arriving at the substrate still consisted of significant solvent content which quickly dried (section 4.5).

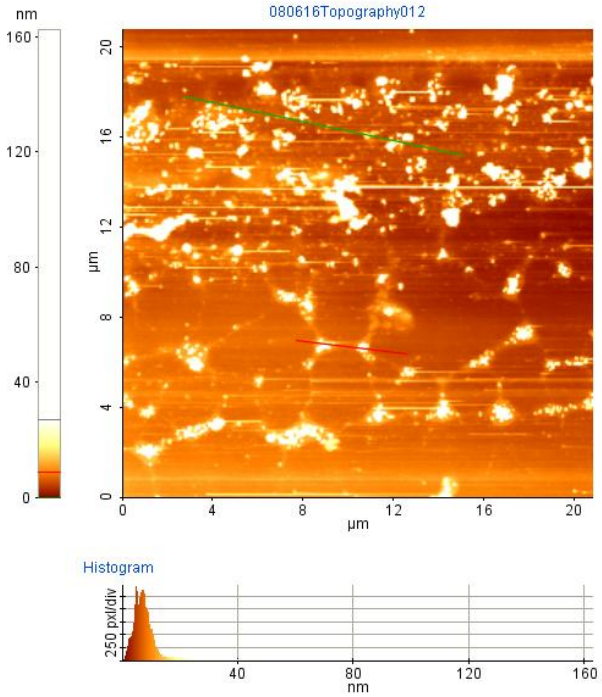

Figure 6.25 – Non-contact AFM topography (20µmx20µm) of 100nm tsCuPc film prepared by in vacuum ESD on a Si substrate. Histogram displaying the rms average roughness of the surface to be 8nm.

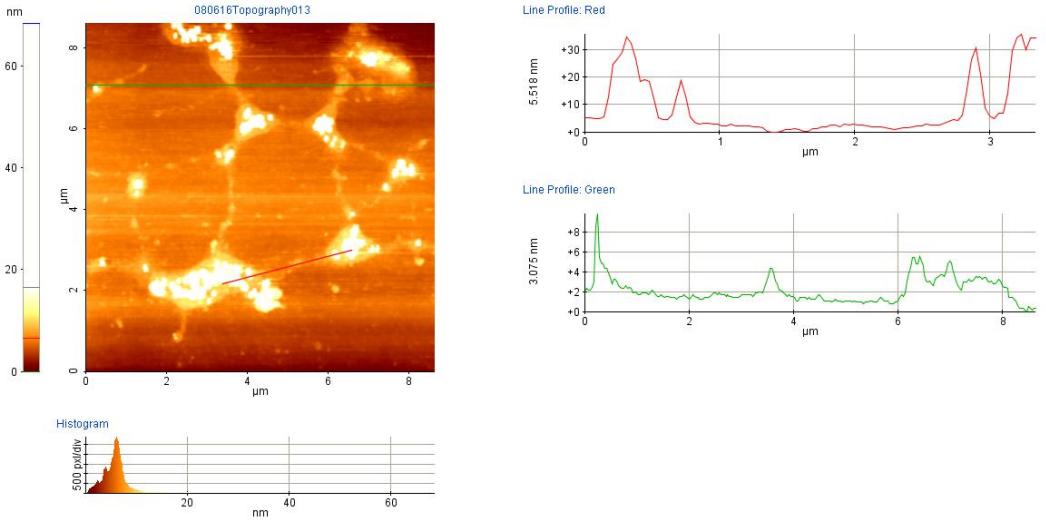

Line	Min(nm)	Max(nm)	Mid(nm)	Mean(nm)	Rpv(nm)	Rq(nm)	Ra(nm)	Rz(nm)	Rsk	Rku
Red	5.518	41.447	23.483	13.398	35.930	9.991	7.781	9.488	-1.595	4.169
Green	3.075	12.956	8.015	5.204	9.881	1.316	0.997	1.483	-1.845	8.989

Figure 6.26 – Non-contact AFM topography (9µmx9µm) of tsCuPc film. Line profiles drawn through the molecular islands revealing the cross sections shown in red and green on image and relevant statistics therein..

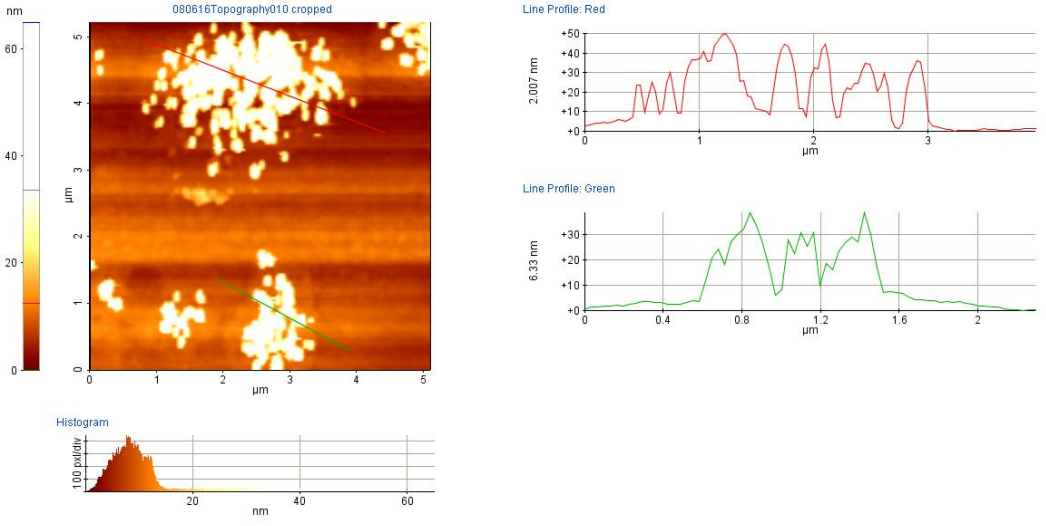

Line	Min(nm)	Max(nm)	Mid(nm)	Mean(nm)	Rpv(nm)	Rq(nm)	Ra(nm)	Rz(nm)	Rsk	Rku
Red	2.007	52.341	27.174	19.290	50.334	15.190	13.528	6.649	-0.471	1.872
Green	6.330	45.084	25.707	17.375	38.754	11.660	10.319	5.738	-0.893	2.281

Figure 6.27 – Non-contact AFM topography (5.5µmx5.5µm) of tsCuPc film. Line profiles drawn through the molecular islands revealing the cross sections shown in red and green on image and statistics therein.

The tsCuPc sample displayed aggregation of the molecules on the surface, as shown in figures 6.25-6.27, therefore the tsCuPc sample was not of uniform thickness however this was of not of concern for the luminescent experiments. Distinct islands of tsCuPc are observed of relatively thick (35nm) cross-sections. The aggregation of the molecules appears to have occurred post deposition as the phthalocyanines have migrated revealing bare Si substrate. Recent real-time XPS results (Aberystwyth University Materials Research Group) have shown self organisation of phthalocyanines to occur post deposition which would agree strongly with the results presented here. The features displayed in figure 6.26 are known as cell networks [70], these are indicative of a fast drying solution of molecules on a surface. Therefore this would suggest a wet deposition with a significant solvent presence at the substrate.

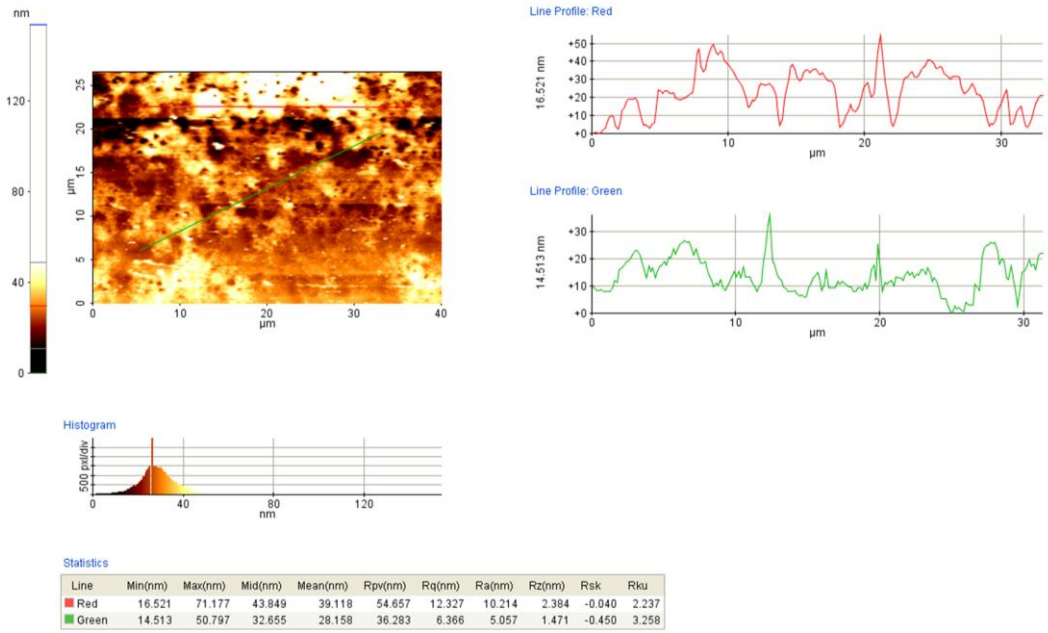

Line	Min(nm)	Max(nm)	Mid(nm)	Mean(nm)	Rpv(nm)	Rq(nm)	Ra(nm)	Rz(nm)	Rsk	Rku
Red	16.521	71.177	43.849	39.118	54.657	12.327	10.214	2.384	-0.040	2.237
Green	14.513	50.797	32.655	28.158	36.283	6.366	5.057	1.471	-0.450	3.258

Figure 6.28 – Contact AFM topography (40µmx25µm) of 100nm tsCuPc/PEO film prepared by in vacuum ESD on a Si substrate. Histogram displays the rms average roughness of the surface to be 32nm.

The tsCuPc/PEO sample (figure 6.28) displayed a similar average roughness to the PEO sample but with a smoother morphology. This suggests that the growth mode of the tsCuPc/PEO material was due to greater surface mobility compared to the case of the PEO. The features of the deposited film are significantly different to those of the PEO sample as shown in figures 6.28 and 6.29. These features suggest a phase separation within a drying solution which create the distinctive patterns observed in process known as spinodal decomposition [71].

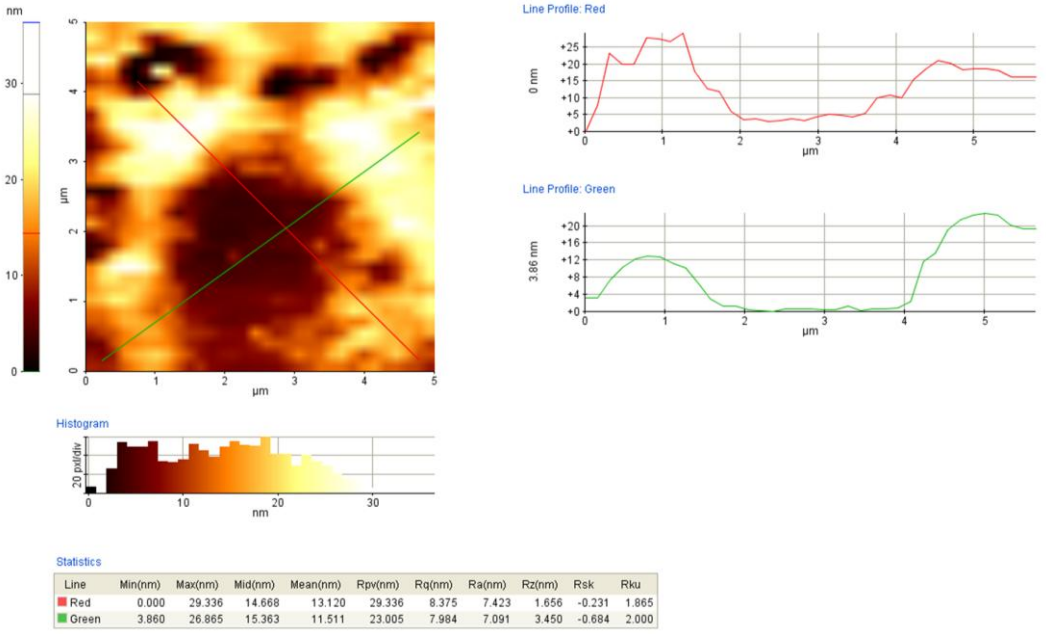

Line	Min(nm)	Max(nm)	Mid(nm)	Mean(nm)	Rpv(nm)	Rq(nm)	Ra(nm)	Rz(nm)	Rsk	Rku
Red	0.000	29.336	14.668	13.120	29.336	8.375	7.423	1.656	-0.231	1.865
Green	3.860	26.865	15.363	11.511	23.005	7.984	7.091	3.450	-0.684	2.000

Figure 6.29 – Contact AFM image of disc like structure within tsCuPc/PEO film. Line profile drawn through the centre of the feature reveals the cross section shown in red and green and relevant statistics therein.

In summary all the samples were deposited with significant solvent at the substrate surface. Subsequent rapid drying of the solution within the vacuum resulted in features alike those of spinodal decomposition and cellular networks. However for the purposes of this study the growth mechanisms of the thin films were not of concern.

6.3.4 Luminescence results

All of the ESD prepared films were studied using PL. Only that of the tsCuPc/PEO sample yielded emission within the detectable range (200-1000nm) therefore the luminescent results presented are for the hybrid tsCuPc/PEO material only.

6.3.4.1 Photoluminescece (PL)

6.3.4.1.1 Experimental procedure

The PL investigation of tsCuPc/PEO was conducted offline using MoLES as the luminescence detection chamber and the same procedure outlined in section 6.2.4.1. Experiments were conducted using a 2.786eV (445nm) laser as the excitation source. All data was collected using the medium energy grating of the monochromator (range 500-930nm at 1.5nm resolution).

6.3.4.1.2 PL results

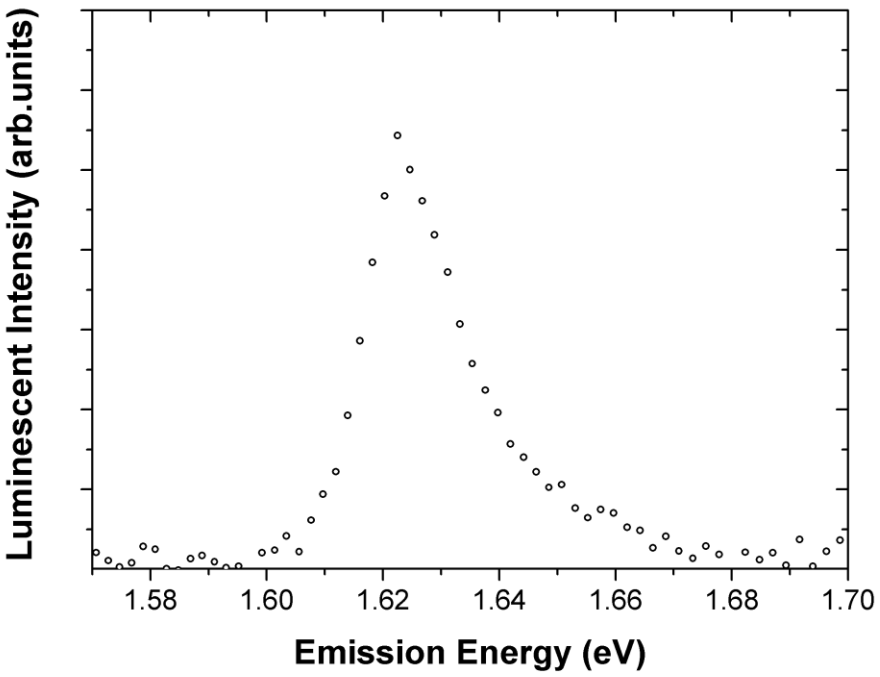

Figure 6.30 – PL spectra of tsCuPc/PEO recorded with excitation energy 2.786eV (445nm) at 300K.

The PL of tsCuPc/PEO is shown in figure 6.30. A single emission band at 1.625eV (763nm) can be clearly identified in the near infrared region of the spectrum. The emission is relatively narrow of FWHM 0.2eV.

6.3.4.1.3 Discussion

The emission of the tsCuPc/PEO sample can be considered with reference to emission from other CuPc based materials reported in the literature.

The emission of solid state CuPc has been reported to occur at 1100nm, attributed to phosphorescent decay of the triplet state [61]. When compared to the absorption spectra there is clearly a large shift to lower energy between the Q band absorption (~700nm) and this 1100nm emission. This is attributed to efficient intersystem

crossing between the singlet and triplet states, caused by π stacking in the solid state [69].

For the case of tsCuPc emission has only been reported for monomeric structures in solution, centred about the Q band absorption at 628nm [72].

There has only been one reported occurrence of light emission from a CuPc/PEO hybrid material [73]. In this study Tang *et al* deposited thin films of tetra amino CuPc (taCuPc) and PEO proving the addition of the PEO to the taCuPc to yield visible emission centred at 450nm. This emission band was attributed to recombination about the Soret absorption band of the taCuPc, quite different to that observed for the tsCuPc/PEO material studied here.

The light emission observed for the tsCuPc/PEO is the first occurrence of luminescent emission from a tsCuPc based thin film. The mechanism of light emission appears to be fluorescent due to singlet to singlet recombination, as its energy is closely related to the Q band absorption energy. The observation of emission from the tsCuPc/PEO sample suggests the PEO acts to suppress the Pc triplet state by disstacking the tsCuPc into individual molecules within the film.

6.3.4.2 OD-NEXAFS of tsCuPc/PEO

The light emission of the tsCuPc/PEO sample was used to investigate the bonding states of the LUMO by OD-NEXAFS.

6.3.4.2.1 Experimental procedure

Experiments were conducted on beamline MPW6.1 at the SRS, Daresbury using the same procedure outlined in section 6.2.4.2.

6.3.4.2.2 Results

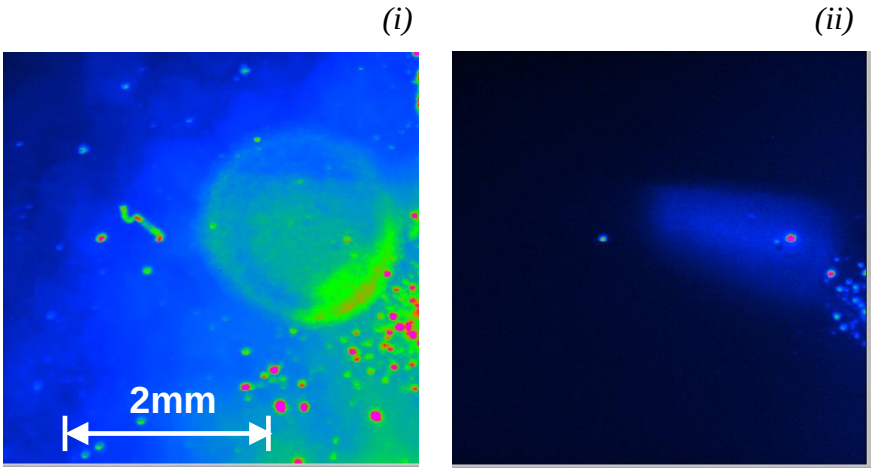

Figure 6.31 – tsCuPc/PEO film imaged in (i) reflected light and (ii) total luminescent yield. Beamline footprint of 2mmx1mm area.

The SR beam was positioned over the whole area of the deposited material as shown in figure 6.31. No spatial variation in the emission was observed, therefore the results shown in figure 6.32 are volume-integrated over the whole sample. There are several resonant peaks within the OD-NEXAFS of the tsCuPc/PEO material, the energetic positions of which are indicated in figure 6.32.

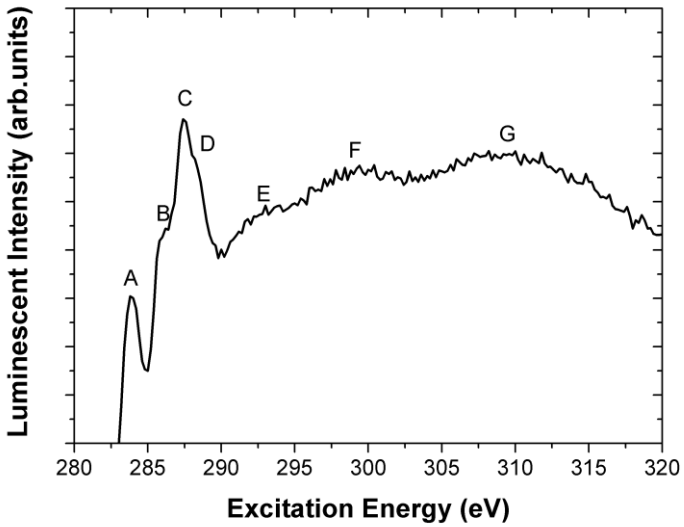

Peak	Position (eV)
A	283.94
B	286.08
C	287.43
D	288.34
E	292.62
F	299.37
G	309.62

Figure 6.32 – OD-NEXAFS of tsCuPc/PEO taken in total luminescent yield, denoted peaks refer to resonances as summarised in table.

6.3.4.2.3 Discussion

The OD-NEXAFS results described here are the first XAS for a tsCuPc/PEO material, therefore no definitive ascription of the individual resonances can be made. However several conclusions can be drawn from the results with reference to the literature. Firstly, the emission must be solely due to the tsCuPc as PEO is known to be non-luminescent, also its NEXAFS resonances exist at energies above 288eV [75]. Secondly, comparison of the OD-NEXAFS to the NEXAFS spectra of pure CuPc [74] can be used to tentatively ascribe the initial peaks (A-D) to C1s-π^* resonances and all of those of lower binding energy to C1s-σ^* resonances. Thirdly, the binding energy of the initial C1s-π^* (A) resonance is significantly higher than the other π^* resonances (B-C), this can be attributed to the pyrole bonded carbons which are known to have higher binding energies than the other benzene bonded carbons [76].

Only one other report of OD-NEXAFS for a Pc based material exists [77], in which a study of the luminescent emission from thick films of MgPc found its emission to be centred at 860nm. In this study the OD-NEXAFS signal was shown to mirror that of the electron yield NEXAFS, however the K-edge jump was negative due to sample thickness effects. The positive carbon K-edge jump of the tsCuPc/PEO thin film is indicative of radiative transitions localised to the carbon LUMO states, therefore the tsCuPc triplet related non-radiative decay channel is suppressed by the presence of the PEO.

1. H. Shirakawa, E.J. Louis, A.G. Macdiarmid, C.K. Chiang and A.J. Heeger. *Synthesis Of Electrically Conducting Organic Polymers - Halogen Derivatives Of Polyacetylene, (Ch)X,* Journal of the Chemical Society-Chemical Communications, 1977(16): 578-580.

2. A.G. Macdiarmid, J.C. Chiang, A.F. Richter and A.J. Epstein. *Polyaniline: a new concept in conducting polymers,* Synthetic Metals, 1987. **18**(1-3): 285.

3. A.G. MacDiarmid, Y. Min, J.M. Wiesinger, E.J. Oh, E.M. Scherr and A.J. Epstein. *Towards optimization of electrical and mechanical properties of polyaniline: Is crosslinking between chains the key?* Synthetic Metals, 1993. **55**(2-3): 753.

4. W.S. Huang and A.G. MacDiarmid. *Optical properties of polyaniline,* Polymer, 1993. **34**(9): 1833.

5. A.G. MacDiarmid. *Nobel Lecture: "Synthetic metals": A novel role for organic polymers,* Reviews of Modern Physics, 2001. **73**(3): 701-712.

6. E.A. Silinsh and V. Capek. *Organic Molecular Crystals,* 1994: AIP Press, New York.

7. S. Marchant and P.J.S. Foot. *Optoelectronic properties of poly(3-hexylthiophene) thin films,* Materials Science and Engineering B, 1991. **9**(1-3): 269.

8. S.A. Visser, W.T. Gruenbaum, E.H. Magin and P.M. Borsenberger. *Hole transport in arylamine doped polymers,* Chemical Physics, 1999. **240**(1-2): 197-203.

9. I.G. Hill, A. Kahn, Z.G. Soos and J.R.A. Pascal. *Charge-separation energy in films of [pi]-conjugated organic molecules,* Chemical Physics Letters, 2000. **327**(3-4): 181.

10. W. Brutting. *Device physics of organic light-emitting diodes based on molecular materials,* Organic Electronics, 2001. **2**(1): 1-36.

11. M. Pope, H.P. Kallmann and P. Magnante. *Electroluminescence in organic crystals,* The journal of Chemical Physics, 1963. **38**(8): 2042-2043.

12. C.W. Tang and S.A. Vanslyke. *Organic Electroluminescent Diodes,* Applied Physics Letters, 1987. **51**(12): 913-915.

13. J. Dresner. *Double Injection Electroluminescence in Anthracene,* RCA Review, 1969. **30**: 322-334.

14. W. Helfrich and W.G. Schneidere. *Recombination Radiation in Anthracene Crystals,* Physical Review Letters, 1965. **14**(7): 229-231.

15. W. Helfrich and W.G. Schneidere. Journal of Chemical Physics, 1965. **14**: 2902.

16. D.F. Williams and M. Schadt. *A simple Organic Electroluminescent Diode,* Proceedings of the IEEE, 1970. **58**(3): 476.

17. J.H. Burroughes, D.D.C. Bradley, A.R. Brown, R.N. Marks, K. Mackay, R.H. Friend, P.L. Burns and A.B. Holmes. *Light-emitting diodes based on conjugated polymers,* Nature, 1990. **347**(6293): 539-541.

18. M.J.M. De Jong and M.C.J.M. Vissenberg. *Theory of luminescence quenching and photobleaching in conjugated polymers,* Philips Journal of Research, 1998. **51**(4): 495.

19. Z.G. Soos, M.H. Hennessy and G. Wen. *Frenkel and charge transfer states of conjugated polymers and molecules,* Chemical Physics, 1998. **227**(1-2): 19.

20. R. Schuster, M. Knupfer and H. Berger. *Exciton Band Structure of Pentacene Molecular Solids: Breakdown of the Frenkel Exciton Model,* Physical Review Letters, 2007. **98**(3): 037402.

21. M. Yano, Y. Okino, Y. Ichihara, M. Tatsumi, M. Oyama, K. Sato and T. Takui. *Organic high-spin systems: Synthesis, electrochemical and spectroscopic studies of [pi]-extended tetraaryl m-phenylenediamines,* Polyhedron, 2009. **28**(9-10): 1764.

22. R.H. Friend, R.W. Gymer, A.B. Holmes, J.H. Burroughes, R.N. Marks, C. Taliani, D.D.C. Bradley, D.A. dos Santos, J.L. Bredas, M. Logdlund and W.R. Salaneck. *Electroluminescence in conjugated polymers,* Nature, 1999. **397**(6715): 121-128.

23. M. Segal, M.A. Baldo, M.K. Lee, J. Shinar and Z.G. Soos. *Frequency response and origin of the spin-1/2 photoluminescence-detected magnetic resonance in a pi-conjugated polymer.,* Physical Review B, 2005. **71**(245201).

24. J. Cornil, D. Beljonne, D.A. Dos Santos, Z. Shuai and J.L. Bredas. *Towards a better understanding of polymer-based light-emitting diodes: A theoretical insight into the basic phenomena,* Synthetic Metals, 1996. **78**(3): 209.

25. M.S. Weaver, D.G. Lidzey, T.A. Fisher, M.A. Pate, D. O'Brien, A. Bleyer, A. Tajbakhsh, D.D.C. Bradley, M.S. Skolnick and G. Hill. *Recent progress in polymers for electroluminescence: microcavity devices and electron transport polymers,* Thin Solid Films, 1996. **273**(1-2): 39.

26. D.R. Baigent, N.C. Greenham, J. Gruner, R.N. Marks, R.H. Friend, S.C. Moratti and A.B. Holmes. *Light-emitting diodes fabricated with conjugated polymers — recent progress,* Synthetic Metals, 1994. **67**(1-3): 3-10.

27. D. Braun. *Semiconducting polymer LEDs,* Materials Today, 2002. **5**(6): 32.

28. M. Yan, L.J. Rotheberg, F. Padadimitrakopoulos, M.E. Galvin and T.M. Miller. *Defect quenching of conjugated polymer luminescence,* Physical Review Letters, 1994. **73**(5): 744-777.

29. D.Y. Kim, H.N. Cho and C.Y. Kim. *Blue light emitting polymers,* Progress in Polymer Science, 2000. **25**(8): 1089.

30. H. Schenk, H. Becker, O. Gelsen, E. Kluge, W. Kreuder and H. Spreitzer. *Polymers for light emitting diodes,* Proceedings to EuroDisplay'99, 1999: 33-37.

31. J.C. Scott, J.H. Kaufman, P.J. Brock, R. DiPietro, J. Salem and J.A. Goitia. *Degradation and failure of MEH-PPV light-emitting diodes,* Journal of Applied Physics, 1996. **79**(5): 2745-2751.

32. B.H. Cumpston and K.F. Jensen. *Photo-oxidation of polymers used in electroluminescent devices,* Synthetic Metals, 1995. **73**(3): 195.

33. U. Scherf and E.J.W. List. *Semiconducting polyfluorenes - Towards reliable structure - Property relationships,* Advanced Materials, 2002. **14**(7): 477-487.

34. S.A. Carter, M. Angelopoulos, S. Karg, P.J. Brock and J.C. Scott. *Polymeric anodes for improved polymer light-emitting diode performance,* Applied Physics Letters, 1997. **70**(16): 2067-2069.

35. J.P. Chen, G. Klaerner, J.I. Lee, D. Markiewicz, V.Y. Lee, R.D. Miller and J.C. Scott. *Efficient, blue light-emitting diodes using cross-linked layers of polymeric arylamine and fluorene,* Synthetic Metals, 1999. **107**(2): 129.

36. J.M. Ginder, A.J. Epstein and A.G. MacDiarmid. *Phenyl ring rotations, structural order and electronic states in polyaniline,* Synthetic Metals, 1990. **37**(1-3): 45.

37. A.G. Macdiarmid and A.J. Epstein. *Polyanilines - A Novel Class Of Conducting Polymers,* Faraday Discussions of the Chemical Society, 1989. **87**: 317.

38. B.C. Wang, H.R. Liao, J.C. Chang, L. Chen and J.T. Yeh. *Electronic structure and molecular orbital study of hole-transport material triphenylamine derivatives,* Journal of Luminescence, 2007. **124**(2): 333.

39. T. Kato, T. Mori and T. Mizutani. *Effect of fabrication conditions on photoluminescence and absorption of hole transport materials,* Thin Solid Films, 2001. **393**: 109-113.

40. R.J. Bushby, C.A. Kilner, N. Taylor and M.E. Vale. *Disjoint and coextensive amminium radical cations: a general problem in making amminium radical cation based high-spin polymers,* Tetrahedron, 2007. **63**(46): 11458.

41. P.S. Antonel, E.M. Andrade and F.V. Molina. *Potential and film thickness dependence of the photoluminescence of aryl amine polymers*, Electrochimica Acta, 2004. **49**(22-23): 3687.

42. R.R. Cooney and S.G. Urquhart. *Chemical trends in the Near edge X-ray absorption fine structure of monosubstituted and para-bisubstituted benzenes*, Journal of Physical Chemistry B, 2004. **108**(47): 18185-18191.

43. J. Stohr. *NEXAFS Spectroscopy*, 1996: Springer.

44. C. Battocchio, I. Fratoddi, M.V. Russo and G. Polzonetti. *NEXAFS study of a Pt-containing rod-like organometallic polymer (Pt-DEBP): molecular orientation onto HOPG, Au/Si(1 1 1), Cr/Si(1 1 1) and Si(1 1 1) surfaces*, Chemical Physics Letters, 2004. **400**(4-6): 290.

45. J. Stöhr and D.A. Outka. *Determination of molecular orientations on surfaces from the angular dependence of near-edge x-ray-absorption fine-structure spectra*, Physical Review B, 1987. **36**(15): 7891.

46. M.A. Baldo, Z.G. Soos and S.R. Forrest. *Local order in amorphous organic molecular thin films*, Chemical Physics Letters, 2001. **347**(4-6): 297.

47. E. Kawabe, D. Yoshimura, K. Kanai, Y. Ouchi, S. Hasegawa, K.K. Okudaira, N. Ueno and K. Seki. *Epitaxial growth of hexadecafluorozincphthalocyanine (F16ZnPc) film deposited on GeS(0 0 1)*, Surface Science, 2008. **602**(7): 1328.

48. G. Iucci, V. Carravetta, G. Paolucci, A. Goldoni, M.V. Russo and G. Polzonetti. *Phenylacetylene adsorption on Rh(1 0 0): a photoemission and photoabsorption investigation*, Chemical Physics, 2005. **310**(1-3): 43.

49. G. Polzonetti, V. Carravetta, M.V. Russo, G. Contini, P. Parent and C. Laffon. *Phenylacetylene chemisorbed on Pt (111), reactivity and molecular orientation as probed by NEXAFS Comparison with condensed multilayer and polyphenylacetylene*, Journal of Electron Spectroscopy and Related Phenomena, 1999. **98-99**: 175.

50. M.V. Russo, G. Infante, G. Polzonetti, G. Contini, G. Tourillon, P. Parent and C. Laffon. *Evidence of the molecular orientation of Pt- and Pd-containing organometallic polymers in thick layers: a NEXAFS study*, Journal of Electron Spectroscopy and Related Phenomena, 1997. **85**(1-2): 53.

51. O. Werzer, K. Matoy, P. Strohriegl and R. Resel. *Temperature treatment of semiconducting polymers: An X-ray reflectivity study*, Thin Solid Films, 2007. **515**(14): 5601.

52. L. Sabbatini, C. Malitesta, E. De Giglio, I. Losito, L. Torsi and P.G. Zambonin. *Electrosynthesised thin polymer films: the role of XPS in the design of application oriented innovative materials*, Journal of Electron Spectroscopy and Related Phenomena, 1999. **100**(1-3): 35.

53. Q. Luo, X. Chen, Z. Liu, Z. Sun and N. Ming. *Deposition of oriented polymer films for liquid crystal alignment by pulsed laser ablation,* Applied Surface Science, 1997. **108**(1): 89.

54. K. Yoshino, M. Hikida, M. Tatsumi, K. Kaneto and Y. Inuishi. *Emission Spectra of Phthalocyanine Crystals,* Journal of the Physical Society of Japan, 1973. **34**(2): 441.

55. P.S. Vincett, E.M. Voigt and K.E. Rieckhoff. *Phosphorescence and Fluorescence of Phthalocyanines,* Journal of Chemical Physics, 1971. **55**(8): 4131.

56. T. Katsumi. *Photochemical and photophysical behaviour of porphyrins and phthalocyanines irradiated with violet or ultraviolet light,* Journal of Porphyrins and Phthalocyanines, 2001. **5**(1): 77-86.

57. Z. Sheng, X. Ye, Z. Zheng, S. Yu, K. Dennis, T. Ngai and C. Wu. *Transient Absorption and Fluorescence Studies of Disstacking Phthalocyanine by Poly(ethylene oxide),* Macromolecules, 2002. **35**(9): 3681-3685.

58. T. Ngai, G. Zhang, X. Li, K. Dennis and C. Wu. *Disstacking of Phthalocyanine in Water by Poly(ethylene Oxide),* Langmuir, 2001. **17**(5): 1381-1383.

59. A.N. Vzorov, L.G. Marzilli, R.W. Compans and D.W. Dixon. *Prevention of HIV-1 infection by phthalocyanines,* Antiviral Research, 2003. **59**(2): 99.

60. K. Toyota, J. Hasegawa and H. Nakatsuji. *Excited States of Free Base Phthalocyanine Studied by the SAC-CI Method,* Journal of Physical Chemistry A, 1997. **101**(4): 446.

61. Z.G. Guo, C.H. Cheng, Z.Q. Fan, W. He, S.K. Yu, Y.C. Chang, X.G. Du, X. Wang and G.T. Du. *Near-infrared emission from organic light-emitting diodes based on copper phthalocyanine with a periodically arranged Alq(3): CuPc/DCM multilayer structure,* Chinese Physics Letters, 2008. **25**(2): 715-718.

62. D.W. Dixon, A.F. Gill and B.R. Sook. *Characterization of sulfonated phthalocyanines by mass spectroscopy and capillary electrophoresis*, Journal of Porphyrins and Phthalocyanines, 2004. **8**(11): 1300-1310.

63. J.F. Lipskier and T.H. Tran-Thi. *Supramolecular assemblies of porphyrins and phthalocyanines bearing oppositely charged substituents. First evidence of heterotrimer formation,* Inorganic Chemistry, 1993. **32**(5): 722.

64. Y. Takahashi and H. Tadokoro. *Structural Studies of Polyethers, (-(CH2)m-O-)n. X. Crystal Structure of Poly(ethylene oxide),* Macromolecules, 1973. **6**(5): 672.

65. Q.J. Sun, H.Q. Wang, C.H. Yang, X.G. Wang, D.S. Liu and Y.F. Li. *Polymer light-emitting electrochemical cells with the block copolymers containing PEO segments,* Thin Solid Films, 2002. **417**(1-2): 14.

66. R.G. Linford. *EXAFS studies of polymer electrolytes,* Chemical Society Reviews, 1995. **24**(4): 267-277.

67. P. Dayal, V. Pillay, R.J. Babu and M. Singh. *Box-Behnken Experimental Design in the Development of a Nasal Drug Delivery System of Model Drug Hydroxyurea: Characterization of Viscosity, In Vitro Drug Release, Drolet Size and Dynamic Surface Tension,* AAPS PharmSciTech, 2005. **6**(4): 573-585.

68. HE Haifeng, CAO Hongqing, WAN Xinhua, TU Yingfeng, CHEN Xiaofang and Z. Qifeng. *Synthesis and ordered aggregation in water of a blue light-emitting PEO-PHP-PEO triblock oligomer,* Chinese Science Bulletin, 2003. **48**(15): 1525-1530.

69. J. Thompson, V. Arima, F. Matino, R. Cingolani and R.I.R. Blyth. *Characterisation of thin films of organic phosphorescent materials using synchrotron radiation,* Applied Surface Science, 2005. **248**(1-4): 36.

70. P. Moriarty, M.D.R. Taylor and M. Brust. *Nanostructured Cellular Networks,* Physical Review Letters, 2002. **89**(24): 248303.

71. M.D.R. Taylor, P. Moriarty and M. Brust. *Polydisperse Au nanoclusters on silicon: fractal aggregates via spinodal decomposition?* Chemical Physics Letters, 2001. **348**(1-2): 27-33.

72. B. Brozek-Pluska, I. Szymczyk and H. Abramczyk. *Raman spectroscopy of phthalocyanines and their sulfonated derivatives,* Journal of Molecular Structure, 2005. **744-747**: 481.

73. S. Tang, C. Shao, Y. Liu, S. Li and R. Mu. *Electrospun nanofibres of poly(ethylene oxide)/teraamino-phthalocyanine copper(II) hybrids and its photoluminescence properties.,* Journal of Physics and Chemistry of Solids, 2007. **68**(12): 2337-2340.

74. T. Toader, G. Gavrila, J. Ivanco, W. Braun and D.R.T. Zahn. *Controlling geometric and electronic properties of highly ordered CuPc thin films,* Applied Surface Science, 2009. **255**(15): 6806-6808.

75. J. Kikuma and B.P. Tonner. *XANES spectra of a variety of widely used organic polymers at the C K-edge,* Journal of Electron Spectroscopy and Related Phenomena, 1996. **82**(1-2): 53-60.

76. Y. Niwa, H. Kobayash and T. Tsuchiya. *X-ray photoelectron spectroscopy of tetraphenylporphin and phthalocyanine,* Journal of Chemical Physics, 1974. **60**(3): 799-807.

77. N. Peltekis, B.N. Holland, S. Krishnamurthy, I.T. McGovern, N.R.J. Poolton, S. Patel and C. McGuinness. *Electronic and Optical Properties of Magnesium Phthalocyanine (MgPc) Solid Films Studied by Soft X-Ray Excited Optical Luminescence and X-Ray Absorption Spectroscopies*, Journal of the American Chemical Society, 2008. **130**(39): 13008.

Chapter 7

Conclusions and future work

The electrospray deposition (ESD) system built as part of this work was used to deposit thin films of PEO into a high vacuum of 10^{-7}mBar. The planarity of the PEO thin films was shown to be improved by higher vacuum levels, and distinct areas of bead, chain, dendrite and fibrous growth were identified within the films. However a significant solvent presence at the substrate was noted for all samples indicating there to be a low drying efficiency of the ES droplets within the differential pumping system. The future aim for the ESD system is to deposit organic thin films directly into UHV enabling real time XPS analysis of film growth on surfaces. Therefore in order for this to be achieved the vacuum levels within the differential pumping system must be improved. Several improvements are planned including in flight manipulation of the deposition beam, additional pumping stages and an inert gas (N_2) chamber at the emitter tip.

A plasma deposition chamber is also planned, in which substrate surfaces will be prepared prior to electrospray deposition. This is of particular interest in the modification of diamond surface terminations. Investigations into the modification of small organic molecules on diamond surfaces are one of the current research interests of the Materials Research Group at Aberystwyth University.

Low energy luminescent emission (XEOL) was used as a probe into the electronic structure of hexagonal (h-BN) and cubic (c-BN) boron nitride using synchrotron based techniques. For h-BN emission was in the deep UV and UV/visible regions of

the spectrum, deep UV bands were resolved at 5.32eV, 5.49eV and 5.62eV and visible bands at 2.84eV, 3.25eV, 3.99eV and 4.49eV. For c-BN the emission was in the UV/visible region of the spectrum, emission bands were resolved at 2.98eV, 3.28eV, 3.95eV and 4.32eV. The XEOL emission of both phases was shown to exhibit phonon contribution which was correlated to the energies of Raman spectra lines.

Spatially resolved XEOL and OD-XANES was used to investigate c-BN identifying structural variation which was not identified in the volume-integrated measurements. OD-XANES mapping indicated structural variations between individual crystals, including identification of surface carbon states and crystal thickness variation. Infrared emission from both the 10-20μm and 100μm c-BN samples was attributed to the presence of calcium within the structure and was shown to originate from the surface states of the 100μm crystals. The ratio of infrared to visible emission was used as an indication of Ca content proving the 10-20μm c-BN crystals to be of higher purity than the 100μm c-BN crystals.

The band gap energies of c-BN and h-BN were determined using OD-XAS in the VUV region of the spectrum. The band edge spectra of the two phases were markedly different which can be attributed to the presence of shallow defect states only found in the hexagonal phase (XEOL). Band gap energies of 5.96eV ± 0.04eV and 6.36eV ± 0.03eV were resolved for h-BN and c-BN respectively.

Pump probe spectroscopy determined defect state energies within the band gaps of both h-BN and c-BN. For h-BN a defect state 2.87eV above the valence band was

attributed to an emission energy of 3.09eV. Correlation to the XEOL spectra proved this to be located within 0.01eV of the predicted zero phonon energy of the 2.84eV emission band. For c-BN a defect state 2.63eV above the valence band was attributed to an emission energy of 3.73eV. Correlation to the XEOL spectra proved this to be located within 0.02eV of the predicted zero phonon line of the 2.98eV emission band.

Future work required on BN includes further characterisation of the defect states and the chemical environment in which they reside. One possible method for investigation is to use magnetic resonance in conjunction with luminescent detection. This type of experiment will yield the chemical environment of the defect state within the materials.

The optically detected experimental investigations conducted on BN within this thesis could be extended to other wide band gap semi-conductors including other phases of BN and diamonds.

The orientation of poly(tri-phenlyamine) thin films was investigated using angular resolved NEXAFS. The angular dependence of the initial C1s-π^* resonance was proven, indicating the phenyl rings of the polymer to be standing up from the surface plane with a tilt angle of less than 20˚. Photo-luminescent emission was in the blue region of the spectrum with two excitonic bands resolved at 2.820eV and 2.978eV. Spatially resolved OD-NEXAFS of the poly(tri-phenylamine) indicated segmented growth within the film in which areas of different orientation were identified.

In order to build a better understanding of the self-organisation mechanisms of poly(tri-phenylamine) further study is required. The substrate material has an unknown role in the self organisation of these materials, therefore deposition onto a

range of substrates would be advantageous. One possible method is ESD which would allow samples of varied thickness to be grown.

Investigations of the luminescent properties of ESD prepared organic thin films were presented. Thin films of PEO, tsCuPc and tsCuPc/PEO materials were deposited onto silicon in high vacuum. The surface morphologies of the samples were investigated using AFM which indicated the tsCuPc aggregated upon the surface whereas the polymer based samples were shown to have amorphous structure. All the films were investigated using PL and OD-NEXAFS with only the tsCuPc/PEO material emitting light within the detectable range (200-1000nm). OD-NEXAFS confirmed the origin of the light emission to be localised to the tsCuPc within the tsCuPc/PEO material. It is concluded that PEO disstacked the tsCuPc within the deposited film resulting in suppression of non-radiative decay channels, thus enabling Q-band luminescent emission at 1.625eV (763nm), the first witnessed from a tsCuPc based thin film.

Future work required upon the tsCuPc/PEO material includes time-resolved measurements of the luminescent decay to establish whether the emission is fluorescent or phosphorescent in nature. If phosphorescent, the tsCuPc/PEO material could be used to produce OLEDs with high quantum efficiencies. Therefore novel devices based upon this material would need to be fabricated and investigated using electro-luminescence.

Further work is required to investigate the effect of PEO addition to other phthalocyanines and small molecules, as novel light emitting materials are of importance in the development of OLEDs.